



RESEARCH AND DEVELOPMENT OF $\text{Li}_{0.5}\text{La}_{0.5}\text{TiO}_3$ AND $\text{Li}_{6.25}\text{Ga}_{0.25}\text{La}_3\text{Zr}_2\text{O}_{12}$
SOLID-STATE ELECTROLYTE MATERIALS FOR COMPOSITE POLYMER
ELECTROLYTE IN SEMI-SOLID-STATE
LITHIUM BATTERIES FOR ENERGY STORAGE DEVICES

BY
SUPASIT PAENGSON

A Thesis Submitted in Partial Fulfillment of the Requirements for
The Doctor of Philosophy Degree in Physics
Sakon Nakhon Rajabhat University

May 2024

All Rights Reserved by Sakon Nakhon Rajabhat University

RESEARCH AND DEVELOPMENT OF $\text{Li}_{0.5}\text{La}_{0.5}\text{TiO}_3$ AND $\text{Li}_{6.25}\text{Ga}_{0.25}\text{La}_3\text{Zr}_2\text{O}_{12}$
SOLID-STATE ELECTROLYTE MATERIALS FOR COMPOSITE POLYMER
ELECTROLYTE IN SEMI-SOLID-STATE
LITHIUM BATTERIES FOR ENERGY STORAGE DEVICES

BY

SUPASIT PAENGSON

A Thesis Submitted in Partial Fulfillment of the Requirements for

The Doctor of Philosophy Degree in Physics

Sakon Nakhon Rajabhat University

May 2024

All Rights Reserved by Sakon Nakhon Rajabhat University



DISSERTATION APPROVAL
SAKON NAKHON RAJAPHAT UNIVERSITY
DOCTOR OF PHILOSOPHY
PROGRAM IN PHYSICS

Thesis Title: Research and Development of $\text{Li}_{0.5}\text{La}_{0.5}\text{TiO}_3$ and $\text{Li}_{6.25}\text{Ga}_{0.25}\text{La}_3\text{Zr}_2\text{O}_{12}$ Solid-State Electrolyte Materials for Composite Polymer Electrolyte in Semi-Solid-State Lithium Batteries for Energy Storage Devices

Author: Supasit Paengson

Dissertation Examination Committee

N. Meethong
..... Chairperson
(Assoc. Prof. Dr. Nongrak Meethong)

Wirat Jarernboon
..... Committee
(Assist. Prof. Dr. Wirat Jarernboon)

Wilawan Kumharn
..... Committee
(Assoc. Prof. Dr. Wilawan Kumharn)

T. Seetawan
..... Committee
(Prof. Dr. Tosawat Seetawan) and Advisor

Athorn Vora-ud
..... Committee
(Assoc. Prof. Dr. Athorn Vora-ud)

Hassakorn Wattanasarn
..... Committee
(Assist. Prof. Dr. Hassakorn Wattanasarn)

Approval by the Curriculum Committee

Athorn Vora-ud
.....
(Assoc. Prof. Dr. Athorn Vora-ud)

Chair of the Committee for Curriculum
Administration Approval
Sakon Nakhon Rajabhat University

Approval by Graduate School

Surasak Santhaveesuk
.....
(Assist. Prof. Dr. Surasak Santhaveesuk)

The Director of Graduate School
Sakon Nakhon Rajabhat University

27 MAY 2024

ACKNOWLEDGEMENTS

First and foremost, I would like to express my sincere gratitude to my supervisor, Prof. Dr. Tosawat Seetawan, for providing me with the opportunity to pursue my research in the field of energy storage under his guidance. He has consistently been an exceptional advisor and a patient teacher. This dissertation could not have been realized without his unwavering support and guidance. I would also like to extend my thanks to Assoc. Prof. Dr. Daisuke Mori, Assist. Prof. Dr. Sao Taminato, and Prof. Nobuyuki Imanishi for their invaluable advice on the ceramic and polymer aspects of my work, including guidance on maintaining homogenous ceramics distribution in polymer matrices, insights into possible electrolyte effects on ionic conductivity, and assistance with apparatus for characterizations.

I am grateful to my research mates Panida Pilasuta, Yuzo Kanamori, Mao Mikami, Kazuki Yonezawa, Atsushi Suzuki, and friends from the Imanishi's group for their contributions to my research and their insightful discussions during our time at Mie University. Special thanks to Assoc. Prof. Ronariddh Nakhongwong for introducing electrochemical measurement techniques at Ubon Ratchathani Rajabhat University, and to my family for their unwavering support during the challenging times of COVID-19.

I extend my gratitude to the thesis committee members, including Assoc. Prof. Dr. Nonglak Meethong, Assist. Prof. Dr. Wirat Jarembon, Assoc. Prof. Dr. Wilawan Kumharn, Assoc. Prof. Dr. Athorn Vora-ud, and Assist. Prof. Dr. Hassakorn Wattanasarn, for their valuable advice and helpful suggestions.

Acknowledgment is also due to all the staff at the Center of Excellence on Alternative Energy (CEAE), Program of Physics at Sakon Nakhon Rajabhat University, for their assistance with my thesis. I am thankful to Kinetics Corporation Ltd. for their helpful suggestions regarding concepts and trends to develop research topics.

Finally, I would like to acknowledge this research project is supported by the National Research Council of Thailand (NRCT) grant number NRCT5-RGJ63015-149 through the Royal Golden Jubilee 22 scholarship (RGJ22) Ph.D. Program.

Supasit Paengson

ชื่อเรื่อง	การวิจัยและพัฒนาวัสดุอิเล็กโทรไลต์แบบของแข็ง $\text{Li}_{0.5}\text{La}_{0.5}\text{TiO}_3$ และ $\text{Li}_{6.25}\text{Ga}_{0.25}\text{La}_3\text{Zr}_2\text{O}_{12}$ สำหรับอิเล็กโทรไลต์โพลีเมอร์คอมโพสิตในแบตเตอรี่ลิเทียมกึ่งของแข็งสำหรับอุปกรณ์กักเก็บพลังงาน
ผู้วิจัย	นายสุภศิษฏ์ แพงสอน
ที่ปรึกษา	ศาสตราจารย์ ดร. ทศวรรษ สีตะวัน
ปริญญา	ปร.ด. (ฟิสิกส์)
สถาบัน	มหาวิทยาลัยราชภัฏสกลนคร
ปีที่พิมพ์	2567

บทคัดย่อ

แบตเตอรี่ลิเทียมแบบของแข็งทั้งหมด ได้รับความสนใจอย่างมากในช่วงไม่กี่ปีที่ผ่านมา เนื่องจากมีศักยภาพในการให้ความหนาแน่นของพลังงานที่สูงขึ้นและเพิ่มความปลอดภัยเมื่อเปรียบเทียบกับแบตเตอรี่ลิเทียมไอออน (LIB) ที่ใช้อิเล็กโทรไลต์ของเหลวทั่วไป ลิเทียมแลนทานัมไททาเนต (LLTO) เป็นอิเล็กโทรไลต์แบบของแข็งที่มีศักยภาพสำหรับแบตเตอรี่ลิเทียมรุ่นต่อไป เนื่องจากมีการนำไอออนนิกสูงประมาณ $10^{-3} \text{ S}\cdot\text{cm}^{-1}$ ที่อุณหภูมิห้อง (RT) ในการศึกษาวัสดุ $\text{Li}_{0.5-x}\text{La}_{0.5-x}\text{Sr}_x\text{Ti}_{1-x}\text{Ta}_x\text{O}_3$ ที่เจือด้วย Sr และ Ta ถูกสังเคราะห์โดยวิธีปฏิกิริยาสถานะของแข็ง โดย Sr^{2+} และ Ta^{5+} ที่มีรัศมีไอออนมากกว่าถูกนำมาใช้สำหรับการแทนที่ร่วมในตำแหน่ง La^{3+} และ Ti^{4+} ตามลำดับ เพื่อเพิ่มขนาดคอขวดของไซต์ A และขยายความยาวพันธะเฉลี่ยของไซต์ B บน โครงสร้างเพอร์รอฟสไกต์ (ABO_3) จึงเพิ่มความคล่องตัวของลิเทียมไอออน เม็ด $\text{LLSr}_x\text{TTa}_x\text{O}_3$ ($0 \leq x \leq 0.12$) มีความหนาแน่นสัมพัทธ์สูง และมีค่าการนำไฟฟ้าของเกรนสูง โดยที่ค่าการนำไอออนรวมของ $\text{LLSr}_{0.09}\text{TTa}_{0.09}\text{O}_3$ สูงถึง $4.12 \times 10^{-5} \text{ S}\cdot\text{cm}^{-1}$ เมื่อเปรียบเทียบกับชิ้นงานทดสอบบริสุทธิ์ที่ไม่ได้ทำการเจือ ค่าการนำไฟฟ้ายรวมของชิ้นงานที่เจือมีค่าประมาณมากกว่า 2.7 เท่าที่อุณหภูมิห้อง เซลล์แบตเตอรี่แบบเต็ม LFP/10 wt.% $\text{LLSr}_{0.09}\text{TTa}_{0.09}\text{O}_3$ /Li กึ่งของแข็งที่ประกอบมีความจุการคายประจุจำเพาะที่ 0.1C เท่ากับ $156 \text{ mAh}\cdot\text{g}^{-1}$ และอัตราการคงอยู่ความจุที่ 1C ร้อยละ 86 หลังจาก 290 รอบที่อุณหภูมิห้อง

นอกจากนี้ คอมโพสิตโพลีเมอร์อิเล็กโทรไลต์ (CPEs) ที่มีความปลอดภัยสูงยังได้รับการพัฒนาโดยการรวมผง $\text{Li}_{6.25}\text{Ga}_{0.25}\text{La}_3\text{Zr}_2\text{O}_{12}$ (LLZO-Ga) ชนิดโกลเม็นที่เป็นวัสดุนำ

ไอออนสูงเข้ากับเมทริกซ์โพลีไวนิลิดีนฟลูออไรด์-โค-เฮกซาฟลูออโรโพรพิลีน (PVDF-HFP) พร้อมด้วยลิเทียม บิส(ไตรฟลูออโรมีเทนซัลโฟนิล)อีไมด์ (LiTFSI) คอมโพลีเมอร์ อิเล็กโทรไลต์ที่มีน้ำหนัก 10% LLZO-Ga บรรลุค่าการนำไฟฟ้าไอออนิกที่ $7.12 \times 10^{-4} \text{ S cm}^{-1}$ และช่วงศักย์ไฟฟ้าไฟฟ้าขยายได้ถึง 4.90 V เทียบกับ Li/Li^+ นอกจากนี้ การก่อตัวและองค์ประกอบของชั้นซัลไฟด์อิเล็กโทรไลต์อินเทอร์เฟซ (SEI) ได้รับการวิเคราะห์ผ่าน เอ็กซ์เรย์โฟโตอิเล็กตรอนสเปกโทรสโกปี (XPS) เมื่อประกอบเซลล์จับคู่ร่วมกับแคโทด LFP และ NMC111 และการใช้อิเล็กโทรไลต์ที่มีความเข้มข้นสูง (4M LiFSI: DEE) เซลล์อิเล็กโทรไลต์โพลีเมอร์คอมโพลีเมอร์กึ่งแข็ง (QCPEs) แสดงประสิทธิภาพวงรอบการวัดที่มีแนวโน้มในอัตราที่แตกต่างกัน โดยรักษาความสามารถในการคายประจุเท่ากับ 108.7 mAh g^{-1} (LFP) และ 115.6 mAh g^{-1} (NMC111) ที่ 1C ตามลำดับ การทดสอบทางกลกับเซลล์กระเปาะของการตัด การตัด และการเผาไหม้ แสดงให้เห็นถึงความปลอดภัยที่เหนือกว่าและการใช้งานที่เป็นไปได้ของแบตเตอรี่กึ่งแข็งที่ใช้โพลีไวนิลิดีนฟลูออไรด์-โค-เฮกซาฟลูออโรโพรพิลีน พร้อมโลหะลิเทียมขั้วแอโนดที่อุณหภูมิห้อง

คำสำคัญ: ลูกบาศก์เพอร์รอฟสไกต์ อิเล็กโทรไลต์กึ่งแข็ง แบตเตอรี่ลิเทียม
โกเมน- $\text{Li}_{6.25}\text{Ga}_{0.25}\text{La}_3\text{Zr}_{12}\text{O}_{12}$ อิเล็กโทรไลต์โพลีเมอร์คอมโพลีเมอร์กึ่งแข็ง

TITLE	Research and Development of $\text{Li}_{0.5}\text{La}_{0.5}\text{TiO}_3$ and $\text{Li}_{6.25}\text{Ga}_{0.25}\text{La}_3\text{Zr}_2\text{O}_{12}$ Solid-State Electrolyte Materials for Composite Polymer Electrolyte in Semi-Solid-State Lithium Batteries for Energy Storage Devices
AUTHOR	Mr. Supasit Paengson
ADVISOR	Prof. Dr. Tosawat Seetawan
DEGREE	Ph.D. (Physics)
INSTITUTION	Sakon Nakhon Rajabhat University
YEAR	2024

ABSTRACT

All-solid-state lithium batteries (ASSBs) have gained significant attention in recent years because of their potential to offer higher energy density and enhanced safety compared to conventional liquid-electrolyte-based lithium-ion batteries (LIBs). Lithium lanthanum titanate (LLTO) is a promising solid electrolyte for next-generation lithium batteries owing to its high ionic conductivity of approximately $10^{-3} \text{ S}\cdot\text{cm}^{-1}$ at room temperature (RT). The Sr and Ta co-doped $\text{Li}_{0.5-x}\text{La}_{0.5-x}\text{Sr}_x\text{Ti}_{1-x}\text{Ta}_x\text{O}_3$ perovskites were synthesized by solid-state reaction. In this study, Sr^{2+} and Ta^{5+} , with larger ionic radii, were used for co-substitution in the La^{3+} and Ti^{4+} sites, respectively, to increase the bottleneck size of the A-site and expand the average bond length of the B-site on the perovskite structure (ABO_3), thereby increasing the Li^+ ion mobility. The $\text{LLSr}_x\text{TTa}_x\text{O}_3$ ($0 \leq x \leq 0.12$) pellets have high relative densities and high grain conductivities, where the total conductivity of $\text{LLSr}_{0.09}\text{TTa}_{0.09}\text{O}_3$ reached $4.12 \times 10^{-5} \text{ S}\cdot\text{cm}^{-1}$. Compared with the pure specimen, the total conductivities of the doped specimens are approximately more than 2.7 times at RT. The assembled semi-solid LFP/10 wt.% $\text{LLSr}_{0.09}\text{TTa}_{0.09}\text{O}_3/\text{Li}$ full battery has a 0.1C specific discharge capacity of $156 \text{ mAh}\cdot\text{g}^{-1}$ and a 1C capacity retention rate of 86% after 290 cycles at RT.

Furthermore, the highly secure composite polymer electrolytes (CPEs) were developed by incorporating the highly ion-conductive garnet-type $\text{Li}_{6.25}\text{Ga}_{0.25}\text{La}_3\text{Zr}_2\text{O}_{12}$ (LLZO-Ga) material into a polyvinylidene fluoride-co-hexafluoropropylene (PVDF-HFP) matrix along with lithium bis(trifluoromethanesulfonyl)imide (LiTFSI). The CPEs with 10% wt. LLZO-Ga achieved an ionic conductivity of $7.12 \times 10^{-4} \text{ S cm}^{-1}$ and an extended electrochemical window up to 4.90 V vs Li/Li⁺. Furthermore, the formation and composition of the solid electrolyte interphase (SEI) layer were analyzed through X-ray photoelectron spectroscopy (XPS). When coupled with LFP and NMC111 cathodes and using a high-concentration electrolyte (4MLiFSI: DEE), the quasi-solid composite polymer electrolyte cells (QCPEs) exhibited promising cycling performance at different rates, maintaining discharge capacities of 108.7 mAh g⁻¹ (LFP) and 115.6 mAh g⁻¹ (NMC111) at 1C, respectively. The mechanical tests with pouch cells of bending, cutting, and burning further highlighted the superior safety and potential applications of the PVDF-HFP-based quasi-solid batteries with Li metal at room temperature.

Keywords: Cubic-perovskite, Semi solid electrolyte, Lithium battery, Garnet- $\text{Li}_{6.25}\text{Ga}_{0.25}\text{La}_3\text{Zr}_2\text{O}_{12}$, Composite polymer electrolyte

TABLE OF CONTENTS

CHAPTER	Page
1 INTRODUCTION.....	1
RECHARGEABLE LITHIUM BATTERIES	1
LISICON	5
LIPON	5
NASICON	5
Sulfide	6
Garnet	6
Perovskite	7
RESEARCH OBJECTIVES.....	7
MOTIVATION AND SCOPE OF THE THESIS.....	7
ANTICIPATED OUTCOMES OF THE THESIS.....	9
THESIS STRUCTURE.....	9
2 THEORETICAL BACKGROUND AND LITERATURE REVIEWS.....	10
LI-ION BATTERY (LIB): STRUCTURE AND FUNCTIONAL MECHANISM	10
COMPONENTS OF A LI-ION BATTERY	12
Cathode materials	12
Anode	13
Electrolyte.....	13
MECHANISM OF LI-ION TRANSPORT IN SOLID AND	
COMPOSITE ELECTROLYTES	15
Electrochemical impedance spectroscopy (EIS).....	15
Temperature dependent conductivity measurements.....	16
Linear sweep voltammetry	17

TABLE OF CONTENTS

CHAPTER	Page
STRUCTURE OF PEROVSKITE OXIDE	18
LITHIUM LANTHANUM TITANATE ($\text{Li}_{3x}\text{La}_{2/3-x}\text{TiO}_3$)	20
Literature reviews of lithium lanthanum titanate ($\text{Li}_{3x}\text{La}_{2/3-x}\text{TiO}_3$) ...	23
GARNET-TYPE SOLID-STATE ELECTROLYTE MATERIALS.....	34
Li-ion conduction mechanism in Garnet-type	36
POLYMER ELECTROLYTES (PEs).....	37
COMPOSITE POLYMER ELECTROLYTES (CPEs)	39
Literature reviews of composite polymer electrolyte	40
3 MATERIALS AND METHODOLOGY	51
SYNTHESIS AND PREPARATION PEROVSKITE SOLID STATE ELECTROLYTE	51
Synthesis perovskite- $\text{Li}_{3x}\text{La}_{2/3-x}\text{TiO}_3$	51
Sintering bulk samples	55
Composite polymer electrolytes with $\text{LLSr}_{0.09}\text{TTa}_{0.09}\text{O}_3$ powder.....	58
SYNTHESIS AND PREPARATION GARNET SOLID STATE ELECTROLYTE...	59
Synthesis garnet - $\text{Li}_{6.75}\text{Ga}_{0.25}\text{La}_3\text{Zr}_2\text{O}_{12}$	59
Composite polymer electrolytes with $\text{Li}_{6.5}\text{Ga}_{0.25}\text{La}_3\text{Zr}_2\text{O}_{12}$ powder ..	62
CHARACTERIZATION TECHNIQUES	63
X-ray diffraction	63
Scanning electron microscopy	64
Archimedes density measurement	64
X-ray photoelectron spectroscopy.....	65
ELECTROCHEMICAL CHARACTERIZATIONS	67

TABLE OF CONTENTS (continued)

CHAPTER	Page
Electrochemical impedance spectroscopy	67
Lithium transference number.....	69
Electrochemical performance.....	70
Cyclic voltammetry and linear sweep voltammetry.....	70
ASSEMBLY OF ALL-SOLID-STATE LITHIUM BATTERIES.....	72
ASSEMBLY SEMI-SOLID-STATE BATTERIES FULL CELL.....	73
4 RESULTS AND DISCUSSION	75
CHARACTERIZATIONS OF PEROVSKITE-	
$\text{Li}_{0.5-x}\text{La}_{0.5-x}\text{Sr}_x\text{Ti}_{1-x}\text{Ta}_x\text{O}_3$ ($0 \leq x \leq 0.12$).....	75
Crystal structure, morphology, and chemical composition	75
Electrochemical properties and performance of full cells	85
CHARACTERIZATIONS OF GARNET- $\text{Li}_{6.75}\text{Ga}_{0.25}\text{La}_3\text{Zr}_2\text{O}_{12}$	
COMPOSITE POLYMER ELECTROLYTES.....	93
Crystal structure, morphology, and chemical composition	93
Electrochemical properties and performance of full cells	97
5 CONCLUSIONS AND SUGGESTION	112
CONCLUSIONS.....	112
All-solid-state and semi-solid-state	
perovskite- $\text{Li}_{0.5-x}\text{La}_{0.5-x}\text{Sr}_x\text{Ti}_{1-x}\text{Ta}_x\text{O}_3$ ($0 \leq x \leq 0.12$).....	112
Quasi-solid-state batteries with garnet- $\text{Li}_{6.75}\text{Ga}_{0.25}\text{La}_3\text{Zr}_2\text{O}_{12}$	
composite polymer electrolytes	113
SUGGESTIONS	114

TABLE OF CONTENTS (continued)

CHAPTER	Page
REFERENCES.....	115
APPENDICE	131
APPENDICE A: HISTORICAL DEVELOPMENT OF SOLID ELECTROLYTE, RAW DATA OF EIS, AND CALCULATION OF BOND DISTANCE	132
APPENDICE B: INTERNATIONAL CONFERENCE	147
APPENDICE C: PUBLICATIONS.....	150
APPENDICE D: RESEARCH VISITNG AT MIE UNIVERSITY JAPAN.....	163
APPENDICE E: A BRIEF HISTORY OF RESEARCHER	165

LIST OF TABLES

Table		Page
1	All possible lattice types, space groups and structural features of LLTO systems.....	21
2	The ionic and electronic conductivity of LLSTM sample at room temperature and E_a	26
3	Summary of bulk conductivity, grain–boundary conductivity, total conductivity, electronic conductivity, and activation energy of LSLTO samples.	27
4	Structural parameters, interatomic distances, densities, and total conductivities of $\text{LiSr}_{1-0.5x}\text{TiTaO}_{6-x}\text{F}_x$ perovskites. All patterns refined in the cubic $\text{Pm}\bar{3}\text{m}$ space group (N1 221).	28
5	Fit parameters and conductivity values of LLTO nanoparticles	32
6	Ionic conductivity σ_{bulk} , σ_{gb} and electronic conductivity σ_e for LLTGx ceramics at room temperature.	35
7	List of chemicals used for synthesis and preparation perovskite composite polymer electrolyte method their formula, supplier, and purity.....	52
8	List of equipment used for synthesis of powder, preparation of bulk, characterization, and measurement of thermoelectric properties together with their model and area of application	53
9	List of chemicals used for synthesis and preparation garnet composite polymer electrolyte method their formula, supplier, and purity.....	60
10	The data of all samples of lattice parameter, cell volume, density, and relative density for $\text{Li}_{0.5-x}\text{La}_{0.5-x}\text{Sr}_x\text{Ti}_{1-x}\text{Ta}_x\text{O}_3$ ($0 \leq x \leq 0.12$).....	78

LIST OF TABLES (continued)

Table	Page
11	The parameters of bulk resistance (R_g), grain–boundary resistance (R_{gb}) and total resistance (R_{total}) as well as corresponding ionic conductivity grain (σ_g), grain boundary (σ_{gb}), and total (σ_{total}), are obtained from the EIS curve fittings and calculations. 86
12.	Measured values of parameters and the corresponding calculated values of Li transference number at 25 °C..... 102
13	Raw data of EIS on LLTO sample..... 135
14	Raw data of EIS for $LLSr_{0.09}TTO_{0.9}O_3$ sample..... 147

LIST OF FIGURES

Figure		Page
1	Schematic of thermal runaway stage of liquid electrolyte in lithium-ion batteries.....	3
2	The comparative of advantage and disadvantage between liquid and solid electrolyte for lithium-ion batteries.....	4
3	Relative energies of the electrolyte window, E_g , and the relationship between electrochemical potentials of electrodes and the HOMO or LUMO of the electrolyte.	11
4	Schematic energy diagram of thermodynamically stable Li-ion battery.....	12
5	Nyquist plot.....	16
6	LSV curve of solid polymer electrolytes (SPEs) and composite polymer electrolytes (CPEs).....	18
7	ABO_3 cubic perovskite oxides unit cell.	19
8	(a) Cubic crystal structure of perovskite-type LLTO. (b) An AO_{12}	20
9	(a) Crystal structure of perovskite-type $La_{0.62}Li_{0.16}TiO_3$ (b) Scattering amplitude distribution in the vicinity of the (002) plane ($0.35 < z < 0.65$) of $La_{0.62}Li_{0.16}TiO_{3.0}$ at room temperature (c) Atomic arrangement on the (002) plane (d)Arrangement of A-site ion and oxide ions, and lithium-ion conduction in a perovskite type.	22
10	Crystal structure and bulk ionic conductivity of perovskite-type solid electrolytes $Li_{3x}La_{2/3-x}TiO_3$	23
11	(a) A comparison of Li^+ conductivities along with schematics of the domain microstructures of the LLTO electrolytes: low-T LLTO, high-T LLTO and Li-excess LLTO. (b) Arrhenius plots of the boundary conductivities for measured over a temperature range of -20 to 70 °C. The activation energy (E_a) values calculated are indicated.....	24

LIST OF FIGURES (Continued)

Figure		Page
12	Arrhenius plots for LLSTM samples.	25
13	Arrhenius plots of LSLTO–3, LSLTO–4, LSLTO–5, and LSLTO–6 samples.	27
14	Current vs. time curves of Au/LSLTO–3, LSLTO–4, LSLTO–5, and LSLTO–6/Au cells at a dc polarization potential of 4 V and a temperature of 20 °C.	27
15	Variations of the total conductivities of LLTM _x O (M = Sn or Ta) ceramics as function of x value at room temperature.	29
16	Arrhenius plots of the (a) LLTSn _x O (0 ≤ x ≤ 0.08) and (b) LLTTa _x O (0 ≤ x ≤ 0.08) ceramic specimens.	29
17	Refined lattice parameter a of Li _{0.33+x} La _{0.56-x} Sr _x TiO ₃ (x = 0, 0.03, 0.06, 0.09 and 0.12). Equivalent unit parameter for tetragonal structured sample (x = 0) is shown for comparison.	30
18	Ionic conductivities at RT and activation energy versus Sr doping amount with solid lines given as a visual guide.	31
19	(a) TEM micrograph of LLTO samples at different magnification. (b) SAED pattern spots indexed with corresponding (hkl) planes.	32
20	SEM patterns of LLTG _x ceramics. (a)x=0 wt%, (b)x=0.5 wt%, (c) x=1.0 wt%, (d) x=1.5 wt% and (e) x=2.0 wt%. Graph (f) is the EDS spectrum of the blue and green point marked in the patterns.	33
21	Different chemical compositions are possible in garnet–type Li–ion conductors.	35
22	(a) Variation of Li occupancy of tetrahedral and octahedral sites and room temperature conductivity as a function of Li content in the garnet structure (b) Distribution of Li–ions in tetrahedral (24d) and octahedral positions (48g and 96h).	37

LIST OF FIGURES (Continued)

Figure		Page
23	(a) Schematic of crystalline and amorphous regions in polymer (b) Li ion conduction mechanism in polymer-salt matrix.	38
24	Schematic diagram of the preparation process of the composite solid-state electrolyte for lithium metal batteries.	40
25	The schematic of the fabrication process of PLHL-CSE membrane.	42
26	Schematic representation of the preparation process of the PEO-based CSE enhanced by the 3D LLZO/PVDF-HFP fiber network structure.	43
27	(a) DFT calculation of PEO and PVDF, (b), (c) LSV and EIS curves of PVDF LLZTNO 10% CSSEs and PVDF membranes, (d) Galvanostatic cycling profiles of Li/ Li ⁺ symmetric cells at 0.1 mA cm ⁻² , 0.1 mAh cm ⁻²	44
28	The concept of poly (vinylidene fluoride)/ Li _{6.4} Ga _{0.2} La ₃ Zr ₂ O ₁₂ /succinonitrile composite solid electrolytes toward enhanced rate performance in all- solid-state lithium batteries.	45
29	(a) Efficiency of Li metal plating/stripping on a Cu substrate in LiFSI-DME and LiFSI-DEE. The optical images of the cycled Li-metal anode in (b) LiFSI-DME and f) LiFSI-DEE. SEM images of the Li-metal anode in the cell using (c-e) LiFSI-DME (c, d-top-view and e-cross- section) and g-i) LiFSI-DEE (g, h-top-view and i-cross-section).	46
30	Cycling of Li/LFP cells in LiFSI-DME and LiFSI-DEE. (a) discharge capacity and (b) efficiency. Rate performance of the Li/LFP cell using LiFSI in DME and DEE. (c) charging with an increasing C-rate but discharging at a rate of 0.5 C-rate and (d) charging at a 0.5 C-rate but discharging at an increasing C-rate.	47

LIST OF FIGURES (Continued)

Figure		Page
31	Electrochemical behavior of different ether electrolytes in Li NMC811 batteries. Cycling performance of Li NMC811 cells. (a) Efficiency and (b) discharge capacity using the HCE–DME and HCE–DEE electrolytes.	48
32	Electrochemical behaviors of anode–free Cu NMC811 batteries. (a) Efficiency and (b) sum of reversibly cycled Li over 50 cycles (charge/discharge current density of 0.3 C/1.0 C) obtained from Cu NMC811 cells in HCE–DME (4.0 m LiFSI–DME) and HCE–DEE (3.5 m LiFSI–DEE).....	49
33	High temperature furnace maximum temperature 1700 °C.....	54
34	Schematic of heating profile for calcination used to all samples in air.	55
35	Schematic of heating profile used for sintering of the samples with indicated heating /cooling rates in air.	56
36	Flowchart of $\text{Li}_{0.5-x}\text{La}_{0.5-x}\text{Sr}_x\text{Ti}_{1-x}\text{Ta}_x\text{O}_3$ ($0 \leq x \leq 0.12$) synthesis process.	57
37	Flowchart illustrating the preparation process of the perovskite composite polymer electrolytes.....	59
38	Flowchart of $\text{Li}_{6.25}\text{Ga}_{0.25}\text{La}_3\text{Zr}_2\text{O}_{12}$ synthesis process.	61
39	Flowchart illustrating the preparation process of the CPES.....	62
40	X–ray diffraction (a) Bragg’s law and (b) construction of an X–ray diffractometer (Myers 1997).	63
41	Processes that result from x–ray bombardment of a surface include (a) emission of a photoelectron, (b) x–ray fluorescence, and (c) emission of an Auger electron.	66
42	Energy level diagram illustrates schematically the basic XPS equation, including the x–ray source energy ($h\nu$), the binding energy of the electron (BE), the measured kinetic energy of the electron ($\text{KE}_{\text{measured}}$), and the work function of the spectrometer ($\Phi_{\text{spectrometer}}$).....	67

LIST OF FIGURES (Continued)

Figure	Page
43	Schematic for ac conductivity measurement sandwiched between two lithium electrodes. 68
44	Typical LSV experiment with a) voltage profile over time, b) current–voltage curve generated by voltage profile (Bard, A. J., Faulkner, L. R., & White, H. S. (2022)). 71
45	Typical CV experiment with a) voltage profile over time, b) current–voltage curve generated by voltage profile (Bard, A. J., Faulkner, L. R., & White, H. S. (2022)). 72
46	The preparation of all–solid–state batteries full cell. 73
47	The preparation 2032–type battery of semi–solid–state batteries with coin cell. 74
48	Crystal structure of Perovskite $\text{Li}_{3x}\text{La}_{2/3-x}\text{TiO}_3$ (LLTO)–type with $(0.04 < x < 0.16)$ 76
49	XRD pattern of (a) $\text{Li}_{0.5-x}\text{La}_{0.5-x}\text{Sr}_x\text{Ti}_{1-x}\text{Ta}_x\text{O}_3$ ($0 \leq x \leq 0.12$) sintered powders, and (b) the 2Theta of $31.5\text{--}34^\circ$ 77
50	The La–Ti, La–O and Ti–O bond distance of all samples $\text{Li}_{0.5-x}\text{La}_{0.5-x}\text{Sr}_x\text{Ti}_{1-x}\text{Ta}_x\text{O}_3$ ($0 \leq x \leq 0.12$). 78
51	The SEM of bulk samples (a) undoped $x = 0$, (b) $x = 0.01$, (c) $x = 0.03$, (d) $x = 0.06$, (e) $x = 0.09$, and (f) $x = 0.12$ 80
52	The histograms of grain size of bulk samples (a) undoped $x = 0$, (b) $x = 0.01$, (c) $x = 0.03$, (d) $x = 0.06$, (e) $x = 0.09$, and (f) $x = 0.12$ 81
53	The elemental mapping of the images of $\text{LLSr}_{0.09}\text{TTa}_{0.09}\text{O}_3$ (a) SEM surface, (b) Oxygen, (c) Lanthanum, (d) Strontium, (e) Titanium, and (f) Tantalum. 82

LIST OF FIGURES (Continued)

Figure	Page
54	The EDX graph and elemental contents of all samples $\text{Li}_{0.5-x}\text{La}_{0.5-x}\text{Sr}_x\text{Ti}_{1-x}\text{Ta}_x\text{O}_3$ ($0 \leq x \leq 0.12$)..... 82
55	The XPS analysis of (a) La 3d, (b) Sr 3d, (c) Ti 2p, and (d) Ta 4f of cubic-perovskite $\text{LLSr}_{0.09}\text{TTa}_{0.09}\text{O}_3$ sample..... 84
56	XPS Ti 2p spectra of bulk samples (a) undoped $x = 0$ and (b) $x = 0.09$ 84
57	EIS plots of $\text{Li}_{0.5-x}\text{La}_{0.5-x}\text{Sr}_x\text{Ti}_{1-x}\text{Ta}_x\text{O}_3$ ($0 \leq x \leq 0.12$) at 298 K (a) grain impedance, (b) grain boundary impedance with equivalent circuit model, (c) conductivities of all specimens and (d) grain and grain boundary conductivity mechanism. 87
58	Arrhenius plot of $\text{Li}_{0.5-x}\text{La}_{0.5-x}\text{Sr}_x\text{Ti}_{1-x}\text{Ta}_x\text{O}_3$ ($0 \leq x \leq 0.12$) at a temperature rang 298 to 373 K. (a) total conductivity, (b) grain conductivity, (c) grain boundary conductivity, and (d) the activation energy with doping contents..... 88
59	Potentiostatic polarization patterns of all samples under 4 V at 298 K..... 59
60	The sample (a) $\text{LLSr}_{0.09}\text{TTa}_{0.09}\text{O}_3$ pellet after full cell assembled and (b) composite polymer electrolyte of 10 wt.% $\text{LLSr}_{0.09}\text{TTa}_{0.09}\text{O}_3$ 90
61	The EIS of composite polymer electrolyte with 0–20 wt.% $\text{LLSr}_{0.09}\text{TTa}_{0.09}\text{O}_3$ powders at 30 °C..... 91
62	EIS of composite polymer electrolyte with CPE=0 and CPE=10 in Li- symmetric cells at 30 °C. 91
63	Electrochemical performance of $\text{LiFePO}_4/\text{Li}$ full cell (a) rate capability with 0.1C to 1 C, (b) charge–discharge profile in different C rate, (c) 1C rate charge–discharge profile stability of 290 cycles, and (d) cycling performance a 1C rate and coulombic efficiency. 93

LIST OF FIGURES (Continued)

Figure	Page
64	XRD patterns of LLZO–Ga powder, SPEs and CPEs with various contents of LLZO–Ga filler 5 to 20 %wt. 94
65	The FT – IR spectra of PVDF – HFP pellets, SPEs, and CPEs membranes with varying LLZO – Ga filler contents from 5 %wt. to 20 %wt. 96
66	(a) Optical image of SPEs and (b) CPEs – 10 membrane (c) The SEM of images of surface SPEs and (d) surface of CPEs – 10 membrane (e) The EDS elements mapping images of CPEs – 10 membranes..... 97
67	EIS curves of CSEs at different filled with LLZO–Ga contents. 98
68	Arrhenius plots of SPEs and CPEs at temperatures ranging from 10 to 80 C..... 99
69	LSV plots of the Au/ SPEs /Li and Au/CPEs–10/Li cell structures at room temperature. 100
70	Chronoamperometry curves of (a) Li/SPEs/Li and Li/CPEs – 10/Li with 4MLiFSI: DEE membrane with a bias potential of 10 mV; the inset is the impedances before and after polarization..... 101
71	Voltage profiles of Li plating and stripping cycling for the (a) SPEs, (b) CPEs – 10, with the current density of 0.1 mA cm^{-2} 103
72	Photograph of commercial separator Celgard, SPEs, and CPEs–10 films before and after heating at 25°C, 100°C, and 130 °C. 104
73	Electrochemical performances of the LFP/QCPEs–10/Li cell at RT (a) rate capability with 0.1 C to 1 C, (b) the corresponding specific capacity and voltage profile, (c) charge–discharge profile performance under 1C rate of 280 cycles and (d) corresponding charge–discharge curves of cyclic performance a 1c rate and coulombic efficiency. 105

LIST OF FIGURES (Continued)

Figure		Page
73	Electrochemical performances of the LFP/QCPEs–10/Li cell at RT (a) rate capability with 0.1 C to 1 C, (b) the corresponding specific capacity and voltage profile, (c) charge–discharge profile performance under 1C rate of 280 cycles and (d) corresponding charge–discharge curves of cyclic performance a 1c rate and coulombic efficiency.....	105
74	(a) Rate capability of NMC111/ QCPEs–10/Li cell at RT with different 0.1 C to 1 C. (b) charge and discharge curves of the quasi–solid cell (c) charge–discharge curves cycle performance of the quasi–solid cells at 0.3 C 80 cycles. (d) cyclic performance a 0.3 C rate and coulombic efficiency.....	107
75	XPS characterization of the SEI components on the cycled NMC111 electrodes in different electrolytes after 100 cycles compared with pristine (a), (b) C 1s and (c), (d) F 1s and (e), (f) S2p and (g), (f) Li 1s.	109
76	(a) Rate performance corresponding specific capacity and (b) voltage curve of pouch cell NCM111/ QCPEs–10/Li batteries at 0.1C – 1 C, respectively. (c) The galvanostatic cycle performance corresponding charge–discharge curves of pouch cell NCM111/ QCPEs–10/Li battery at 0.3C (d) cyclic performance a 0.3 C rate and coulombic efficiency.	111
77	The optical images of (a) normal, (b) bending, (c) cutting and (d) burning test of pouch–type NMC111/QCPEs–10/Li cell.	111

CHAPTER 1

INTRODUCTION

RECHARGEABLE LITHIUM BATTERIES

The energy storage device of lithium-ion batteries (LIBs) is widely used in solar cells, electric vehicles (EV), and electronic devices because of their high volumetric and gravimetric energy density among other rechargeable energy storage systems. The advantages of LIBs are high power density, high energy density, high depth of discharge rate long live cycle, etc. Conventional materials of lithium batteries were composed of Li metal because of their very large capacity (3860 Ah kg^{-1}) and the lowest negative electrochemical potential. It is natural to consider Li metal electrodes for the negative electrode. Unfortunately, Li metal electrodes in rechargeable batteries have proved challenging due to the growth of metallic dendrites during Li plating/stripping, with short circuits caused by the dendrites leading to thermal runaway and risk of fire explosion. The LIBs were improving this problem and still had advantageous properties. In 1991's, the first LIBs were developed by Sony for use in personal electronics such as (laptops, cameras, tablets, etc.) due to their high energy density, long life cycle, and ease of manufacturing (Goodenough, J. B., & Kim, Y., 2010; Scrosati, B., et al., 2011; Armand, M., & Tarascon, J. M., 2008; Li, L., et al., 2015; Kim, J. G., et al., 2015). For cathode and anode materials, the current research is focused on how to improve the energy density as much as possible. The various cathode materials including LiCoO_2 , LiNiO_2 , $\text{LiNi}_x\text{Mn}_y\text{Co}_z\text{O}_2$ and $\text{LiNi}_{0.8}\text{Co}_{0.15}\text{Al}_{0.05}\text{O}_2$ with a layered structure, LiMn_2O_4 with spinel structure and LiFePO_4 with olivine structure continuously strive to increase capacity and energy density to satisfy power demand, and the frontier research is to develop nickel-rich and high-

voltage cathode materials (Xu, J., et al., 2017; Kraytsberg, A., et al., 2012; Zhang, W. J. 2011; Nayak, P. K., et al., 2018). At the same time, the difficulties of developing new anode materials lie in how to solve the large volume expansion to insure cycle life, the low conductivity, the dendrite formation, and the instability of solid electrolyte interface (SEI) film (Ashuri, M., et al., 2016; Goriparti, S., et al., 2014; Feng, J., et al., 2014). While for the most flammable component of LIBs, the commercial organic electrolyte consisting of carbonate solvent with low boiling point and lithium hexafluorophosphate (LiPF_6) has been used for decades since the invention of lithium-ion battery. Although high-capacity electrode materials like silicon anode and high-nickel ternary cathode have been well developed and put into commercial production, there is still no breakthrough in the electrolyte area or is far from practical application. A good electrolyte needs a comprehensive consideration on conductivity, viscosity, melting point, toxicity, and intricate compatibility with the electrodes. Any changes to the physical or chemical properties of the electrolyte can have an obvious effect on battery performance. Based on the current application status, there are still large thermal risks for lithium-ion batteries with LiPF_6 based electrolytes under abuse conditions like overcharge, internal short circuit, extrusion, high temperature, and others, especially for the charged system.

Electrolytes as the blood of lithium-ion batteries play a decisive role in the safety performance. Traditional commercial electrolyte is usually a nonaqueous system consisting of organic carbonate solvents and LiPF_6 . At present, although such a combination of electrolyte solvent and lithium salt provides the best balance on electrochemical performance, cost, and toxicity, it is not safe enough. The instability of electrolytes comes from both the solvent and the lithium salt. Electrolyte solvents with excellent electrochemical performances must have good physical and chemical properties to ensure rapid lithium-ion transmission, good electrode interface compatibility, and chemical inertness. Commonly used electrolyte organic solvents include ethylene carbonate (EC), propylene carbonate (PC), dimethyl carbonate (DMC), diethyl carbonate (DEC), methyl ethyl carbonated (EMC), γ -butyrolactone (GBL), etc.

To satisfy the application requirements of electrolytes on dielectric constant, viscosity, conductivity, density volatility, and so on, the electrolyte solvent is often a mixture of these various organic liquids (Roth, E. P., & Orendorff, C. J. 2012; Q. Li., et al., 2016). However, they are usually flammable, when lithium-ion batteries are under abuse conditions, they are easy to be firstly ignited producing a lot of heat and causing thermal runaway. Various test means have been used to study the thermal stability and decomposition mechanism of the electrolyte. Gnanaraj et al. studied the thermal reaction of electrolyte solution containing different lithium salts by using an accelerating rate calorimeter (ARC) in Fig. 1 (J. Gnanaraj, et al., 2003; Zinigrad, E., et al., 2005).

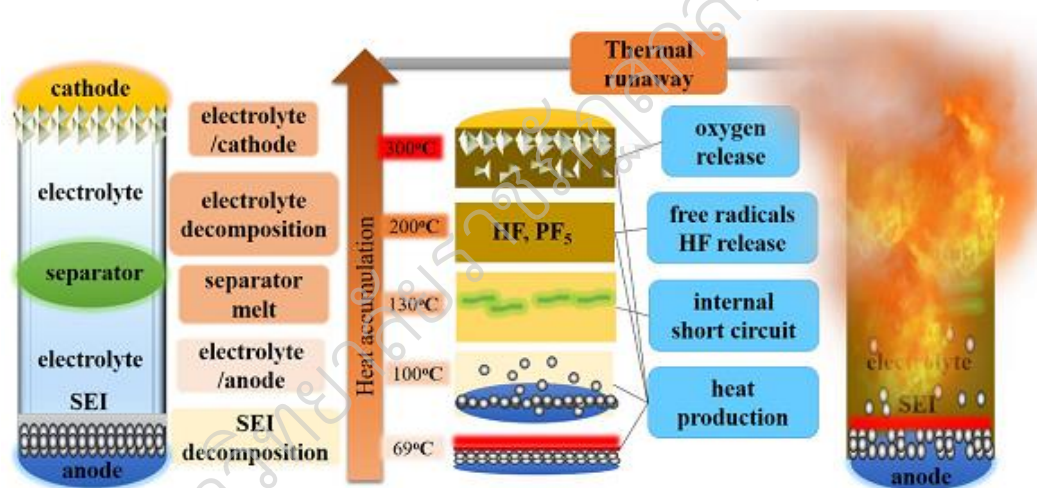


Fig. 1. Schematic of thermal runaway stage of liquid electrolyte in lithium-ion batteries.

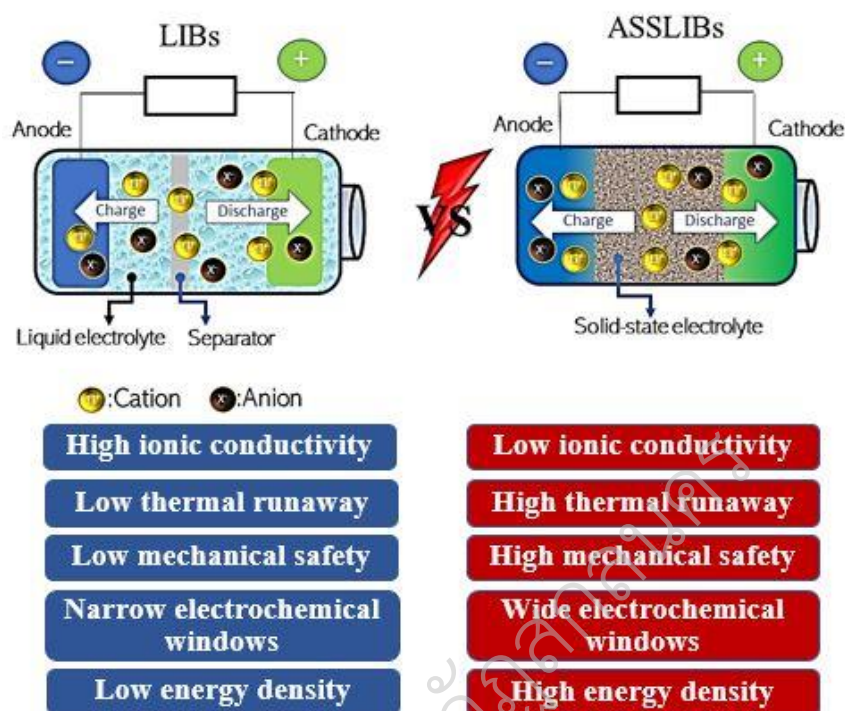


Fig. 2. The comparative advantages and disadvantages between liquid and solid electrolytes for lithium-ion batteries.

All-solid-state lithium batteries (ASSLBs) are recognized for extensive attention as next-generation technology for rechargeable storage because of improvements to the high safety, volume energy density, and non-generate toxic gas as compared with conventional liquid electrolyte batteries. The inorganic solid electrolyte for use in commercialized should have ionic conductivity higher than $10^{-2} \text{ S}\cdot\text{cm}^{-1}$ at room temperature, low electronic conductivity, electrochemical stability, and low cost for making in mass production shown in Fig. 2. Different groups of inorganic solid electrolytes have been studied in detail such as LISICON (lithium superionic conductor), perovskite, LIPON (lithium phosphorous oxynitride), garnet type, and many more. A brief review of some of these inorganic compounds is presented below.

LISICON

LISICON is an acronym for lithium superionic conductor. The general structural formula is $\text{Li}_{16-2x}\text{D}_x(\text{TO}_4)_4$ where D and T are the ion of the element that has a +2 charge (Mn^{2+} , Zn^{2+}) and the transition metal ions containing charge +4 (Ge^{4+} , Si^{4+}), respectively. $\text{Li}_{14}\text{Zn}(\text{GeO}_4)_4$ was the first LISICON structure solid electrolyte with high ionic conductivity of $1.25 \times 10^{-1} \text{ S cm}^{-1}$ at 300 °C (Hong, H. Y. P., 1978). More studies have reported conductivity of $2 \times 10^{-6} \text{ S cm}^{-1}$ at 50 °C and $1.3 \times 10^{-6} \text{ S cm}^{-1}$ at 33 °C (Kuwano, J., and West, A. R., 1980; Deng, Y., et al., 2017). Other examples of LISICON-type solid electrolytes such as $\text{Li}_{3.5}\text{Ge}_{0.5}\text{VO}_4$ and $\text{Li}_{3.6}\text{Ge}_{0.6}\text{V}_{0.4}\text{O}_4$ have been prepared and showed ionic conductivity of $4 \times 10^{-5} \text{ S cm}^{-1}$ and $\sim 10^{-5} \text{ S cm}^{-1}$ at 18 °C (Song, S., et al., 2015). The ionic conductivity of LISICON-type solid electrolytes is very low to be practically used in solid-state lithium-ion batteries.

LIPON

LIPON-type electrolytes are lithium phosphorous oxynitride compounds. The first LIPON was synthesized by radio frequency magneto sputtering using Li_3PO_4 as a target in N_2 atmosphere which showed ionic conductivity of $2 \times 10^{-6} \text{ S cm}^{-1}$ at 25 °C (Bates et al., 1993). LIPONs' low ionic conductivity hinders practical use in bulk all solid-state batteries.

NASICON

NASICON-type electrolytes are sodium superionic conductors. The general structural formula is $\text{AM}_2(\text{PO}_4)_3$ where A and M are the ions of the alkaline element (Li^+ , Na^+ , K^{2+}) and the transition metal ions containing charge +4 (Ge^{4+} , Si^{4+} , Ti^{4+} , Zr^{4+}), respectively. Furthermore, the crystal structure NASICON type usually is rhombohedral such as $\text{LiZr}_2(\text{PO}_4)_3$ (LZP), $\text{LiTi}_2(\text{PO}_4)_3$ (LTP), and $\text{LiGe}_2(\text{PO}_4)_3$ (LGP) (Xu H., et al., 2017). The first NASICON-type Li-ion conductor was investigated in 1997 by Jie Fu. (Fu, J., 1997). $\text{LiGe}_2(\text{PO}_4)_3$ and its ionic conductivity were reported as $\sim 10^{-4} \text{ S cm}^{-1}$ at room temperature. However, the GeO_2 is expensive and must be replaced by using TiO_2 or ZrO_2 for decreasing cost.

Sulfide

The general structural formula Sulfide-type is $(100-x)\text{Li}_2\text{S}-x\text{P}_2\text{S}_5$ such as Li_3PS_4 ($x = 25$) and $\text{Li}_7\text{P}_3\text{S}_{11}$ ($x = 30$) shows high ionic conductivity as $\sim 10^{-3} \text{ S}\cdot\text{cm}^{-1}$ at room temperature (Liu et al., 2013; Zhang et al., 2017). In addition, the high ionic conductivity has promoted for making mass products after that many researchers studying on doping of sulfide system following $9\text{Li}_2\text{S}-3\text{P}_2\text{S}_5-1\text{Ni}_3\text{S}_2$, $\text{Li}_7\text{P}_{2.9}\text{S}_{10.85}\text{Mo}_{0.01}$, $\text{Li}_7\text{P}_{2.9}\text{Mn}_{0.1}\text{S}_{10.7}\text{I}_{0.3}$, $90(0.7\text{Li}_2\text{S}-0.3\text{P}_2\text{S}_5)-10\text{LiBr}$ and $95(0.8\text{Li}_2\text{S}-0.2\text{P}_2\text{S}_5)-5\text{LiI}$ (Park et al., 2017; Xu et al., 2017; Xu et al., 2017; Ujiie et al., 2014; Ujiie et al., 2013). However, the ionic conductivity is still in the range of $\sim 10^{-3} \text{ S}\cdot\text{cm}^{-1}$ at room temperature. The next strategies for improvement ionic conductivity are doped GeS_2 , SiS_2 , SnS_2 or Al_2S_3 then creating structure $\text{Li}_2\text{S}-\text{M}_x\text{S}_y-\text{P}_2\text{S}_5$ such as $\text{Li}_{10}\text{GeP}_2\text{S}_{12}$, $\text{Li}_{9.54}\text{Si}_{1.74}\text{P}_{1.44}\text{S}_{11.7}\text{Cl}_{0.3}$, and $\text{Li}_{10.35}[\text{Sn}_{0.27}\text{Si}_{1.08}]\text{P}_{1.65}\text{S}_{12}$. It was found that the improvement in ionic conductivity was increased to a range of $10^{-2} \text{ S}\cdot\text{cm}^{-1}$ although the sulfide system is shown high ionic conductivity but is unstable in air and reacts with moisture H_2S gas produced, risk of toxicity and there was a flammable (Minami et al., 2010; Kamaya et al., 2011; Kato et al., 2016; Sun et al., 2017).

Garnet

Different classes of solid-state compounds and their examples have been briefly introduced above. However, they are far from being applicable in lithium-ion batteries due to their low ionic conductivity at room temperature which is affected by high grain boundary resistance. Garnet structure compounds exhibit the general formula of $\text{A}_3\text{B}_2\text{C}_3\text{O}_{12}$ where (A = Ca, Mg, Y, La or rare earth elements; B = Al, Fe, Ge, Ga, Mn, Ni and C = Si, Ge, Al) are arranged in 10 faced centered cubic. The first garnet-like structure Li ion conductor was investigated in 2006 by Weppner and Thangadurai. (Thangadurai, V., and Weppner, W., 2006). as $\text{Li}_5\text{La}_3\text{M}_2\text{O}_{12}$ (M = Nb, Ta) and its bulk ionic conductivity was reported as $\sim 10^{-6} \text{ S}\cdot\text{cm}^{-1}$ at 25 °C (Allen, J. et al., 2012). Among all the garnet-like materials that are Li-rich and have potential as solid electrolytes, $\text{Li}_7\text{La}_3\text{Zr}_2\text{O}_{12}$ (LLZO) has exhibited the highest total ionic conductivity at room temperature ($2.2 \times 10^{-4} \text{ S}\cdot\text{cm}^{-1}$ at 25°C). However, this structure is still unstable

in the atmosphere. As it reacts with moisture and CO_2 a contamination phase. $\text{LiOH}\cdot\text{H}_2\text{O}$ and $\text{La}(\text{OH})_3$ (Ying and McGinn, 2013). The grain boundary which affects the conductivity of reduced ions, thus increasing the stability of the LLZO in the atmosphere is therefore very important (Ahn, C. W., et al., 2014).

Perovskite

There is a general structural formula ABO_3 where position A is the ion of the element that has a +2 charge, where B is the transition metal ions containing charge +4 (Ti^{4+}). The first perovskite structure solid electrolyte was introduced by Inaguma et al., 1993 as $\text{Li}_{3x}\text{La}_{2/3-x}\text{TiO}_3$ (LLTO) with bulk ionic conductivity as high as $1 \times 10^{-3} \text{ S cm}^{-1}$ (Inaguma, Y., et al., 1993). The main problem with LLTO is instability against potentials below 1.8 V vs. Li/Li^+ due to Ti^{4+} reduction at low voltages. This issue has been resolved in different studies such as partial substitution of Ti^{4+} by Zr^{4+} , Sn^{4+} , and Ta^{4+} (Yao, R., et al., 2020; Morata-Orrantia, A. et al., 2003). However, the doped perovskites show lower ionic conductivity, e.g., in $\text{LiSr}_{1.65}\text{Zr}_{1.3}\text{Ta}_{1.7}\text{O}_9$ (LSZT) the ionic conductivity is $1.3 \times 10^{-5} \text{ S cm}^{-1}$ at 30°C (Chen, K., 2012).

RESEARCH OBJECTIVES

1. To synthesize, and study microstructures, and electrochemical properties of solid electrolytes.
2. To fabricate a prototype of solid-state lithium-ion batteries.

MOTIVATION AND SCOPE OF THE THESIS

The thesis aims to investigate perovskite- $\text{Li}_{3x}\text{La}_{2/3-x}\text{TiO}_3$ (LLTO) with high conductivity at room temperature while having robust mechanical properties. In the present thesis, perovskite- $\text{Li}_{3x}\text{La}_{2/3-x}\text{TiO}_3$ was improved by using a reduced grain boundary to increase the total ionic conductivity. The strategies of a reduced grain boundary are using doping A-site with alkaline earth B-site with transition metal and

solid-state reaction method for forming particle to cubic structure of $\text{Li}_{3x}\text{La}_{2/3-x}\text{TiO}_3$. The cubic- $\text{Li}_{0.5}\text{La}_{0.5}\text{TiO}_3$ structure was selected for the co-substitution of the La site with Sr and Ti site with Ta, both of which have larger ionic radii at different concentrations, to enhance the bottleneck size for Li^+ migration channels and maintain the cubic structure, leading to an increase in ionic conductivity. Additionally, Sr and Ta co-substitution improved the pellet sample density during sintering. The Sr and Ta co-substitution was significantly effective in enhancing the total conductivity of cubic- $\text{Li}_{0.5}\text{La}_{0.5}\text{TiO}_3$, making it a potential candidate for use as a composite polymer electrolyte in perovskite-type Li metal batteries. Moreover, we have successfully developed a straightforward process for fabricating thin and flexible composite polymer electrolytes (CPEs) using the solution casting technique. These CPEs are based on the garnet-type $\text{Li}_{6.25}\text{Ga}_{0.25}\text{La}_3\text{Zr}_2\text{O}_{12}$ (LLZO-Ga) material, which is embedded in a PVDF-HFP polymer matrix along with LiTFSI. The inclusion of LLZO-Ga in the PVDF-HFP polymer matrix serves as a plasticizer, reducing the crystallization of the polymer matrices and enhancing the ionic conductivity of the CPEs. A thorough investigation was conducted to analyze the structure, morphology, thermal stability, and electrochemical properties of these CPEs. CPEs with a LLZO-Ga content of 10% by weight (CPEs-10) in the PVDF-HFP composite polymer electrolyte exhibited an expanded electrochemical potential window and a reasonable lithium-ion transference number. In the fabrication of cells with LiFePO_4 (LFP) and $\text{LiNi}_{1/3}\text{Mn}_{1/3}\text{Co}_{1/3}\text{O}_2$ (NMC111) as the cathodes, CPEs-10 as the electrolyte, a high-concentration electrolyte (4MLiFSI: DEE), and lithium metal as the anode, excellent cycle stability and good rate performance were demonstrated at room temperature. This research contributes to the advancement of LLZO-Ga-based composite polymer electrolytes for lithium metal batteries.

ANTICIPATED OUTCOMES OF THE THESIS

1. The process for the synthesis of the high density of perovskite- $\text{Li}_{3x}\text{La}_{2/3-x}\text{TiO}_3$ and garnet-type $\text{Li}_{6.25}\text{Ga}_{0.25}\text{La}_3\text{Zr}_2\text{O}_{12}$.
2. The improvement of ionic conductivity in perovskite- $\text{Li}_{3x}\text{La}_{2/3-x}\text{TiO}_3$. and composite polymer electrolytes.
3. The fabrication prototype of full cell solid and semi solid-state lithium batteries.

THESIS STRUCTURE

The thesis consists of 5 chapters; Chapter 1 introductions, objectives, motivation, and scope of this thesis. Chapter 2 reviews the fundamental lithium batteries, the development of solid-state and semi-solid electrolytes as well as the fabrication of solid-state and semi-solid lithium batteries and applications. The research methodology is presented in Chapter 3. The results and discussion of this thesis are shown in Chapter 4. The conclusion and suggestions for further work are presented in Chapter 5.

CHAPTER 2

THEORETICAL BACKGROUND AND LITERATURE REVIEWS

LI-ION BATTERY (LIB): STRUCTURE AND FUNCTIONAL MECHANISM

LIBs are the most popular rechargeable batteries because of their high energy and power density. The development of advanced materials for LIBs is the focus of research in material science, chemistry, physics, and chemical engineering. LIBs are now the major power sources for portable electronic devices and are expected to be utilized in EVs.

The fundamental mechanism of LIBs is based on a series of reversible chemical reactions known as “redox” (reduction and oxidation) reactions which take place at the surface of the electrodes. The anode electrode is where the oxidation reaction occurs, while reduction happens at the surface of the cathode. Fig. 3 is a schematic energy level diagram of electrons in electrodes and electrolytes. In a thermodynamically stable battery, the chemical potential energy of anode μ_A should fall below the lowest unoccupied molecular orbital (LUMO) of the electrolyte and the chemical potential of cathode μ_C should be higher than the highest occupied molecular orbital (HOMO) of the electrolyte. This will prevent the oxidation of electrolytes on the anode side and the reduction of electrolytes on the cathode side. The energy difference between LUMO and HOMO (E_g) is the electrolyte voltage stability window and the energy difference between the electrode's chemical potential is the cell's open circuit voltage V_{oc} (Liu, C. et al., 2016).

$$\mu_A - \mu_C = eV_{oc} \quad (2.1)$$

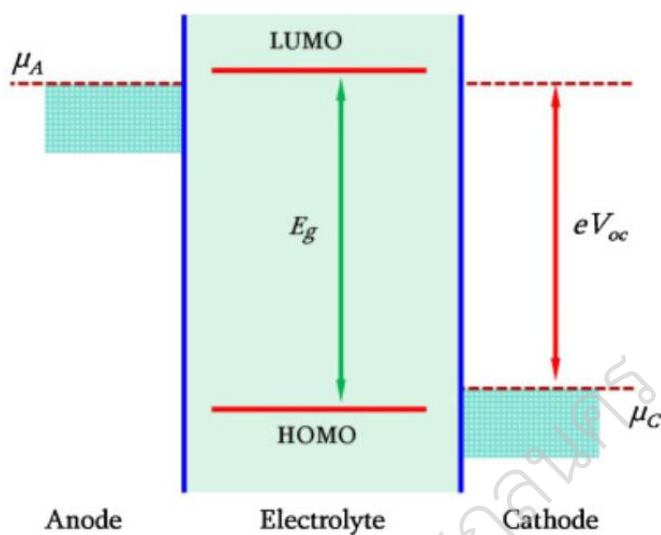


Fig. 3. Relative energies of the electrolyte window, E_g , and the relationship between electrochemical potentials of electrodes and the HOMO or LUMO of the electrolyte.

The reversible chemical reaction in Li-ion battery consists of two half-reactions which happen at the electrodes. Fig 4. below represents the structure of a lithium-ion battery with LiCoO_2 as cathode and graphite as anode.

Charging (Cathode half reaction): $\text{LiCoO}_2 \rightarrow \text{Li}^+ + \text{e}^- + \text{CoO}_2$ (0.6V)

(Anode half reaction): $\text{Li}^+ + \text{e}^- + 6\text{C} \rightarrow \text{LiC}_6$ (-3.0V)

Full reaction: $\text{LiCoO}_2 + 6\text{C} \rightarrow \text{CoO}_2 + \text{LiC}_6$ ($V_{oc}=3.6\text{V}$)

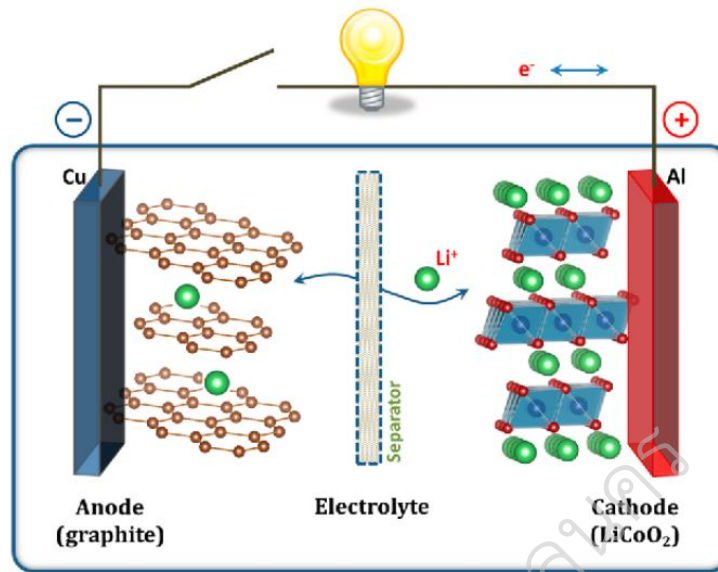


Fig. 4. Schematic energy diagram of thermodynamically stable Li-ion battery (Liu, C. et al., 2016).

COMPONENTS OF A LI-ION BATTERY

Cathode materials

Electrode materials are compounds that can accommodate Li-ions and release them when needed in an irreversible process. Electrode materials can store Li-ions in their empty (1D, 2D or 3D) channels, vacant sites or even react with Li-ions in different ways such as conversion or alloying (Poizot, P. et al., 2000; Park, C. et al., 2010). The cathode materials are mainly in the form of layered structures such as lithium transition metal oxides LiMO_2 where $M = \text{V, Cr, Mn, Ni, Co, ...}$. For example, LiCoO_2 (LCO) was first introduced by Goodenough in 1980 and commercialized by SONY in 1991 (Mizushima, K. et al., 1980). LCO is a great cathode material because of its high theoretical specific capacity ($280 \text{ mAh}\cdot\text{g}^{-1}$), low self-discharge, high cycle life, and high discharge voltage (3.6 V) (Du Pasquier, A. et al., 2003). However, charging to higher voltages may cause safety concerns due to oxygen evolution. Other

forms of layered materials are Spinel (LiMn_2O_4), Olivines (LiFePO_4), and other transition metal oxides such as MnO_2 , V_2O_5 , etc. (Whittingham, M. S., 2004).

Anode

The anode electrode is where Li ions are stored in the fully charged battery. One of the widely used materials as an anode in Li-ion batteries is graphite which provides a high gravimetric capacity of as high as $1200 \text{ mAh}\cdot\text{g}^{-1}$ in the first cycle and $850 \text{ mAh}\cdot\text{g}^{-1}$ in the 40th cycle (Takamura, T. et al., 2007). Another type of anode material that has high capacity is alloyed anode materials: $x\text{Li}^+ + xe^- + \text{M} \rightarrow \text{Li}_x\text{M}$ where examples of M are Si, Ge, Sn, P, etc. In general, alloyed materials show higher capacity compared to graphite (Huggins, R. A., 1999). The main challenge with alloyed materials is a drastic change in volume due to lithiation/de-lithiation (3 times in Si) which can cause fracture in structure and capacity fading. Despite various available anode materials, Li metal is still the ideal anode for Li-ion batteries due to its high specific capacity of $3860 \text{ mAh}\cdot\text{g}^{-1}$ (Lu, J. et al., 2018). However, repeated Li metal deposition and stripping during the charge/discharge process on the anode surface lead to the formation of Li-dendrites, internal circuiting, and battery failure (Tarascon, J. M., & Armand, M., 2001). Different studies have been done to understand the dendrite formation mechanism and ways to suppress it (Wang, X. et al., 2018; Feng, Q. et al., 2012; Aryanfar, A. et al., 2015)

Electrolyte

The performance of a battery strongly depends on the properties of its electrolyte. The electrolyte in the battery provides a pathway for Li-ions to travel between the anode and cathode. Because of the crucial role of electrolytes in a battery, its primary requirements need to be satisfied. First and most important, the electrolyte material needs to be an ion-conductor. In other words, Li-ions can freely pass through electrolytes without any other unwanted side reactions. It is believed that the potential electrolyte should have a minimum bulk conductivity of $10^{-3} \text{ S cm}^{-1}$ at room temperature. The electrolyte is directly in contact with electrodes, which are the centers of chemical reactions (redox), hence the electrolyte must be chemically stable

against the cathode and anode to prevent side reactions and decomposition of electrolyte which leads to capacity fade, heat generation, and gas production. Finally, electrolyte materials need to be resistant to thermal, electrical, and mechanical shocks. The efforts in finding the perfect formulation to match the requirements ended up in LiPF_6 dissolved in ethylene carbonate (EC)/ dimethyl carbonate (DMC). However, LiPF_6 reacts with both anode and cathode materials which leads to the formation of the solid electrolyte interface (SEI) on the surface of the electrodes. The SEI layer inhibits further reactions, decomposition of electrolytes, and capacity fade. The breakdown of the passivation layer, especially at voltages above 4.3 V results in power and capacity loss (Ueda, A., & Ohzuku, T., 1994). Liquid electrolytes are not electrochemically and physically stable enough to be used against high-voltage cathodes or Li metal anodes. To safely expand the voltage window of battery cells, thermally and electrochemically stable electrolytes against redox reactions, Li dendrite growth, and mechanical and electrical shocks are needed. Other than liquid electrolytes, polymer electrolytes, gel electrolytes, solid electrolytes, and composite solid polymer electrolytes have been studied. However, challenges remain regarding ionic conductivity, mechanical integrity, and thermal stability. Moving from low-density liquid electrolytes ($\rho \sim 0.8 - 0.9 \text{ g}\cdot\text{cm}^{-3}$) to high theoretical density solid electrolytes ($\rho \sim 2.5 - 6 \text{ g}\cdot\text{cm}^{-3}$) results in losing gravimetric energy density (Langer, F., et al 2016). Thus, thin film solid electrolytes are needed. However, thin film processes such as physical vapor deposition including pulsed laser deposition or magnetron sputtering are not suitable for large-scale manufacturing (Tan, J., & Tiwari, A., 2012; Reinacher, J. et al., 2014; Kuwata, N. et al., 2004; Kalita, D. J. et al., 2012).

MECHANISM OF LI-ION TRANSPORT IN SOLID AND COMPOSITE ELECTROLYTES

Electrochemical impedance spectroscopy (EIS)

The ionic conduction mechanism of solid and composite electrolytes is not well understood because of the complex contribution of polymer chain's dipole-dipole interaction and polymer segments and salt molecules interaction in overall conductance. Electrochemical impedance spectroscopy is a well-suited method to elucidate the mechanism of ionic conductivity in complex systems such as polymer electrolytes from the point of view of polarization, alignment, and relaxation of dipoles. In impedance spectroscopy, an alternating electric signal is applied to the cell and the response of the system is measured in a wide range of frequencies. In this research, the frequency-dependent electrical impedance (EI) of the films was measured using a Bio-Logic Science Instrument VSP-300 electrochemical impedance analyzer in the frequency range of 100 mHz – 7MHz. The samples were sandwiched between two gold (Au) or stainless-steel blocking electrodes, and the sandwich structure was placed on a compact ceramic heater for temperature-dependent EI measurements. The impedance spectrum can be presented as a common way of presenting the data is to plot $-Z''$ ($\text{Im } Z^*$) vs. Z' ($\text{Re } Z^*$), called Nyquist plot (see Fig. 5.). Figure 5 shows examples of our bulk samples with equivalent circuit fit. Generally, the Nyquist plot shows a depressed semicircle at a high-frequency region which arises from a non-ideal capacitive behavior with a low-frequency tilted spike representing the electrical double layer due to the charge accumulation at the interface of electrode/electrolyte. One can assign an equivalent circuit (see Fig. 5) to simulate the experimental Nyquist plot. The impedance of resistors (R), capacitors ($\frac{1}{i\omega c}$), and constant phase element (CPE) ($\frac{1}{Q_0(i\omega)^n}$) where $Q_0 = 1/|Z|$ at $\omega = 1$ rad/s and $0 < n < 1$ to describe imperfect capacitor, are adjusted to generate the Nyquist curve corresponding to the measured one.

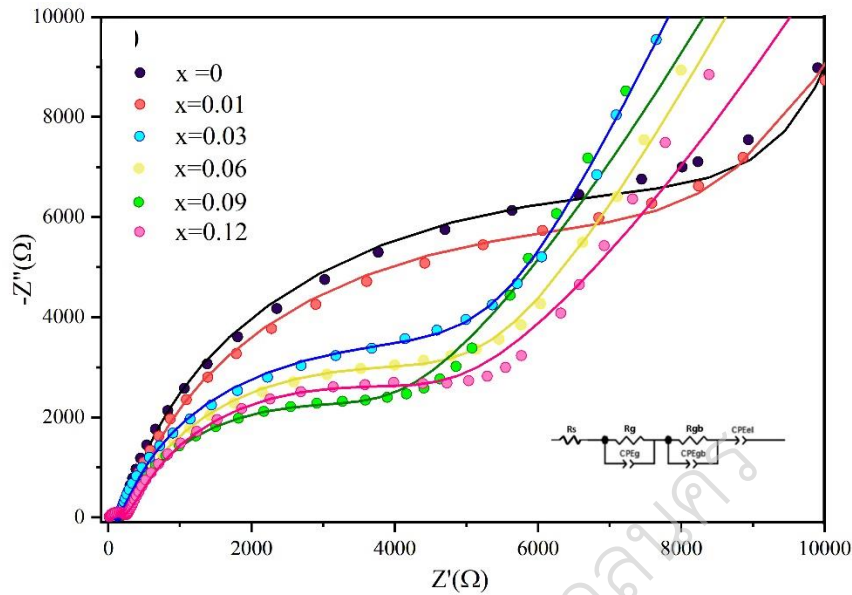


Fig. 5. Nyquist plot.

In addition, the equivalent circuit depends on the cell structure; wherein, R_s , R_g and CPE_g are the resistance of series circuit, the resistance in the grain and constant phase element of Li^+ migration in the grain, respectively. R_{gb} and CPE_{gb} represent the resistance and constant phase element for Li^+ migration across the grain boundary, respectively; and CPE_{el} is affected by the polarization between the Au-blocking electrodes. The total ionic conductivity was calculated using Eq. (2.2):

$$\sigma_{total} = \frac{L}{R_{total} \times A}, \quad (2.2)$$

where σ_{total} , R_{total} , A , and L represent the total conductivity, total resistance (grain + grain boundary resistance), cross-sectional surface area, and thickness of the pellet, respectively.

Temperature-dependent conductivity measurements

Li -ion transport in SSEs can be mainly classified into two types: ion transport in polymeric and inorganic materials. The temperature dependence of ionic conductivity in SSEs is usually modeled by the Arrhenius (for crystalline materials) or

Vogel–Tammann–Fulcher (VTF) equations (for amorphous materials) (Ratner, M.A., et al., 200). The Arrhenius equation.

$$\sigma_i = \frac{A}{T} \exp\left[-\frac{E_a}{kT}\right] \quad (2.3)$$

where A refers to the pre-exponential factor, k is the rate constant, and E_a is the activation energy for conductivity. The ionic conductivity in SPEs is usually modeled by the VTF equation with a non-linear relationship due to the ion conduction involving ion hopping associated with the motion of polymeric chains (Quartarone, E. et al., 2011), and the equation.

$$\sigma_i = \sigma_0 T^{\frac{1}{2}} \exp\left[-\frac{B}{T-T_0}\right] \quad (2.4)$$

where B is the pseudo-activation energy

σ_0 is the preexponential factor

T_0 is the reference temperature.

Linear sweep voltammetry

Linear sweep voltammetry (LSV) is a simple method to determine the electrochemical potential stability window of the electrolyte vs. Li/Li⁺. In this method, the electrolyte is sandwiched between Li metal as the reference electrode and gold or stainless-steel disk as a working electrode. The voltage is then applied across the sandwich structure and increased linearly at a scan rate of 10 mV/s from 1.8 V to 6 V. Within the negative working electrode voltage range the Li-ions from Li metal electrode migrate and get deposited onto gold (cathodic current). As the voltage further increases, the electrolyte will reach the breakdown voltage which means polymer electrolyte will no longer act as an electronic insulator. The voltage at which the current starts to increase steeply determines the electrochemical voltage stability window. A typical LSV curve is shown in Fig. 6.

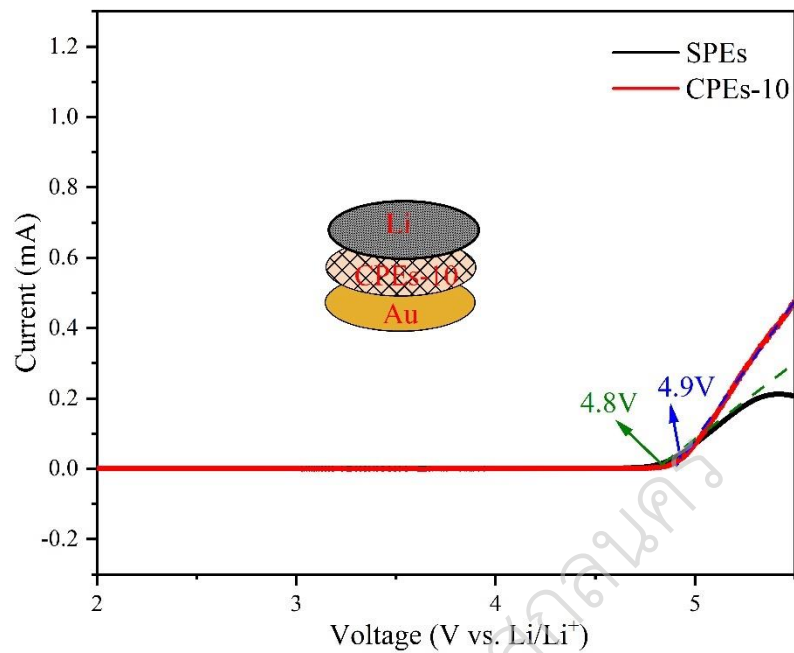


Fig. 6. LSV curve of solid polymer electrolytes (SPEs) and composite polymer electrolytes (CPEs)

STRUCTURE OF PEROVSKITE OXIDE

Perovskite oxides are a family with a chemical formula of ABO_3 . In a typical perovskite oxide, 'A' and 'B' denote two different cations which are attached to an O_8 anion. The most representative example is calcium titanium oxide which was founded by Gustav Rose in 1839 the typical structures of oxides of perovskite consist of higher cations 12 coordinated at site A, whereas they have smaller 6 coordinated cations at site B (S. S. Cavalcante et al., 2008).

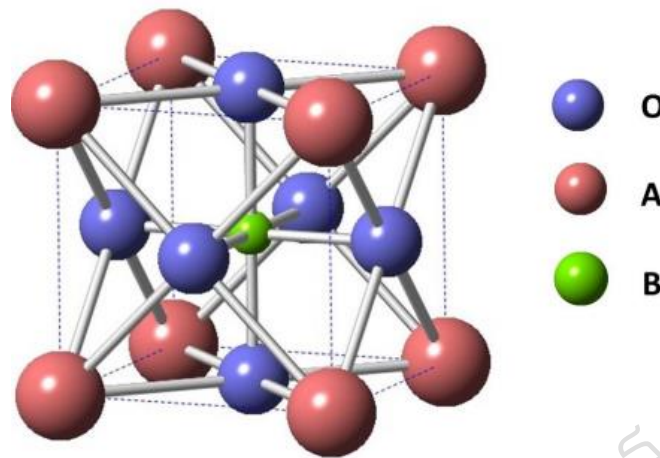


Fig. 7. ABO_3 cubic perovskite oxides unit cell

In general, the ideal structure of perovskite oxide is a cubic lattice. In this structure, the cations A are in the corners of the cubes, while the cation B is in the center. Oxygen ions sit in the face-centered position. Fig. 7. shows a typical unit cell of perovskite oxides. However, not many compounds have this structure. In many perovskite oxides, they have lower symmetrical due to slightly distorted variants. Normally, the perovskite structure is determined primarily by the size of the octahedron of oxygen-containing B atoms, and at the same time, the atoms of site A must fit into the holes between the octahedra. In the case of the ideal structure, the relations between the radii of the ions A, B, and O^{2-} are shown below:

$$r_A + r_O = \sqrt{2}(r_B + r_O) \quad (2.5)$$

Where r_A , r_O , and r_B correspond to the ionic radii of the cations site A and site B and the oxygen ion.

In a non-ideal cubic perovskite structure, the expression would change due to distortion. To allow this distortion, a tolerance factor t , would be used in this equation (V. M. Goldschmidt., 1962):

$$\tau = \frac{r_A + r_O}{\sqrt{2}(r_B + r_O)} \quad (2.6)$$

This tolerance factor is normally used to measure the degree of distortion. In perovskite-type compounds of cubic structure, the value of τ can be considered as 1. When τ is greater than 1, a small polar distortion in the structure can be found, which is attributed to the distance A–O, as well as to the small atom B, compared to the octahedron of oxygen. In this case, hexagonal symmetry can be found. In the case that when τ is smaller than 1, the A atom is smaller than the hole between the oxygen octahedra. Therefore, atom A cannot effectively bond with the 12 neighboring O atoms, which will show a structure with hexagonal crystallography. Because there are various structures and chemical compositions, it is well known that perovskite oxides can exhibit a wide variety of properties, such as ferroelectricity in BaTiO₃-based oxides, superconductivity in perovskite oxide La–Ba–Cu–O and Li_{3x}La_{2/3-x}TiO₃ was found to have the highest ionic conductivity in perovskite oxides (Bednorz, J. G., & Müller, K. A., 1986; Y. Inaguma et al., 1993).

LITHIUM LANTHANUM TITANATE (Li_{3x}La_{2/3-x}TiO₃)

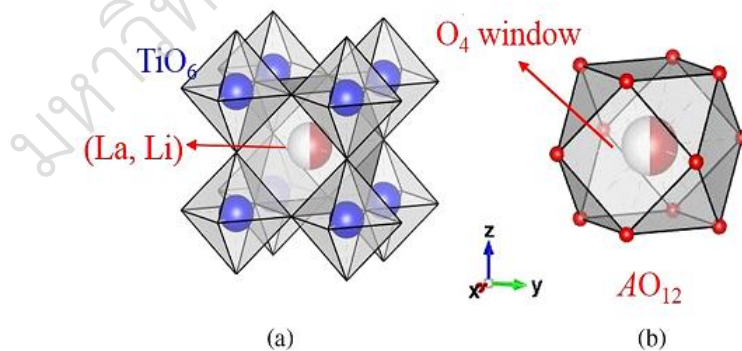


Fig. 8. (a) Cubic crystal structure of perovskite-type LLTO. (b) An AO₁₂ cuboctahedron, i.e. A-cage. For A-cage, its surface consists of six O₄ squares. windows and eight O₃ equilateral triangles (Thangadurai, V. et al., 2014).

The space group structures of LLTO with different compositions under the heating conditions, it is found that LLTO exhibits a simple cubic structure at the high temperature (>1673 K). Fig. 8 (a) shows the unit cell of high-temperature phase LLTO with a conventional perovskite ABO_3 structure. Eight TiO_6 octahedrons sharing corner in pairs form an AO_{12} cuboctahedron, so-called A-cage, in the center of which Li^+ , La^{3+} , and vacancies are situated. The O_4 window between two adjacent A-cages is made up of four neighboring TiO_6 octahedrons (see Fig. 8 (b)) (Varez, A. et al., 2004; Harada, Y. et al., 1999; Catti, M. et al., 2007).

The various ordered distributions of Li/La ions as well as the distortion of TiO_6 octahedrons, plenty of structural variations, and symmetries (see Table 1) are derived from the simple cubic perovskite-type LLTO.

Table 1 All possible lattice types, space groups, and structural features of LLTO Systems

Lattice type	Space group	Structural feature
Cubic	$Pm\bar{3}m$	La^{3+} , Li^+ and vacancy: disorderly distributed over the A-sites TiO_6 octahedron: regular octahedron
Rhombohedral	$R\bar{3}c$	Li^+ : partially occupying the O_4 windows. La^{3+} and vacancy: disorderly distributed over the A-sites
Tetragonal	$P4/mmm$, $4/mcm$	Li^+ : partially occupying the interior or windows of A-cages.
O_4	$P4/nbm$	
Orthorhombic	$Cmmm$, $Pmmm$ $Pmma$	La^{3+} : La-rich layer and La-poor layer. alternately stacking along c-axis.
Monoclinic	$P2/m$	TiO_6 octahedron: distorting.

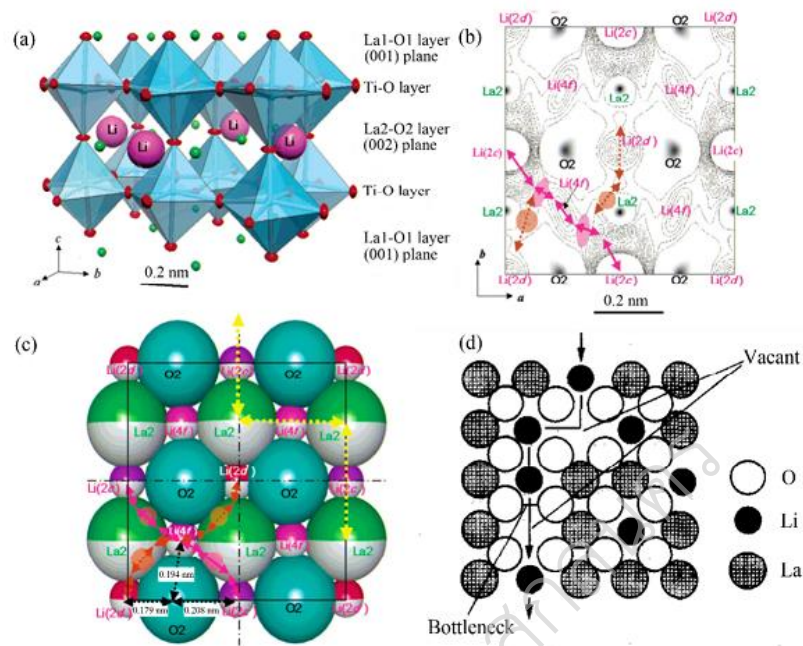


Fig. 9. (a) Crystal structure of perovskite-type $\text{La}_{0.62}\text{Li}_{0.16}\text{TiO}_3$ (b) Scattering amplitude distribution in the vicinity of the (002) plane ($0.35 < z < 0.65$) of $\text{La}_{0.62}\text{Li}_{0.16}\text{TiO}_{3.0}$ at room temperature (c) Atomic arrangement on the (002) plane (d) Arrangement of A-site ion and oxide ions, and lithium-ion conduction in a perovskite-type.

The conductivity of lithium-ion depends on a few factors, such as lithium and vacancy concentration and their relative ratio, the ionic radius of other A atoms, temperature, pressure, etc. The situation is more complicated, and lanthanum is indispensable not only for its structure framing affects that make way for lithium-ion transportation through a “bottleneck” (cation’s size-dependent at “A” sites) but also for its high valency that results in numerous vacancies. In a more detailed analysis, the LLTO compound has a layered perovskite-type structure consisting of La-poor layers, La-rich layers, and Ti-O layers which can be differentiated in Fig. 9. (a-c) (Yashima, M. et al., 2005). The La-rich layers and La-poor layers are distributed alternately along the c-axis as revealed by the neutron scattering study of the $\text{La}_{0.62}\text{Li}_{0.16}\text{TiO}_3$ perovskite by Yashima.

Literature reviews of Lithium lanthanum titanate ($\text{Li}_{3x}\text{La}_{2/3-x}\text{TiO}_3$)

This part will present previous work on all aspects, including the synthesis method, characterizations, ionic conductivity, and electrochemical measurements for the $\text{Li}_{3x}\text{La}_{2/3-x}\text{TiO}_3$ solid electrolyte. All this work has contributed to the improvement of ionic conductivity and the fabrication of solid-state batteries in this research.

Inaguma et al. (1993) firstly prepared perovskite-type solid electrolytes $\text{Li}_{3x}\text{La}_{2/3-x}\text{TiO}_3$ (LLTO) by solid-state reaction method (SSR), which showed bulk ionic conductivity of $1 \times 10^{-3} \text{ Scm}^{-1}$ and total ionic conductivity of higher than $2 \times 10^{-5} \text{ Scm}^{-1}$ at room temperature for $\text{Li}_{0.34(1)}\text{La}_{0.51(1)}\text{TiO}_{2.94(2)}$. The crystal structure of LLTO is shown as cubic perovskite whose cell parameter is about 3.8710 Angstrom in Fig. 10 (Inaguma, Y. et al., 1993)

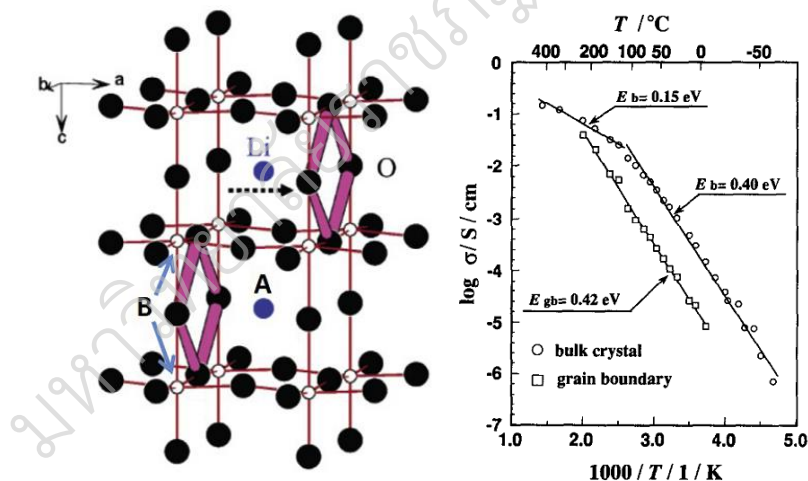


Fig. 10. Crystal structure and bulk ionic conductivity of perovskite-type solid electrolytes $\text{Li}_{3x}\text{La}_{2/3-x}\text{TiO}_3$.

W Ju Kwon, et al. (2017, pp. 6257–6262) synthesized $\text{Li}_{3x}\text{La}_{2/3-x}\text{TiO}_3$ (LLTOs) by using the Pechini method using citric acid. The LLTO of the sintering sample at 1200 °C for low temperature–LLTO, sintering at 1400 °C for high temperature–LLTO, and sintering at 1400 °C + Li excess 30 % for Li excess sample

shows a comparison of Li^+ conductivities along with schematics of the domain microstructures of the LLTO electrolytes. First, the low-T LLTO is characterized by a smaller domain size and a higher domain boundary resistance (i.e., low Li^+ conductivity) compared with the others. The presence of smaller domains with irregular boundaries would impede Li^+ conduction in the LLTO. Therefore, we suggest that a large domain size is more favorable for reducing the boundary resistances of LLTO as experimentally proven by the study on the high-T LLTO. Second, both the high-T LLTO and Li-excess LLTO have similar domain sizes; however, the Li-excess LLTO with Li-rich domain boundaries shows a lower domain boundary resistance and by extension, a higher total conductivity than that of the high-T LLTO (Fig. 11 (a)). Moreover, the activation energy (E_a) for Li migration across the domain boundary was reduced in the order of low-T LLTO (0.453 eV) > high-T LLTO (0.432 eV) > Li-excess LLTO (0.391 eV) (Fig. 11 (b)) (Kwon, W. J. et al., 2017).

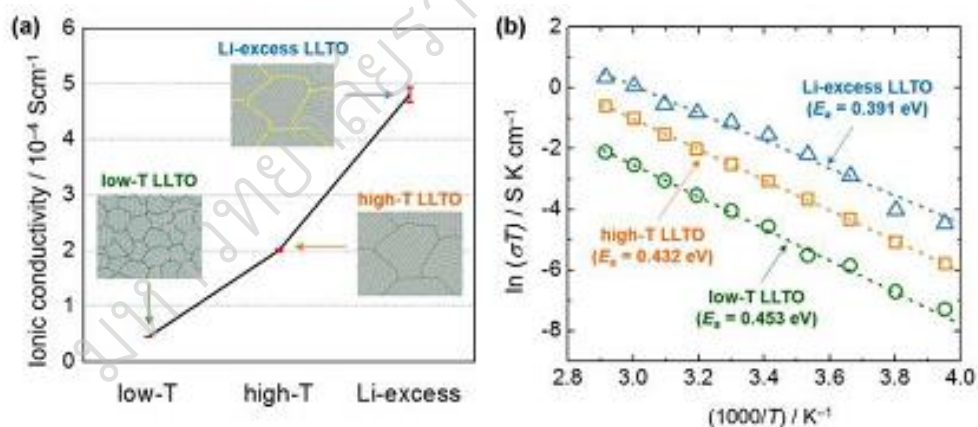


Fig. 11. (a) A comparison of Li^+ conductivities along with schematics of the domain microstructures of the LLTO electrolytes: low-T LLTO, high-T LLTO, and Li-excess LLTO. (b) Arrhenius plots of the boundary conductivities measured over a temperature range of -20 to 70 $^{\circ}\text{C}$. The activation energy (E_a) values calculated are indicated.

The Improvement of $\text{Li}_{3-x}\text{La}_{2/3-x}\text{TiO}_3$ (LLTO) has been increased in ionic conductivity by using substitution in A-site, B-site, or co-substitution LLTO structure.

K. Yu, et al. (2019, pp. 23941–23947) synthesized perovskite-type solid electrolyte $\text{Li}_{0.355}\text{La}_{0.35}\text{Sr}_{0.3}\text{Ti}_{0.995}\text{M}_{0.005}\text{O}_3$ (LLSTM, M=Al, Co, and In) lanthanum titanate (LLTO) via a conventional solid phase reaction method. All samples exhibited a cubic perovskite structure, meanwhile, the lattice parameter increased when the larger B-site ions were substituted compared to Ti^{4+} and vice versa. The ionic conductivity decreased with increasing the radii of B-site ions due to the change in interatomic bond strength. The peak shifts to a higher angle slightly as the ionic radii of Al^{3+} (0.535Å) is smaller than Ti^{4+} (0.605Å), and then shifts to a lower angle visibly as the Co^{3+} (0.61Å) and In^{3+} (0.80Å) in fig. 12 (Yu, K. et al., 2019).

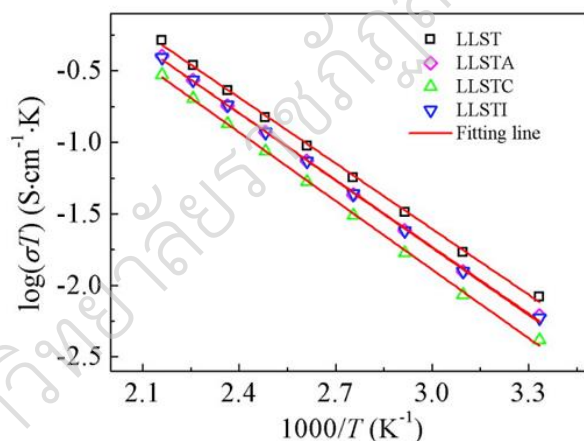


Fig. 12. Arrhenius plots for LLSTM samples.

Table 2 The ionic and electronic conductivity of LLSTM sample at room temperature and E_a .

Sample	σ_i (S/cm)	E_a (eV)	σ_e (S/cm)
LLST	2.78×10^{-5}	0.30	8.44×10^{-11}
LLSTA	2.05×10^{-5}	0.31	4.55×10^{-11}
LLSTC	1.37×10^{-5}	0.32	4.67×10^{-11}
LLSTI	1.97×10^{-5}	0.31	3.37×10^{-11}

J. Lu, et al. (2020, pp. 7741–7747) successfully synthesized $\text{Li}_{2x-y}\text{Sr}_{1-x-y}\text{La}_y\text{TiO}_3$ ($x = 3y/4$, $y = 1/7, 2/7, 3/7, 1/2, 15/28$, and $4/7$) by using conventional solid-state reaction method. X-ray diffraction analysis revealed that with the increase in La^{3+} content, $\text{Li}_{2x-y}\text{Sr}_{1-x-y}\text{La}_y\text{TiO}_3$ structure changes from cubic to tetragonal perovskite-type structure. Electrochemical impedance spectroscopy revealed that with the increase in y -value, enhanced conductivity was initially observed, followed by a decrease. $\text{Li}_{15/56}\text{Sr}_{1/16}\text{La}_{15/28}\text{TiO}_3$ electrolyte exhibited optimal total Li-ion conductivity of $4.84 \times 10^{-4} \text{ S cm}^{-1}$, electronic conductivity of $6.84 \times 10^{-10} \text{ S cm}^{-1}$, and activation energy of 0.29 eV in Fig. 13. and Table 3. On the other hand, cyclic voltammetry revealed unstable $\text{Li}_{1/8}\text{Sr}_{1/8}\text{La}_{1/2}\text{TiO}_3$, $\text{Li}_{15/56}\text{Sr}_{1/16}\text{La}_{15/28}\text{TiO}_3$, and $\text{Li}_{2/7}\text{La}_{4/7}\text{TiO}_3$ specimens at voltages of less than $\sim 2 \text{ V}$, indicative of their incompatibility with lithium metal or $\text{Li}_4\text{Ti}_5\text{O}_{12}$ in all-solid-state batteries. Charge-discharge tests confirmed the utility of electrolytes as solid separators with good performance in semi-solid-state batteries. Overall, these results are beneficial for future research on solid electrolytes and their applications in all-solid-state lithium-ion batteries in Fig. 14 (Lu, J. et al., 2020).

Table 3 Summary of bulk conductivity, grain-boundary conductivity, total conductivity, electronic conductivity, and activation energy of LSLTO samples.

Sample	σ_b/Scm^{-1}	$\sigma_{gb}/\text{Scm}^{-1}$	$\sigma_{total}/\text{Scm}^{-1}$	σ_e/Scm^{-1}	Activation energy/eV
LSLTO-3	-	-	1.66×10^{-5}	2.65×10^{-9}	0.32
LSLTO-4	-	-	2.50×10^{-4}	2.37×10^{-9}	0.30
LSLTO-5	1.50×10^{-3}	7.15×10^{-4}	4.84×10^{-4}	6.84×10^{-10}	0.29
LSLTO-6	1.38×10^{-3}	5.65×10^{-4}	4.01×10^{-4}	6.75×10^{-10}	0.30

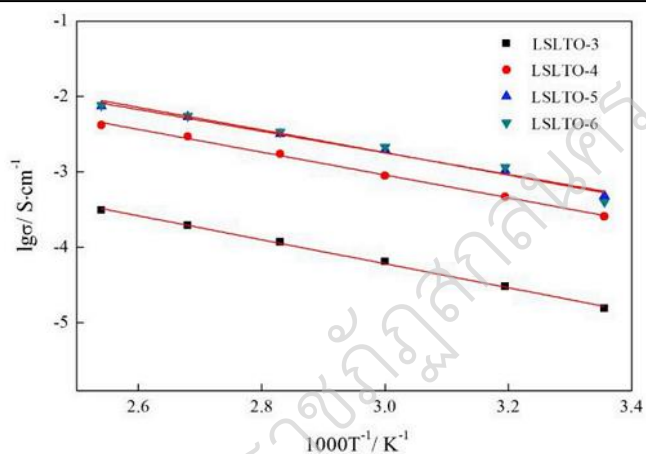


Fig. 13. Arrhenius plots of LSLTO-3, LSLTO-4, LSLTO-5, and LSLTO-6 samples.

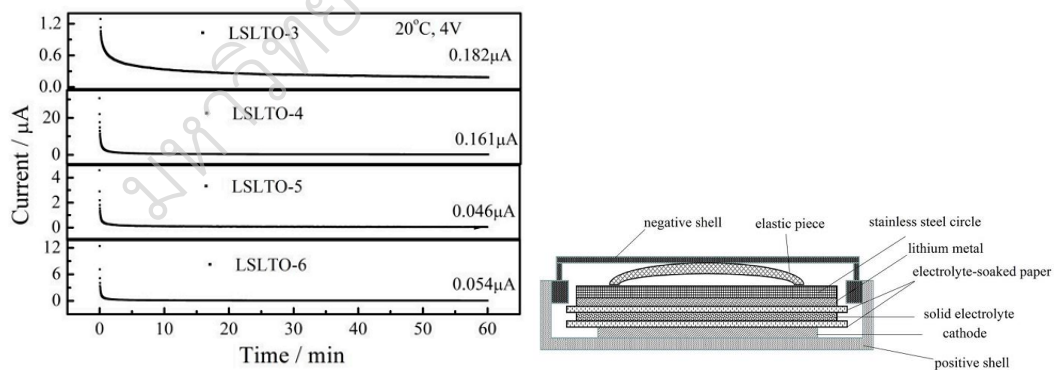


Fig. 14. Current vs. time curves of Au/LSLTO-3, LSLTO-4, LSLTO-5, and LSLTO-6/Au cells at a dc polarization potential of 4 V and a temperature of 20 °C.

L. Liang Sun, et al. (2019, pp. 2381–2384) successfully synthesized perovskite– $\text{LiSr}_{1-0.5x}\text{TiTaO}_{6-x}\text{F}_x$ by conventional solid–state reactions. The strategy of replacing O^{2-} anions with F^- in perovskite–type structure. The influence of fluorine ion (F^-) content in these compounds was systematically investigated regarding ion conductivity. The total conductivity attained was as high as $3.67 \times 10^{-4} \text{ S}\cdot\text{cm}^{-1}$ at room temperature in samples with $x = 0.1$ in Table 4 (Sun, L. et al., 2019).

Table 4 Structural parameters, interatomic distances, densities, and total conductivities of $\text{LiSr}_{1-0.5x}\text{TiTaO}_{6-x}\text{F}_x$ perovskites. All patterns were refined in the cubic $\text{Pm}\bar{3}\text{m}$ space group (N1 221).

x	0	0.1	0.2	0.3	0.4
a (Å)	3.9292	3.9259	3.9272	3.9283	3.9278
Ti/Ta–O (Å)	1.9676	1.9629	1.9636	1.9642	1.9647
Sr/Li–O (Å)	2.7782	2.7763	2.7768	2.7776	2.7774
Density ($\text{g}\cdot\text{cm}^{-3}$)	5.546	5.553	5.549	5.493	5.342
Conductivity ($10^{-4} \text{ S}\cdot\text{cm}^{-1}$)	2.90	3.67	3.60	2.91	1.36

R. Yao, et al. (2020, pp. 156023) studied the effect of Sn and Ta doping on Ti–site in $\text{Li}_{0.24}\text{La}_{0.587}\text{TiO}_3$ solid electrolyte by using solid state reaction and cold isostatic pressing. The XRD of all samples showed a tetragonal structure and high relative densities of about 96.2–97.8%. The total conductivity of $\text{LLTTa}_{0.04}\text{O}$ and $\text{LLTSn}_{0.02}\text{O}$ are $4.09 \times 10^{-4} \text{ S cm}^{-1}$ and $2.98 \times 10^{-4} \text{ S cm}^{-1}$ respectively, which are more than doubled compared with the pure specimen ($1.52 \times 10^{-4} \text{ S cm}^{-1}$) in Fig.15 and 16 (a–b). it was found that Ta or Sn doping is effective in increasing conductivity and decreasing activation energy, which is attributed to higher relative density, more disordered structure, larger Li–ion transmission channels and more Li–ion vacancies (Yao, R. et al., 2020).

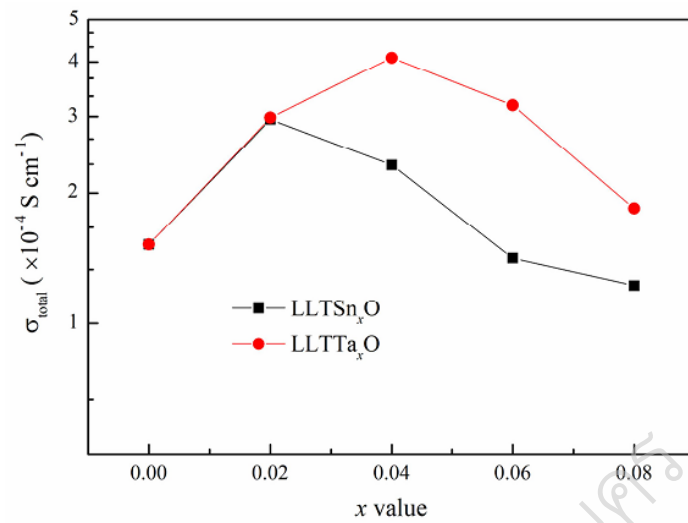


Fig. 15. Variations of the total conductivities of LLTM_xO (M = Sn or Ta ceramics) as function of x value at room temperature.

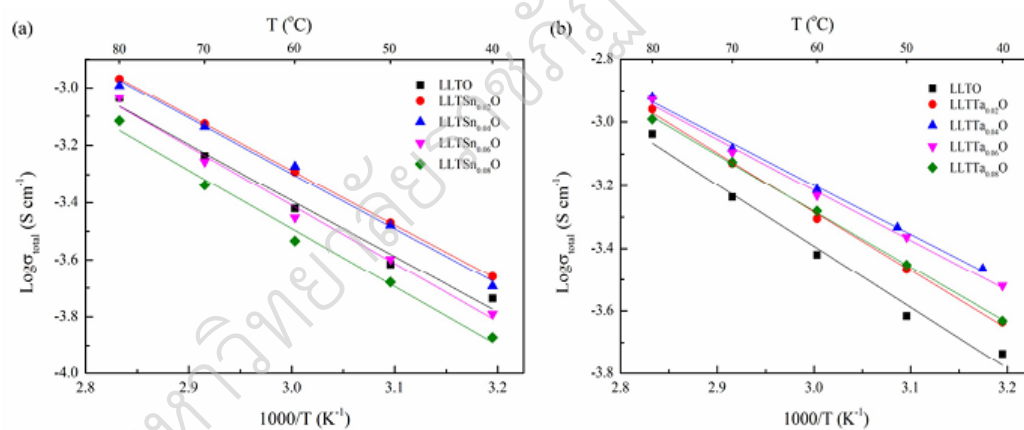


Fig. 16. Arrhenius plots of the (a) LLTSn_xO (0 ≤ x ≤ 0.08) and (b) LLTTa_xO (0 ≤ x ≤ 0.08) ceramic specimens.

The Improvement of Li_{3x}La_{2/3-x}TiO₃ (LLTO) has increased ionic conductivity by using the synthesis of nanoparticle LLTO. Sol-gel synthesis of nanoparticles is a hassle-free, rapid, and cost-effective method requiring no exceptional setup. Further, this method offers the benefit of control over particle size, chemical reaction parameters, and microstructure.

S. Zhang, et al. (2019, pp. 39–46) used so-gel method for synthesizing $\text{Li}_{0.33+x}\text{La}_{0.56-x}\text{Sr}_x\text{TiO}_3$ (LLSTO) powder and then used the solid-state reaction method for densification. The Sr substitution induces structure transformation from tetragonal to cubic structure. The prepared dense $\text{Li}_{0.36}\text{La}_{0.53}\text{Sr}_{0.03}\text{TiO}_3$ ($x = 0.03$) ceramic electrolyte exhibits a high ionic conductivity of $1.95 \times 10^{-3} \text{ Scm}^{-1}$ at 303 K, which is about twice as high as that of the pristine material in Fig. 17 and Fig. 18 (Zhang, S. et al., 2019).

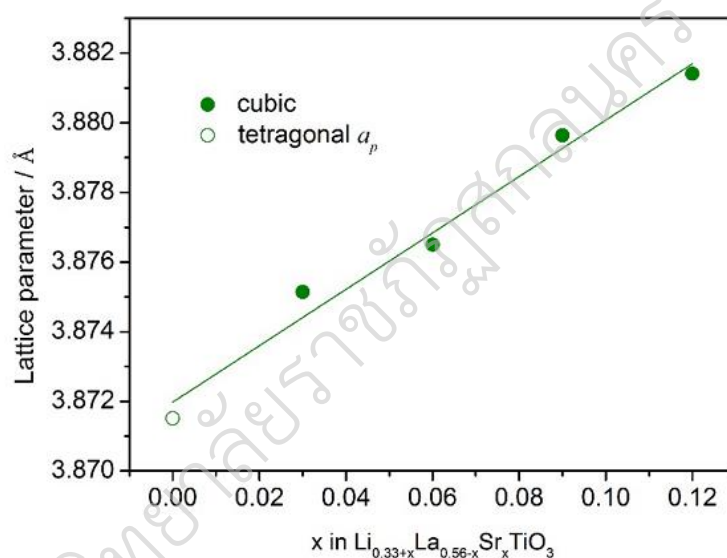


Fig. 17. Refined lattice parameter a of $\text{Li}_{0.33+x}\text{La}_{0.56-x}\text{Sr}_x\text{TiO}_3$ ($x = 0, 0.03, 0.06, 0.09$ and 0.12). Equivalent unit parameter for tetragonal structured sample ($x = 0$) is shown for comparison.

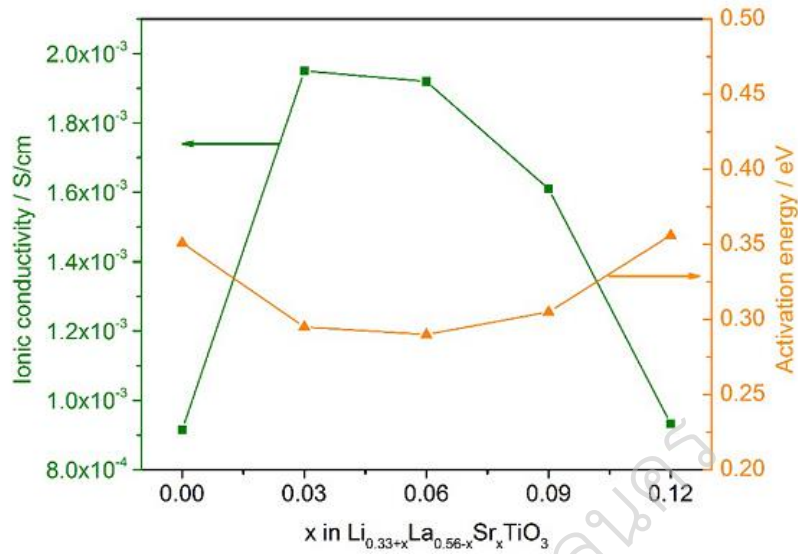


Fig. 18. Ionic conductivities at RT and activation energy versus Sr doping amount with solid lines given as a visual guide.

D. Lakshmi, et al. (2020, pp. 1343–1354) successfully synthesized perovskite $\text{Li}_{3x}\text{La}_{2/3-x}\text{TiO}_3$ (LLTO) solid electrolyte prepared by sol–gel and microwave–assisted sol–gel method and sintering process. The LLTO prepared by microwave–assisted method and sintering process for 1 h duration yields superior ionic conductivity in the range of $1.05 \times 10^{-3} \text{ S cm}^{-1}$ compared to the other LLTO samples which are in the range of high values reported for this material in Fig. 19. Also, higher electrochemical activity is observed for the LLTO sample treated in microwave radiation for an hour of duration in Table 5. (Lakshmi, D. et al., 2020).

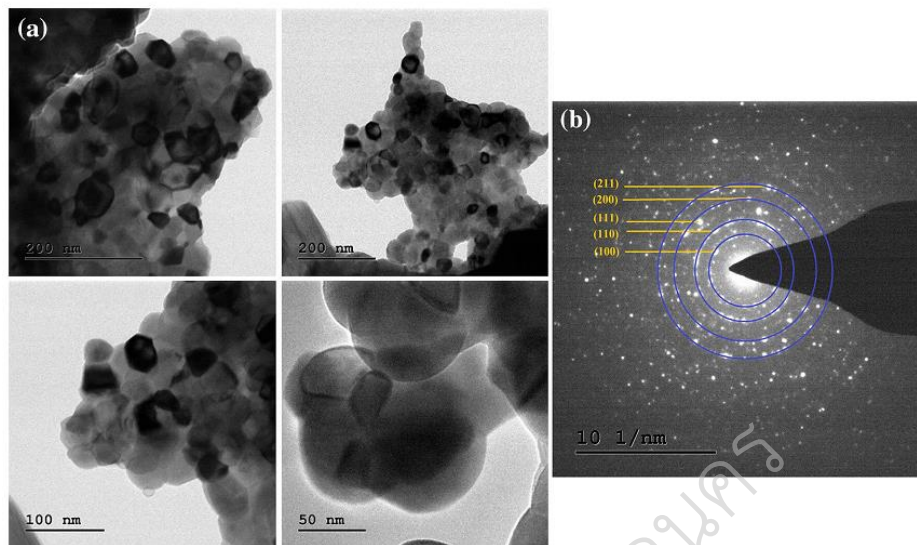


Fig. 19. (a) TEM micrograph of LLTO samples at different magnifications. (b) SAED pattern spots indexed with corresponding (hkl) planes.

Table 5 Fit parameters and conductivity values of LLTO nanoparticles

Sample	R_g (Ω)	R_{gb} (Ω)	R_{int} (Ω)	CPE-g (nF)	n	CPE-gb (μ F)	n	σ_g ($\times 10^{-3}$ S cm $^{-1}$)	σ_{gb} ($\times 10^{-3}$ S cm $^{-1}$)	Total conductivity ($\times 10^{-3}$ S cm $^{-1}$)
S-LLTO	35.15	57178	51383	0.30	0.85	1.60	0.50	0.15	0.16	0.16
LLTO-1 h	15.37	6973	9329	0.11	0.39	2.70	0.54	1.21	0.90	1.05
LLTO-2 h	21.21	27731	51609	0.17	0.89	3.11	0.39	0.30	0.16	0.24
LLTO-4 h	22.78	25877	27968	0.38	0.98	1.45	0.43	0.33	0.30	0.31
LLTO-8 h	36.78	17651	69802	0.58	0.81	3.84	0.40	0.48	0.12	0.30

Kun Yu, Rui Gu, et al. (2018, pp. 892– 896) prepared the $\text{LiO}_2\text{-SiO}_2\text{-B}_2\text{O}_3$ (LBS) glass-doped solid electrolyte $\text{Li}_{0.5}\text{La}_{0.5}\text{TiO}_3$ (LLTO) ceramics by using solid-state reaction method. The results show that the samples present mainly tetragonal perovskite structure and grain size increases with glass content increases in Fig. 20. The frequency-dependent AC conductivity shows two plateaus that correspond to the bulk and grain boundary responses as associated with two semi-circles observed in AC impedance spectrum. The maximum bulk ionic conductivity appeared at 1.0 wt% glass addition calculated by an equivalent circuit at a value of 1.12×10^{-3} S/cm, which is nearly 1.7 times compared to pure LLTO at room temperature. The overall electronic

conductivity is about $10^{-9} \text{ S cm}^{-1}$ calculated from a long-time leakage current measurement, which is 6 orders of magnitude lower than the ionic conductivity (Yu, K. et al., 2018).

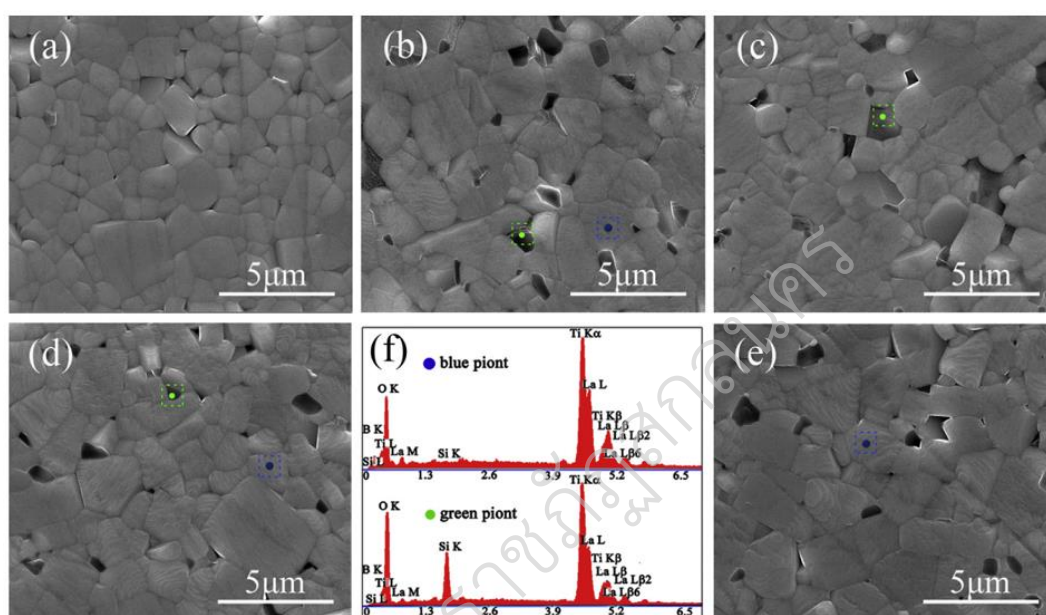


Fig. 20. SEM patterns of LLTG_x ceramics. (a)x=0 wt%, (b)x=0.5 wt%, (c) x=1.0 wt%, (d) x=1.5 wt% and (e) x=2.0 wt%. Graph (f) is the EDS spectrum of the blue and green points marked in the patterns.

All the green and blue points show similar EDS patterns in these graphs. (For interpretation of the references to color in this figure legend, the reader is referred to the Web version of this article.

Table 6 Ionic conductivity σ_{bulk} , σ_{gb} , and electronic conductivity σ_e for LLTGx ceramics at room temperature.

x content (wt%)	σ_{bulk} (S/cm)	σ_{gb} (S/cm)	σ_e (S/cm)
0	6.76×10^{-4}	1.47×10^{-5}	3.04×10^{-9}
0.5	9.23×10^{-4}	1.12×10^{-5}	1.34×10^{-9}
1.0	1.12×10^{-3}	5.51×10^{-6}	1.25×10^{-9}
1.5	8.96×10^{-4}	6.44×10^{-6}	2.16×10^{-9}
2.0	8.36×10^{-4}	6.16×10^{-6}	2.14×10^{-9}

GARNET-TYPE SOLID-STATE ELECTROLYTE MATERIALS

Garnet-type Li-ion conductors have been intensively studied as solid electrolytes for LIBs following the first report by Thangadurai et al (Thangadurai, V. et al., 2003). Garnet-type electrolytes are considered the prospective electrolytes for all-solid-state LIBs due to their stability toward Li metal, wide electrochemical stability window (>6 V vs Li/Li⁺ from CV studies and ~ 3 V from computational analyses), and high ionic conductivity (Zhu, Y. et al., 2015; Thangadurai, V., et al. 2014; Murugan, R. et al., 2007; Kim, Y. et al., 2016). Ideal garnets are a group of orthosilicates having the general formula of $A_3^{\text{II}}B_2^{\text{III}}(\text{SiO}_4)_3$ (A = Ca, Mg; B = Al, Cr, Fe) where A, B, and Si cations occupy the eight, six, and four coordination sites, which generally crystallize in cubic structure (space group $la\bar{3}d$) (Thangadurai, V. et al., 2014; Cox, E. G., 1951). The analogous Li containing garnet-type structure is $\text{Li}_3\text{La}_3\text{Te}_2\text{O}_{12}$ where Li replaces the tetrahedral Si^{4+} . However, $\text{Li}_3\text{La}_3\text{Te}_2\text{O}_{12}$ exhibits poor Li-ion conductivity. Therefore, it is required to increase the Li content, forming the so-called “Li-stuffed” garnet compositions. Various chemical compositions possible in a garnet-type structure by doping at different sites are shown in Fig. 21. Garnet-type electrolytes can be classified into four different subtypes, Li3, Li5, Li6, and Li7. The general trend is that the ionic conductivity of Li-containing garnets increases almost exponentially with Li content in a wide Li content scale. To examine the relationship between Li site

occupation and Li-ion conductivity, O'Callaghan et al. developed garnet-type $\text{Li}_3\text{Ln}_3\text{Te}_2\text{O}_{12}$ ($\text{Ln} = \text{Y}, \text{Pr}, \text{Nd}, \text{Sm-Lu}$) (O'Callaghan, M. P. et al., 2006). It was suggested that Li ions in $\text{Li}_3\text{Ln}_3\text{Te}_2\text{O}_{12}$ are located solely in the tetrahedral sites. These compounds showed a low ionic conductivity with a high activation energy proposing that these Li ions at tetrahedral positions are less mobile. Partial substitution of the trivalent La^{3+} with divalent ions in $\text{Li}_5\text{La}_3\text{M}_2\text{O}_{12}$ results in Li_6 phase, and the general formula can be represented as $\text{Li}_6\text{A}\text{La}_2\text{M}_2\text{O}_{12}$ ($\text{A} = \text{Mg}, \text{Ca}, \text{Sr}, \text{Ba}$, and $\text{M} = \text{Nb}, \text{Ta}$). Murugan et al. synthesized the cubic-structured $\text{Li}_7\text{La}_3\text{Zr}_2\text{O}_{12}$ in 2007, which has the highest conductivity of $3 \times 10^{-4} \text{ S}\cdot\text{cm}^{-1}$ and the lowest activation energy of 0.3 eV for garnet structure materials (Murugan, R. et al., 2007). The Li_7 phase is obtained by replacing M with Zr in $\text{Li}_5\text{La}_3\text{M}_2\text{O}_{12}$ along with excess Li^+ stuffing for charge balancing.

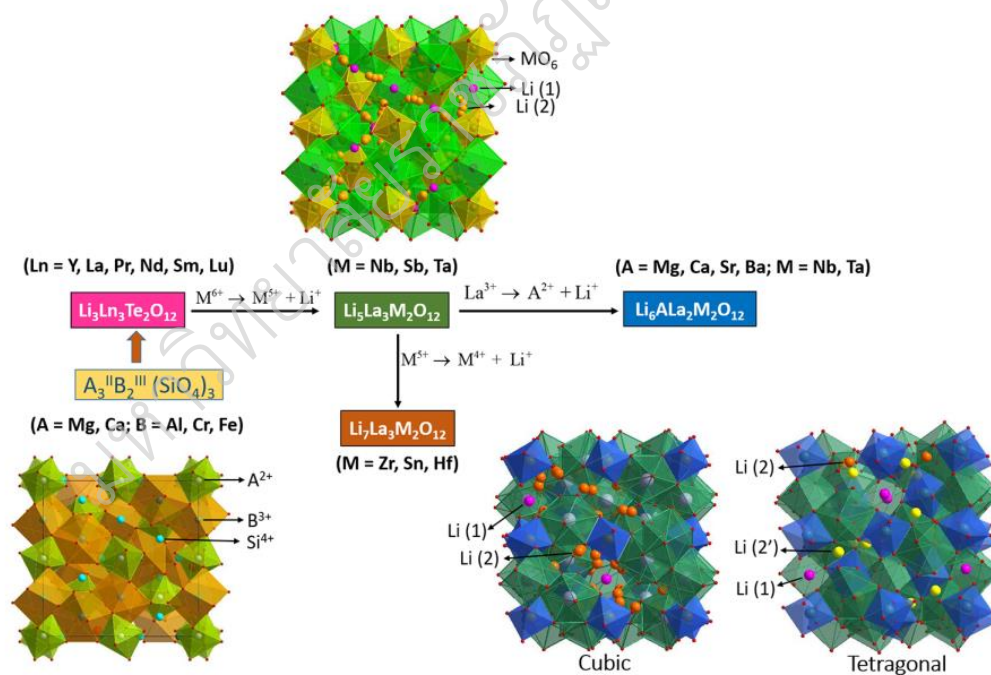


Fig. 21. Different chemical compositions are possible in garnet-type Li-ion conductors.

Li-Ion Conduction Mechanism in Garnet-Type

$\text{Li}_7\text{La}_3\text{Zr}_2\text{O}_{12}$ crystallizes in two stable phases: a cubic phase with a space group $\overline{\text{Ia3d}}$, which exhibits a disordered lithium-ion distribution, and a tetragonal form, with the I41/acd space group, which contains ordered lithium-ion distribution (Murugan, R. et al., 2007; Awaka, J. et al. 2009). Among these phases, the tetragonal polymorph has a conductivity two orders of magnitude lower than that of cubic form. In contrast to cubic polymorph, in tetragonal $\text{Li}_7\text{La}_3\text{Zr}_2\text{O}_{12}$, the tetrahedral Li sites are filled. Li-ions in garnet structures are distributed in three different interstitial sites, namely, (i) tetrahedral (24d), (ii) octahedral (48g), and (iii) off-centered octahedral (96h). In Li_3 phases, all Li-ions are tightly bound to the tetrahedral (24d) positions. Fig. 22(a) shows the variation of Li occupancy of tetrahedral and octahedral sites and room temperature conductivity as a function of Li concentration in cubic garnets (Thangadurai, V. et al., 2014; Cussen, E. J., 2010). The Li stuffed garnets, such as Li_5 , Li_6 , and Li_7 (cubic) subtypes, have Li content higher than three per unit formula. The excess Li-ions are incorporated into the octahedral sites, resulting in tetrahedral vacancy formation. Li^+-Li^+ interaction due to the increased octahedral population displaces Li-ions at central octahedral 48g site to off-centered 96h site near the opposite face, which is shared with the adjacent tetrahedra. As shown in Fig. 22(b), the ionic conductivity of lithium-stuffed garnets increases exponentially as lithium content increases. From the neutron diffraction studies, it has been shown that the maximum Li content in a cubic garnet phase can reach 7.5 per formula. However, the highest Li-ion conductivity has been achieved at a Li content of 6.4 ± 0.1 (Xie, H. et al., 2011; Li, Y. et al., 2012).

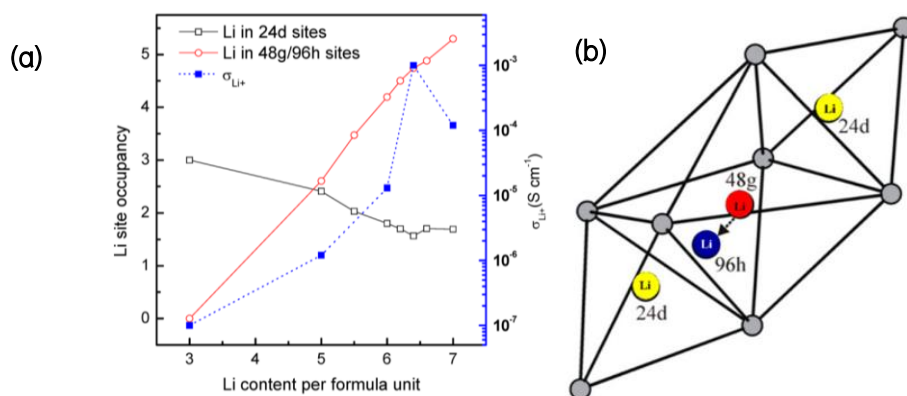


Fig. 22. (a) Variation of Li occupancy of tetrahedral and octahedral sites and room temperature conductivity as a function of Li content in the garnet structure (b) Distribution of Li-ions in tetrahedral (24d) and octahedral positions (48g and 96h). Reproduced with permission from (Thangadurai, V. et al., 2003) Copyright 2014 Royal Society of Chemistry.

POLYMER ELECTROLYTES (PEs)

In 1973, Fenton and colleagues demonstrated the ionic conductivity properties of polymer-Li salt complexation (Fenton, D., 1973). This research, along with others, marked the initial recognition of using polymer salt complexes as solid electrolytes. Utilizing polymer electrolytes offers numerous advantages over liquid and inorganic solid electrolytes, such as exceptional flexibility and resistance to changes in electrode volume during charge/discharge cycles, ease of processing, improved safety measures, and more (Long, L. et al., 2016). However, there are specific requirements for polymer-Li salt complexes to be suitable as electrolytes in Li-ion batteries, outlined as follows:

- High ionic conductivity
- High Li⁺ transference number
- Mechanical integrity
- Wide electrochemical stability window
- Flexible and improved chemical and thermal stability

The ability of the polymers to dissolve alkali metal salts is the crucial factor to choose the right category of polymers for this specific application. Polymers with polar groups, such as — O —, — S —, — N —, — P —, = O, C = O, C = N, C—F are able to dissolve salts [54]. Dissociation of inorganic salts in polymer matrix is easier in polymers with high dielectric constant and when salts have low lattice energy such as LiClO₄, LiPF₆, LiBF₆, LiCF₃SO₃, LiFSI, LiTFSI etc. (Ue, M., 1994; Osman, Z. et al., 2012). However, the ionic conductivity of polymer–salt complex is highly controlled by the crystalline structure of polymer. Fig. 23(a) shows the schematic of semi-crystalline structure in polymers. In solid polymer electrolytes, the Li ions are located at coordination sites near the polar group of the polymer chains (e.g. C—F bond in poly(vinylidene fluoride-co-hexafluoropropylene), PVDF–HFP). When the polymer chain undergoes segmental motions, free volume will be created. Li ions then migrate from one site to another site along the polymer chain (intra-chain) or hop between chains through free volume (inter-chain) Fig. 23(b). Thus, the amorphous regions of the polymer which contain less ordered structure and are more flexible to move are responsible for ion conduction. PVDF–HFP is one of the most studied and promising polymer matrices because of its relatively high dielectric constant ($\epsilon = 8.4$) and thermal stability (T_d ca. 470 °C). Additionally, PVDF–HFP can hold substantially higher amounts of Li–salt or liquid within its structure compared to other hosts, thanks to the amorphous nature of the HFP copolymer (Meyer, W. H., 1998; Liu, Y. et al., 2004; Croce, F. et al., 1998; Castillo, J. et al., 2021).

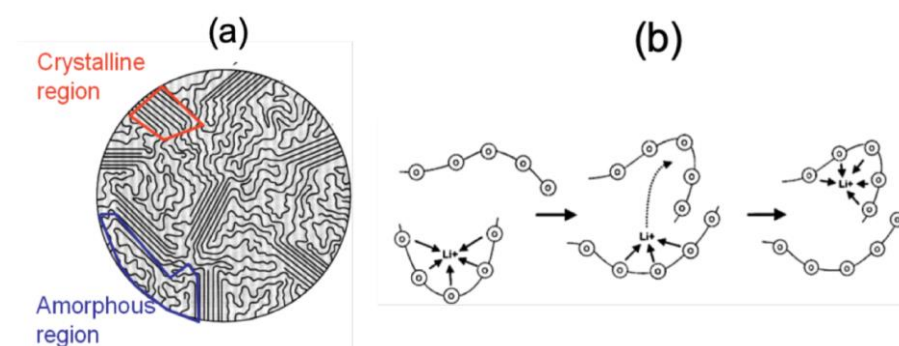


Fig. 23 (a) schematic of crystalline and amorphous regions in polymer (b) Li ion conduction mechanism in polymer–salt matrix.

COMPOSITE POLYMER ELECTROLYTES (CPEs)

Polymer electrolytes such as PEO, PPC, PVA, PVDF, PVCA, and PAN are lightweight, flexible, and demonstrate relatively lower interfacial resistance. Nonetheless, they are hindered by limitations such as reduced ionic conductivity, inadequate thermal stability, and low lithium-ion transference numbers. Among all the polymers, PVDF-HFP stands out due to its robust mechanical strength and exceptional electrochemical stability. The development of composite polymer electrolytes, combining the advantages of both polymer and ceramic electrolytes, emerges as an efficient strategy to address the issues. By finely tuning the mix of ceramic and polymer electrolytes, the drawbacks of each can be minimized without compromising their respective benefits. Composite polymer electrolytes are flexible, and exhibit high lithium-ion conductivity, significant lithium-ion transference numbers, and good thermal stability. In these electrolytes, ceramic filler particles, categorized into non-lithium-ion conductive fillers like Al_2O_3 , SiO_2 , and TiO_2 , and lithium-ion conductive fillers such as LLTO, LAGP, LATP, and LLZO, are dispersed in polymer matrices. A Lewis acid-base interaction occurs between the polymer's polar groups, enhancing the amorphous phase of the polymer chains and improving the thermal stability, mechanical strength, and electrochemical properties of the composite polymer electrolyte membrane.

Literature reviews of composite polymer electrolyte

Si Yuan Du, et al. (2022, pp. 19631–19639) successfully prepared a composite solid electrolyte with excellent performance using a polymer electrolyte poly(vinylidene fluoride–hexafluoropropylene) and an inorganic electrolyte $\text{Li}_{6.4}\text{La}_3\text{Zr}_{1.4}\text{Ta}_{0.6}\text{O}_{12}$. With the assistance of lithium salts and plasticizers, the prepared CSE achieves a high ionic conductivity of $4.05 \times 10^{-4} \text{ S}\cdot\text{cm}^{-1}$ at room temperature. The Li/CSE/Li symmetric cell can be stably cycled for more than 1000 h at $0.1 \text{ mA}/\text{cm}^2$ without short circuits. The all–solid–state lithium metal battery using a LiFePO_4 cathode displays a high discharge capacity of $148.1 \text{ mAh}\cdot\text{g}^{-1}$ and a capacity retention of 90.21% after 100 cycles. Moreover, the high electrochemical window of up to 4.7 V of the CSE makes it suitable for high–voltage service environments. The all–solid–state battery using a lithium nickel manganese cathode shows a high discharge specific capacity of $197.85 \text{ mAh}\cdot\text{g}^{-1}$ with good cycle performance. This work might guide the improvement of future CSEs and the exploration of flexible all–solid–state lithium metal batteries in Fig. 24 (Du, S. Y. et al., 2022).

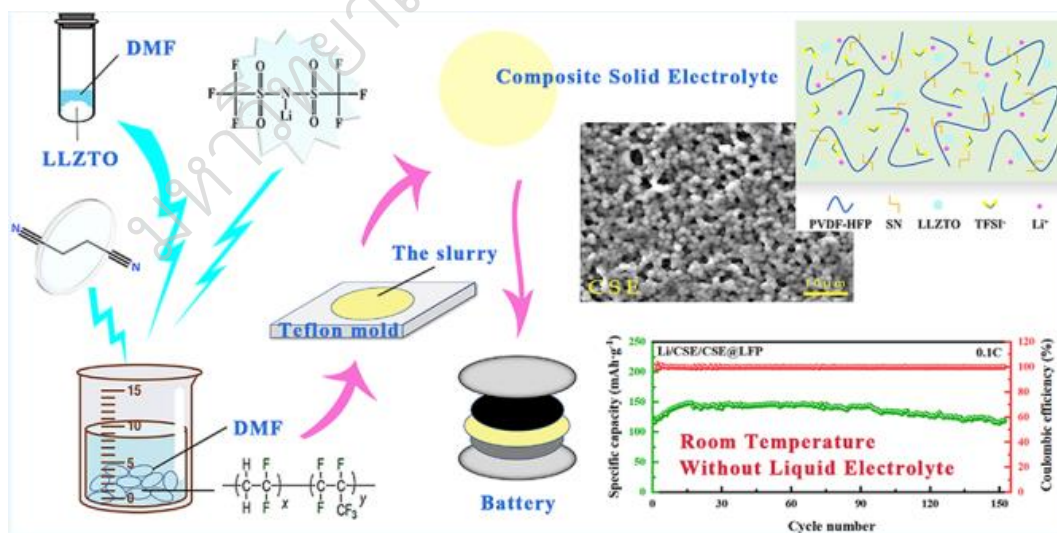


Fig. 24. Schematic diagram of the preparation process of the composite solid–state electrolyte for lithium metal batteries.

Chao Gao, et al. (2023, pp. 1–9) prepared a novel composite solid electrolyte (PLHL–CSE) membrane, which consists of poly (vinylidene fluoride–co–hexafluoropropylene) (PVDF–HFP), hydroxypropyl methylcellulose (HPMC), lithium bis(trifluoromethanesulfonyl)imide (LiTFSI), and $\text{Li}_{6.4}\text{La}_3\text{Zr}_{1.4}\text{Ta}_{0.6}\text{O}_{12}$ (LLZTO), was prepared by solution–casting technique. The incorporation of HPMC into PVDF–HFP–based electrolytes played crucial roles in reducing the crystallinity of PVDF–HFP, promoting the dissociation of lithium salt, and increasing the amount of mobile Li^+ . With the synergistic effects of HPMC and LLZTO, the mechanical and electrochemical performance of PVDF–HFP–based electrolytes were greatly enhanced. The obtained PLHL–CSE membrane showed better mechanical strength (3.0 MPa), enhanced ionic conductivity ($0.25 \text{ mS}\cdot\text{cm}^{-1}$ at $25 \text{ }^\circ\text{C}$), greater lithium–ion transference number (0.7), and broadened electrochemical window of 5.0 V (vs. Li^+/Li) than the PVDF–HFP/LiTFSI solid polymer electrolyte (PL–SPE) membrane. After 300 cycles at 1 C, the assembled $\text{LiFePO}_4/\text{PLHL–CSE}/\text{Li}$ cell with PLHL–CSE membrane as the hybrid composite solid electrolyte displayed a high–capacity retention (95.6%). In addition, the positive effects of HPMC and LLZTO on promoting the generation of stable SEI and uniform lithium deposition were also confirmed by the SEM results of cycled lithium metals. These findings point to the good potential of PLHL–CSE membrane as a hybrid composite solid electrolyte for practical application in lithium batteries in fig. 25 (Gao, C. et al., 2023).

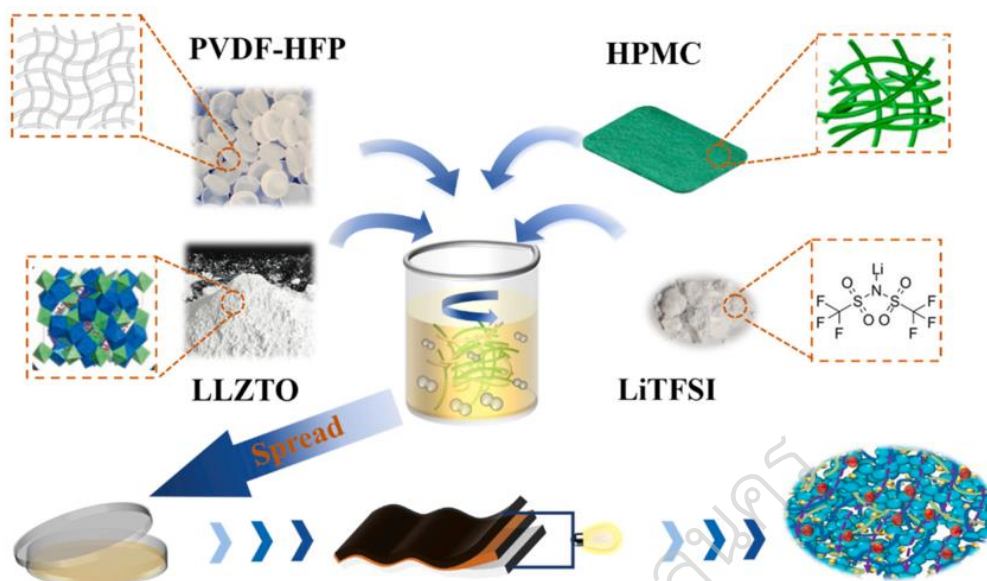


Fig. 25. The schematic of the fabrication process of PLHL-CSE membrane.

Wen He, et al. (2023, pp. 1–11) successfully prepared a construct polyethylene oxide-based ultrathin CSE membrane that is enhanced by a 3D fiber network composed of Poly (vinylidene fluoride-co-hexafluoropropylene) fibers and $\text{Li}_7\text{La}_3\text{Zr}_2\text{O}_{12}$ particles directly fabricated on the cathode. The 3D fiber network facilitates the rapid transport and uniform deposition of Li^+ , and enhances the mechanical strength of the electrolyte membrane, thereby effectively inhibiting the growth of lithium dendrites. Moreover, the unique preparation method reduces the interfacial impedance, and it can also greatly reduce the electrolyte thickness, which is beneficial to increasing the energy density of the battery. The lithium symmetric battery shows stable cycling over 1500 h under $0.2 \text{ mA}\cdot\text{cm}^{-2}$. Li/LiFePO₄ battery with the CSE membrane exhibits a high reversible capacity of $155.8 \text{ mAh}\cdot\text{g}^{-1}$ at 0.2 C for 100 cycles and the capacity retention rate is 98.0%. Furthermore, the obtained CSE membrane has a broadened electrochemical window of 4.83 V, and the reversible capacity of the Li/LiNi_{0.8}Co_{0.1}Mn_{0.1}O₂ battery is $160.6 \text{ mAh}\cdot\text{g}^{-1}$ at 0.2 C for 100 cycles. These findings showed that the structure proposed here is a viable electrolyte strategy for advanced solid-state lithium metal batteries in Fig 26 (He, W. et al., 2023).

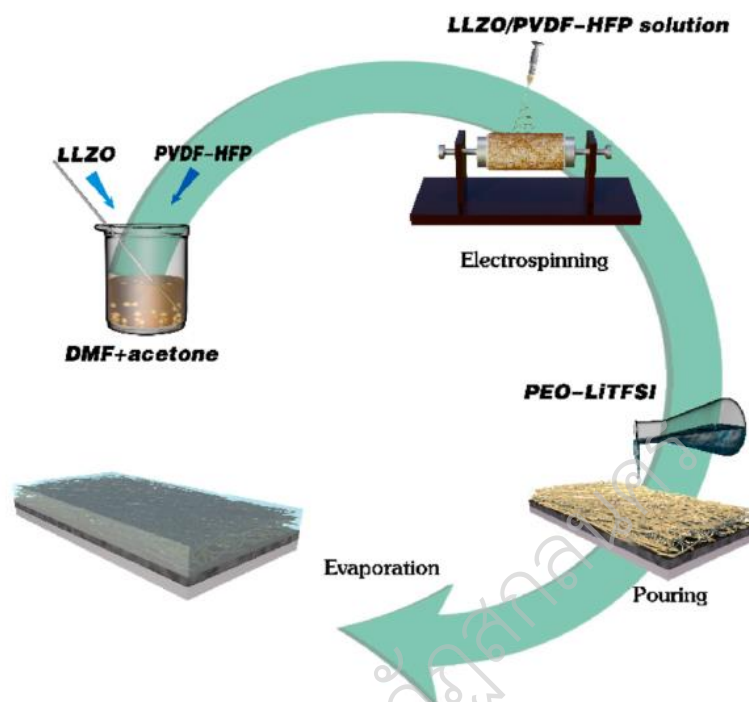


Fig. 26. Schematic representation of the preparation process of the PEO-based CSE enhanced by the 3D LLZO/PVDF-HFP fiber network structure.

Xin Long, et al. (2023, , pp. 1–10) successfully prepared a high-safety composite solid-state electrolyte (CSSE) constructed by embedding the high ionic conductivity garnet type $\text{Li}_{6.5}\text{La}_3\text{Zr}_{1.5}\text{Ta}_{0.1}\text{Nb}_{0.4}\text{O}_{12}$ (LLZTNO) powder into a polyvinylidene fluoride (PVDF) matrix. The ionic conductivity of the CSSE containing 10% LLZTNO could reach $1.05 \times 10^{-4} \text{ S cm}^{-1}$, and the electrochemical window was extended to 4.80 V vs Li/Li⁺. In addition, the evolution and composition of the SEI layer were characterized by in-situ optical microscopic observation, X-ray photoelectron spectroscopy, and cryogenic electron microscopy (cryo-EM). When paired with an NCM811 cathode, the batteries showed good rate cycling performance, and the discharge capacity could be maintained at 137.1 and 91.2 mAh g⁻¹ at 0.3C and 2C after 80 and 100 cycles. The needle penetration test further demonstrated superior safety and potential applications of the PVDF-based room-temperature CSSE batteries in Fig. 27 (Song, X. et al., 2023).

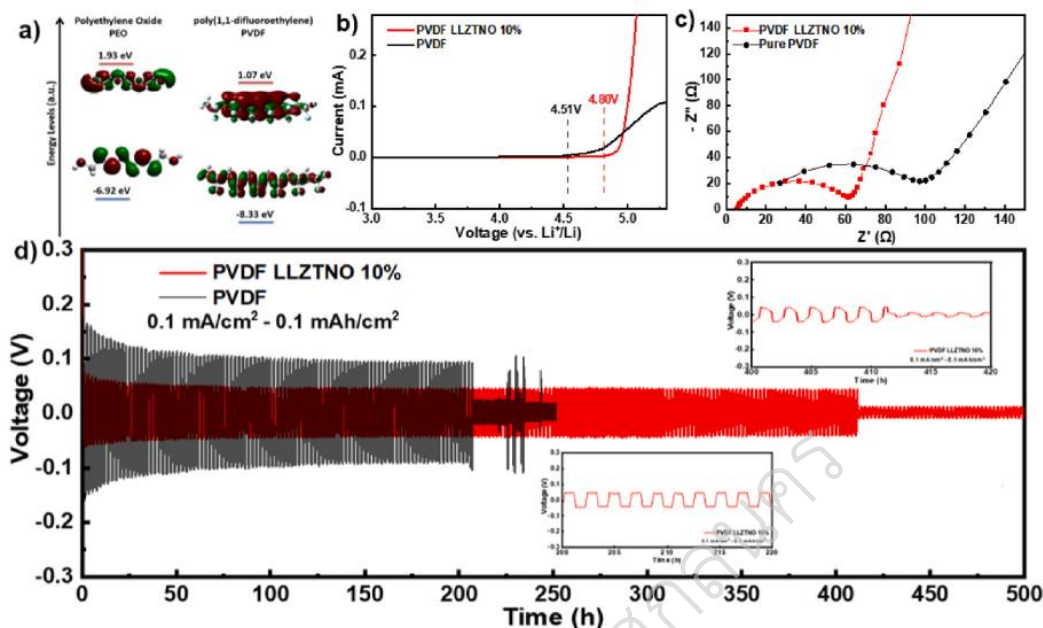


Fig. 27. (a) DFT calculation of PEO and PVDF, (b), (c) LSV and EIS curves of PVDF LLZTNO 10% CSSEs and PVDF membranes, (d) Galvanostatic cycling profiles of Li/ Li⁺ symmetric cells at 0.1 mA cm⁻², 0.1 mAh cm⁻².

Shiyu Cao, et al. (2023, pp. 37422–37432) prepared a dual-coordination mechanism first proposed to construct a high-performance poly (vinylidene fluoride)/Li_{6.4}Ga_{0.2}La₃Zr₂O₁₂/succinonitrile (PVDF/LLZO/SN) composite solid electrolyte. The dual-coordination interactions of SN with both LLZO and Li⁺ in lithium salts allow SN to act like a branched chain of PVDF, realizing an increase in the free volume of the composite electrolyte. Meanwhile, SN molecules are immobilized within the electrolyte membrane by coordinating with LLZO, ensuring good interfacial stability. Profiting from the dual-coordination mechanism, the PVDF/LLZO/SN composite solid electrolyte combines enhanced electrochemical performance and interfacial compatibility. When applied to ASSLBs, the composite solid electrolyte enables the battery to operate at rates up to 6 C. The LiFePO₄/Li batteries operated at 4 C can still deliver a high-capacity retention rate of 96.4% after 50 cycles. Notably, these

batteries also exhibit good long-cycle stability. After 500 cycles at 0.5 C, the discharge capacity was maintained at 145.9 mAh g⁻¹ in Fig. 28 (Cao, S. et al, 2023).

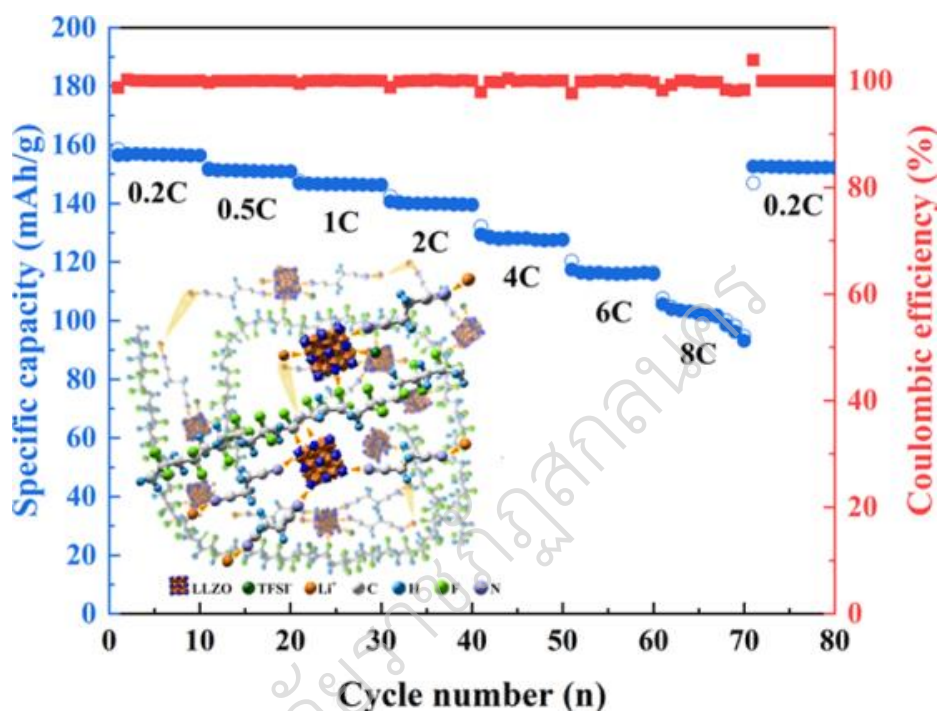


Fig. 28. The concept of poly (vinylidene fluoride)/ Li_{6.4}Ga_{0.2}La₃Zr₂O₁₂/succinonitrile composite solid electrolytes toward enhanced rate performance in all-solid-state lithium batteries.

Thuy Duong Phame and Kyung-Koo Lee (2021, pp. 1–12) successfully prepared the practical application of Li metal batteries with 1,2-diethoxyethane (DEE) is proposed as a new electrolytic solvent for lithium metal batteries (LMBs), and the performances of 1.0 m LiFSI in DEE are evaluated. Because of the low dielectric constant and dipole moment of DEE, the majority of the FSI⁻ exists in associated states like contact ion pairs and aggregates, which are like highly concentrated electrolytes. These associated complexes are involved in the reduction reaction on the Li metal anode, forming sound solid electrolyte interphase layers. Furthermore, free FSI⁻ ions in DEE are observed to participate in the formation of cathode electrolyte interphase

layers. These passivation layers not only suppress dendrite growth on the Li anode but also prevent unwanted side reactions on the LiFePO_4 cathode. The average CE of the Li||Cu cells in LiFSI–DME is observed to be 98.0%. Moreover, LiFSI–DME also plays an important role in enhancing the cycling stability of the Li||LFP cell with a capacity retention of 93.5% after 200 cycles. These results demonstrate the benefits of LiFSI–DME, which creates new possibilities for high–energy–density rechargeable LMBs in Fig. 29 and 30 (Pham, T. D., & Lee, K. K., 2021).

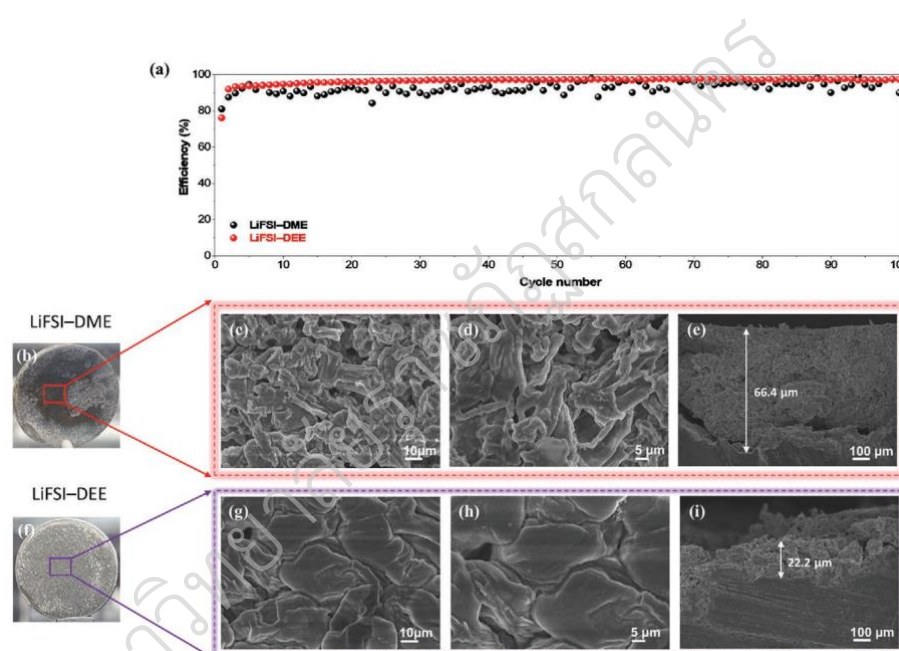


Fig. 29. (a) Efficiency of Li metal plating/stripping on a Cu substrate in LiFSI–DME and LiFSI–DDE. The Li||Cu cells are evaluated at 25 °C under a constant current density of 0.5 mA cm^{-2} for 1 h, followed by stripping at the same current density until a cut–off voltage of 1.0 V versus Li/Li^+ is reached. Morphology of the Li metal anode/electrolyte interface collected from the Li||Cu cells after 20 cycles (80 h) under the same conditions with Li||Cu cells in Figure 3a. The optical images of the cycled Li–metal anode in (b) LiFSI–DME and (f) LiFSI–DDE. SEM images of the Li–metal anode in the cell using (c–e) LiFSI–DME (c,d–top–view and e–cross–section) and (g–i) LiFSI–DDE (g,h–top–view and i–cross–section).

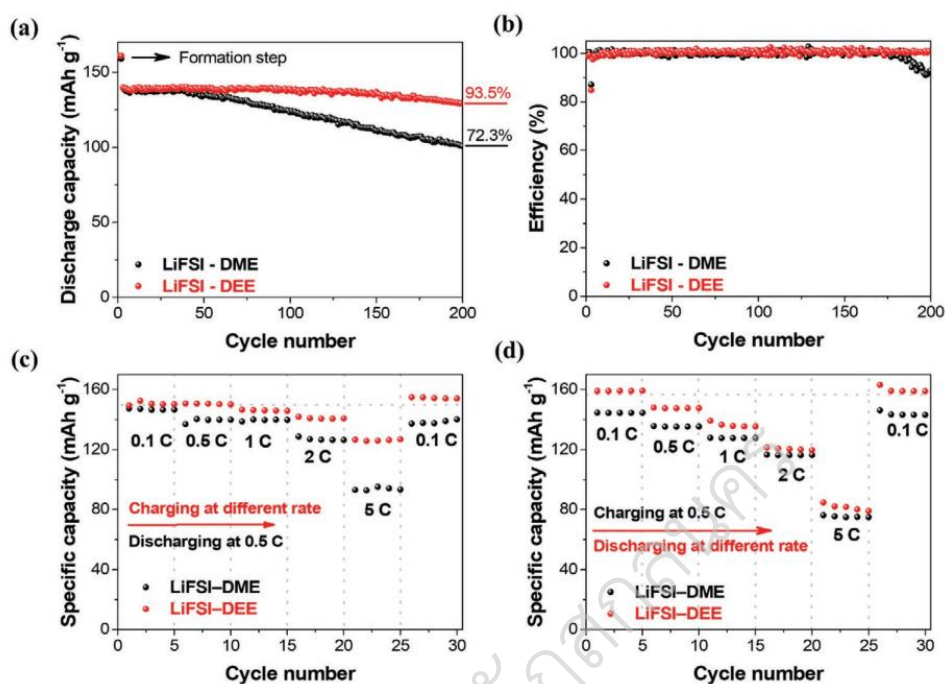


Fig. 30. Cycling of Li||LFP cells in LiFSI–DME and LiFSI–DEE. (a) discharge capacity and (b) efficiency. Rate performance of the Li||LFP cell using LiFSI in DME and DEE. (c) charging with an increasing C–rate but discharging at a rate of 0.5 C–rate and (d) charging at a 0.5 C–rate but discharging at an increasing C–rate.

Thuy Duong Phame et. al (2022, pp. 1–12) successfully designed the practical application of Li metal batteries with high salt concentration (LiFSI), and a weakly solvating solvent (DEE) that can generate solvation structures dominated by associated species, such as CIPs and AGGs at a relatively lower concentration, compared to common super concentrated electrolytes. This resulted in a stable and conductive interface layer at the anode and cathode. Regarding the Li anode, surface analyses such as SEM and XPS verified the formation of a beneficial LiF–rich SEI layer on the cycled Li through salt decomposition before the solvent reduction, owing to the high ratio of associated species in the solvation structure. Therefore, a high average CE of $\approx 98.4\%$ was obtained in the Li||Cu cell with the 3.5 m LiFSI–DEE electrolyte. For Li||NMC811 cells, the high discharge capacity and high–capacity retention of $\approx 94\%$

after 200 cycles was demonstrated at 2.5 mA cm^{-2} at an upper voltage of 4.4 V, indicative of the viability of the system to support high cathode loading and fast charging operations. The structure of NMC811 was maintained after long cycling. The concentrated weakly solvating electrolyte consisting of 3.5 m LiFSI in DEE prohibited Al corrosion under high voltages, thus enabling stable cycling of Li||NMC811 cells at 4.4 V. Additionally, the 3.5 m LiFSI–DEE electrolyte exhibited good performance under practical conditions. The AFBs with the 3.5 m LiFSI–DEE achieved a high efficiency of $\approx 99\%$ and the sum of reversibly cycled Li of $\approx 6800 \text{ mAh g}^{-1}$ after 50 cycles. This study offers an effective strategy for stabilizing Li metal anodes and NMC811 cathodes in DEE-based HCEs, which is a potential solution for high energy density batteries in the future in Fig. 31 and 32 (Pham, T. D. et al., 2022).

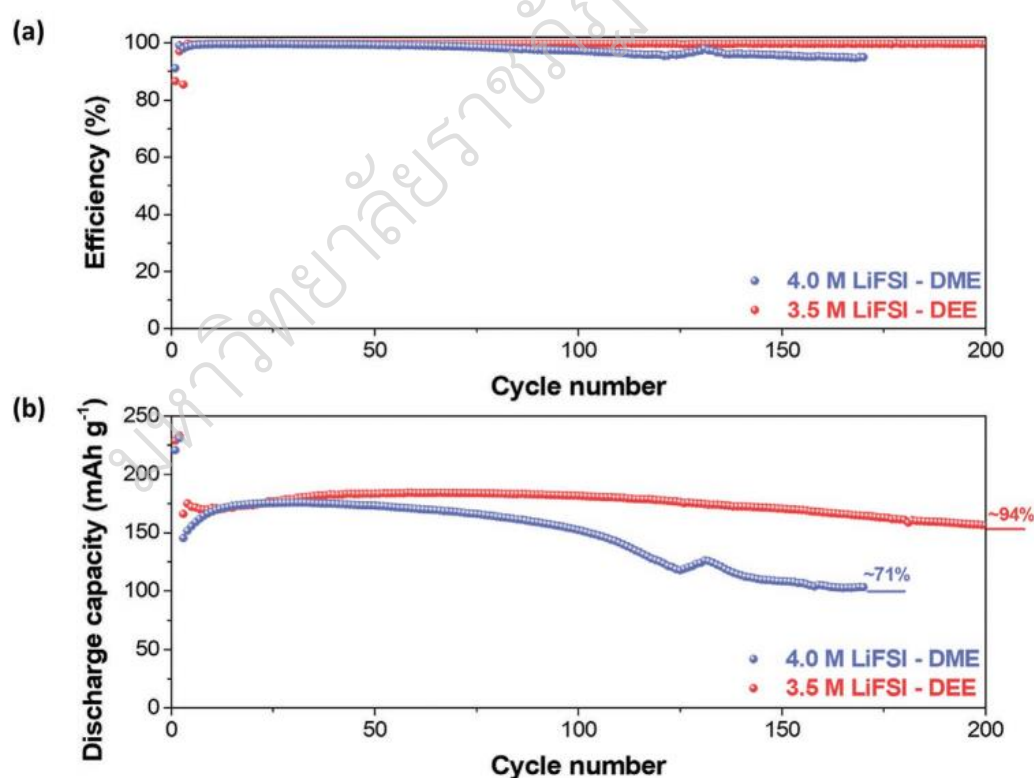


Fig. 31. Electrochemical behavior of different ether electrolytes in Li||NMC811 batteries. Cycling performance of Li||NMC811 cells. (a) Efficiency and (b) discharge capacity using the HCE–DME and HCE–DEE electrolytes.

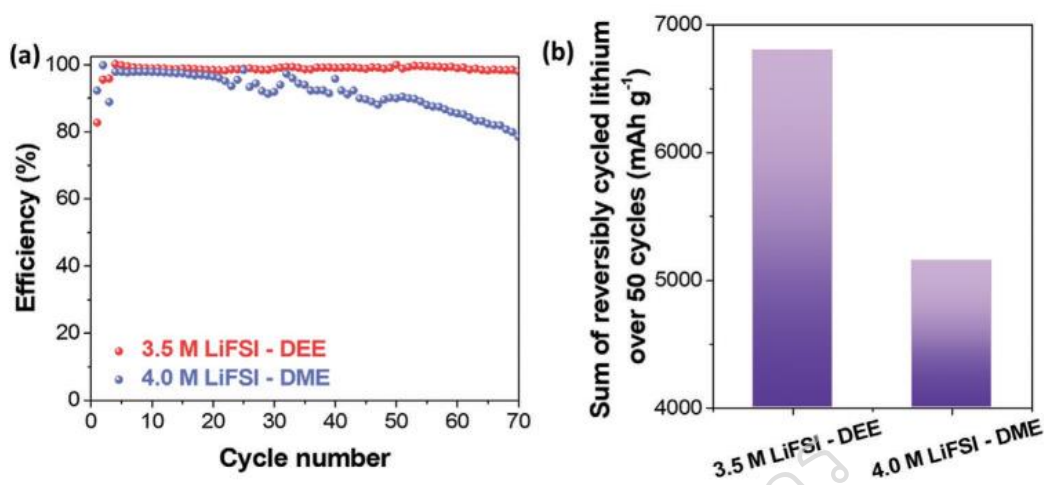


Fig. 32. Electrochemical behavior of anode-free CullNMC811 batteries. (a) Efficiency and (b) sum of reversibly cycled Li over 50 cycles (charge/discharge current density of 0.3 C/1.0 C) obtained from CullNMC811 cells in HCE-DME (4.0 m LiFSI-DME) and HCE-DEE (3.5 m LiFSI-DEE).

In the present thesis, perovskite- $\text{Li}_{3x}\text{La}_{2/3-x}\text{TiO}_3$ was improved by using a reduced grain boundary to increase the total ionic conductivity. The strategies of a reduced grain boundary are using doping A-site with alkaline earth B-site with transition metal conventional solid-state reaction method for forming particle to cubic structure of $\text{Li}_{3x}\text{La}_{2/3-x}\text{TiO}_3$. The cubic- $\text{Li}_{0.5}\text{La}_{0.5}\text{TiO}_3$ structure was selected for the co-substitution of the La site with Sr and Ti site with Ta, both of which have larger ionic radii at different concentrations, to enhance the bottleneck size for Li^+ migration channels and maintain the cubic structure, leading to an increase in ionic conductivity. Additionally, Sr and Ta co-substitution improved the pellet sample density during sintering. The Sr and Ta co-substitution was significantly effective in enhancing the total conductivity of cubic- $\text{Li}_{0.5}\text{La}_{0.5}\text{TiO}_3$, making it a potential candidate for use as a composite polymer electrolyte in perovskite-type Li metal batteries. Moreover, we have developed a straightforward process for fabricating thin and flexible composite polymer electrolytes (CPEs) using the solution casting technique. These CPEs are based on the garnet-type $\text{Li}_{6.25}\text{Ga}_{0.25}\text{La}_3\text{Zr}_2\text{O}_{12}$ (LLZO-Ga) material, which is embedded in a

PVDF–HFP polymer matrix along with LiTFSI. The inclusion of LLZO–Ga in the PVDF–HFP polymer matrix serves as a plasticizer, reducing the crystallization of the polymer matrices and enhancing the ionic conductivity of the CPEs. In the fabrication of cells with LiFePO_4 (LFP) and $\text{LiNi}_{1/3}\text{Mn}_{1/3}\text{Co}_{1/3}\text{O}_2$ (NMC111) as the cathodes, CPEs–10 as the electrolyte, a high–concentration electrolyte (4M LiFSI: DEE), and lithium metal as the anode, excellent cycle stability and good rate performance were demonstrated at room temperature. This research contributes to the advancement of LLZO–Ga–based composite polymer electrolytes for lithium metal batteries.

มหาวิทยาลัยราชภัฏสุราษฎร์ธานี

CHAPTER 3

MATERIALS AND METHODOLOGY

The polycrystalline samples were synthesized by solid-state reaction method which is most widely used for the preparation of polycrystalline solids from the mixing of powder materials. In this work, the precursor powder was mixed by ball milling in ethanol and pressed the powder into bulk samples. Phase identification and morphology were performed using powder X-ray diffraction (XRD), scanning electron microscope (SEM), and the chemical state and composition of the sample were measured by X-ray photoelectron spectroscopy: (XPS). The impedances of the specimens were measured with an impedance analyzer in the frequency range from 18 MHz to 1 Hz at room temperature. All-solid-state and semi-solid full cells were Galvano statically charged and discharged on land test system following by:

SYNTHESIS AND PREPARATION OF PEROVSKITE SOLID-STATE ELECTROLYTE

Synthesis perovskite- $\text{Li}_{3x}\text{La}_{2/3-x}\text{TiO}_3$

The solid-state reaction (SSR) method is the most widely used synthesis compound because easily mixing solid powder precursor follows stoichiometric ratios. This project synthesized $\text{Li}_{0.5-x}\text{La}_{0.5-x}\text{Sr}_x\text{Ti}_{1-x}\text{Ta}_x\text{O}_3$ ($0 \leq x \leq 0.12$) powders by SSR method for success. The chemicals powder and equipment used in this process are shown in Table 7 and Table 8, respectively.

Table 7 List of chemicals used for synthesis and preparation of perovskite composite polymer electrolyte method their formula, supplier, and purity.

Chemical	Formula	Supplier	Purity
Lithium carbonate	Li_2CO_3	QRëC	>99%
Lanthanum oxide	La_2O_3	Fisher	>99%
Strontium pentoxide	SrO_2	Scientific	99.5%
Titanium dioxide	TiO_2	UK	99.5%
Tantalum (V) oxide	Ta_2O_5	QRëC	99.9%
Zirconium dioxide	ZrO_2	Sigma-	>99%
Ethanol	$\text{CH}_3\text{CH}_2\text{OH}$	Aldrich	99.9%
Poly (vinylidene fluoride- co-hexafluoropropylene	$(-\text{CH}_2\text{CF}_2-)_x[-\text{CF}_2\text{CF}(\text{CF}_3)-]_y$	Sigma- Aldrich	99.9%
Lithium bis (trifluoromethanesulfonyl) imide	$\text{CF}_3\text{SO}_2\text{NLiSO}_2\text{CF}_3$	QRëC Sigma- Aldrich	>90%
N, N-dimethylformamide	$\text{HCON}(\text{CH}_3)_2$		>95%
Liquid electrolyte	1M LiPF_6 in EC: DEC v/v%	FUJIFILM Wako Pure Chemical Corporation	>95%
Lithium-Ion Phosphate Super-P	LiFePO_4 C	FUJIFILM Wako Pure	>95% >99%
Acetone	CH_3COCH_3	Chemical	99.5%
Poly(vinylidenedifluoride)	$(\text{CH}_2\text{CF}_2)_n$	lithium	>99%
N-methyl-2-pyrrolidone	$\text{C}_5\text{H}_9\text{NO}$	battery grade, Kishida	99%

Chemical
Hosen
Corp
Alfa Aesar
QRëC
Sigmar-
Aldrich
FUJIFILM
Wako Pure
Chemical

Table 8 List of equipment used for synthesis of powder, preparation of bulk, characterization, and measurement of thermoelectric properties together with their model and area of application.

Equipment	Model	Application
Planetary Ball mill	PM400	Mixing and milling of powders Cleaning of materials
Ultra-sonic cleaner	BAKU BK-3350	Drying of wet powders
Hot plate & stirrer	Vision vs-130SH	Weighing compound
Weight scale	METTLER TOLEDO	Calcination, sintering and annealing.
Furnace 1700 C	XDEM-1700 AF	Cutting of materials
Saw low speed	BUEHLER Isomet	Grinding-Polishing of materials
Grinder-Polisher	BUEHLER Metaseve 3000	Study phases composition.
XRD		Study microstructure and phases composition.
FE-SEM	SHIMADZU-6100 JEOL JMS-7800F	Measurement density of

Density kit	prime	materials
X-ray photoelectron spectroscopy: (XPS)	METTLER TOLEDO MS204	Chemical state and composition
Electrochemical impedance spectroscopy (EIS)		Ionic conductivity
Galvanostatic discharge/charge	Solartron SI 1260	Lithium transference number charge/discharge cycle of full cell
	Bio-Logic Science Instrument VSP-300-	

The $\text{LLSr}_x\text{TTa}_x\text{O}_3$ ($0 \leq x \leq 0.12$) or $\text{LLSr}_x\text{TTa}_x\text{O}_3$ ($0 \leq x \leq 0.12$) pellets were synthesized using the solid-state reaction method. High-purity raw materials, including Li_2CO_3 (>99.9%, Ar), La_2O_3 (99%, Ar), SrO_2 (99%, Ar), TiO_2 (99%, Ar), and Ta_2O_5 (99.9%, Ar), served as the starting materials. The raw powders were weighed in the appropriate stoichiometric proportions and then mixed using a planetary ball mill with agate balls and a vial in ethanol for 24 hours at 350 rpm. Subsequently, they were dried at 80 °C for 24 hours, with an additional 20 mol.% excess of Li_2CO_3 to compensate for lithium volatilization. Furthermore, the La_2O_3 raw material powders were pre-calcined at 800 °C for 10 hours in an air atmosphere to eliminate moisture vapor. The mixed powder was subjected to calcination at 1000 °C for 12 hours in the air atmosphere by furnace shown in Fig. 33. The temperature profile used for calcination is shown in Fig. 34.



Fig. 33. High temperature furnace maximum temperature 1700 °C.

Temperature profile for calcination $\text{Li}_{0.5-x}\text{La}_{0.5-x}\text{Sr}_x\text{Ti}_{1-x}\text{Ta}_x\text{O}_3$ ($0 \leq x \leq 0.12$) powder

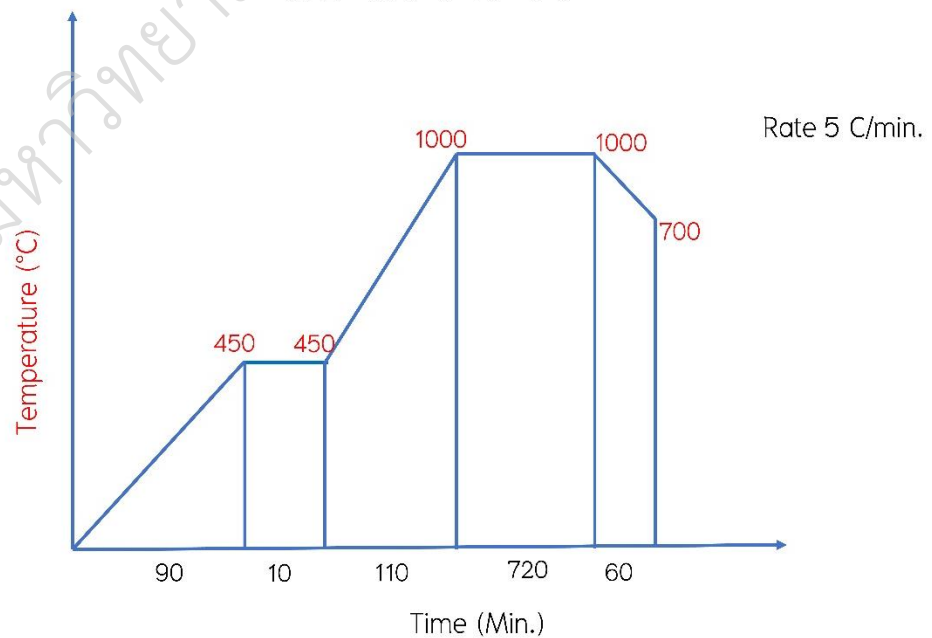


Fig. 34. Schematic of heating profile for calcination used to all samples in Air.

Sintering bulk samples

Following this, the calcined powder was uniaxially pressed at 200 MPa to form pellets with a diameter of 20 mm. To prevent lithium loss during the sintering process, the green pellets were coated with a layer of mother powder. The sintering process took place at 1300 °C for 10 hours in an air atmosphere, with a heating rate of 5 °C per minute in Fig. 35. The flowchart of $\text{Li}_{0.5-x}\text{La}_{0.5-x}\text{Sr}_x\text{Ti}_{1-x}\text{Ta}_x\text{O}_3$ ($0 \leq x \leq 0.12$) synthesis process is given in Fig 36.

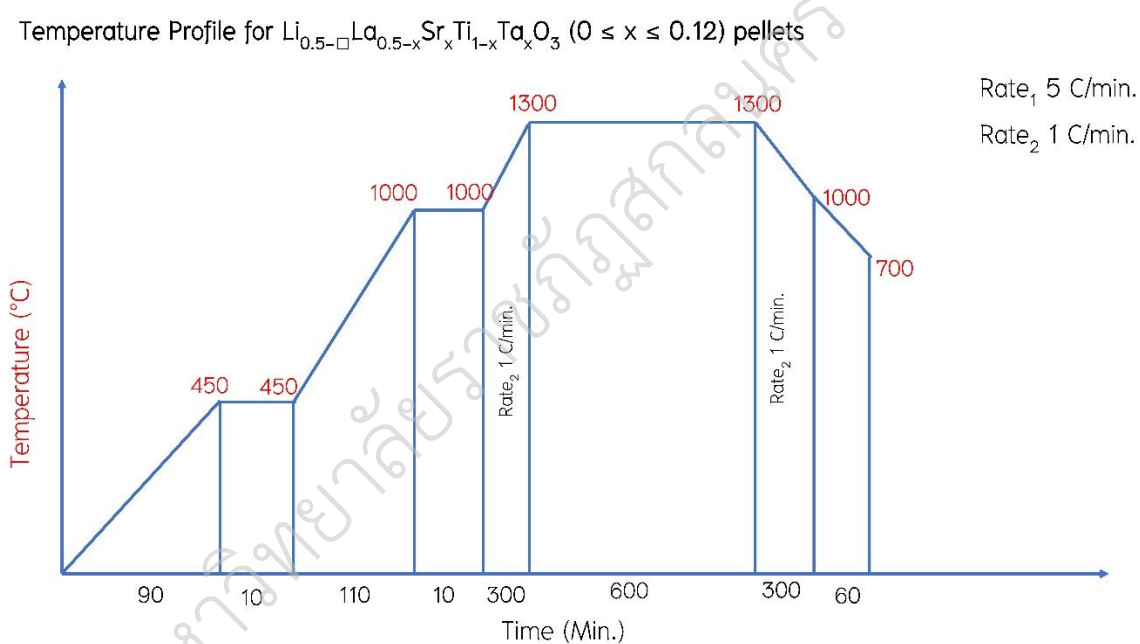


Fig. 35. Schematic of heating profile used for sintering of the samples with indicated heating /cooling rates in air.

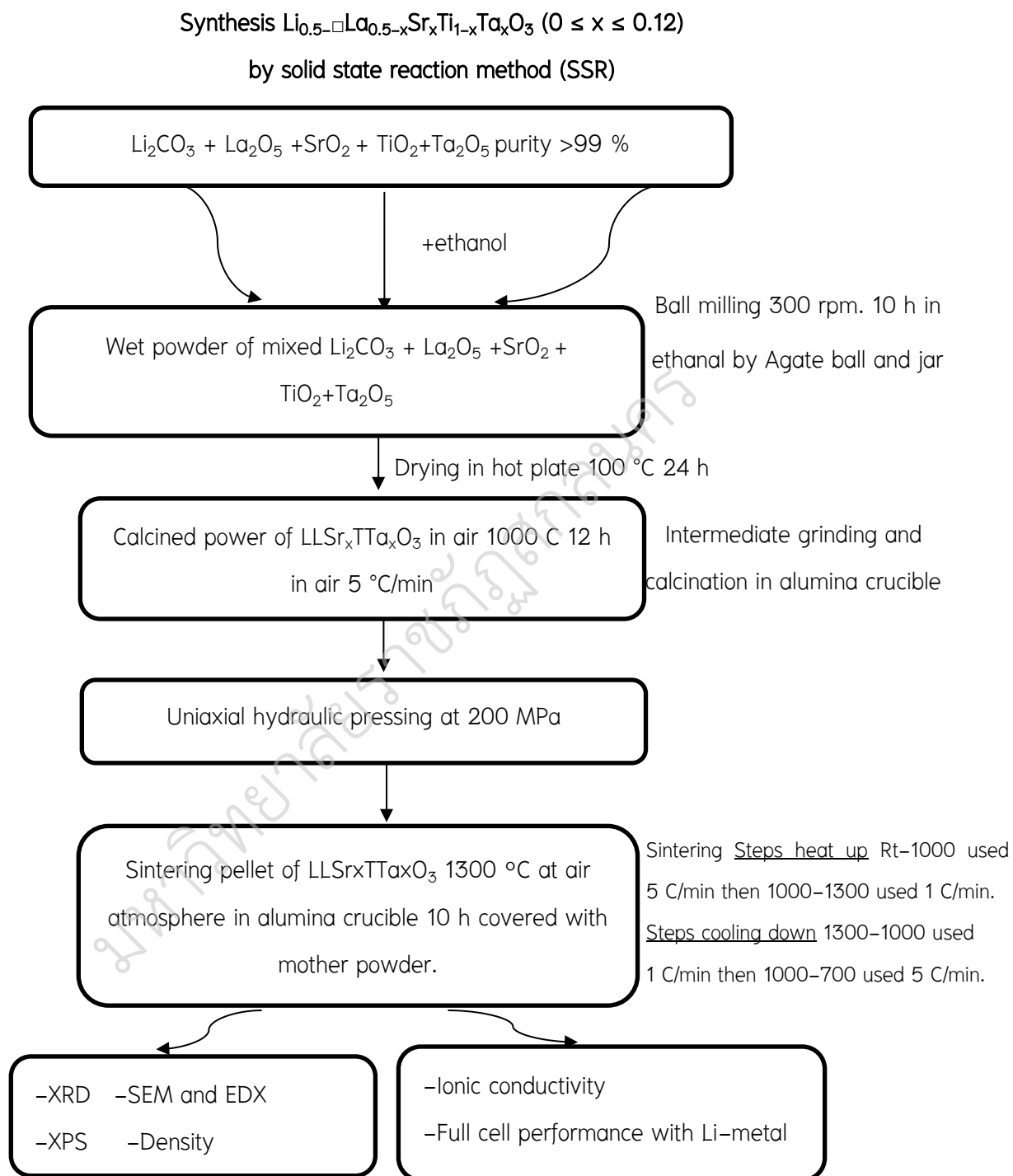


Fig. 36. Flowchart of $\text{Li}_{0.5-x}\text{La}_{0.5-x}\text{Sr}_x\text{Ti}_{1-x}\text{Ta}_x\text{O}_3$ ($0 \leq x \leq 0.12$) synthesis process.

Composite polymer electrolyte with perovskite $\text{LLSr}_{0.09}\text{TTa}_{0.09}\text{O}_3$ powder

The preparation of composite polymer electrolytes consists of polymer and ceramic materials. Before preparing the precursor solution, Poly (vinylidene fluoride-co-hexafluoropropylene) (PVDF-HFP), Lithium Bis (trifluoromethanesulfonyl) imide, (LiTFSI) and sintered powder $\text{LLSr}_{0.09}\text{TTa}_{0.09}\text{O}_3$ were vacuum dried at 80 °C for 24 hours. Initially, PVDF-HFP and LiTFSI (with a weight ratio of 3:2) were dissolved in Dimethylformamide (DMF) and acetone (7:3 ml) within a glove box, and the mixture was stirred at 60 °C for 12 hours to create a salt solution. Subsequently, sintered powder $\text{LLSr}_{0.09}\text{TTa}_{0.09}\text{O}_3$ was added to the salt solution in weight ratios of 0 (CPE-0), 5 (CPE-5), 10 (CPE-10), 15 (CPE-15), and 20 wt.% (CPE-20) relative to the combined weight of LiTFSI and PVDF-HFP. The resulting solution, constituting the CPE, was stirred at 60 °C for 12 hours, yielding a ready-to-use solution. The CPE solution was poured into a Teflon tray to prepare the CPE film. Subsequently, the film was treated with N_2 gas for 12 hours and dried under vacuum for an additional 60 °C for 12 hours, thus rendering the CPE film ready for assembly full cells shown in Fig. 37. The EIS of the CPE membrane was sandwiched between two stainless steel (SS) blocking electrodes to determine the ionic conductivity, and performed on the AC impedance method using a frequency response analyzer multichannel with potentiostat/galvanostat (Bio-Logic Science Instrument VSP-300) in the frequency range from 100 mHz to 7 MHz at RT. In addition, the EIS of CPE-0 and CPE-10 in contact with lithium metal was examined by tests of a Li/CPE/Li symmetric cell with applied 5 μL of liquid electrolyte (1M LiPF_6 in EC: DEC v/v%), which was prepared by sandwiching lithium metal foils, and the CPE in a coin cell 2032 type battery shells as the same the frequency range at RT.

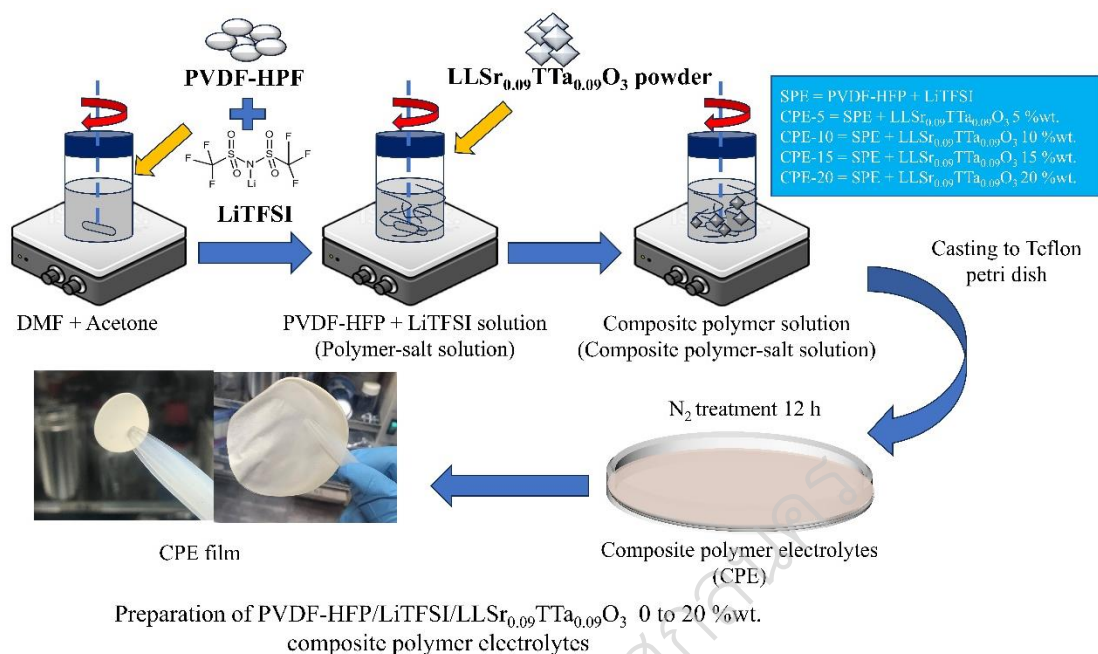


Fig. 37. Flowchart illustrating the preparation process of the perovskite composite polymer electrolytes.

SYNTHESIS AND PREPARATION GARNET SOLID STATE ELECTROLYTE

Synthesis garnet – Li_{6.25}Ga_{0.25}La₃Zr₂O₁₂

Polycrystalline Li_{6.25}Ga_{0.25}La₃Zr₂O₁₂ (LLZO–Ga) was synthesized through a solid–state reaction. Appropriate amounts of Li₂CO₃, La(OH)₃, ZrO₂, Ga₂O₃ were mixed by ball–milling with hexane. To compensate for lithium evaporation during sintering, a 5 mol% excess of lithium was added. For LLZO–Ga, the mixed powder was covered with a gold sheet and calcined in air at 800 °C for 12 h. The sintered samples were then ball–milled again with hexane, pelletized by cold isostatic pressing, and then sintered in air at 1050 °C for 12 h on a gold sheet in an Al₂O₃ crucible to avoid any contamination from the crucible. The sintered pellet was quenched from above 400 °C to prevent reaction with CO₂ and H₂O in the air. Subsequently, the pellet was ground into a powder in hexane and stored in a dry box, ready for use as filler powder shown in Fig.38.

Table 9 List of chemicals used for synthesis and preparation of garnet composite polymer electrolyte method their formula, supplier, and purity.

Chemical	Formula	Supplier	Purity
Lithium carbonate	Li_2CO_3	Nacalai	>99%
Lanthanum hydroxide	$\text{La}(\text{OH})_3$	Tesque,	99.9%
Gallium (III) oxide	Ga_2O_3	Sigma-	99.9%
Zirconium dioxide	ZrO_2	Aldrich	99.9%
Poly (vinylidene fluoride-co-hexafluoropropylene)	$(-\text{CH}_2\text{CF}_2-)_x[-\text{CF}_2\text{CF}(\text{CF}_3)-]_y$	Rare Metallic	99.9%
Lithium bis (trifluoromethanesulfonyl) imide	$\text{CF}_3\text{SO}_2\text{NLiSO}_2\text{CF}_3$	Toso Sigma- Aldrich	>90%
Lithium bis (fluoromethanesulfonyl) imide	$\text{F}_2\text{LiNO}_4\text{S}_2$		>90%
1,2 diethoxyethane		FUJIFILM	
N, N-dimethylformamide	$\text{C}_6\text{H}_{14}\text{O}_2$	Wako Pure	98%
	$\text{HCON}(\text{CH}_3)_2$	Chemical	>95%
Lithium-Ion Phosphate		Kishida	
Lithium nickel manganese cobalt oxide	LiFePO_4	Chemical	>99%
Super-P	$\text{LiNi}_{1/3}\text{Mn}_{1/3}\text{Co}_{1/3}\text{O}_2$		>99%
Acetone	C		
Poly(vinylidenedifluoride)	CH_3COCH_3	Thermo	>99%
N-methyl-2-pyrrolidone	$(\text{CH}_2\text{CF}_2)_n$	scientific	99.5%
	$\text{C}_5\text{H}_9\text{NO}$	FUJIFILM	>99%
		Chemical	99%
		Hosen	

Corp

Hosen

Corp

Alfa Aesar

QRèC

Sigmar-

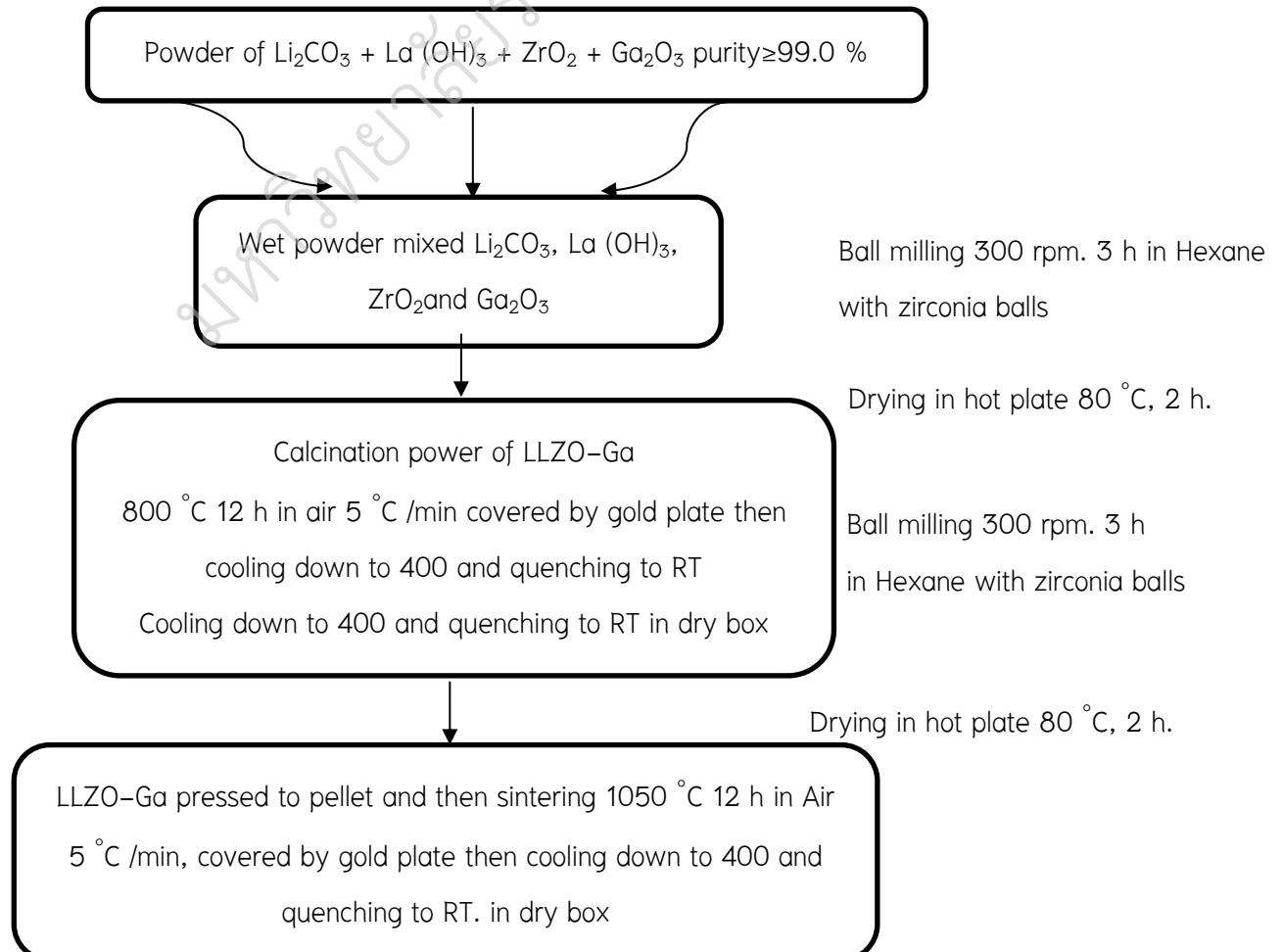
Aldrich

FUJIFILM

Wako Pure

Chemical

Synthesis $\text{Li}_{6.25}\text{Ga}_{0.25}\text{La}_3\text{Zr}_2\text{O}_{12}$ by solid state reaction method



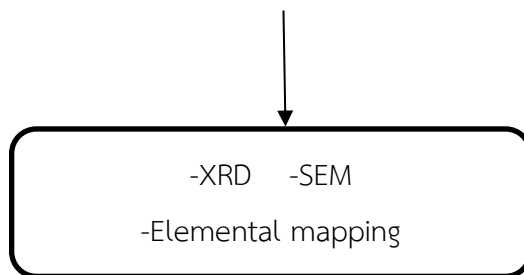


Fig. 38. Flowchart of $\text{Li}_{6.25}\text{Ga}_{0.25}\text{La}_3\text{Zr}_2\text{O}_{12}$ synthesis process.

Composite polymer electrolyte with garnet $\text{Li}_{6.25}\text{Ga}_{0.25}\text{La}_3\text{Zr}_2\text{O}_{12}$ powder

Before preparing the precursor solution, PVDF–HFP, LiTFSI, and sintered powder $\text{Li}_{6.25}\text{Ga}_{0.25}\text{La}_3\text{Zr}_2\text{O}_{12}$ powder were vacuum dried at $80\text{ }^\circ\text{C}$ for 24 hours. Initially, PVDF–HFP and LiTFSI (with a weight ratio of 3:2) were dissolved in DMF and Acetone (7:3 ml) within a glove box, and the mixture was stirred at $60\text{ }^\circ\text{C}$ for 12 hours to create a polymer–salt solution for the solid polymer electrolytes (SPEs). Subsequently, sintered powder $\text{Li}_{6.25}\text{Ga}_{0.25}\text{La}_3\text{Zr}_2\text{O}_{12}$ was added to the salt solution in weight ratios of 0%, 5%, 10%, 15%, and 20% relative to the weight of LiTFSI and PVDF–HFP. The resulting solution, constituting the composite polymer electrolyte (CPEs) was stirred at $60\text{ }^\circ\text{C}$ for 12 hours, yielding a ready–to–use solution. The CPEs solution was poured into a Teflon tray to prepare the CPEs film. Subsequently, the film was treated with N_2 gas for 12 hours and dried under vacuum for an additional $70\text{ }^\circ\text{C}$ 12 hours, rendering the CPEs membrane ready for preparing full cells shown in Fig. 39.



Fig. 39. Flowchart illustrating the preparation process of the CPEs.

มหาวิทยาลัยราชภัฏสุราษฎร์ธานี

CHARACTERIZATION TECHNIQUES

X-Ray Diffraction

X-ray diffraction (XRD) analysis was used to establish phase identification for crystalline material and can provide information on crystal structures such as unit cells. XRD uses scattering and diffraction techniques from x-rays are generated by a cathode ray tube then the x-ray filtered before to sample. The diffraction pattern from XRD is based on Bragg's Law.

$$2d \sin \theta = n\lambda \quad (3.1)$$

Where d is the lattice spacing in the crystal sample, θ is the angle between the incident beam and the atomic plane, λ is the wavelength of electromagnetic radiation from the source, and n is an integer corresponding to an order of diffraction. The radiation from the sample was detected and counted. Due to the random orientation of the sample materials, all possible diffraction directions of the lattice should be attained by scanning the sample through a range of 2θ angles. Since most materials have unique diffraction patterns, compounds can be identified by using a database of diffraction patterns. All images presented in this thesis were taken with SHIMADZU XRD-6100.

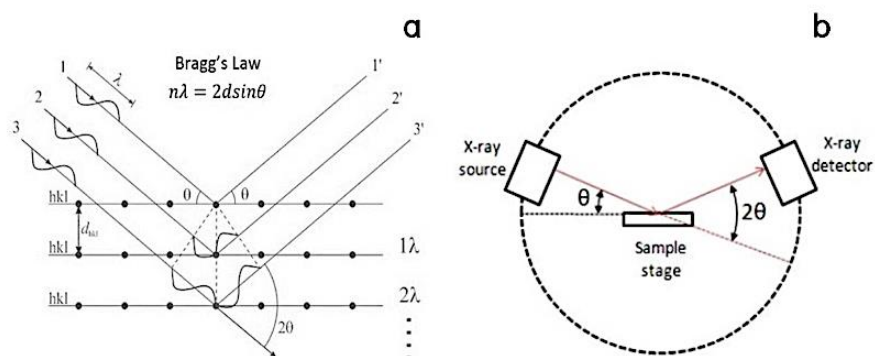


Fig. 40. X-ray diffraction (a) Bragg's law and (b) construction of an X-ray diffractometer (Myers 1997).

Scanning electron microscopy

Scanning electron microscopy (SEM) was used to investigate three-dimensional microstructure and sample composition. All images presented in this thesis were taken with JEOL JMS-7800F prime, JEOL. During analysis, the electron source is excited by high voltage, and the resulting electron beam is focused on an electron scan at or near the surface of the sample and produces an image. This produces several different signals and the ones that were used for analysis. Firstly, secondary electrons (SE) – a result of excitation and replacement of outside shell electrons by the primary electrons enabling us to view the microstructure of the sample. Secondly, backscatter electrons (BSE) – in elastically scattered primary electrons. The energy loss is dependent on the weight of surface atoms electrons are interacting with giving an image of phase segregation. Finally, the characteristic x-rays used in energy dispersive spectroscopy (EDS or EDX) – are produced from excitation by the primary electron beam and enable us to see the phase composition by determining its chemical composition.

Archimedes density measurement

Bulk density was determined by Archimedes method via distilled water using the following equations:

$$\rho = \frac{A}{A-B}(\rho_0 - \rho_L) + \rho_L \quad (3.2)$$

$$V = \alpha \frac{A-B}{\rho_0 - \rho_L} \quad (3.3)$$

where, ρ is the Density of the sample.

A is the Weight of the sample in air.

B is the Weight of the sample in the auxiliary liquid (distilled water).

V is the Volume of the sample.

ρ_0 is the Density of the auxiliary liquid (distilled water).

ρ_L is the Density of air (0.0012 g/cm³).

α is Weight correction factor (0.99985), to take the atmospheric buoyancy of the adjustment weight into account.

The theoretical densities of the samples were calculated using the following formula.

$$d_{th} = \frac{4 \times \text{Molecularweight}}{N_A V} \quad (3.4)$$

Where, V is cell volume obtained from the XRD database.

N_A is Avogadro number = 6.02×10^{23} (1/mol)

4 is the number of united cells in a cell volume.

X-ray photoelectron spectroscopy

In X-ray photoelectron spectroscopy (XPS), the sample is irradiated with soft X-rays (energies lower than ~ 6 keV), and the kinetic energy of the emitted electrons is analyzed in Fig. 41 (a–c). The emitted photoelectron is the result of the complete transfer of the X-ray energy to a core-level electron. This is expressed mathematically in Eq. (3.5). It simply states that the energy of the x-ray ($h\nu$) is equal to the binding energy (BE) of the electron (how tightly it is bound to the atom/orbital to which it is attached), plus the kinetic energy (KE) of the electron that is emitted, plus the spectrometer work function (Φ_{spec}), a constant value,

$$h\nu = BE + KE + \Phi_{spec} \quad (3.5)$$

To determine the binding energy of an electron, Eq. (3.5) can be rearranged to obtain Eq. (3.6), where the terms on the right are either known ($h\nu$ and Φ_{spec}) or measured in the XPS experiment (KE),

$$BE = h\nu - KE - \Phi_{spec} \quad (3.6)$$

This concept is also demonstrated diagrammatically in Fig. 42. Note that the photoelectron binding energy is measured concerning the sample Fermi level (not the vacuum level) which is the reason that Φ_{spec} is included. Photoelectron peaks are

notated by the element and orbital from which they were ejected. For example, “O 1s” describes electrons emitted from the 1s orbital of an oxygen atom. Any electron with a binding energy less than the x-ray source energy should be emitted from the sample and observed with the XPS technique. The binding energy of an electron is a material property and is independent of the X-ray source used to eject it. When experiments are performed with different x-ray sources, the binding energy of photoelectrons will not change; however, the kinetic energy of the photoelectrons emitted will vary as described by Eq. (3.6)

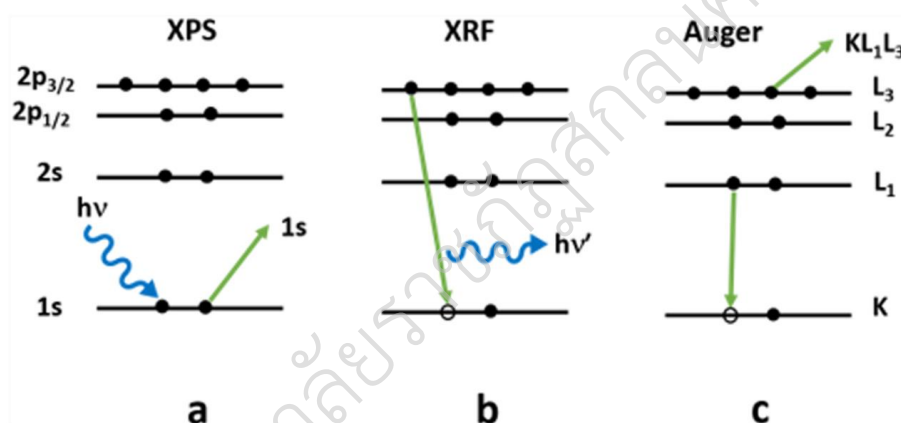


Fig. 41. Processes that result from x-ray bombardment of a surface include (a) emission of a photoelectron, (b) x-ray fluorescence, and (c) emission of an Auger electron.

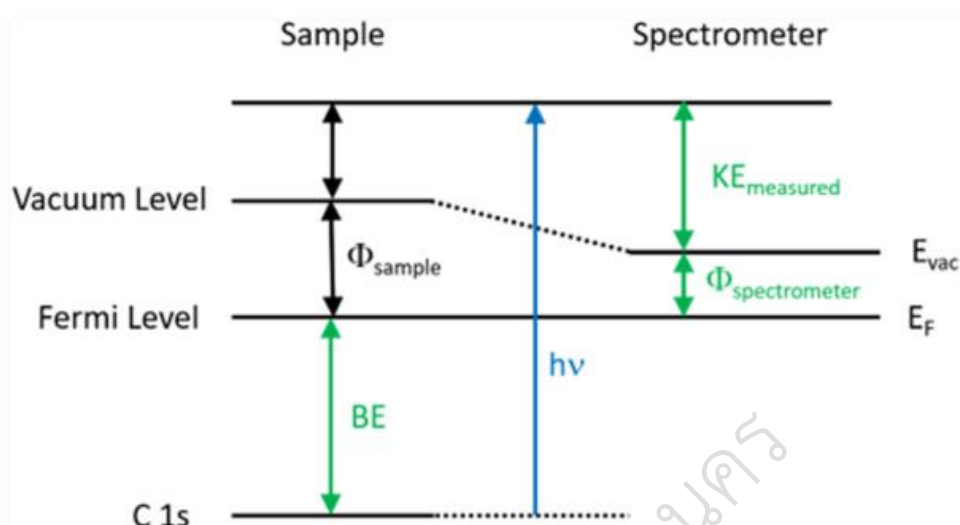


Fig. 42. Energy level diagram illustrates schematically the basic XPS equation, including the x-ray source energy ($h\nu$), the binding energy of the electron (BE), the measured kinetic energy of the electron (KE_{measured}), and the work function of the spectrometer ($\Phi_{\text{spectrometer}}$)

ELECTROCHEMICAL CHARACTERIZATIONS

Electrochemical impedance spectroscopy

The ionic conductivities measurements were determined by electrochemical impedance spectroscopy (EIS) using an impedance analyzer in the frequency A solid electrolyte sample with a known geometry is sandwiched between blocking electrodes (e.g., Au, stainless steel, or Li metal) and the conductivity is calculated from the measured bulk resistance. The configuration of EIS setup is as shown in Fig. 43.

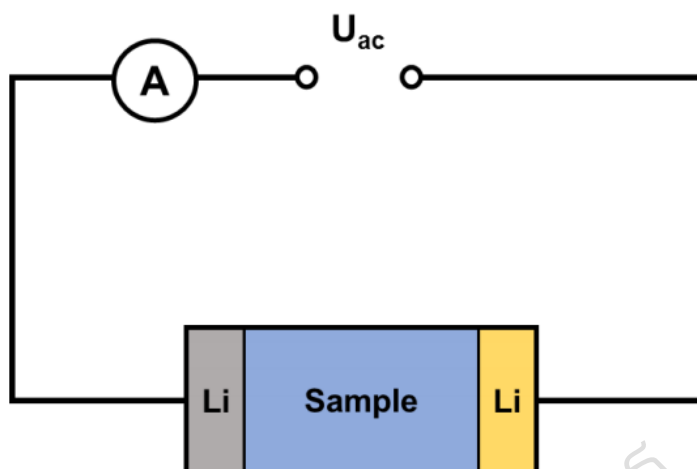


Fig. 43. Schematic for ac conductivity measurement sandwiched between two lithium electrodes.

The Nyquist plot was then analyzed using Z view software by fitting the impedance profile with a suitable equivalent circuit to determine the bulk resistance (R_b), grain boundary resistance (R_{gb}), constant phase element (CPE) and Warburg response (W). Constant phase element (CPE) is an element that frequently use in modelling the ac response of the non-homogeneous system and is particularly helpful in representing slightly distorted or imperfect capacitances. CPE has two parameters, Q and n which is governed by Equation 3.7:

$$Z_{CPE} = Q^{-1}(j\omega)^{-n}, 0 < n < 1 \quad (3.7)$$

where j is the imaginary unit and ω is angular frequency. Q becomes equal to capacitance when $n=1$, Warburg impedance when $n=0.5$ and resistance when $n = 0$. Warburg impedance describes ion diffusion at low frequencies and is characterized as a straight line with a slope of 1 in the Nyquist plot. Warburg element can be further divided into (1) Warburg short (W_s) which describes the impedance of finite-length diffusion with transmissive boundary, whereas (2) Warburg open (W_o) which describes impedance of finite-length diffusion with reflective boundary.

The ionic conductivity, σ of the sample was calculated from using Equation (3.8) as below:

$$\sigma = \frac{l}{\pi r^2 R} \quad (3.8)$$

where R represents the resistance, l is the thickness and r are the radius of the pellet sample, respectively. Meanwhile, the activation energy, E_a was obtained from the conductivity values, σ calculated at different temperatures (e.g., 25–300 °C) via the Arrhenius equation shown in Equation (3.9) and (3.10):

$$\sigma = \frac{A}{T} \exp \frac{-E_a}{kT} \quad (3.9)$$

$$\log_{10} \sigma T = \log_{10} A - \frac{E_a}{2.303kT} \quad (3.10)$$

where A is the pre-exponential factor, k is the Boltzmann constant and T is the temperature in Kelvin.

Lithium transference number

Bruce and Vincent established a potentiostatic polarization method for ideal solid polymer electrolytes (Bruce, P. G., & Vincent, C. A. (1987), which is also suitable for diluted solutions (Mauro, V. et al. (2005). Applying a small constant potential on an electrolyte between non-blocking lithium electrodes leads to a decrease of the initial current value until a steady-state value is reached. If no redox reaction occurs with the anions, the anion current will vanish in the steady state and the total current will be caused by the cations. In this case, the cation transference number can be easily determined by dividing the steady-state cationic current by the initial current just after switching on the polarizing voltage. Passivating layers at the electrodes usually impose an additional contact resistance. The corresponding additional voltage drop has to be subtracted from the applied potential difference. Because the resistances of the lithium electrode surfaces vary with time, the correction must take this change into account. The contact resistance is determined by

impedance measurements shortly before and after the potentiostatic polarization (Evans, J. et al. 1987). For small polarization potentials, the transference number for the cation t_{Li^+} is given by:

$$t_{Li^+} = \frac{I_s(\Delta V - I_o R_o)}{I_o(\Delta V - I_s R_s)} \quad (3.11)$$

where I_s is the steady-state current

I_o is the initial current

ΔV is the applied potential R_s and R_o are the electrode resistances after and before the polarization, respectively.

Electrochemical performance

Galvanostatic cycling is an important method for the electrochemical evaluation of battery materials. A constant current is applied to the cell and the potential is monitored as a function of time. The total amount of charge passed per unit mass (i.e., capacity, C) of the electrode material, during charge and discharge is given by equation (3.11):

$$C = \frac{I \times t}{m} \quad (3.12)$$

Where I, t and m represent the current (ampere), time (hour), and mass (gram) respectively. Galvanostatic charge and discharge behaviors of batteries were identified using a potentiostat/galvanostat under a constant current based on the targeted C-rate of the active materials. For 1 C–10C, the battery is estimated to be theoretically completely discharged or charged within one hour. Similarly, the lower C-rate of C/10 and C/100 will take 10 hours and 100 hours to reach the full theoretical discharge/charge respectively. For the battery running at a higher temperature, the cells were pre-heated for 6 h to reach the set temperature before testing.

Cyclic voltammetry and linear sweep voltammetry

Cyclic voltammetry (CV) is a very versatile electrochemical technique that allows probing the mechanics of redox and transport properties of a system. In

cyclic voltammetry, the potential of the working electrode is swept at a specific sweep rate (V s^{-1}) back and forth linearly between two preset values, and the resulting current as a function of time is measured. The current flow into and out of the working electrode is plotted as the y-axis and the applied voltage in the x-axis to give a cyclic voltammogram.

When the potential of the working electrode is more positive than that of the redox couple present, the corresponding species may be oxidized and produce an anodic current. Similarly, on the return scan, the working electrode becomes more negative than the reduction potential of a redox couple, hence reduction may cause a cathodic current. For a stable reversible redox reaction, the ratio of anodic current to cathodic current should be 1.

Cyclic voltammetry and linear sweep voltammetry (LSV) belong to the family of potential sweep methods, where the potential is varied linearly over time, to give a sweep or scan rate ν (V/s or mV/s). While it is possible to plot the potential and current as a function of time, typical plots report current (A or subunits) versus potential (V or subunits). Examples of LSV and CV experiments are shown in Fig. 44 and Fig. 45.

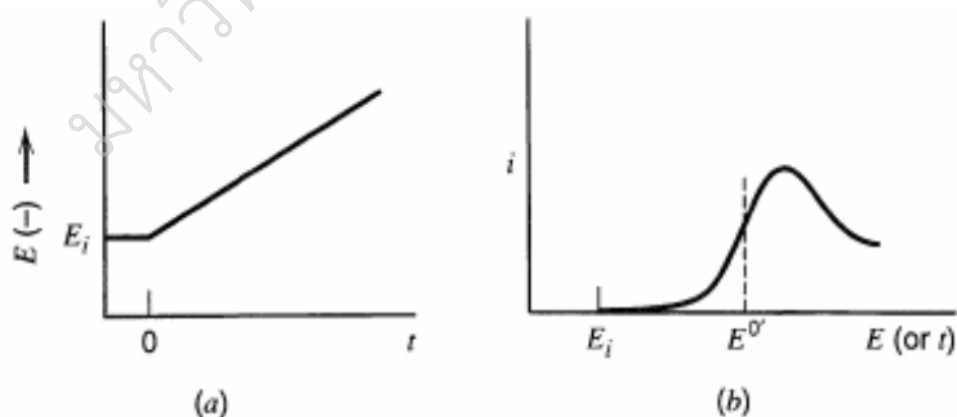


Fig. 44. Typical LSV experiment with a) voltage profile over time, b) current–voltage curve generated by voltage profile

(Bard, A. J., Faulkner, L. R., & White, H. S. (2022).

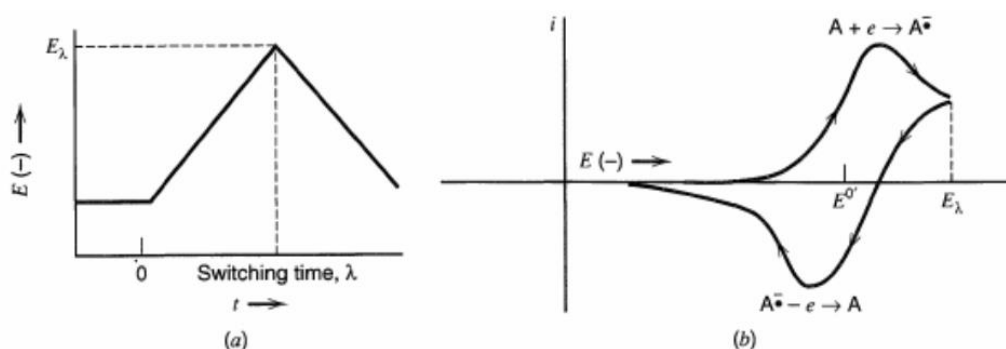


Fig. 45. Typical CV experiment with a) voltage profile over time, b) current–voltage curve generated by voltage profile
(Bard, A. J., Faulkner, L. R., & White, H. S. (2022).

Here, potential is represented with the symbol E , and has the units of volts. As can be seen in the above figures, LSV and CV experiments are relatively similar. While distinct experimental techniques, they are related and make use of the same principles; since LSV can be regarded as essentially a half-cycle of CV, this section will focus on describing some of the principles underlying CV, and which are still applicable to LSV. It might be helpful at this point, as a comparison, to make an analogy between the roles of LSV and CV, LSV as providing information on a material's “electrochemical stability window” (ESW) or “electrochemical window” (EW)

ASSEMBLY OF ALL-SOLID-STATE LITHIUM BATTERIES

The all-solid-state full cell was $\text{LiFePO}_4/\text{Li}$ cell fabricated using a solid $\text{LLSr}_{0.09}\text{TTa}_{0.09}\text{O}_3$ pellet and a Li metal anode. All battery components were assembled within an argon-filled glove box using laminate-type batteries. The $\text{LLSr}_{0.09}\text{TTa}_{0.09}\text{O}_3$ pellet size of a diameter of 10 mm and thickness of 0.8 mm was assembled with an LFP cathode on aluminum (mass loading 1.5 mg) and Li-metal size diameter of 12 mm thickness of 0.3 mm then connected with nickel wire to measurement electrochemical properties in Fig. 46.

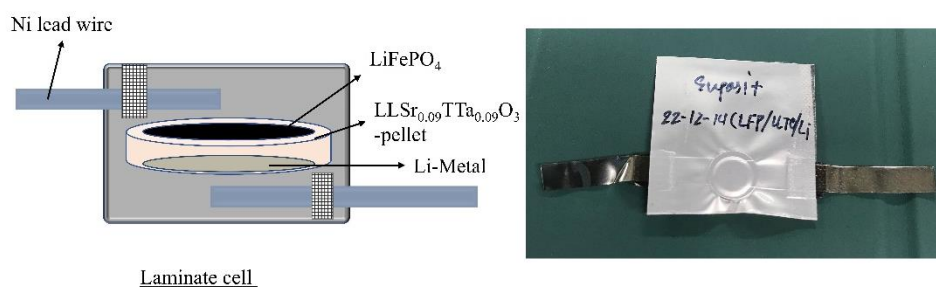


Fig. 46. The preparation of all-solid-state batteries full cell.

ASSEMBLY SEMI-SOLID-STATE BATTERIES FULL CELL

The semi-solid full cell LiFePO₄/Li cell was fabricated using a composite polymer electrolyte (CPE) and a Li metal anode, offering the possibility of using a Li metal anode without the short-circuit effect resulting from the decomposition of Ti⁴⁺ to Ti³⁺ compared to the solid LLSr_{0.09}TTa_{0.09}O₃ pellet. All battery components were assembled within an argon-filled glove box, using 2032-type battery shells with LiFePO₄ (LFP) electrodes measuring 12 mm in diameter and loaded with approximately 2 mg of active material. During the assembly process, 5 μL of liquid electrolyte was applied to the surface of the composite polymer electrolyte membrane to minimize interface impedance at the cathode and Li metal anode shown in Fig. 47. The LFP cathode was prepared with a composition of active material, Super-P, and PVDF binder in a weight ratio of 7:2:1, respectively. NMP solvent was added to these mixtures, and the well-mixed slurry was cast onto aluminum foil using the doctor blade technique. The cathode film was dried at 80°C for 6 hours and dried under vacuum at 80°C for 12 hours to remove residual solvent. The mass loading of active materials on each aluminum current collector for the coin cell was approximately 2 mg.

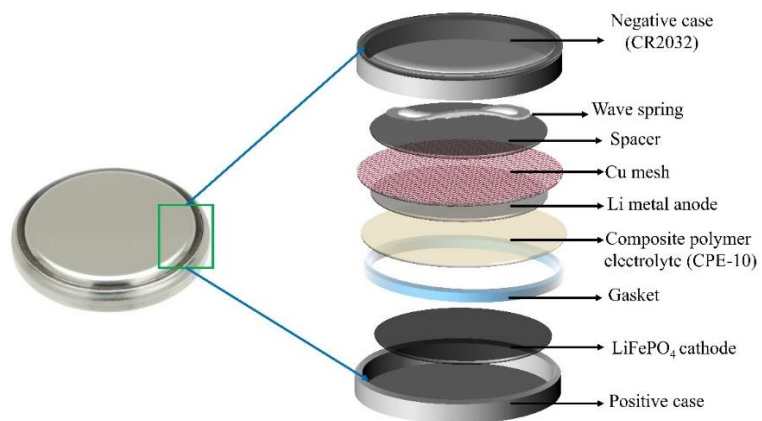


Fig. 47. The preparation of 2032-type battery of semi-solid-state batteries with coin cell.

มหาวิทยาลัยราชภัฏสุราษฎร์ธานี

CHAPTER 4

RESULTS AND DISCUSSION

This chapter presents all the results and discussions on the characteristics of perovskite- $\text{Li}_{0.5-x}\text{La}_{0.5-x}\text{Sr}_x\text{Ti}_{1-x}\text{Ta}_x\text{O}_3$ ($0 \leq x \leq 0.12$), garnet- $\text{Li}_{6.75}\text{Ga}_{0.25}\text{La}_3\text{Zr}_2\text{O}_{12}$, the preparation of all-solid-state, semi-solid-state and quasi-solid-state batteries, electrochemical properties, performance, and mechanical testing of full cells as follows:

CHARACTERIZATIONS OF PEROVSKITE- $\text{Li}_{0.5-x}\text{La}_{0.5-x}\text{Sr}_x\text{Ti}_{1-x}\text{Ta}_x\text{O}_3$ ($0 \leq x \leq 0.12$)

Crystal structure, morphology, and chemical composition

The perovskite $\text{Li}_{3x}\text{La}_{2/3-x}\text{TiO}_3$ (LLTO) ($0.04 < x < 0.16$) exhibits an ABO_3 structure, as depicted in Fig. 48. In this structure, lithium (Li), lanthanum (La), including La-rich and La-poor layers, and vacancies occupy the A-sites, while titanium (Ti) and oxygen (O) occupy the B-sites, with Ti being octahedrally coordinated by oxygen atoms (Inaguma, Y. et al., 1993; Morata-Orrantia, A. et al., 2003). The stack layer of LLTO consists of La-rich and La-poor layers, in which Li^+ -ion migration mainly occurs on the La-poor layers. The mechanism of Li^+ -ion migration was explained by the movement through O_4 windows on a high concentration of vacancies, in which Li^+ -ion conduction between the neighboring vacant A-site related to O_4 windows or a bottleneck. The O_4 windows or bottleneck of cubic-LLTO ($Pm\bar{3}m$) structure are larger than those of other structures such as the tetragonal ($P4/mmm$) and orthorhombic ($Pmma$) structures owing to their larger lattice parameters (Ling, M. E. et al., 2020; Teranishi, T., 2014; Catti, M., 2007). Therefore, Li^+ -ion conduction of cubic-LLTO structure often exhibits high ionic conductivity. The structure of LLTO affects Li^+ -ion

conduction; in addition, the conduction depends on factors such as lithium and vacancy concentrations, number of grains, ionic radii of other A and B atoms, temperature, and pressure. Ionic conduction could be improved by enhancing ionic conductivity through three approaches: (I) The La-site was substituted by Sr^{2+} with a larger ionic radius to enlarge O_4 windows or bottlenecks. (II) The Ti-site was substituted by Ta^{5+} with a larger ionic radius to expand the Ti-O bonding. (III) After co-substitution, the samples maintained a cubic structure with a large area of O_4 windows or bottleneck.

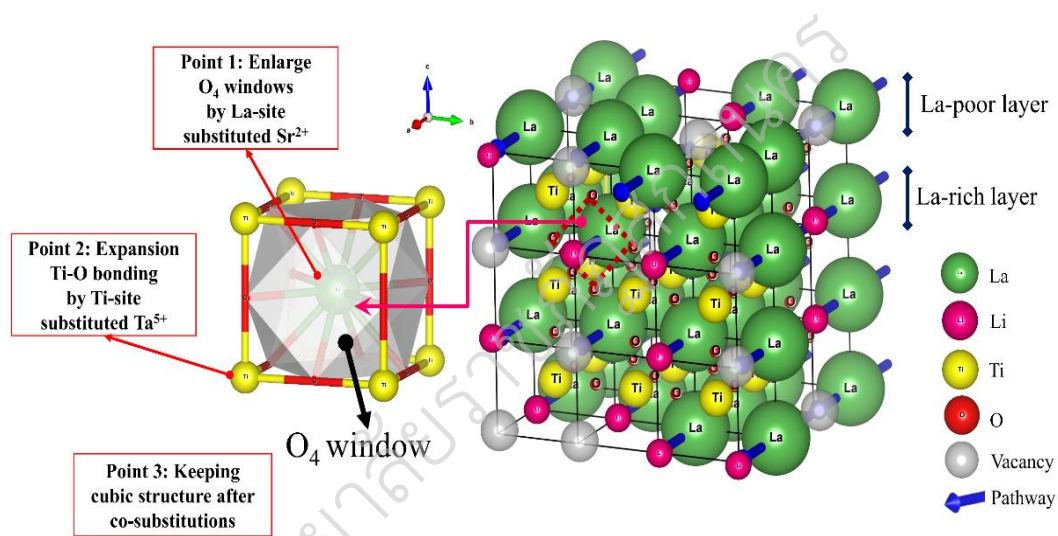


Fig. 48. Crystal structure of Perovskite $\text{Li}_{3x}\text{La}_{2/3-x}\text{TiO}_3$ (LLTO)-type with $(0.04 < x < 0.16)$.

Fig. 49 (a). shows the XRD patterns of $\text{Li}_{0.5-x}\text{La}_{0.5-x}\text{Sr}_x\text{Ti}_{1-x}\text{Ta}_x\text{O}_3$ ($0 \leq x \leq 0.12$) powders, which were obtained following the sintering of the ground pellets. The main phases of all samples present a cubic perovskite structure (ICDD #01-089-4928) with the space group $Pm\bar{3}m$, and a small amount of Li_2TiO_3 phase of samples $x = 0, 0.01$ and 0.03 , whereas at samples of $x = 0.06, 0.09$ and 0.12 the $\text{Li}_2\text{Ti}_3\text{O}_7$ phases are observed (Chouiekh, A. et al. 2023; Jonderian, A. et al., 2021). The undoped lithium sample with a high concentration of 0.5 is closely related to the Sr or Ge doped cubic-structured $\text{Li}_{0.35}\text{La}_{0.5}\text{TiO}_3$ (Zhang, S., et al., 2019; Hu, Z., et al., 2018). However, $\text{Li}_{0.5}\text{La}_{0.5}\text{TiO}_3$ and $\text{Li}_{0.35}\text{La}_{0.55}\text{TiO}_3$ differ in that the undoped

$\text{Li}_{0.5}\text{La}_{0.5}\text{TiO}_3$ sample adopts a cubic structure (Ling, M. E., et al., 2016; Deng, Y., et al., 2009; Avila, V., et al., 2020), whereas $\text{Li}_{0.35}\text{La}_{0.5}\text{TiO}_3$ exhibits a tetragonal structure (Li, R. et al., 2020).

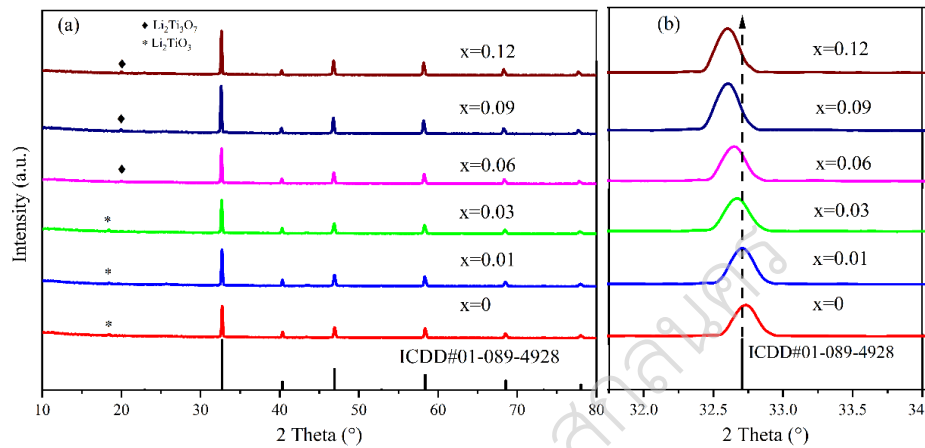


Fig. 49. XRD pattern of (a) $\text{Li}_{0.5-x}\text{La}_{0.5-x}\text{Sr}_x\text{Ti}_{1-x}\text{Ta}_x\text{O}_3$ ($0 \leq x \leq 0.12$) sintered powders, and (b) the 2Theta of $31.5\text{--}34^\circ$.

The co-doping of Sr and Ta was confirmed by XRD, which indicated that Sr^{2+} and Ta^{5+} were substituted in the LLTO structure. To reveal the effects of the dopants, the strongest peak in the XRD pattern was magnified for ease of comparison, as shown in Fig. 49 (b). With an increasing amount of A-site La^{3+} ($r = 1.36 \text{ \AA}$) substituted by Sr^{2+} ($r = 1.44 \text{ \AA}$) and B-site Ti^{4+} ($r = 0.605 \text{ \AA}$) substituted by Ta^{5+} ($r = 0.640 \text{ \AA}$) with a larger ionic radius. The XRD peaks shifted to the low-angle region, indicating a positive relationship between the Sr^{2+} and Ta^{5+} doping concentrations and lattice expansion (Table 10). In addition, the XRD changes were thoroughly examined using the calculated bond distances Fig. 50 corresponding to the La-Ti, La-O, and Ti-O average bond distances detailed in appendices A, which increased with increasing Sr^{2+} and Ta^{5+} contents, resulting in increasing cell volume. Therefore, Sr and Ta are successfully substituted for La and Ti (Li, R. et al., 2020; Yao, R. et al., 2020).

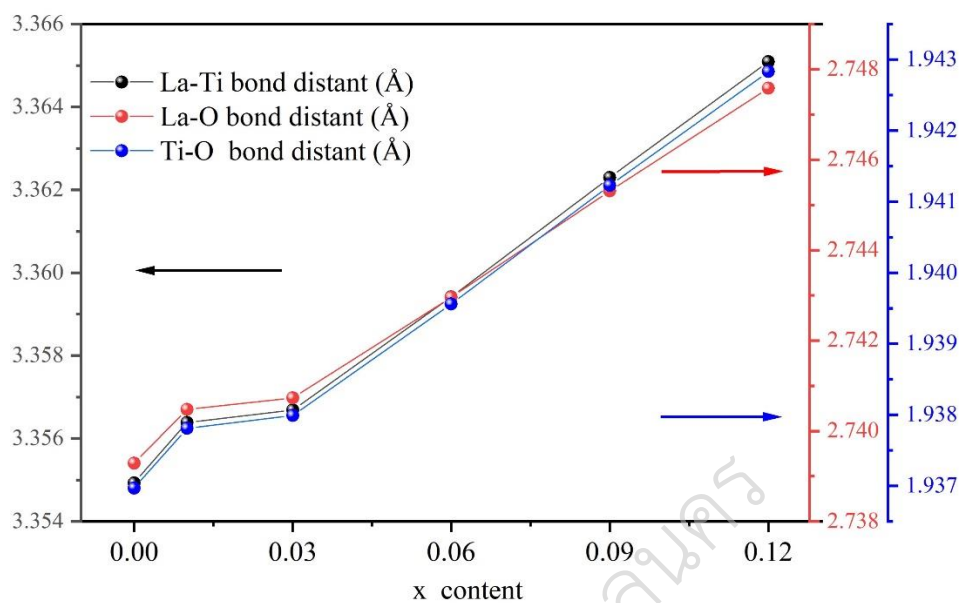


Fig. 50. The La-Ti, La-O and Ti-O bond distance of all samples



Table 10 The data of all samples of lattice parameter, cell volume, density, and relative density for $\text{Li}_{0.5-x}\text{La}_{0.5-x}\text{Sr}_x\text{Ti}_{1-x}\text{Ta}_x\text{O}_3$ ($0 \leq x \leq 0.12$).

Sample	Contents	Lattice parameter (Å)	Cell Volume (Å ³)	Density (g/cm ³)	Relative density (%)
$\text{Li}_{0.5}\text{La}_{0.5}\text{TiO}_3$	x=0	3.8739(4)	58.1378(1)	4.55	94.10
$\text{LLSr}_{0.01}\text{TTa}_{0.01}\text{O}_3$	x =0.01	3.8756(2)	58.2134(8)	4.57	94.55
$\text{LLSr}_{0.03}\text{TTa}_{0.03}\text{O}_3$	x=0.03	3.8760(2)	58.2315(0)	4.60	95.34
$\text{LLSr}_{0.06}\text{TTa}_{0.06}\text{O}_3$	x=0.06	3.8791(3)	58.3717(8)	4.61	95.48
$\text{LLSr}_{0.09}\text{TTa}_{0.09}\text{O}_3$	x =0.09	3.8824(5)	58.5217(9)	4.69	97.68
$\text{LLSr}_{0.12}\text{TTa}_{0.12}\text{O}_3$	x=0.12	3.8856(7)	58.6675(2)	4.72	97.62

All samples exhibited good densification of approximately 94%–97% during the sintering process, which is essential for grain connection for easy Li^+ -ion migration (Silva, J. H. L., et al., 2020). In addition, the increase in the density of the doped

samples with the substitution of the heavy element Ta^{5+} was slightly higher than that of Ti^{4+} , and the good sintering by Ta^{5+} aided in connecting neighboring grains (Huang, B., et al. 2016; Kwon, W. J. et al., 2017). However, the effect of Sr^{2+} on the grain size or density was not significant (Li, R. et al., 2019; Zhang, S. et al., 2019).

The cross-sectional microstructures of the $\text{Li}_{0.5-x}\text{La}_{0.5-x}\text{Sr}_x\text{Ti}_{1-x}\text{Ta}_x\text{O}_3$ ($0 \leq x \leq 0.12$) bulk samples are shown in Fig. 51 (a–f). The grain sizes of all the samples are rectangular, which is characteristic of the unit cell of the cubic perovskite structure (Lu, J., et al., 2020). All samples exhibited similar microstructures, such as connect area, and small rectangular particles related to neighboring grains. The grains have good densities with only a few visible pores. In addition, the grains have smooth surfaces and are in close contact with each other, indicating that the samples have good densities and mechanical properties. The doped samples with x contents of 0.01–0.09 exhibit larger melting areas, predominantly due to the substitution of Ti^{4+} with Ta^{5+} resulting in improved sintering ability. This process results in a low number of visible pores in the samples. However, the separation of grains in the doped sample with x content of 0.12 can be observed because of the increased Ta^{5+} content, thereby influencing the large liquid phase during the sintering process. Subsequently, during cooling, the domain boundary mismatch and low diffusion capacity of Ta^{5+} lead to an increase in the number of grains (Yao, R., et al., 2020). We observed a decrease in the mean grain size with increasing x and y contents.

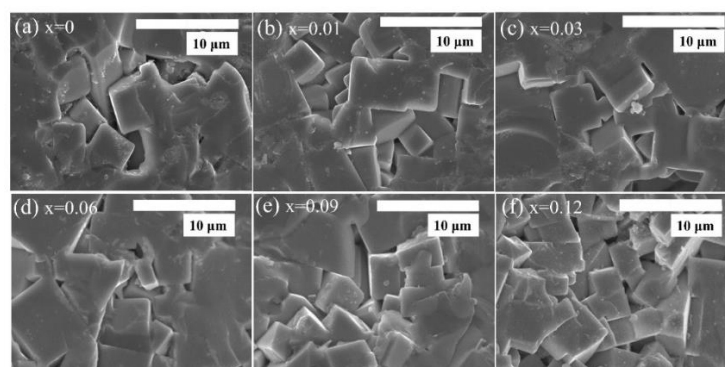


Fig. 51. The SEM of bulk samples (a) undoped $x = 0$, (b) $x = 0.01$, (c) $x = 0.03$, (d) $x = 0.06$, (e) $x = 0.09$, and (f) $x = 0.12$.

Fig. 52 shows a histogram plotted using the ImageJ software retrieved from an SEM image obtained for measuring the grain size. The grain size of the undoped $\text{Li}_{0.5}\text{La}_{0.5}\text{TiO}_3$ sample is approximately $6.97 \mu\text{m}$, and doped samples with $x = 0.01, 0.03, 0.06,$ and 0.09 have grain sizes of approximately $6.85, 6.73, 6.30,$ and $5.38 \mu\text{m}$. The grain sizes slightly decreased with increasing doping contents and blended with the large melting area. Furthermore, the average grain size of the doped sample $x = 0.12$ decreased to approximately $4.21 \mu\text{m}$ corresponding to the increasing Ta^{5+} contents to induce the number of grains.

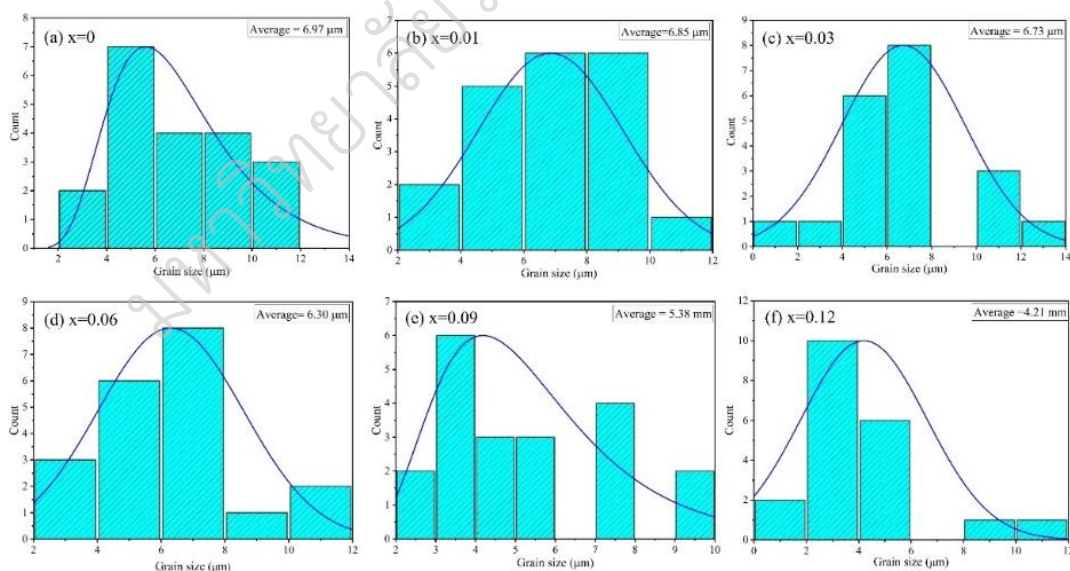


Fig. 52. The histograms of grain size of bulk samples (a) undoped $x = 0$, (b) $x = 0.01$, (c) $x = 0.03$, (d) $x = 0.06$, (e) $x = 0.09$, and (f) $x = 0.12$.

To discern the doping composition and distribution of Sr and Ta in the $\text{LLSr}_{0.09}\text{TTa}_{0.09}\text{O}_3$ pellet, the cross-sectioned non-polished areas of the sample were observed by EDX mapping. Fig. 53 shows a pellet with a homogeneous elemental distribution of O, La, Sr, Ti, and Ta, throughout the sample. This confirms that Sr and Ta were successfully co-doped into the cubic-LLTO structure. Moreover, the EDX analysis in Fig. 54 demonstrates that the Sr and Ta substitution contents in all the samples align with the expected stoichiometric ratios.

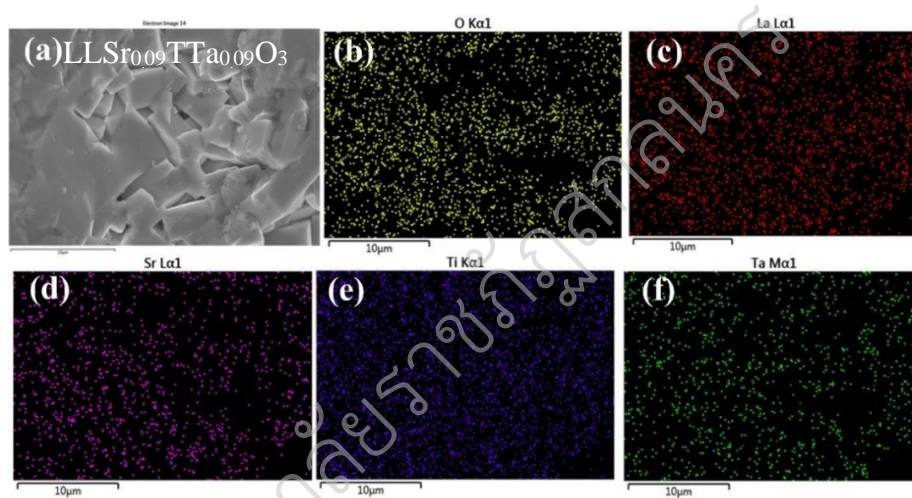


Fig. 53. The elemental mapping of the images of $\text{LLSr}_{0.09}\text{TTa}_{0.09}\text{O}_3$ (a) SEM surface, (b) Oxygen, (c) Lanthanum, (d) Strontium, (e) Titanium, and (f) Tantalum.

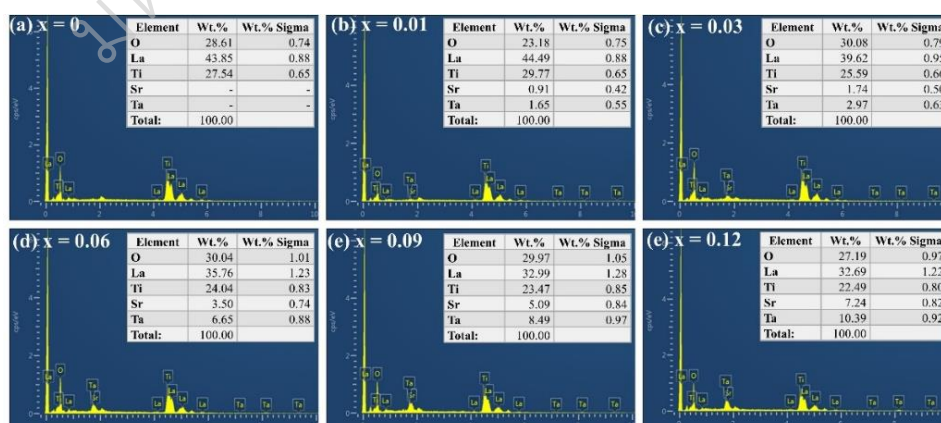
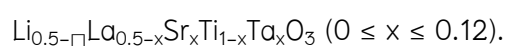


Fig. 54. The EDX graph and elemental contents of all samples



The XPS was performed to acquire further information on the composition and chemical state of Ta and Sr co-doped $\text{LLSr}_{0.09}\text{TTa}_{0.09}\text{O}_3$ ($x = 0.09$). The main peaks of La, Sr, Ti, and Ta shown in Fig. 55 confirm the substitution at the La and Ti sites. The component centers of La 3d are separated into spin orbits of La $3d_{5/2}$ at 834.1 and 838.3 eV, and La $3d_{3/2}$ at 851.2 and 855.3 eV. The La 3d orbital was measured for the $\text{LLSr}_{0.09}\text{TTa}_{0.09}\text{O}_3$ sample, and the confirmation of La^{3+} in this sample is by the previous study shown in Fig. 55. (a) (Li, R., et al., 2019). The Sr 3d spectrum had a Sr $3d_{5/2}$ peak at 133.1 eV, and Sr $3d_{3/2}$ peak at 134.7 eV, which correspond to the $3d_{5/2}$ and $3d_{3/2}$ peaks of the Sr^{2+} -containing oxides, respectively, demonstrating that La^{3+} was partially substituted by Sr^{2+} in the LLTO pellet (Fig. 55(b)) [51]. The Ti 2p XPS spectrum consists of two peaks centered at Ti $2p_{3/2}$ at 458.1 eV, and Ti $2p_{1/2}$ at 463.8 eV, which correspond to Ti^{4+} ; no other centered peaks corresponding to Ti^{3+} are observed in the low-energy side in Fig. 55(c). Analyzing the Ti 2p spectra, we observed that the main peaks originate from Ti^{4+} . The $\text{Ti}^{3+}/\text{Ti}^{4+}$ area ratios decreased with increasing Ta^{5+} doping contents from 0.14 to 0.03 in the undoped and doped ($x = 0.09$) samples, as shown in Fig. 56. The reduction in the peak area of Ti^{3+} and Ti^{2+} in the spectra of doped samples is a crucial factor in the substitution of Ta^{5+} or changes in the Ti-site content. Furthermore, the decomposition of Ti^{4+} to Ti^{3+} significantly accelerates dendrite formation and the induction of short circuits in battery cells with a Li metal anode. Therefore, reducing the amount of Ti^{3+} can lead to a decrease in short circuits, as evidenced by previous studies (Kwon, W. J., et al., 2017; Lu, J., et al., 2020; Xu, L., et al., 2022; Gu, R., et al., 2022). In addition, the Ta 4f peak could be deconvoluted into two peaks centered at $4f_{7/2}$ at 25.4 eV, and $4f_{7/2}$ at 27.3 eV, which could be attributed to Ta^{5+} in (Fig. 55(d)).

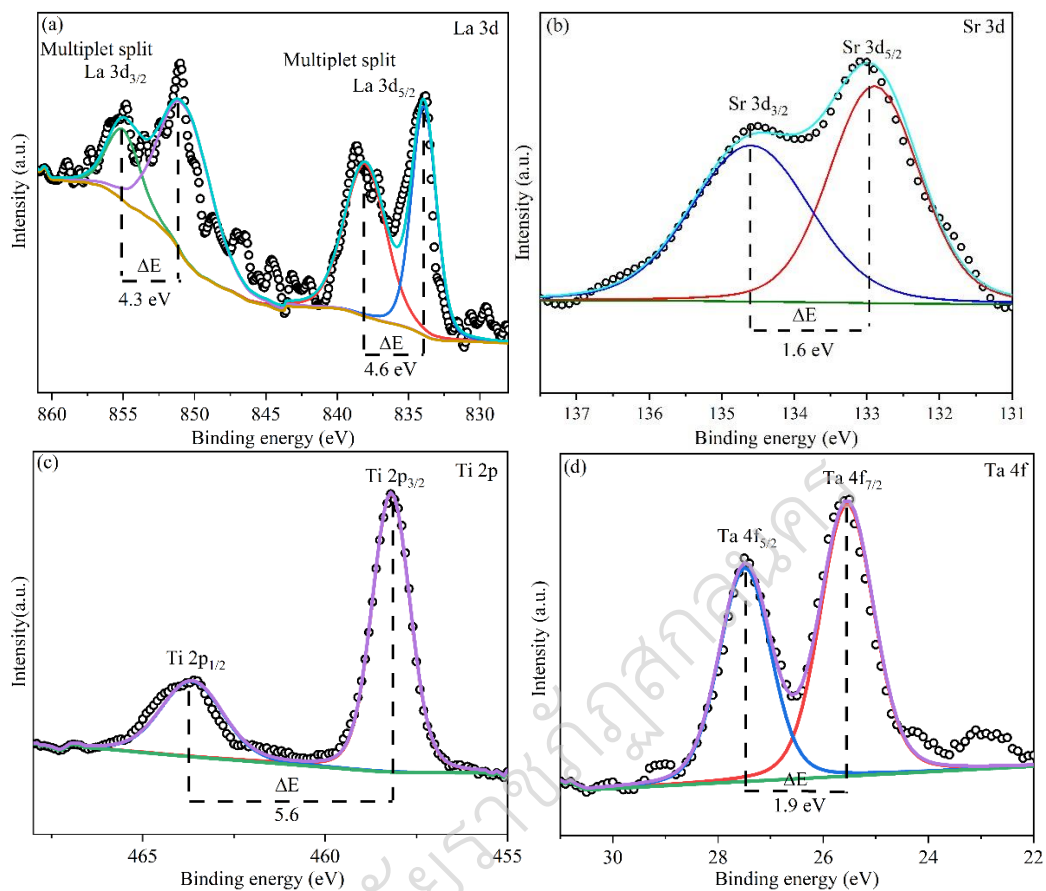


Fig. 55. The XPS analysis of (a) La 3d, (b) Sr 3d, (c) Ti 2p, and (d) Ta 4f of cubic-perovskite $\text{LLSr}_{0.09}\text{TTa}_{0.09}\text{O}_3$ sample.

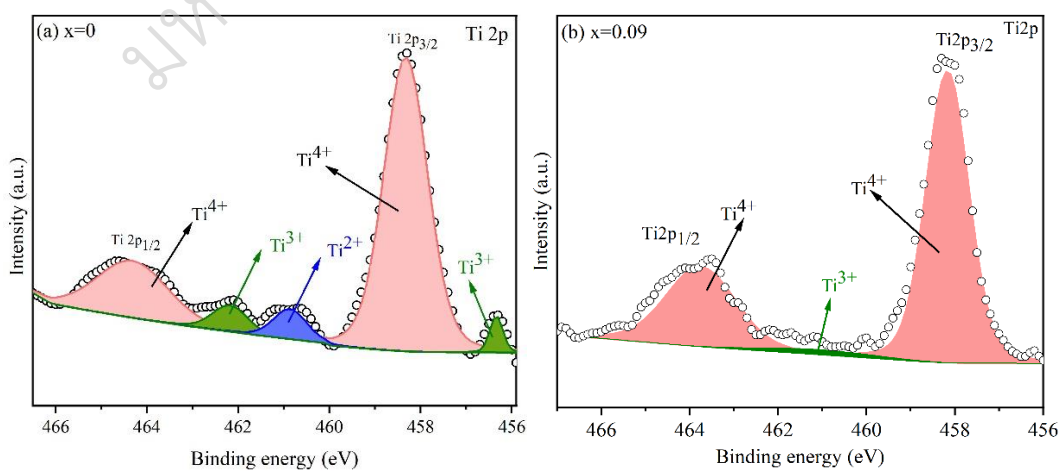


Fig. 56. XPS Ti 2p spectra of bulk samples (a) undoped $x = 0$ and (b) $x = 0.09$.

Electrochemical properties and performance of full cells

EIS was performed at RT (298 K) to calculate the ionic conductivity and activation energy of Li^+ migration in the solid electrolyte. The EIS plots of all samples are composed of two semicircles at high frequencies (1 Hz–18 MHz) and an approximately straight line at low frequencies. The total resistance of all samples was attributed to the grain and grain boundary resistances and then fitted with the equivalent circuit model shown in Fig. 57. In addition, the equivalent circuit depends on the cell structure; wherein, R_s , R_g and CPE_g are the resistance of series circuit, the resistance in the grain and constant phase element of Li^+ migration in the grain, respectively. R_{gb} and CPE_{gb} represent the resistance and constant phase element for Li^+ migration across the grain boundary, respectively; and CPE_e is affected by the polarization between the Au blocking electrodes. The total ionic conductivity was calculated using Eq. (4.1):

$$\sigma_{total} = \frac{L}{R_{total} \times A}, \quad (4.1)$$

where σ_{total} , R_{total} , A , and L represent the total conductivity, total resistance (grain + grain boundary resistance), cross-sectional surface area, and thickness of the pellet, respectively.

Fig. 57(a) shows the grain impedance of $\text{Li}_{0.5-x}\text{La}_{0.5-x}\text{Sr}_x\text{Ti}_{1-x}\text{Ta}_x\text{O}_3$ samples with varying amounts of x ($0 \leq x \leq 0.12$) at 298 K. The substitution of $x = 0.01$ and 0.03 dopant contents can enhance the grain conductivity of the samples by increasing the conductivity due to bottleneck expansion and increasing the unit cell volume as the lattice parameter increases. However, this phenomenon originates because of the restricted space of the A-site vacancies that impact ionic conductors. In this case, the optimal bottleneck size required for Li^+ -ion diffusion was determined. Notably, excess doping, a factor that influences ionic conductivity, leads to a significant reduction in conductivity (Zhang, S. et al., 2019).

Nevertheless, as shown in Fig. 57(b), the grain boundary conductivity resistance decreases with increasing x content. The grain boundary resistance begins

decreasing for $x = 0.01$ and reaches the smallest value at $x = 0.09$, corresponding to the highest total ionic conductivity and an expanding lattice constant with a bottleneck in the unit cell. Additionally, the partial substitution of Ti–O bonds with Ta⁵⁺ with a larger ionic radius increases the interatomic Ti–O bond distance, corroborating the bottleneck expansion and TiO₆ filling (Zhang, S., et al., 2019; Lu, J., et al., 2020). However, the reduction in samples with $x = 0.12$ was influenced by over-doping and a low diffusion coefficient of Ta⁵⁺, which resulted in structure-induced grain separation and an increasing number of grains. This phenomenon, as shown in the SEM image in Fig. 51 (f), interrupts the Li⁺ migration.

The calculations of R_g , R_b , R_{gb} , R_{total} , σ_g , σ_{gb} , and σ_{total} for all samples are listed in Table 11. The LLTO structure material system has a boundary impedance that is much larger than the bulk impedance, and the total conductivity is dominated by the grain boundary conductivity. The highest σ_{total} is $4.12 \times 10^{-5} \text{ S}\cdot\text{cm}^{-1}$ at 298 K in LLSr_{0.09}TTa_{0.09}O₃ which is approximately 2.7 times higher than that of the undoped sample $1.49 \times 10^{-5} \text{ S}\cdot\text{cm}^{-1}$ in Fig. 57 (c) and Fig. 57 (d) shown the ion conduction process at the grains and grain boundaries of LLTO.

Table 11 The parameters of bulk resistance (R_g), grain-boundary resistance (R_{gb}), and total resistance (R_{total}) as well as corresponding ionic conductivity grain (σ_g), grain boundary (σ_{gb}), and total (σ_{total}), obtained from the EIS curve fittings and calculations.

Samples	$R_g(\Omega)$	$R_{gb}(\Omega)$	$R_{total}(\Omega)$	$\sigma_g(\text{S}\cdot\text{cm}^{-1})$	$\sigma_{gb}(\text{S}\cdot\text{cm}^{-1})$	$\sigma_{total}(\text{S}\cdot\text{cm}^{-1})$
Li _{0.5} La _{0.5} TiO ₃	176.44	14996	15172.44	1.28×10^{-3}	1.51×10^{-5}	1.49×10^{-5}
LLSr _{0.01} TTa _{0.01} O ₃	152.09	14765	14917.09	1.53×10^{-3}	1.58×10^{-5}	1.56×10^{-5}
LLSr _{0.03} TTa _{0.03} O ₃	129.65	8314.7	8447.05	1.69×10^{-3}	2.63×10^{-5}	2.59×10^{-5}
LLSr _{0.06} TTa _{0.06} O ₃	173.54	7534.8	7708.34	1.3×10^{-3}	3.04×10^{-5}	2.97×10^{-5}
LLSr _{0.09} TTa _{0.09} O ₃	207.70	5597	5624.7	1.11×10^{-3}	4.15×10^{-5}	4.12×10^{-5}
LLSr _{0.12} TTa _{0.12} O ₃	259.41	6608.6	6868.01	8.85×10^{-4}	3.47×10^{-5}	3.34×10^{-5}

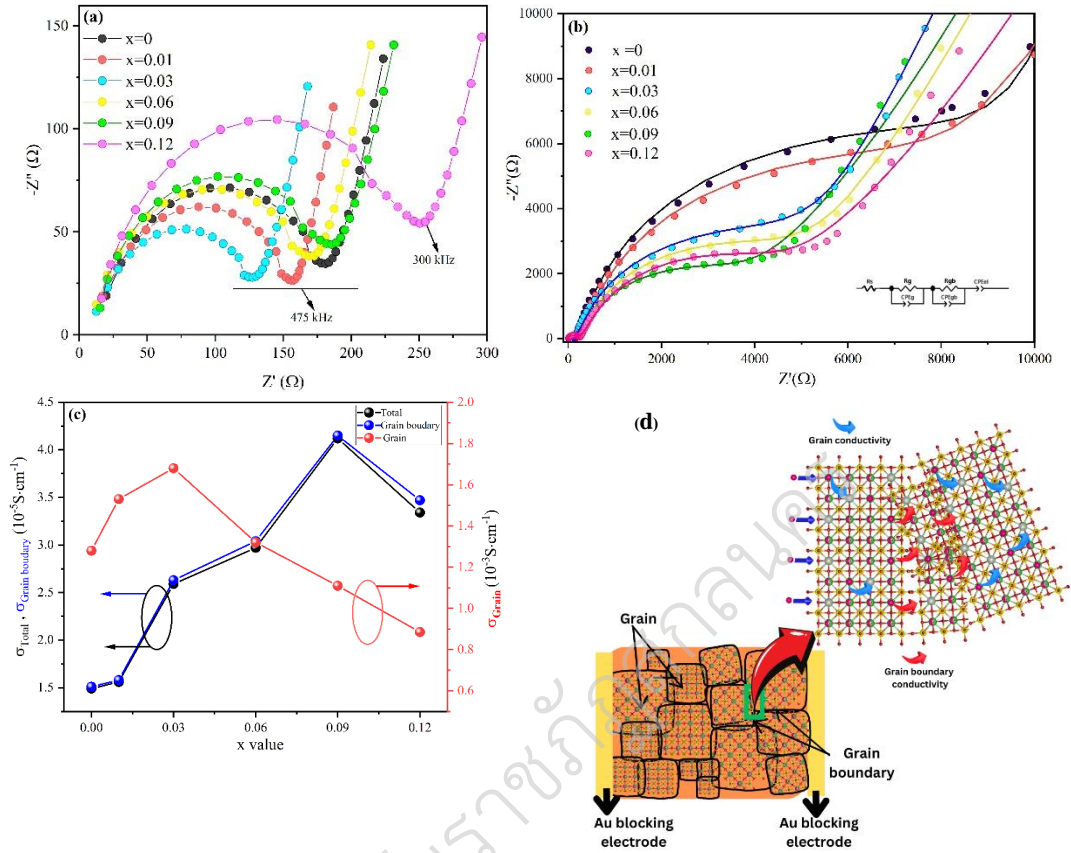


Fig. 57. EIS plots of $\text{Li}_{0.5-x}\text{La}_{0.5-x}\text{Sr}_x\text{Ti}_{1-x}\text{Ta}_x\text{O}_3$ ($0 \leq x \leq 0.12$) at 298 K (a) grain impedance, (b) grain boundary impedance with equivalent circuit model, (c) conductivities of all specimens, and (d) grain and grain boundary conductivity mechanism.

Arrhenius plots based on the total, grain, and grain boundaries at different temperatures are shown in Fig. 58 (a-c). The conductivities exhibit an excellent linear relationship fit as a function of temperature and are also affected by the migration of Li^+ in the grains and across the grain boundaries, which can be determined by the change in conductivity with temperature, following the Arrhenius equation for ion conduction, as given in Eq. (4.2),

$$\sigma_{\text{total}} = \sigma_0 \exp\left(\frac{-E_a}{k_B T}\right), \quad (4.2)$$

where σ_0 , k_B , E_a and T are the pre-exponential factor, Boltzmann constant, activation energy, and absolute temperature, respectively.

As shown in Fig. 59 (d), the total activation energy of $\text{LLSr}_{0.09}\text{TTa}_{0.09}\text{O}_3$ is approximately 0.47 eV. The lowest grain boundary activation energy was approximately 0.38 eV for the $\text{LLSr}_{0.03}\text{TTa}_{0.03}\text{O}_3$ sample, which corresponds to its grain conductivity. Therefore, Sr^{2+} and Ta^{5+} substitution helps expand the bottleneck, allowing Li^+ ions to move more easily, while the strength of partial Ta–O bonds increases and that of Li–O bonds decreases, improving Li-ion mobility and enhancing the ionic conductivity (Yu, K., et al., 2019; He, L. X., et al., 2003).

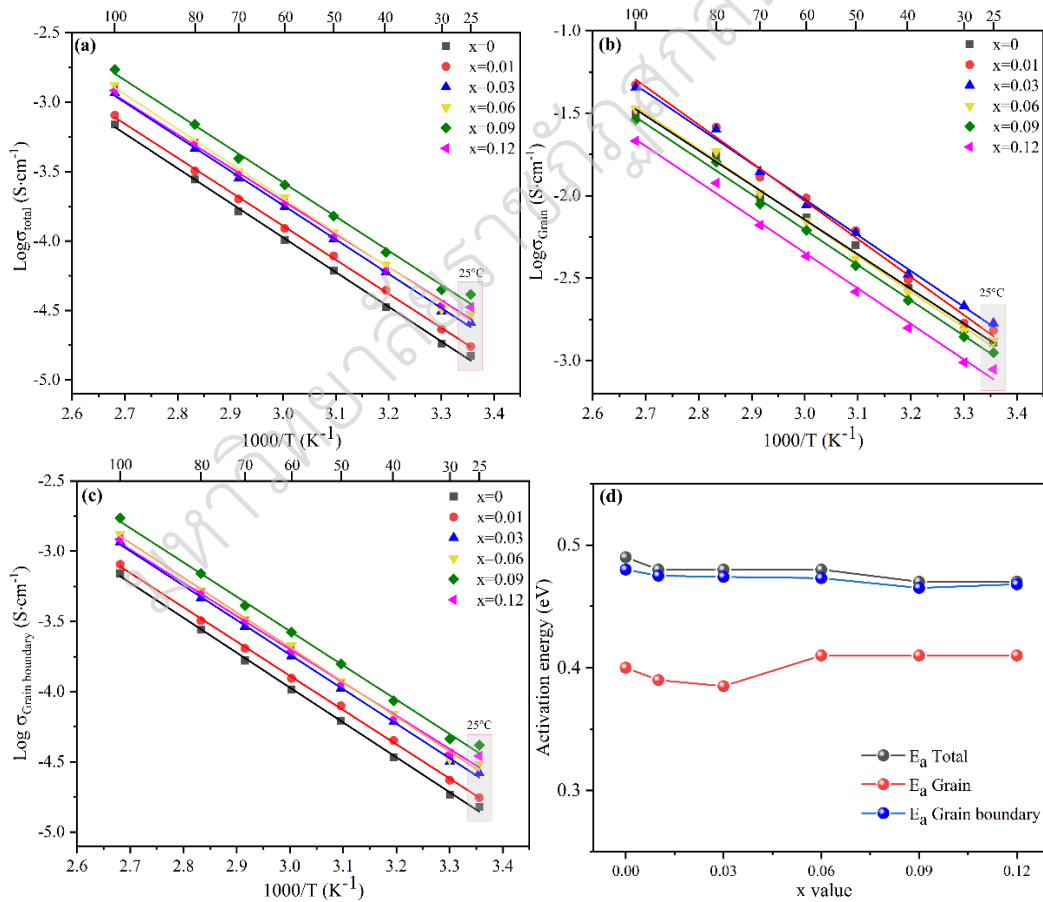


Fig. 58. Arrhenius plot of $\text{Li}_{0.5-x}\text{La}_{0.5-x}\text{Sr}_x\text{Ti}_{1-x}\text{Ta}_x\text{O}_3$ ($0 \leq x \leq 0.12$) at a temperature range 298 to 373 K. (a) total conductivity, (b) grain conductivity, (c) grain boundary conductivity, and (d) the activation energy with doping contents.

The electronic conductivities σ_e of the undoped sample with $x = 0$ and the doped sample with $x = 0.09$ were calculated using Eq. (4.3).

$$\sigma_e = \frac{I \cdot l}{U \cdot A}, \quad (4.3)$$

where U , l , l , and A are the constant DC voltage (4 V), stable current, thickness of the sample, and surface area of the sample, respectively. Ideally, an excellent ionic conductor should have high ionic conductivity and low electronic conductivity. As shown in Fig. 59, the potentiostatic polarization measurement is applied to survey the leakage current of $\text{Li}_{0.5}\text{La}_{0.5}\text{TiO}_3$ and $\text{LLSr}_{0.09}\text{TTa}_{0.09}\text{O}_3$ ceramics, then the direct current decreases and remains stable at approximately 0.327 and 0.066 μA , respectively. Moreover, the Au electrode is a blocking electrode, and the stable current is mainly contributed by electrons. The σ_e value of $\text{LLSr}_{0.09}\text{TTa}_{0.09}\text{O}_3$ (approximately $1.66 \times 10^{-9} \text{ S} \cdot \text{cm}^{-1}$) is lower than that of the undoped sample (approximately $8.19 \times 10^{-9} \text{ S} \cdot \text{cm}^{-1}$). Their ionic conductivities of approximately $4.12 \times 10^{-5} \text{ S} \cdot \text{cm}^{-1}$ demonstrate that $\text{LLSr}_{0.09}\text{TTa}_{0.09}\text{O}_3$ electrolytes are optimal lithium-ion electrolyte materials.

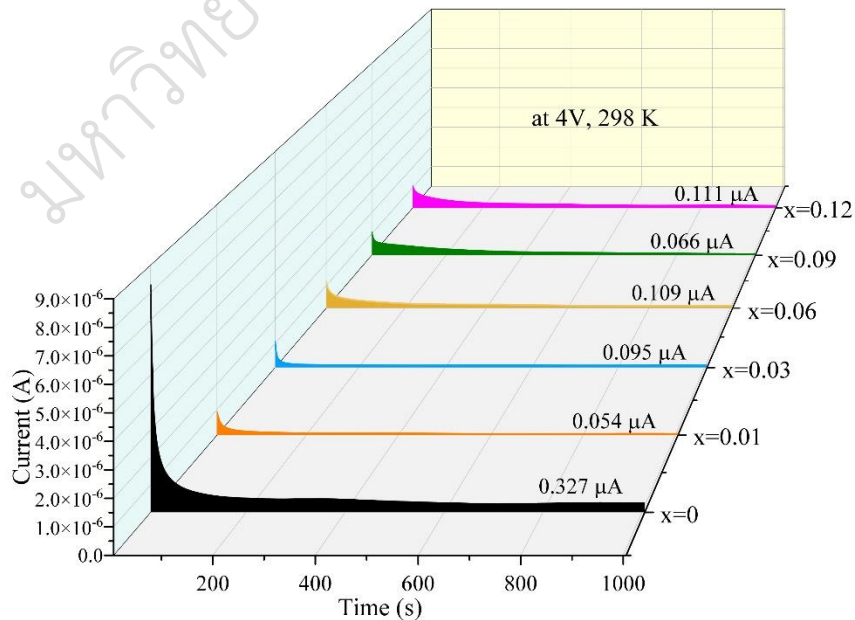


Fig. 59. Potentiostatic polarization patterns of all samples under 4 V at 298 K.

In addition, the practical application of the $\text{LLSr}_{0.09}\text{TTa}_{0.09}\text{O}_3$ electrolyte membrane was evaluated in solid-state Li-ion cells by employing a Li metal anode and a LiFePO_4 cathode operating at 60 °C. However, during the assembly in Fig. 60(a), the decomposition of titanium from Ti^{4+} to Ti^{3+} caused by the Li-metal anode leads to an inability to assemble the cells, resulting in short circuits which the details in appendices A (Xu, L., et al., 2022). Consequently, the addition of sintered 10 %wt. $\text{LLSr}_{0.09}\text{TTa}_{0.09}\text{O}_3$ powder mixed with PVDF-HFP/LiTFSI (3:2) as the CPE for semi-solid $\text{LiFePO}_4/\text{CPE}/\text{Li}$ full cell assembly, is a viable solution in Fig. 60(b).

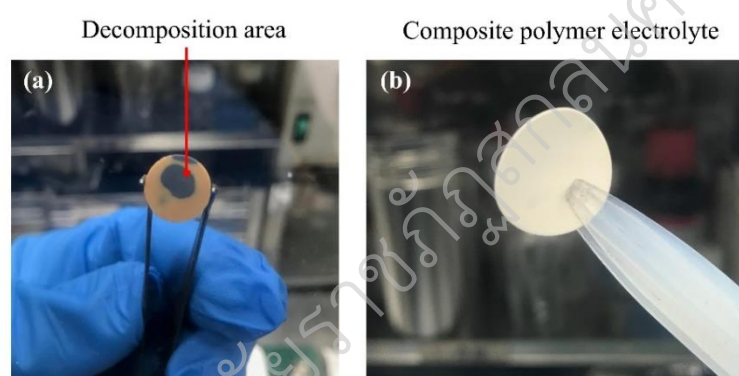


Fig. 60. The sample (a) $\text{LLSr}_{0.09}\text{TTa}_{0.09}\text{O}_3$ pellet after full cell assembled and (b) composite polymer electrolyte of 10 wt.% $\text{LLSr}_{0.09}\text{TTa}_{0.09}\text{O}_3$.

The EIS curve exhibits the highest ionic conductivity of $1.35 \times 10^{-3} \text{ S} \cdot \text{cm}^{-1}$ (Fig. 61.) when using CPE containing CPE-10 at 30 °C, aligning with the ionic conductivity of Li-symmetric cells $2.42 \times 10^{-3} \text{ S} \cdot \text{cm}^{-1}$ (Fig. 62.). The ionic conductivity of CPE-10 in Li-symmetric cells was calculated from the resistance of CPE (R_{CPE}) using Equation 1, excluding the charge transfer resistance1 (R_{CT1}) and charge transfer resistance2 (R_{CT2}).

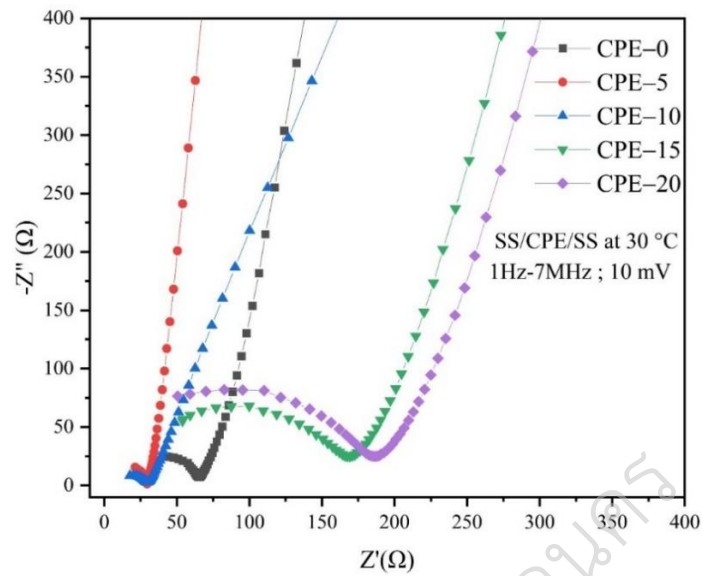


Fig. 61. The EIS of composite polymer electrolyte with 0–20 wt.% $\text{LLSr}_{0.09}\text{TTa}_{0.09}\text{O}_3$ powders at 30 °C.

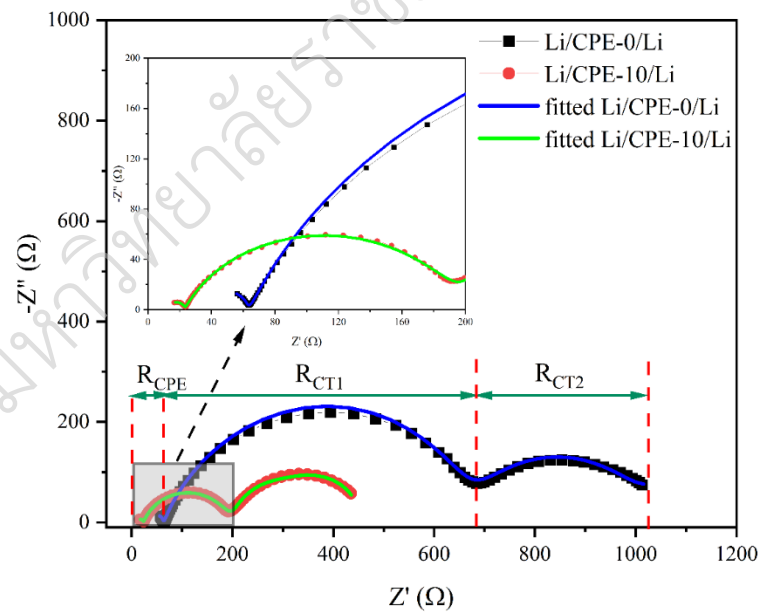


Fig. 62. EIS of composite polymer electrolyte with CPE-0 and CPE-10 in Li-symmetric cells at 30 °C.

Therefore, the CPE-10 was selected to fabricate the full cell $\text{LiFePO}_4/\text{Li}$ with mass loading 2 mg. Fig. 63(a) and (b) show the rate capability and voltage profile of the semi-solid $\text{LiFePO}_4/\text{Li}$ full cell, demonstrating a significantly stable voltage plateau of 2.5 – 4.0 V with capacities of 156.4, 148.7, 137.6, 117.1, and 96.7 $\text{mAh}\cdot\text{g}^{-1}$ at 0.1, 0.2, 0.3, 0.5, and 1C rates, respectively. While returning to 0.2 C, the reversible capacity recovers to 145.5 $\text{mAh}\cdot\text{g}^{-1}$, achieving a Coulombic efficiency of 99% during the testing. Fig. 63 (c) and (d) illustrate the long-term cycling performance, voltage profile, and capacity retention of the CPE-10 cells at 1C rate, corresponding to voltage profile and specific capacity of 80.9 $\text{mAh}\cdot\text{g}^{-1}$ with Coulombic efficiency of 98% and capacity retention of approximately 86% at 290 cycles. These findings demonstrate the feasibility of this design for practical applications in semi-solid-state Li batteries with $\text{LLSr}_{0.09}\text{Ta}_{0.09}\text{O}_3$ perovskite materials.

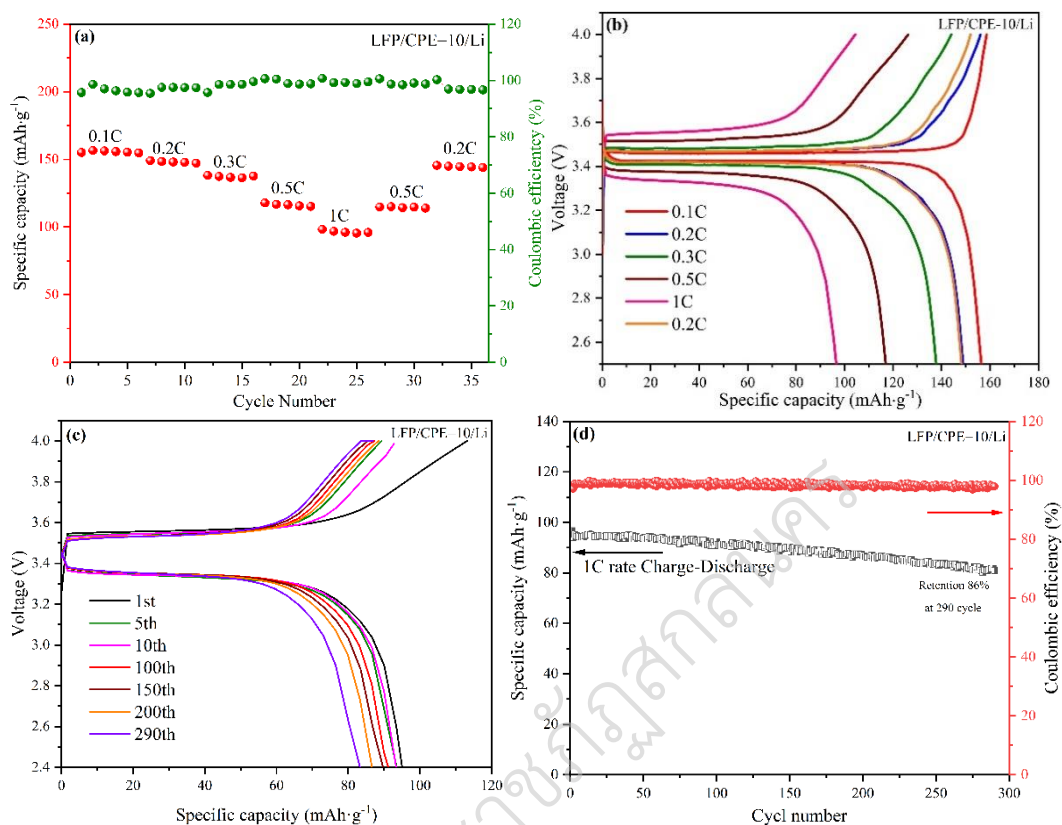


Fig. 63. Electrochemical performance of LiFePO₄/Li full cell (a) rate capability with 0.1C to 1 C, (b) charge–discharge profile in different C rate, (c) 1C rate charge–discharge profile stability of 290 cycles, and (d) cycling performance a 1C rate and Coulombic efficiency.

CHARACTERIZATIONS OF GARNET– Li_{6.75}Ga_{0.25}La₃Zr₂O₁₂ COMPOSITE POLYMER ELECTROLYTES

Crystal structure, morphology, and chemical composition

The X-ray diffraction (XRD) patterns of LLZO–Ga powder, PVDF–HFP/LiTFSI or solid polymer electrolytes (SPEs) membrane, and PVDF–HFP/LiTFSI filled with various contents of LLZO–Ga powder 5 to 20 %wt. or composite polymer electrolytes (CPEs) membrane is shown in Fig. 64. The XRD analysis of Li_{6.25}Ga_{0.25}La₃Zr₂O₁₂ (LLZO–Ga) powder reveals a cubic phase, indicating its successful incorporation as a

filler in the CPEs membranes. The crystalline phases of PVDF–HFP (β and γ phases) are characterized by peaks around 2θ values ranging from 18 to 22° in the SPEs sample. In the case of CPEs membranes, the intensity of the characteristic crystallinity phase peak decreases with an increasing content of LLZO–Ga filler, and more pronounced characteristic peaks corresponding to the cubic LLZO–Ga filler become evident. This decrease in crystallinity of PVDF–HFP is attributed to cross-linking between the polymer and the LLZO–Ga ceramic component due to a dehydrofluorination effect resulting from Lewis’s acid–base reactions. Furthermore, the passivation of LLZO–Ga filler contributes to the improvement of Li^+ ion mobility by reducing the crystallinity of PVDF–HFP and the crystalline peaks of LLZO–Ga ceramic filler within the CPE membrane closely matched those found in the pure LLZO–Ga powder, signifying its successful preservation within the polymer part composite membranes.

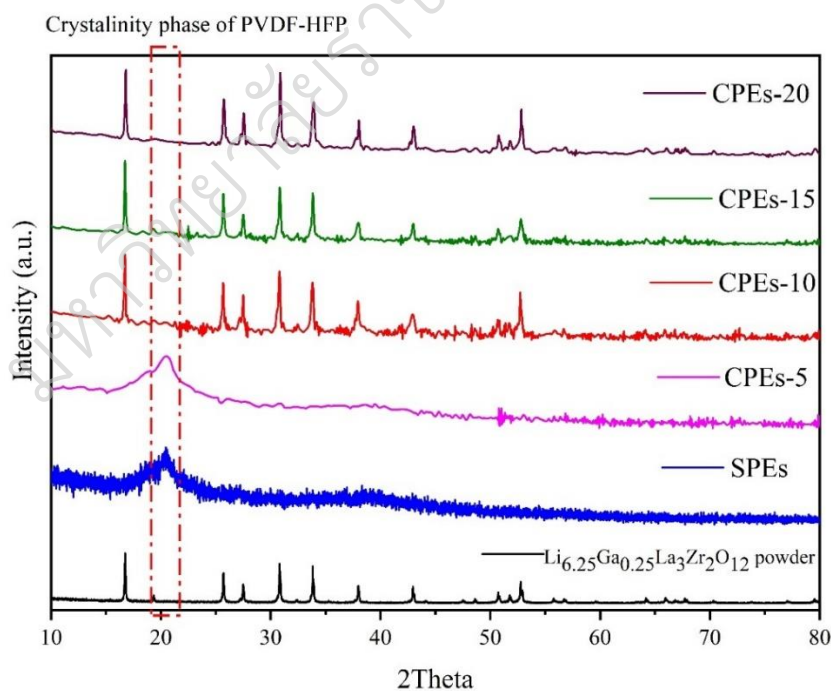


Fig. 64. XRD patterns of LLZO–Ga powder, SPEs and CPEs with various contents of LLZO–Ga filler 5 to 20 %wt.

Fig. 65. presents the FT – IR spectra of PVDF–HFP pellets, SPEs, and CPE membranes with varying LLZO – Ga filler contents from 5 %wt. to 20 %wt. The absorption bands at 761, 976 (α -phase), 835, and 874 cm^{-1} (β -phase) represent the crystalline phase of PVDF – HFP, the peak intensity decreases with an increase in LLZO – Ga filler content, which correlates with the XRD result of the reduction in PVDF – HFP crystallinity. Furthermore, the peaks observed at 1135 cm^{-1} and 1353 cm^{-1} illustrate the interaction of Li^+ with —CF_3 and asymmetric SO_2 stretching modes from LiTFSI, respectively. The peak at 1390 cm^{-1} is observed in membranes, corresponding to the formation vibration of —CH_2 groups. Additional peaks at 1103 and 1180 cm^{-1} are evident in both spectra, attributed to the symmetrical stretching modes of the —CH_2 and —CF_2 groups, respectively. The peak at 1510 cm^{-1} is the stretching vibration of $\text{C}=\text{C}$, while the absorption peak at 1058 cm^{-1} corresponds to the C—C skeleton vibration. As the concentration of LLZO–Ga increases, the absorption peak intensity of $\text{C}=\text{C}$ increases, while the absorption peak intensity of C—C decreases. These observations suggest that LLZO–Ga catalyzes the dehydrofluorination of the PVDF–HFP chains; hence, the strength of the $\text{C}=\text{C}$ absorption peak increases with higher LLZO concentration, indicative of the production of more $\text{C}=\text{C}$ bonds. Besides, a sharp peak at 1660 cm^{-1} is observed corresponding to the $\text{C}=\text{C}$ stretching vibration, indicating the presence of the C—H group and C—F groups, which results from the interaction between the PVDF – HFP backbone DMF, and LiTFSI. These observations indicate that LLZO – Ga filler plays a role as a catalyst in the dehydrofluorination process of the PVDF–HFP chains. The strength of the C—C absorption peak increases with higher concentrations of LLZO, suggesting a greater production of C—C bonds. The partially dehydrofluorinated PVDF–HFP and LLZO materials have the capability to form complexes with Li^+ ions through acid–base interactions. Furthermore, LLZO particles effectively trap TFSI⁻ anions, facilitating the dissociation of LiTFSI and thereby enhancing the carrier concentrations of Li^+ for conduction.

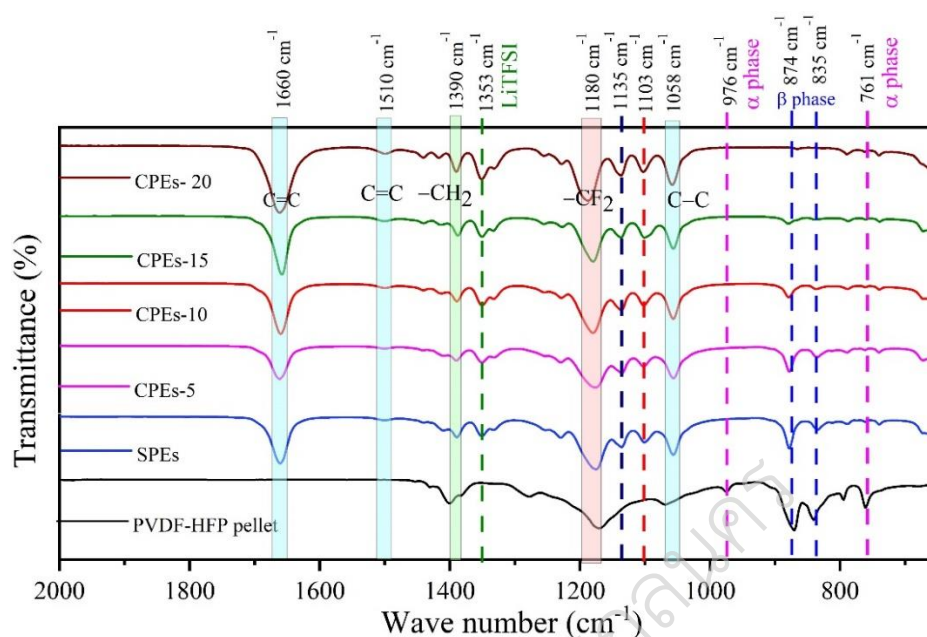


Fig. 65. The FT – IR spectra of PVDF – HFP pellets, SPEs, and CPEs membranes with varying LLZO – Ga filler contents from 5 %wt. to 20 %wt.

The resulting CPEs membrane undergoes a color transformation from the initial white hue of the SPEs membrane to a yellowish–brown shade. This change is attributed to the dehydrofluorination effect arising from the cross–linking between the polymer component and the LLZO–Ga filler. Additionally, the membrane exhibits flexibility and can be easily cut into preferred shapes, as illustrated in Fig. 66 (a – b). The SEM images and EDS elemental mappings of the membrane are presented in Fig. 66 (c – e). These images reveal the porosity of surface membranes and homogeneous dispersion of micro sized LLZO–Ga particles within the sample CPEs–10, establishing continuous jump sites conducive to Li^+ ion movement. The interfacial regions between PVDF–HFP and LLZO–Ga additionally facilitate rapid lithium–ion transmission channels, markedly enhancing the long–range migration capabilities of lithium ions. Nevertheless, with an escalating concentration of inorganic fillers, the initially uniform distribution of LLZO–Ga powders tends to aggregate, resulting in the interruption of contiguous lithium–ion pathways. Consequently, the optimal composition

of the composite polymer electrolyte was ascertained as PVDF–HFP 3 g: LiTFSI 2 g: LLZO–Ga 0.5 g, respectively.

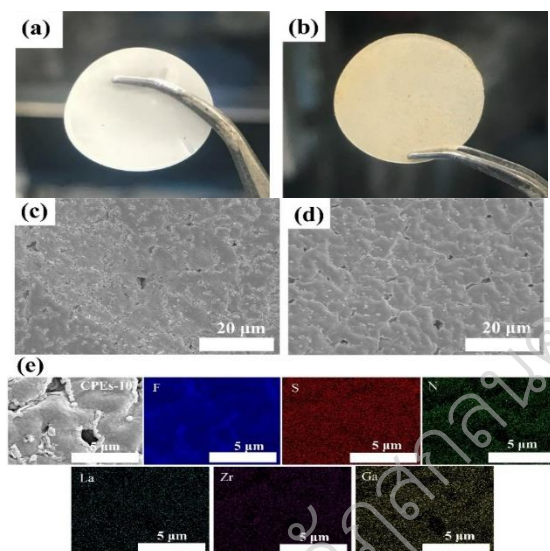


Fig. 66. (a) Optical image of SPEs and (b) CPEs – 10 membrane (c) The SEM of images of surface SPEs and (d) surface of CPEs – 10 membrane (e) The EDS elements mapping images of CPEs – 10 membranes.

Electrochemical properties and performance of full cells

The EIS measurement of SS/CPEs/SS cell at 303 K symmetric cell with stainless steel blocking electrode at a different of filled LLZO – Ga filled contents are shown in Fig. 67. Additionally, our previous work has demonstrated that LLZO – Ga obtained through this process exhibits high ionic conductivity, measuring $9.6 \times 10^{-4} \text{ S} \cdot \text{cm}^{-1}$. After being blended with PVDF–HFP and LiTFSI, the CPEs achieve the highest ionic conductivity of $7.12 \times 10^{-4} \text{ S} \cdot \text{cm}^{-1}$ at 303 K, much higher than most of the SPEs membrane ($7.52 \times 10^{-5} \text{ S} \cdot \text{cm}^{-1}$). In general, the intercept on the Z' -axis is regarded as the bulk resistance of the CPEs. The CPEs–10 consists primarily of a gel polymer electrolyte matrix interspersed with sizable LLZO–Ga particles. This gel polymer matrix is infused with a substantial quantity of highly ion–conductive liquid plasticizer, promoting swift migration of Li^+ ions. It is widely recognized that within such composite

electrolytes, the gel polymer matrix surrounding the LLZO–Ga particles serves as the principal pathway for Li^+ ion transport. Furthermore, the interconnected LLZO–Ga particles aid in the facilitation of Li^+ ion transportation, a process evidenced by the reduction in crystallinity observed in the polymer matrix, as corroborated by XRD and FT–IR analyses. Consequently, the thoughtfully engineered CPE–10 composite electrolyte exhibits a markedly enhanced level of ionic conductivity.

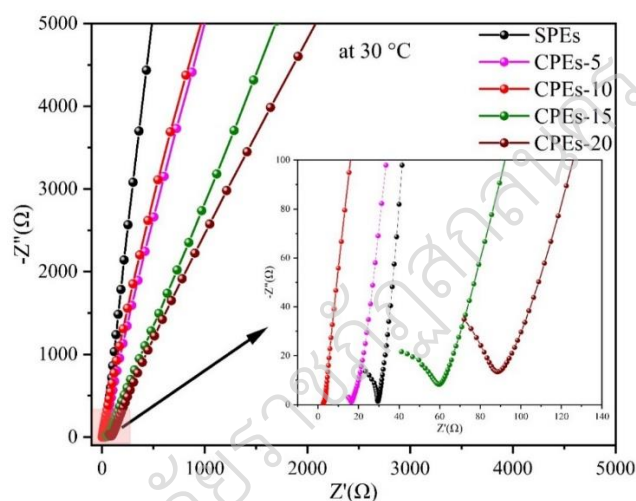


Fig. 67. EIS curves of CSEs at different filled with LLZO–Ga contents.

The Arrhenius plots are displayed in Fig. 68., It can be observed that the CPEs – 5 and CPEs – 10 membranes with LLZO – Ga fillers exhibit higher ionic conductivities than the pure PVDF–HFP/LiTFSI (SPEs), in a wide temperature range from 10 to 80 °C. With the increasing content of LLZO – Ga particles, the ionic conductivity of the CPEs increased initially, reached the maximum at 10 %wt. and then dropped at 15 and 20 %wt. The ionic conductivities from SPEs to CPEs – 10 were interrelated with the interactions between the PVDF–HFP matrix and the LLZO – Ga fillers. The conductivity enhancement for CPEs – 10 may be attributed to the following several reasons. First, LLZO – Ga particles can decrease the crystallinity of the PVDF–HFP matrix and enhance the segmental motion of chains, which has been confirmed by the XRD patterns. Second, when the content of LLZO – Ga reaches the percolation

threshold, the Li-ions can not only migrate through the polymer segments but also transfer along the interface of PVDF – HFP and LLZO – Ga particles due to the percolation effect. Third, activated C=C induced by partial dehydrofluorination of PVDF–HFP could facilitate the Lewis acid–base interactions between PVDF – HFP/LiTFSI and LLZO – Ga in the CPEs, leading to a higher free Li⁺ concentration and a rapid Li⁺ transmission path at the PVDF–HFP/LiTFSI/LLZO – Ga interface. However, more LLZO – Ga particles (15 and 20 %wt.), where the amount of LLZO – Ga surpassed the percolation threshold, resulted in a disparity of the Li distribution due to the aggregation of particles and blocking the interfacial Li⁺ channels, leading to a decrease in ionic conductivity.

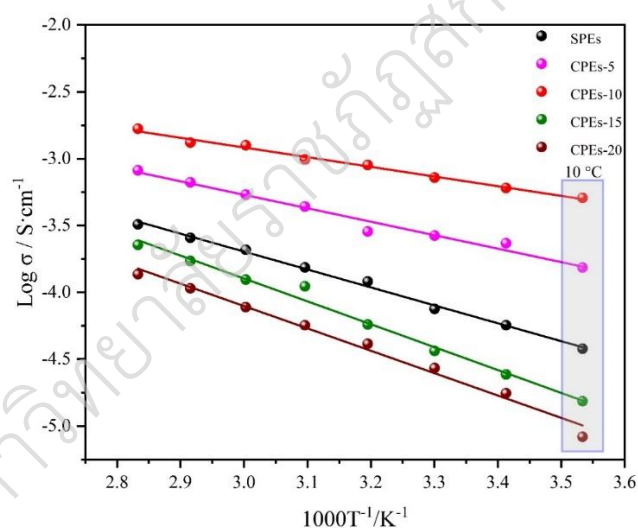


Fig. 68. Arrhenius plots of SPEs and CPEs at temperatures ranging from 10 to 80 °C.

Linear sweep voltammetry (LSV) tests were conducted on SPEs and CPEs – 10 membranes at a temperature of 25 °C, within a potential range of 2–6 V vs. Li/Li⁺, to evaluate the stability of the electrochemical windows for the membrane in Fig. 70. When applied to a high-voltage, the performance of the Au/SPEs/Li Au and Au/CPEs – 10/Li membranes are enhanced up to 4.9 V, compared to 4.8 V for SPEs. This suggests that the inclusion of LLZO–Ga fillers can expand the electrochemical window

and improve the electrochemical stability of the CPEs, thereby fulfilling the requirements of high-voltage active cathode materials.

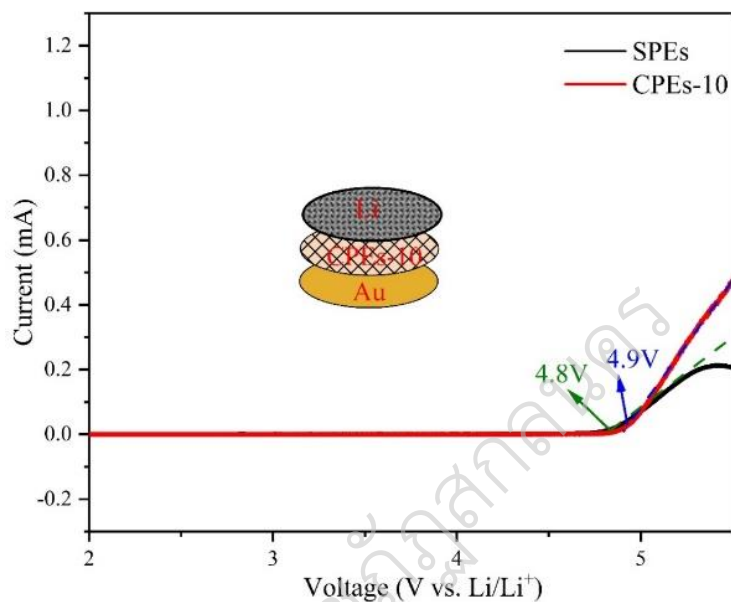


Fig. 69. (a) LSV plots of the Au/ SPEs /Li and Au/CPEs-10/Li cell structures at room temperature.

Fig. 70 (a) and (b) display the direct current polarization results of both the SPEs and CPEs-10 with 5 μL of 4MLiFSI: DEE membranes at room temperature. The inset illustrates the corresponding electrochemical impedance spectra before and after polarization. The lithium-ion transference number (t_{Li^+}) of composite polymer electrolyte was measured using chronoamperometry test on the Li/CPEs/Li cell with 4MLiFSI: DEE, and applied voltage of 10 mV. The value of t_{Li^+} was calculated by Bruce-Vincent equation.

$$t_{\text{Li}^+} = \frac{I_s(\Delta V - I_o R_o)}{I_o(\Delta V - I_s R_s)} \quad (4.4)$$

where ΔV is the potential applied across the cell, the before polarization or initial (I_o) and after polarization or steady-state (I_s) currents are obtained from the

chronoamperometric curve. R_0 and R_s measured by EIS, reflect the initial and steady-state resistances of the passivated layers.

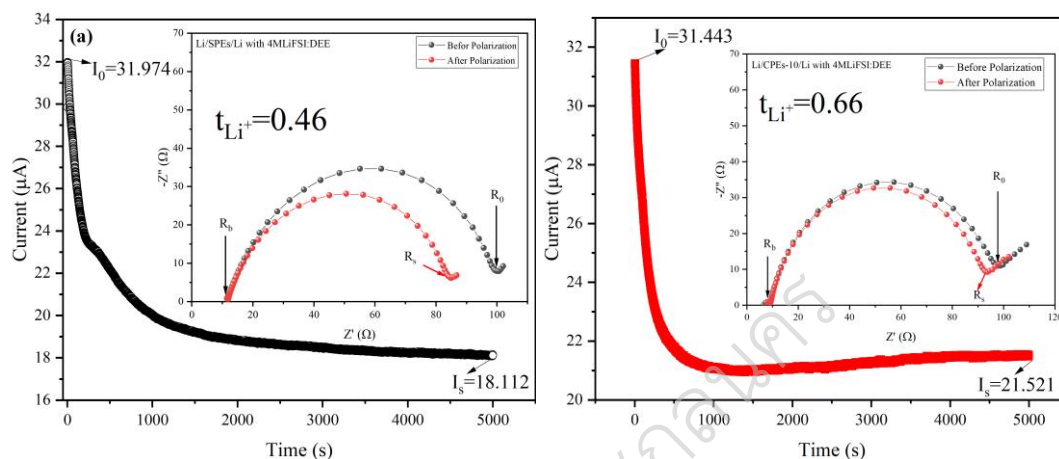


Fig. 70. Chronoamperometry curves of (a) Li/SPEs/Li and Li/CPEs – 10/Li with 4MLiFSI: DEE membrane with a bias potential of 10 mV; the inset is the impedances before and after polarization.

Notably, the calculated Li^+ transference number for CPEs – 10 is measured at 0.60, significantly surpassing that of SPEs (0.47). This elevated Li^+ transference number in CPEs–10 underscores its efficient Li – ion transport capability, which holds promise for immobilizing TFSI^- and inhibiting dendritic Li deposition. In electrolytes where t_{Li^+} is about 0.5, the movement of cations contributes more to the overall ionic conductivity in comparison to anions. It is widely recognized that a high t_{Li^+} can enhance electrode kinetics and potentially suppress the growth of Li dendrites. Our results reveal that electrolytes with a high concentration of LiFSI in DEE exhibit t_{Li^+} of about 0.5, indicating a predominant contribution of cations to the total ionic conductivity compared to anions. These findings suggest a decrease in the relative mobility of anions in LiFSI–DEE electrolytes, resulting in a heightened contribution of Li^+ to the overall ionic conductivity (Pham, T. D., & Lee, K. K., 2021; Pham, T. D. et al. 2022).

Table 12 Measured values of parameters and the corresponding calculated values of Li transference number at 25 °C.

Sample	I_0 (μA)	I_s (μA)	R_0 (Ω)	R_s (Ω)	ΔV (mV)	t_{Li^+}
Li/SPEs/Li	31.974	18.112	90.64	74.94	10	0.47
Li/CPEs-10/Li	31.443	21.521	91.34	87.09	10	0.60

To examine the stability of the prepared Li/SPEs/Li and Li/CPEs – 10/Li cells, galvanostatic cycling experiments were conducted using symmetric Li cells with applied 5 μL of high concentration electrolyte (4MLiFSI: DEE). These experiments were carried out at a constant current density of 0.1 mA cm^{-2} at room temperature, as illustrated in Fig. 72. The cycling voltage profiles of Li/SPEs/Li cell is presented in Fig. 72 (a). Following 140 hours of cycling, a noticeable increase in voltage polarization was observed in the SPEs cell, with subsequent fluctuations in voltage amplitude observed up to 600 hours. The inset image in Fig. 72 (a) depicts the unsmoothed voltage amplitude of the SPEs, indicating variations in the voltage profiles attributed to poor interfacial contact and an unstable interface between the Li metal and the SPEs membrane. These fluctuations result in uneven localized high current densities, which are recognized as the primary factors contributing to the initiation and growth of Li dendrites during subsequent Li cycling. In contrast, compared with that of Li/CPEs – 10/Li cell in Fig. 72 (b), the cell with CPEs – 10 exhibited a relatively stable voltage and much smaller and stable overpotential, and no signs of short-circuiting were observed even after 600 h of cycling. The inset voltage amplitude shows that the CPEs – 10 is smooth, demonstrating a remarkably connected well with interfacial contact and inhibitory effect on the growth of lithium dendrites. The excellent dendrite suppression could be ascribed to the enhanced mechanical strength of the CPEs – 10 membrane and the uniform Li deposition resulting from stable interfacial properties between Li and the flexible CPEs. Thus, it is apparent that the developed CPEs-10

membrane is effective in suppressing the Li dendrite formation and ensuring long-term cycling stability of the cell against failure by a short circuit.

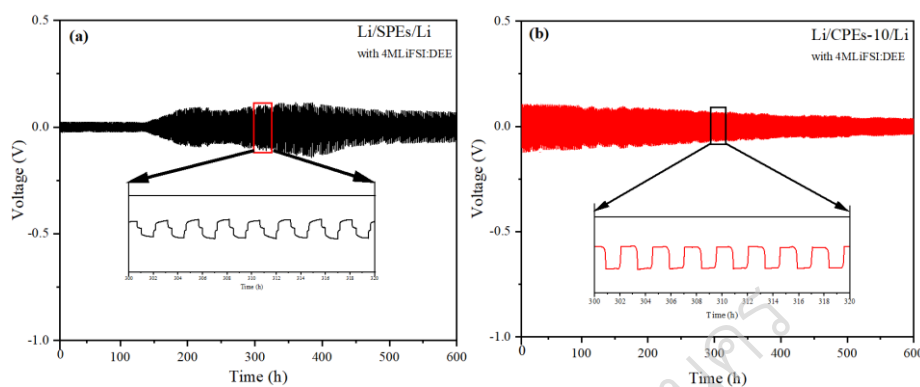


Fig. 71. Voltage profiles of Li plating and stripping cycling for the (a) SPEs, (b) CPEs – 10, with the current density of 0.1 mA cm^{-2} .

The optical images of the thermally shrunk commercial Celgard, SPEs, and CPEs–10 membranes are shown in the initial state (25°C) in Fig. 73. When compared to that at 100°C , the commercial Celgard membrane shrank, whereas the SPEs and CPEs membranes exhibited minimal size reduction. Interestingly, the SPEs and CPE membrane showed no apparent size reduction at 130°C for 30 minutes, further confirming their superior thermal stability. These comparative tests indicate that the PDVF–HFP base of SPEs and CPEs demonstrates excellent thermal stability and a higher melting point from polymer attributed to introducing a more heat-resistant nature supported by LLZO–Ga particles of the CPEs–10 sample.

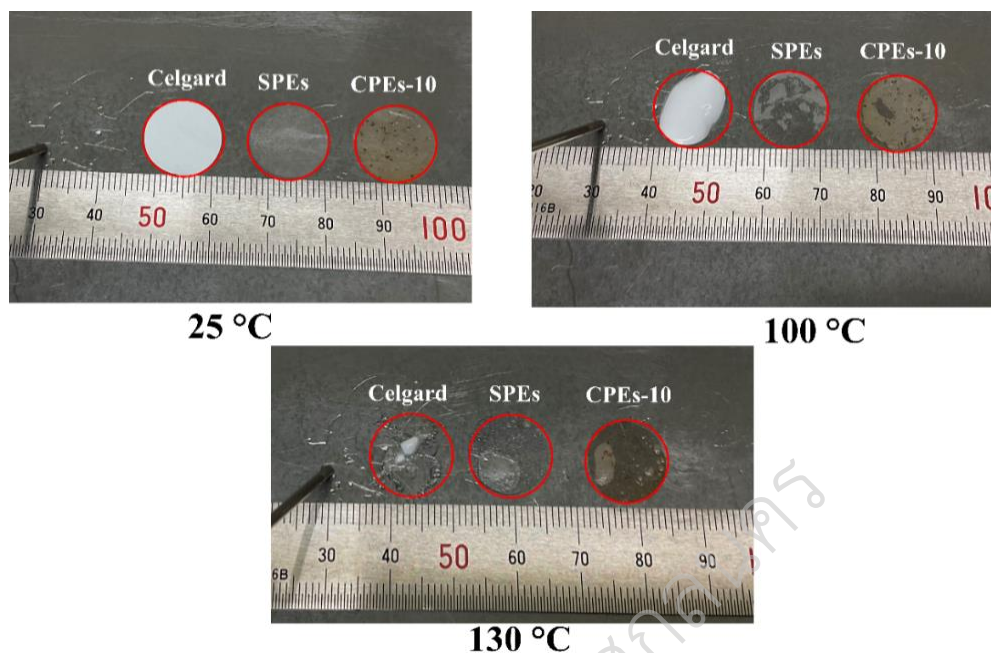


Fig. 72. Photograph of commercial separator Celgard, SPEs, and CPEs–10 films before and after heating at 25°C, 100°C, and 130 °C.

The CR2032 coin cells with an LFP cathode of mass loading 2 mg, Li metal anode, CPEs–10 membrane, and applied 5 μL of high concentration electrolyte (4MLiFSI: DEE) were assembled and examined between 2.5 to 4.0 V to investigate the electrochemical performance of quasi–solid composite polymer electrolytes cell (QCPEs–10) further. Fig. 74 (a) and (b) present the rate capability and voltage profile of the quasi–solid LFP/QCPEs–10/Li full cell at room temperature. When testing with cutting off voltage 2.5–4.0 V at 0.1C, 0.2C, 0.5C, and 1C, the LFP/ QCPEs–10/Li cell shows discharge capacities of 150.4, 145.1, 127.8, and 108.7 $\text{mAh}\cdot\text{g}^{-1}$, respectively. While returning to 0.1 C, the reversible capacity recovers to 150.8 $\text{mAh}\cdot\text{g}^{-1}$, achieving a Coulombic efficiency of 99.4% during the testing. Fig. 74 (c) and (d) illustrate the long–term cycling performance, voltage profile, and capacity retention of the QCPEs–10 cells at 1 C rate, corresponding to voltage profile and specific capacity of 107.8 $\text{mAh}\cdot\text{g}^{-1}$ with Coulombic efficiency of 99% and capacity retention of approximately

83.11% at 280 cycles. These findings demonstrate the feasibility of this design for practical applications in quasi-solid-state Li metal batteries.

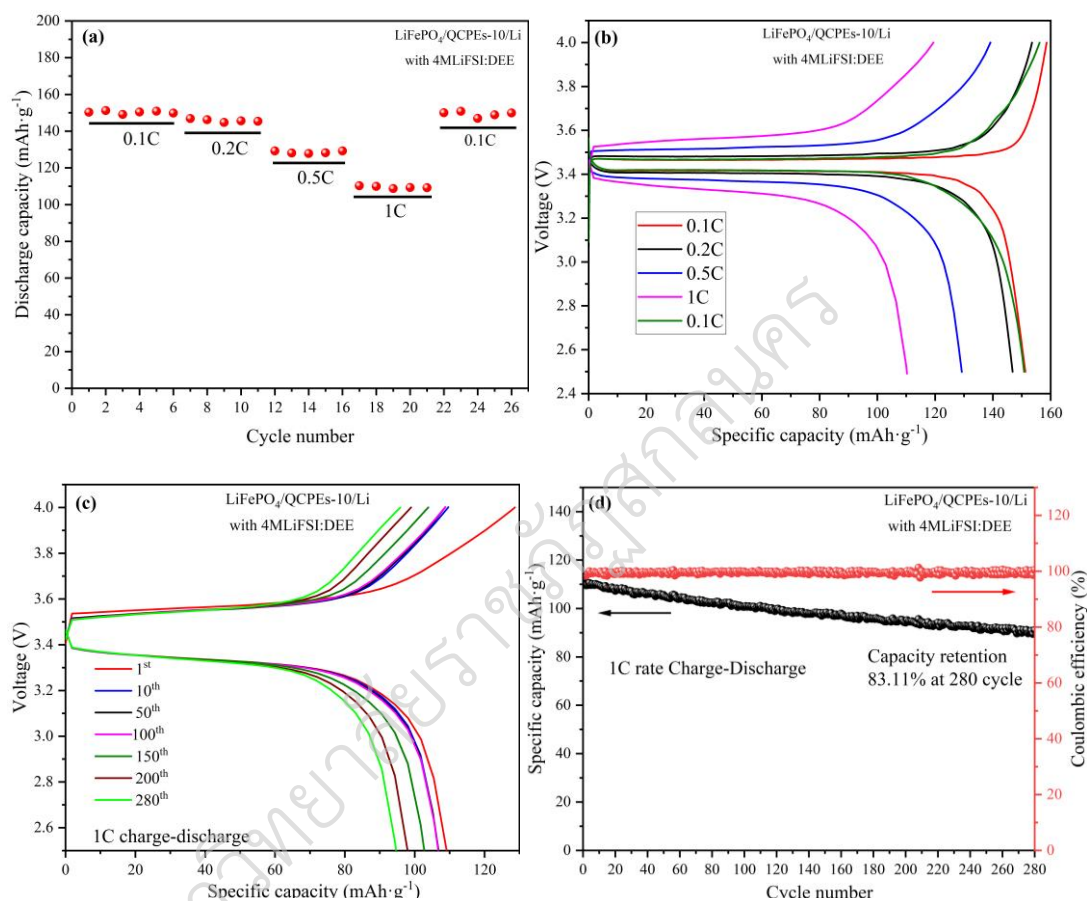


Fig. 73. Electrochemical performance of the LFP/QCPEs-10/Li cell at RT (a) rate capability with 0.1 C to 1 C, (b) the corresponding specific capacity and voltage profile, (c) charge-discharge profile performance under 1C rate of 280 cycles and (d) corresponding charge-discharge curves of cyclic performance a 1c rate and Coulombic efficiency.

The CR2032 coin cells with an NMC111 cathode of mass loading 2.5 mg, Li metal anode, CPEs-10 membrane, and applied 5 μL of high concentration electrolyte (4MLiFSI: DEE) were assembled QCPEs-10 cell and examined between 2.8 to 4.3 V to investigate the electrochemical performance further. Fig. 75 (a) and (b) depict the rate capability and voltage behavior of the quasi-solid NMC111/QCPEs-10/Li full cell at room temperature. Under varying rates of 0.1C, 0.2C, 0.5C, and 1C with a cut-off voltage of 2.8–4.3 V, the NMC111/QCPEs-10/Li cell demonstrates discharge capacities of 152.7, 146.2, 134.2, and 115.6 $\text{mAh}\cdot\text{g}^{-1}$, respectively. When back to 0.1 C, the capacity still returns to the close with an initial state, representing that the quasi-solid-state battery has well reversibility to 145.8 $\text{mAh}\cdot\text{g}^{-1}$, achieving a Coulombic efficiency of 99.5 % throughout the test. Fig. 75 (c) and (d) showcase the extended cycling performance, voltage characteristics, and capacity retention of the QCPEs-10 cells at a rate of 0.3 C, exhibiting a specific capacity of 136.7 $\text{mAh}\cdot\text{g}^{-1}$ with a Coulombic efficiency of 99% and a capacity retention of approximately 82.52% after 80 cycles.

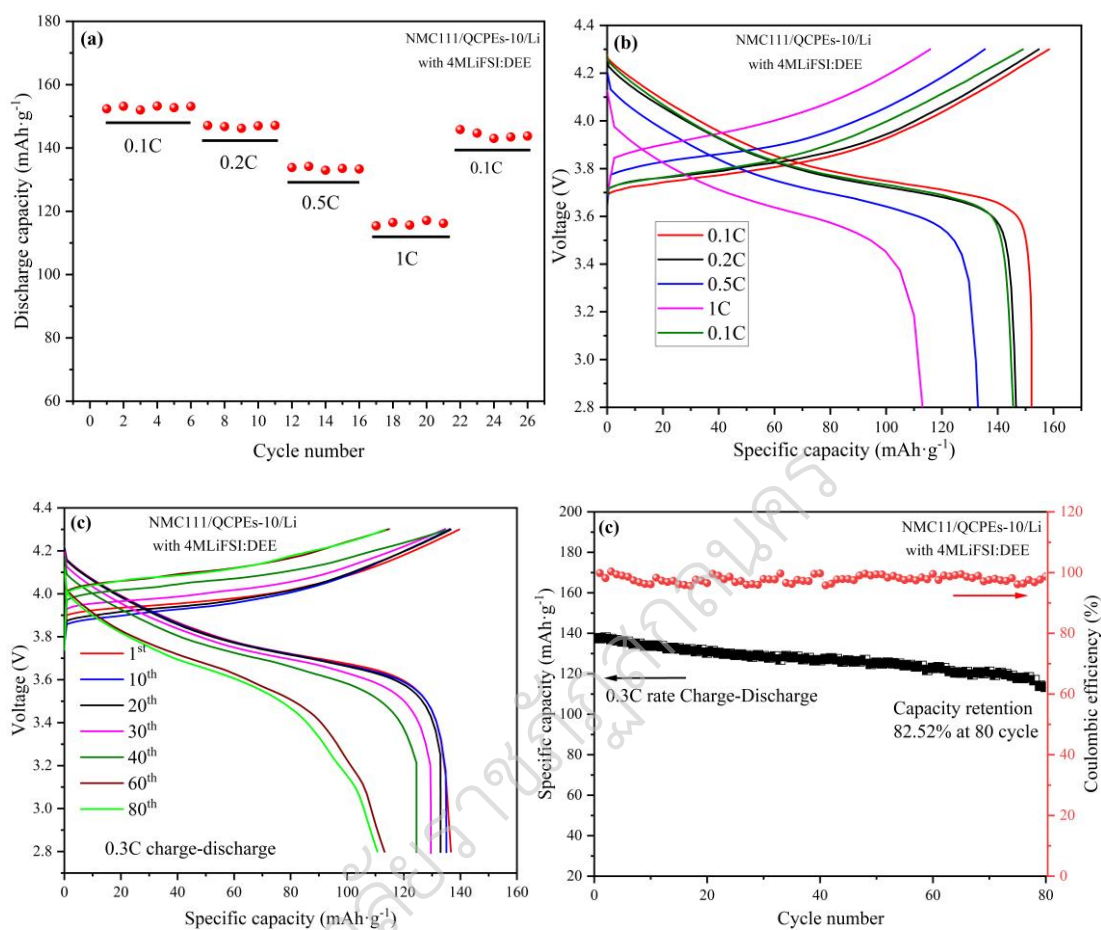


Fig. 74. (a) Rate capability of NMC111/ QCPEs-10/Li cell at RT with different 0.1 C to 1 C. (b) charge and discharge curves of the quasi-solid cell (c) charge–discharge curves cycle performance of the quasi-solid cells at 0.3 C 80 cycles. (d) cyclic performance at a 0.3 C rate and Coulombic efficiency.

XPS analysis was conducted on the CPEs-10 membrane at the Li-metal anode interface, both initially and after 100 cycles, to examine the impact of the solid electrolyte interface (SEI) and interfacial composition on the NMC111/QCPEs-10/Li cell. Initially, the spectra Fig. 75 (a) showed the presence of hydrocarbon C peaks attributed to CPEs-10 C—C (284.3 eV), the PVDF-HFP co-polymer C—O (286.1 eV), COOR (carboxylate) (288.4 eV), C—F (291.7 eV), and LiFSI with organic solvent ROCO₂Li (carboxylate-Li salt) (290.5 eV). The F 1s peak Fig. 75 (c) showed primarily

LiFSI (688.5 eV) with a small portion of LiF (685.25 eV), while the S 2p in Fig. 75 (e) revealed LiFSI (170.6 eV), the polythionate complex, $S_xO_6^{2-}$ (169.4 eV), and Li_2SO_3 (167 eV). Fig. 75 (g) shows the Li 1s peak of Li_2O (56 eV) from LLZO–Ga oxide layer and LiFSI (56.5 eV). After 100 cycles of charge–discharge, the strong C–C (284.3 eV), C–O (285.5 eV), and LiFSI were observed, indicating their role in SEI formation, while other signals may correspond to decomposition products of the organic solvent C–F, $ROCO_2Li$, and COOR as shown in Fig. 75 (b). Decomposition products of LiFSI, such as C–F and the LiF–rich SEI on the surface, promoting uniform Li deposition, high Li–ion conductivity, and suppress the creation of Li dendrites as seen in Fig. 75 (d). Additionally, Fig. 75 (f) high–strength Li_2SO_3 and polythionate complexes were detected, indicating that the SEI was primarily formed due to the decomposition of LiFSI. The Li 1s spectrum confirmed the increasing of Li_2O layer from LLZO–Ga oxide (55.2 eV) and further decomposition of LiFSI (60.5 eV) on the SEI as shown in Fig. 75 (h). These findings suggest that both electrolyte and LLZO–Ga content in CPEs–10 influence interfacial stability and electrochemical performance through the formation of LiF and Li_2O layers.

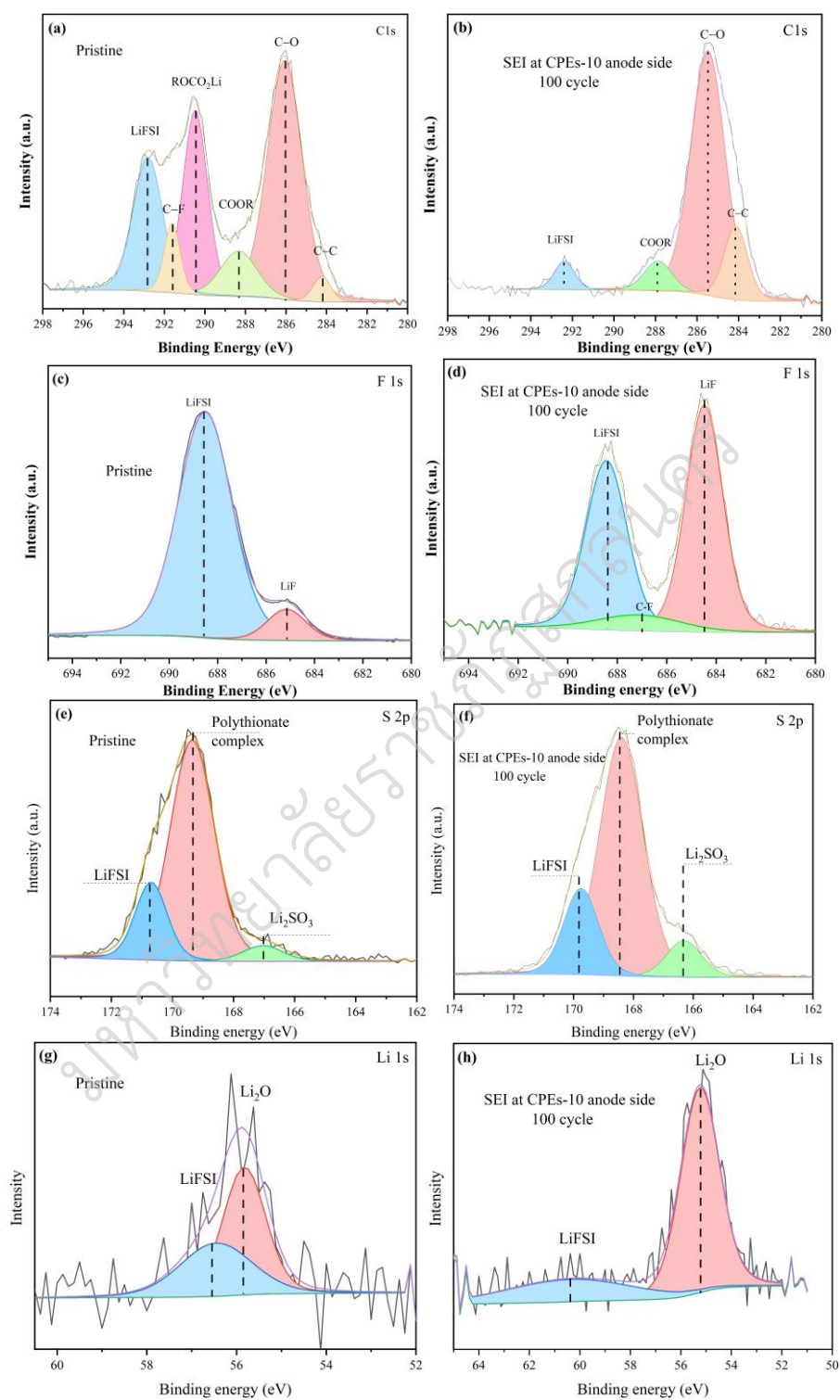


Fig. 75 XPS characterization of the SEI components on the cycled NMC111 electrodes in different electrolyte after 100 cycles compared with pristine (a), (b) C1s and (c), (d), F1s and (e), (f) S2p and (g), (f) Li 1s.

A pouch cell was constructed using an NMC111 cathode of size $5 \times 2 \text{ cm}^2$, Li metal anode size $5 \times 2.5 \text{ cm}^2$, CPEs-10 membrane size $6 \times 3 \text{ cm}^2$, and $50 \mu\text{L}$ 4MLiFSI: DEE. The assembled pouch cell of QCPEs-10 measuring $6 \times 3 \text{ cm}^2$ was then tested between 2.8 and 4.3 V to assess its electrochemical performance. Fig. 76 (a) and (b) illustrate the rate capability and voltage profile of the pouch cell quasi-solid NMC111/QCPEs-10/Li at ambient temperature. Across various rates of 0.1C, 0.2C, 0.5C, and 1C, with a cut-off voltage range of 2.8 to 4.3 V, the pouch cell NMC111/QCPEs-10/Li exhibits discharge capacities of 148.7, 120.4, 60.8, and 30.9 $\text{mAh}\cdot\text{g}^{-1}$, respectively. Upon returning to 0.1 C, the capacity regains its initial value, demonstrating good reversibility at $137.8 \text{ mAh}\cdot\text{g}^{-1}$, achieving a Coulombic efficiency of 99.2% throughout the test. Fig. 76 (c) and (d) present the extended cycling performance, voltage characteristics, and capacity retention of the pouch cell QCPEs-10 at a rate of 0.3 C, showing a specific capacity of $104.1 \text{ mAh}\cdot\text{g}^{-1}$ with a Coulombic efficiency of 99.4% and a capacity retention of approximately 78.1% after 150 cycles. Furthermore, the mechanical testing of the pouch cell QCPEs-10 included normal, bending, cutting, and burning tests with light on a diode array and keeping voltage, demonstrating the safety of the NMC111/QCPEs-10/Li cell in fire incidents shown in Fig. 77 (a – d). These findings demonstrate the feasibility of this design for practical applications in pouch-type quasi-solid-state Li metal batteries.

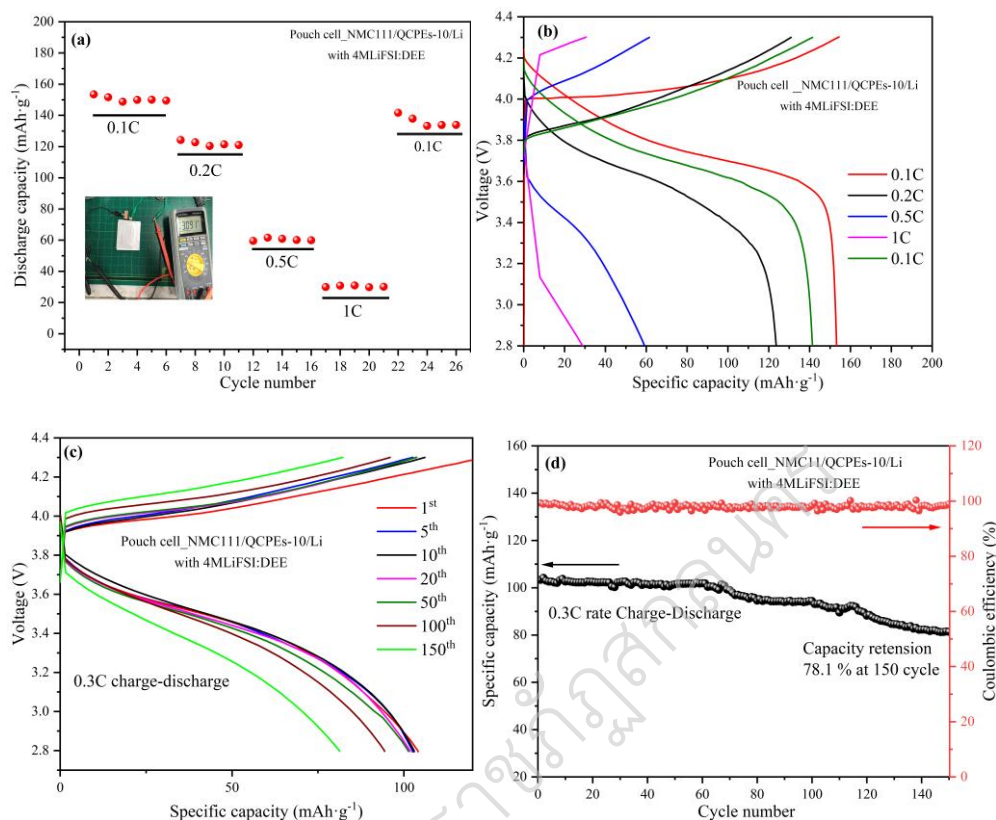


Fig. 76. (a) and (b) Rate performance corresponding to specific capacity and voltage curve of pouch cell NCM111/ QCPEs-10/Li batteries at 0.1C – 1 C, respectively. (c) The galvanostatic cycle performance corresponding charge-discharge curves of pouch cell NCM111/ QCPEs-10/Li battery at 0.3C (d) cyclic performance a 0.3 C rate and Coulombic efficiency.

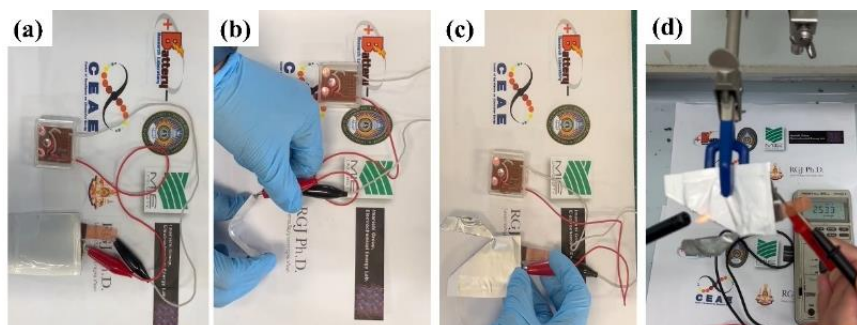


Fig. 77. The optical images of (a) normal, (b) bending, (c) cutting, and (d) burning test of pouch-type NMC111/QCPEs-10/Li cell.

CHAPTER 5

CONCLUSIONS AND SUGGESTION

CONCLUSIONS

This thesis focuses on the research and development of energy store devices for synthesis, and fabrication of cells of all-solid-state, semi-solid state, or quasi-solid-state batteries. Battery cells were fabricated by using composite polymer electrolyte of perovskite- $\text{Li}_{0.5-x}\text{La}_{0.5-x}\text{Sr}_x\text{Ti}_{1-x}\text{Ta}_x\text{O}_3$ ($0 \leq x \leq 0.12$) and garnet- $\text{Li}_{6.75}\text{Ga}_{0.25}\text{La}_3\text{Zr}_2\text{O}_{12}$ with cathode materials of LiFePO_4 (LFP) and $\text{LiNi}_{1/3}\text{Mn}_{1/3}\text{Co}_{1/3}\text{O}_2$ (NMC111) with Li metal anode. In addition, Importantly, electrochemical analyses were investigated to deeper understanding of the electrolyte/electrode interface inside the battery, and the composite electrolyte is capable of suppressing Li dendrite growth effectively, as evidenced by the prolonged stable cycling of the Li/Li symmetric cell. Therefore, the full cell exhibits superior rate performance and long cyclic life. These attractive properties give composite polymer electrolytes the potential to boost the practical application of safe and long-life Li metal batteries.

All-solid-state and semi-solid-state perovskite- $\text{Li}_{0.5-x}\text{La}_{0.5-x}\text{Sr}_x\text{Ti}_{1-x}\text{Ta}_x\text{O}_3$ ($0 \leq x \leq 0.12$)

$\text{Li}_{0.5}\text{La}_{0.5}\text{TiO}_3$ cubic perovskites co-substituted with Sr and Ta with similar doping contents ($x = 0 - 0.12$) were successfully synthesized using a solid-state reaction. All samples exhibited a cubic structure with the space group $Pm\bar{3}m$ and an increasing lattice parameter in the substituted samples. This suggests enhancement of the A site as a bottleneck for Li^+ migration. Furthermore, the average bond length of the B site was enhanced by the partial substitution with Sr^{2+} and Ta^{5+} which increased the highest grain conductivity at $x = 0.03$. However, the grain boundary conductivity,

which mainly contributes to the total conductivity, increased with increasing Sr^{2+} and Ta^{5+} contents, reaching a maximum at $x = 0.09$. The $\text{LLSr}_{0.09}\text{TTa}_{0.09}\text{O}_3$ sample achieved the highest total ionic conductivity at approximately $4.12 \times 10^{-5} \text{ S}\cdot\text{cm}^{-1}$ at 298 K, with the lowest activation energy at 0.47 eV. Moreover, $\text{LLSr}_{0.09}\text{TTa}_{0.09}\text{O}_3$ exhibited good separation properties with extremely low electronic conductivity of $1.66 \times 10^{-9} \text{ S}\cdot\text{cm}^{-1}$. A practical solution was adopted using perovskite $\text{LLSr}_{0.09}\text{TTa}_{0.09}\text{O}_3$ with full $\text{LiFePO}_4/\text{Li}$ cells, in which 10 wt.% polymer electrolyte was mixed to prevent the detrimental effects of Ti^{4+} decomposition to Ti^{3+} , which could lead to short-circuiting of the battery cells. The assembled LFP/CPE-10/Li full battery exhibited a specific discharge capacity of $156 \text{ mAh}\cdot\text{g}^{-1}$ at 0.1C rate and 1C charge-discharge capacity retention rate of 86% after 290 cycles at RT.

Quasi-solid-state batteries with garnet- $\text{Li}_{6.25}\text{Ga}_{0.25}\text{La}_3\text{Zr}_2\text{O}_{12}$ composite polymer electrolytes

In this study, we developed a composite solid electrolyte with decreasing crystallinity, uniform phase distribution, simple process, and excellent performance by using the polymer electrolyte PVDF-HFP as the matrix, lithium bis (trifluoromethyl sulfonyl) imide as the Li salt, and $\text{Li}_{6.25}\text{Ga}_{0.25}\text{La}_3\text{Zr}_2\text{O}_{12}$ as the active filler. Following a comprehensive exploration, we identified the optimal composition of the CSEs as 54% PVDF-HFP, 36% LiTFSI, and 10% LLZO-Ga by weight fraction. The resulting CPEs-10 exhibit an ionic conductivity of up to $7.12 \times 10^{-4} \text{ S}\cdot\text{cm}^{-1}$ at room temperature, with an electrochemical stability window extending to 4.9 V. The Li/CPEs-10/Li symmetric cell, utilizing a concentrated electrolyte (4MLiFSI: DEE), demonstrates stable current density over more than 600 hours of continuous cycling at $0.1 \text{ mA}\cdot\text{cm}^{-2}$, displaying a flat voltage plateau and low overpotential. Additionally, the QCPEs-10, employing LFP and NMC111 cathodes, exhibit discharge capacities of 108.7 mAh g^{-1} and 115.6 mAh g^{-1} at 1C, respectively. Furthermore, the CSEs have demonstrated suitability for use in quasi-solid-state lithium batteries (QSSLBs) operating in high-voltage environments. Therefore, it is anticipated that the high-performance PVDF-HFP-based CPEs, boasting excellent interfacial compatibility,

represent one of the most promising prototypes for room-temperature quasi-solid-state lithium metal batteries.

SUGGESTIONS

In practical applications, batteries often encounter various forms of abuse. Commercial Li-ion batteries must undergo several safety tests before they can be used, including overcharging, crushing impact, short-circuiting, and nail penetration. These batteries must not ignite or explode under these severe conditions. However, such rigorous testing is largely absent for solid-state full batteries. The performance of batteries during crushing and impact tests is largely determined by the mechanical stability of the inorganic solid electrolyte (ISE). Fractures in the ISE can lead to internal short circuits, potentially generating significant heat and causing fires or explosions. Enhancing the elasticity of ISEs can improve safety and combining an ISE with a flexible solid polymer electrolyte (SPEs) can provide good elasticity, ensuring that the composite polymer electrolytes (CPEs) remain intact under crushing or impact. Moreover, batteries often experience high temperatures during overcharge, short-circuit, nail penetration, and hotplate tests. Therefore, high thermal stability in the SE is crucial for maintaining battery safety. Furthermore, the discussed perovskite-LLTO, and garnet-LLZO solid electrolytes, other materials such as NASICON, LISICON, and sulfide also exhibit reduction decomposition at the Li anode, incompatibility with the cathode, and dendrite growth. Future research should focus on improving ionic conductivity, electrochemical and chemical stability, the discharge-charge performance of full solid-state batteries, and, most importantly, the mechanical and thermal stability to design highly safe full-solid-state batteries.

REFERENCES

มหาวิทยาลัยราชภัฏสุราษฎร์ธานี

REFERENCES

- Aguesse, F., Mandalastas, W., Buannic, L., Lopez del Amo, J. M., Singh, G., Llordés, A., & Kilner, J. (2017). Investigating the dendritic growth during full cell cycling of garnet electrolyte in direct contact with Li metal. *ACS applied materials & interfaces*, *9*(4), 3808–3816.
- Ahn, C. W., Choi, J. J., Ryu, J., Hahn, B. D., Kim, J. W., Yoon, W. H., Choi, J. H., Lee, J. S. & Park, D. S. (2014). Electrochemical properties of $\text{Li}_7\text{La}_3\text{Zr}_2\text{O}_{12}$ -based solid state battery. *Journal of Power Sources*, *272*, 554–558.
- Allen, J. L., Wolfenstine, J., Rangasamy, E., & Sakamoto, J. (2012). Effect of substitution (Ta, Al, Ga) on the conductivity of $\text{Li}_7\text{La}_3\text{Zr}_2\text{O}_{12}$. *Journal of Power Sources*, *206*, 315–319.
- Armand, M., & Tarascon, J. M. (2008). Building better batteries. *nature*, *451*(7179), 652–657.
- Aryanfar, A., Brooks, D., Merinov, B. V., Goddard III, W. A., Colussi, A. J., & Hoffmann, M. R. (2014). Dynamics of lithium dendrite growth and inhibition: pulse charging experiments and Monte Carlo calculations. *The journal of physical chemistry letters*, *5*(10), 1721–1726.
- Ashuri, M., He, Q., & Shaw, L. L. (2016). Silicon as a potential anode material for Li-ion batteries: where size, geometry, and structure matter. *Nanoscale*, *8*(1), 74–103.
- Avila, V., Yoon, B., Neto, R. R. I., Silva, R. S., Ghose, S., Raj, R., & Jesus, L. M. (2020). Reactive flash sintering of the complex oxide $\text{Li}_{0.5}\text{La}_{0.5}\text{TiO}_3$ starting from an amorphous precursor powder. *Scripta Materialia*, *176*, 78–82.
- Awaka, J., Kijima, N., Hayakawa, H., & Akimoto, J. (2009). Synthesis and structure analysis of tetragonal $\text{Li}_7\text{La}_3\text{Zr}_2\text{O}_{12}$ with the garnet-related type structure. *Journal of solid state chemistry*, *182*(8), 2046–2052.
- Bard, A. J., Faulkner, L. R., & White, H. S. (2022). *Electrochemical methods: fundamentals and applications*. NJ: John Wiley & Sons.

- Bates, J. B., Dudney, N. J., Gruzalski, G. R., Zuhr, R. A., Choudhury, A., Luck, C. F. & Robertson, J. D. (1993). Fabrication and characterization of amorphous lithium electrolyte thin films and rechargeable thin-film batteries. *Journal of Power Sources*, *43*, 103–110.
- Bednorz, J. G., & Müller, K. A. (1986). Possible high T_c superconductivity in the Ba–La–Cu–O system. *Zeitschrift für Physik B Condensed Matter*, *64*(2), 189–193.
- Bruce, P. G., & Vincent, C. A. (1987). Steady state current flow in solid binary electrolyte cells. *Journal of electroanalytical chemistry and interfacial electrochemistry*, *225*(1–2), 1–17.
- Cao, S., Chen, F., Shen, Q., & Zhang, L. (2023). Dual-coordination-induced poly(vinylidene fluoride)/Li₆ 4GaO₃ 2La₃Zr₂O₁₂/succinonitrile composite solid electrolytes toward enhanced rate performance in all-solid-state lithium batteries. *ACS Applied Materials & Interfaces*, *15*(31), 37422–37432.
- Castillo, J., Santiago, A., Judez, X., Garbayo, I., Coca Clemente, J. A., Morant-Miñana, M. C., ... & Li, C. (2021). Safe, flexible, and high-performing gel-polymer electrolyte for rechargeable lithium metal batteries. *Chemistry of Materials*, *33*(22), 8812–8821.
- Catti, M. (2007). First-Principles Modeling of Lithium Ordering in the LLTO (Li_xLa_{2/3-x/3}TiO₃) Superionic Conductor. *Chemistry of materials*, *19*(16), 3963–3972.
- Catti, M., Sommariva, M., & Ibberson, R. M. (2007). Tetragonal superstructure and thermal history of Li_{0.3}La_{0.567}TiO₃ (LLTO) solid electrolyte by neutron diffraction. *Journal of Materials Chemistry*, *17*(13), 1300–1307.
- Chen, K., Huang, M., Shen, Y., Lin, Y., & Nan, C. W. (2012). Enhancing ionic conductivity of Li_{0.35}La_{0.55}TiO₃ ceramics by introducing Li₇La₃Zr₂O₁₂. *Electrochimica Acta*, *80*, 133–139.

- Chouiekh, A., Tahiri, A., Bouftila, N. E. H., Nfissi, A., Bih, L., Faik, A., ... & Naji, M. (2023). Experimental and DFT analysis of structural, optical, and electrical properties of $\text{Li}_{3x}\text{La}_{2/3-x}\text{TiO}_3$ ($3x= 0.1, 0.3$ and 0.5) solid electrolyte. *Ceramics International*, *49*(15), 25920–25934.
- Chung, H. T., Kim, J. G., & Kim, H. G. (1998). Dependence of the lithium ionic conductivity on the B-site ion substitution in $(\text{Li}_{0.5}\text{La}_{0.5})\text{Ti}_{1-x}\text{M}_x\text{O}_3$ ($M = \text{Sn}, \text{Zr}, \text{Mn}, \text{Ge}$). *Solid State Ionics*, *107*(1–2), 153–160.
- Croce, F., Appetecchi, G. B., Persi, L., & Scrosati, B. (1998). Nanocomposite polymer electrolytes for lithium batteries. *Nature*, *394*(6692), 456–458.
- Cussen, E. J. (2010). Structure and ionic conductivity in lithium garnets. *Journal of Materials Chemistry*, *20*(25), 5167–5173.
- Deng, Y., Eames, C., Fleutot, B., David, R., Chotard, J. N., Suard, E., Masquelier, C. & Islam, M. S. (2017). Enhancing the Lithium Ion Conductivity in Lithium Superionic Conductor (LISICON) Solid Electrolytes through a Mixed Polyanion Effect. *ACS Applied Materials and Interfaces*, *9*(8), 7050–7058.
- Deng, Y., Shang, S. J., Mei, A., Lin, Y. H., Liu, L. Y., & Nan, C. W. (2009). The preparation and conductivity properties of $\text{Li}_{0.5}\text{La}_{0.5}\text{TiO}_3$ /inactive second phase composites. *Journal of alloys and compounds*, *472*(1–2), 456–460.
- Du Pasquier, A., Plitz, I., Menocal, S., & Amatucci, G. (2003). A comparative study of Li-ion battery, supercapacitor and nonaqueous asymmetric hybrid devices for automotive applications. *Journal of power sources*, *115*(1), 171–178.
- Du, S. Y., Ren, G. X., Zhang, N., & Liu, X. S. (2022). High-performance poly(vinylidene fluoride-hexafluoropropylene)-Based composite electrolytes with excellent interfacial compatibility for room-temperature all-solid-state lithium metal batteries. *ACS omega*, *7*(23), 19631–19639.
- Evans, J., Vincent, C. A., & Bruce, P. G. (1987). Electrochemical measurement of transference numbers in polymer electrolytes. *Polymer*, *28*(13), 2324–2328.

- Feng, J., Yan, B., Lai, M. O., & Li, L. (2014). Design and Fabrication of an All-Solid-State Thin-Film Li-Ion Micro battery with Amorphous TiO_2 as the Anode. *Energy Technology*, *2*(4), 397–400.
- Feng, Y., Wang, M., Gao, L., He, Z., Chen, K., Li, Z., ... & Lin, Y. (2022). Novel Fast Ionic Conductor Ceramic Composite Separator for High-performance Safe Li-Ion Power Batteries. *Journal of Materiomics*, *8*(6), 1184–1190.
- Fenton, D. (1973). Complex of alkali metal ions with poly (ethylene oxide). *polymer*, *14*, 589.
- Fu, J. (1997). Fast Li^+ ion conducting glass-ceramics in the system $\text{Li}_2\text{OAl}_2\text{O}_3\text{GeO}_2\text{P}_2\text{O}_5$. *Solid State Ionics*, *104*(3–4), 191–194.
- Gao, C., Li, X., Wei, G., Wang, S., Zhao, X., & Kong, F. (2023). Flexible PVDF-HFP based hybrid composite solid electrolyte membrane co-filled with hydroxypropyl methyl cellulose and $\text{Li}_{6.4}\text{La}_3\text{Zr}_{1.4}\text{Ta}_{0.6}\text{O}_{12}$ for high-performance solid-state lithium batteries. *Industrial Crops and Products*, *195*, 116426.
- Goodenough, J. B., & Kim, Y. (2010). Challenges for rechargeable Li batteries. *Chemistry of materials*, *22*(3), 587–603.
- Goriparti, S., Miele, E., De Angelis, F., Di Fabrizio, E., Zaccaria, R. P., & Capiglia, C. (2014). Review on recent progress of nanostructured anode materials for Li-ion batteries. *Journal of power sources*, *257*, 421–443.
- Gu, R., Kang, J., Guo, X., Li, J., Yu, K., Ma, R., ... & Wei, X. (2022). Microstructure and ionic conductivity of $\text{Li}_{0.5-x}\text{La}_{0.5}(\text{Ti}_{1-x}\text{Nb}_x)\text{O}_3$ solid-state electrolytes. *Journal of Alloys and Compounds*, *896*, 163084.
- Harada, Y., Hirakoso, Y., Kawai, H., & Kuwano, J. (1999). Order-disorder of the A-site ions and lithium-ion conductivity in the perovskite solid solution $\text{La}_{0.67-x}\text{Li}_{3x}\text{TiO}_3$ ($x=0.11$). *Solid State Ionics*, *121*(1–4), 245–251.
- He, L. X., & Yoo, H. I. (2003). Effects of B-site ion (M) substitution on the ionic conductivity of $(\text{Li}_{3x}\text{La}_{2/3-x})_{1+y/2}(\text{M}_y\text{Ti}_{1-y})\text{O}_3$ (M= Al, Cr). *Electrochimica acta*, *48*(10), 1357–1366.

- He, W., Ding, H., Chen, X., & Yang, W. (2023). Three-dimensional LLZO/PVDF-HFP fiber network-enhanced ultrathin composite solid electrolyte membrane for dendrite-free solid-state lithium metal batteries. *Journal of Membrane Science*, *665*, 121095.
- He, X., Li, S., Cao, G., Hu, J., Zhang, J., Qiao, R., ... & Shao, G. (2020). In situ atomic-scale engineering of the chemistry and structure of the grain boundaries region of $\text{Li}_{3x}\text{La}_{2/3-x}\text{TiO}_3$. *Scripta Materialia*, *185*, 134–139.
- Hong, H. Y. P. (1978). Crystal structure and ionic conductivity of $\text{Li}_{14}\text{Zn}(\text{GeO}_4)_4$ and other new Li^+ superionic conductors. *Materials Research Bulletin*, *13*, 117–124.
- Hu, Z., Sheng, J., Chen, J., Sheng, G., Li, Y., Fu, X. Z., ... & Wong, C. P. (2018). Enhanced Li ion conductivity in Ge-doped $\text{Li}_{0.33}\text{La}_{0.56}\text{TiO}_3$ perovskite solid electrolytes for all-solid-state Li-ion batteries. *New Journal of Chemistry*, *42*(11), 9074–9079.
- Huang, B., Xu, B., Li, Y., Zhou, W., You, Y., Zhong, S., ... & Goodenough, J. B. (2016). Li-ion conduction and stability of perovskite $\text{Li}_{3/8}\text{Sr}_{7/16}\text{Hf}_{1/4}\text{Ta}_{3/4}\text{O}_3$. *ACS applied materials & interfaces*, *8*(23), 14552–14557.
- Huggins, R. A. (1999). Lithium alloy negative electrodes. *Journal of Power Sources*, *81*, 13–19.
- Inaguma, Y., Liqun, C., Itoh, M., Nakamura, T., Uchida, T., Ikuta, H., & Wakihara, M. (1993). High ionic conductivity in lithium lanthanum titanate. *Solid State Communications*, *86*(10), 689–693.
- Itoh, M., Inaguma, Y., Jung, W. H., Chen, L., & Nakamura, T. (1994). High lithium ion conductivity in the perovskite-type compounds $\text{Ln}_{12}\text{Li}_{12}\text{TiO}_3$ (Ln= La, Pr, Nd, Sm). *Solid State Ionics*, *70*, 203–207.
- J. Gnanaraj, E. Zinigrad, L. Asraf, H. Gottlieb, M. Sprecher, M. Schmidt, W. Geissler, D. Aurbach, J. Electrochem. Soc, *150*(2003), A1533–A1537.
- J. Ying & McGinn, P. J. (2013). $\text{Li}_7\text{La}_3\text{Zr}_2\text{O}_{12}$ electrolyte stability in air and fabrication of a $\text{Li}/\text{Li}_7\text{La}_3\text{Zr}_2\text{O}_{12}/\text{Cu}_{0.1}\text{V}_2\text{O}_5$ solid-state battery. *Journal of Power Sources*, *239*, 326–331.

- Jiang, Y., Huang, Y., Hu, Z., Zhou, Y., Zhu, J., & Zhu, X. (2020). Effects of B-site ion (Nb^{5+}) substitution on the microstructure and ionic conductivity of $\text{Li}_{0.5}\text{La}_{0.5}\text{TiO}_3$ solid electrolytes. *Ferroelectrics*, *554*(1), 89–96.
- Jonderian, A., Ting, M., & McCalla, E. (2021). Metastability in Li–La–Ti–O perovskite materials and its impact on ionic conductivity. *Chemistry of Materials*, *33*(12), 4792–4804.
- Kalita, D. J., Lee, S. H., Lee, K. S., Ko, D. H., & Yoon, Y. S. (2012). Ionic conductivity properties of amorphous Li–La–Zr–O solid electrolyte for thin film batteries. *Solid State Ionics*, *229*, 14–19.
- Kamaya, N., Homma, K., Yamakawa, Y., Hirayama, M., Kanno, R., Yonemura, M., Kamiyama, T., Kato, Y., Hama, S., Kawamoto, K. & Mitsui, A. (2011). A lithium superionic conductor. *Nature Materials*, *10*, 682–686.
- Kato, Y., Hori, S., Saito, T., Suzuki, K., Hirayama, M., Mitsui, A., Yonemura, M., Iba, H. & Kanno, R. (2016). High-power all-solid-state batteries using sulfide superionic conductors. *Nature Energy*, *1*, 1–7.
- Kim, J. G., Son, B., Mukherjee, S., Schuppert, N., Bates, A., Kwon, O., ... & Park, S. (2015). A review of lithium and non-lithium based solid state batteries. *Journal of Power Sources*, *282*, 299–322.
- Kim, Y., Yoo, A., Schmidt, R., Sharafi, A., Lee, H., Wolfenstine, J., & Sakamoto, J. (2016). Electrochemical stability of $\text{Li}_{6.5}\text{La}_3\text{Zr}_{1.5}\text{M}_{0.5}\text{O}_{12}$ (M= Nb or Ta) against metallic lithium. *Frontiers in Energy Research*, *4*, 20.
- Kong, Y., Li, Y., Li, J., Hu, C., Wang, X., & Lu, J. (2018). Li ion conduction of perovskite $\text{Li}_{0.375}\text{Sr}_{0.4375}\text{Ti}_{0.25}\text{Ta}_{0.75}\text{O}_3$ and related compounds. *Ceramics International*, *44*(4), 3947–3950.
- Kraytsberg, A., & Ein-Eli, Y. (2012). Higher, Stronger, Better... A Review of 5 Volt Cathode Materials for Advanced Lithium-Ion Batteries. *Advanced Energy Materials*, *2*(8), 922–939.

- Kuwano, J., & West, A. R. (1980). Permanent address: Science University of Tokyo, Department of Industrial Chemistry, Shinjuku-ku, Tokyo, Japan. 1661. *MRS Bull.*, *15*, 1661–1667.
- Kuwata, N., Kawamura, J., Toribami, K., Hattori, T., & Sata, N. (2004). Thin-film lithium-ion battery with amorphous solid electrolyte fabricated by pulsed laser deposition. *Electrochemistry Communications*, *6*(4), 417–421.
- Kwon, W. J., Kim, H., Jung, K. N., Cho, W., Kim, S. H., Lee, J. W., & Park, M. S. (2017). Enhanced Li⁺ conduction in perovskite $\text{Li}_{3x}\text{La}_{2/3-x}\text{□}_{1/3-2x}\text{TiO}_3$ solid-electrolytes via microstructural engineering. *Journal of Materials Chemistry A*, *5*(13), 6257–6262.
- Kwon, W. J., Kim, H., Jung, K. N., Cho, W., Kim, S. H., Lee, J. W., & Park, M. S. (2017). Enhanced Li⁺ conduction in perovskite $\text{Li}_x\text{La}_{2/3-x}\text{□}_{1/3-2x}\text{TiO}_3$ solid-electrolytes via microstructural engineering. *Journal of Materials Chemistry A*, *5*(13), 6257–6262.
- Lakshmi, D., Nalini, B., Jayapandi, S., & Selvin, P. C. (2020). Augmented conductivity in $\text{Li}_{3x}\text{La}_{2/3-x}\text{TiO}_3$ nanoparticles: All-solid-state Li-ion battery applications. *Journal of Materials Science: Materials in Electronics*, *31*(2), 1343–1354.
- Langer, F., Bardenhagen, I., Glenneberg, J., & Kun, R. (2016). Microstructure and temperature dependent lithium ion transport of ceramic-polymer composite electrolyte for solid-state lithium ion batteries based on garnet-type $\text{Li}_7\text{La}_3\text{Zr}_2\text{O}_{12}$. *Solid State Ionics*, *291*, 8–13.
- Li, L., Qu, W., Zhang, X., Lu, J., Chen, R., Wu, F., & Amine, K. (2015). Succinic acid-based leaching system: a sustainable process for recovery of valuable metals from spent Li-ion batteries. *Journal of Power Sources*, *282*, 544–551.
- Li, R., Liao, K., Zhou, W., Li, X., Meng, D., Cai, R., & Shao, Z. (2019). Realizing fourfold enhancement in conductivity of perovskite $\text{Li}_{0.33}\text{La}_{0.557}\text{TiO}_3$ electrolyte membrane via a Sr and Ta co-doping strategy. *Journal of Membrane Science*, *582*, 194–202.
- Li, Y., Han, J. T., Wang, C. A., Xie, H., & Goodenough, J. B. (2012). Optimizing Li⁺ conductivity in a garnet framework. *Journal of Materials Chemistry*, *22*(30), 15357–15361.

- Ling, M. E., Jiang, Y., Huang, Y., Zhou, Y., & Zhu, X. (2020). Enhancement of ionic conductivity in $\text{Li}_{0.5}\text{La}_{0.5}\text{TiO}_3$ with Ag nanoparticles. *Journal of Materials Science*, 55(9), 3750–3759.
- Ling, M. E., Zhu, X., Jiang, Y., & Zhu, J. (2016). Comparative study of solid-state reaction and sol-gel process for synthesis of Zr-doped $\text{Li}_{0.5}\text{La}_{0.5}\text{TiO}_3$ solid electrolytes. *Ionics*, 22, 2151–2156.
- Liu, C., Neale, Z. G., & Cao, G. (2016). Understanding electrochemical potentials of cathode materials in rechargeable batteries. *Materials Today*, 19(2), 109–123.
- Liu, Y., Lee, J. Y., & Hong, L. (2004). In situ preparation of poly (ethylene oxide)- SiO_2 composite polymer electrolytes. *Journal of Power Sources*, 129(2), 303–311.
- Liu, Z., Fu, w., Payzant, E. A., Yu, X., Wu, Z., Dudney, N. J., Kiggans, J., Hong, K., Rondinone, A. J. & Liang, C. (2013). Anomalous high ionic conductivity of nanoporous β - Li_3PS_4 . *Journal of the American Chemical Society*, 135(3), 975–978.
- Long, L., Wang, S., Xiao, M., & Meng, Y. (2016). Polymer electrolytes for lithium polymer batteries. *Journal of Materials Chemistry A*, 4(26), 10038–10069.
- Lu, J., Chen, Z., Pan, F., Cui, Y., & Amine, K. (2018). High-performance anode materials for rechargeable lithium-ion batteries. *Electrochemical Energy Reviews*, 1, 35–53.
- Lu, J., Li, Y., & Ding, Y. (2020). Structure, stability, and ionic conductivity of perovskite $\text{Li}_{2x-y}\text{Sr}_{1-x-y}\text{La}_y\text{TiO}_3$ solid electrolytes. *Ceramics International*, 46(6), 7741–7747.
- Lu, X., Duan, M., Xiang, J., Liang, Y., & Liu, S. (2022). Enhancement of ionic conductivity and fracture toughness by infiltrating porous $\text{Li}_{0.33}\text{La}_{0.56}\text{TiO}_3$ pellets. *Journal of Rare Earths*, 42(2), 392–398.
- Mauro, V., D'Aprano, A., Croce, F., & Salomon, M. (2005). Direct determination of transference numbers of LiClO_4 solutions in propylene carbonate and acetonitrile. *Journal of power sources*, 141(1), 167–170.
- Meyer, W. H. (1998). *Advanced Materials Adv. Mater*, 10, 439.

- Minami, K., Hayashi, A., & Tatsumisago, M. (2010). Preparation and characterization of lithium ion conducting $\text{Li}_2\text{S}-\text{P}_2\text{S}_5-\text{GeS}_2$ glasses and glass-ceramics. *Journal of Non-Crystalline Solids*, *356*(44–49), 2666–2669.
- Mizushima, K. J. P. C., Jones, P. C., Wiseman, P. J., & Goodenough, J. B. (1980). Li_xCoO_2 ($0 < x < 1$): A new cathode material for batteries of high energy density. *Materials Research Bulletin*, *15*(6), 783–789.
- Morata-Orrantia, A., García-Martín, S., & Alario-Franco, M. A. (2003). Optimization of lithium conductivity in La/Li titanates. *Chemistry of materials*, *15*(21), 3991–3995.
- Morata-Orrantia, A., García-Martín, S., & Alario-Franco, M. A. (2003). Optimization of Lithium Conductivity in La/Li Titanates. *Chemistry of Materials*, *15*(21), 3991–3995.
- Murugan, R., Thangadurai, V., & Weppner, W. (2007). Fast lithium ion conduction in garnet-type $\text{Li}_7\text{La}_3\text{Zr}_2\text{O}_{12}$. *ANGEWANDTE CHEMIE-INTERNATIONAL EDITION IN ENGLISH-*, *46*(41), 7778.
- Nayak, P. K., Erickson, E. M., Schipper, F., Penki, T. R., Munichandraiah, N., Adelhelm, P., ... & Aurbach, D. (2018). Review on challenges and recent advances in the electrochemical performance of high capacity Li- and Mn-rich cathode materials for Li-ion batteries. *Advanced Energy Materials*, *8*(8), 1702397.
- O'Callaghan, M. P., Lynham, D. R., Cussen, E. J., & Chen, G. Z. (2006). Structure and ionic-transport properties of lithium-containing garnets $\text{Li}_3\text{Ln}_3\text{Te}_2\text{O}_{12}$ (Ln = Y, Pr, Nd, Sm–Lu). *Chemistry of materials*, *18*(19), 4681–4689.
- Osman, Z., Ghazali, M. M., Othman, L., & Isa, K. M. (2012). AC ionic conductivity and DC polarization method of lithium ion transport in PMMA– LiBF_4 gel polymer electrolytes. *Results in physics*, *2*, 1–4.
- Park, M., Jung, H. G., Jung, W. D., Cho, S. Y., Yun, B. N., Lee, Y. S., Chol, S., Ahn, J., Lim, J., Sung, J. Y., Jang, Y. J., Ahn, J. P., Lee, J. H. and Kim, H. (2017). Chemically Evolved Composite Lithium-Ion Conductors with Lithium Thiophosphates and Nickel Sulfides. *ACS Energy Letters*, *2*(8), 1740–1745.

- Pham, T. D., & Lee, K. K. (2021). Simultaneous stabilization of the solid/cathode electrolyte interface in lithium metal batteries by a new weakly solvating electrolyte. *Small*, *17*(20), 2100133.
- Pham, T. D., Bin Faheem, A., Kim, J., Oh, H. M., & Lee, K. K. (2022). Practical High-Voltage Lithium Metal Batteries Enabled by Tuning the Solvation Structure in Weakly Solvating Electrolyte. *Small*, *18*(14), 2107492.
- Poizot, P. L. S. G., Laruelle, S., Grugeon, S., Dupont, L., & Tarascon, J. M. (2000). Nano-sized transition-metal oxides as negative-electrode materials for lithium-ion batteries. *Nature*, *407*(6803), 496–499.
- Park, C. M., Kim, J. H., Kim, H., & Sohn, H. J. (2010). Li-alloy based anode materials for Li secondary batteries. *Chemical Society Reviews*, *39*(8), 3115–3141.
- Q. Li, J. Chen, L. Fan, X. Kong, Y. Lu, (2016). Progress in electrolytes for rechargeable Li-based batteries and beyond. *Green Energy Environ*, *1*(1), 18–42.
- Quartarone, E., & Mustarelli, P. (2011). Electrolytes for solid-state lithium rechargeable batteries: recent advances and perspectives. *Chem Soc Rev*, *40*, 2525–2540.
- Ratner, M.A., Johansson, P., and Shriver, D.F. (2000). Polymer electrolytes: ionic transport mechanisms and relaxation coupling. *MRS Bull*, *25*, 31–37.
- Reinacher, J., Berendts, S., & Janek, J. (2014). Preparation and electrical properties of garnet-type $\text{Li}_6\text{BaLa}_2\text{Ta}_2\text{O}_{12}$ lithium solid electrolyte thin films prepared by pulsed laser deposition. *Solid State Ionics*, *258*, 1–7.
- Roth, E. P., & Orendorff, C. J. (2012). How electrolytes influence battery safety. *The Electrochemical Society Interface*, *21*(2), 45.
- S. S. Cavalcante, V. S. Marques, J. C. Sczancoski, M. T. Escote, M. R. Joya, J. A. Varela, R. M. C. Santos, P. S. Pizani y E. Longo, (2008). *Chemical Engineering Journal*, *143*, 299–307.
- Scrosati, B., Hassoun, J., & Sun, Y. K. (2011). Lithium-ion batteries. A look into the future. *Energy & Environmental Science*, *4*(9), 3287–3295.

- Silva, J. H. L., Alves, Y. G. S., Almeida, A., Moreira, J. A., Vilarinho, R., Santos, J. C. A., ... & Silva, R. S. (2020). Study of the ionic conductivity of $\text{Li}_{0.5}\text{La}_{0.5}\text{TiO}_3$ laser-sintered ceramics. *Journal of the European Ceramic Society*, *40*(15), 5619–5625.
- Song, S., Lu, J., Zheng, F., Duong, H. M., and Lu, L. (2015). A facile strategy to achieve high conduction and excellent chemical stability of lithium solid electrolytes. *RSC Advances*, *5*(9), 6588–6594.
- Song, X., Zhang, T., Huang, S., Mi, J., Zhang, Y., Travas-Sejdic, J., ... & Cao, P. (2023). Constructing a PVDF-based composite solid-state electrolyte with high ionic conductivity $\text{Li}_{6.5}\text{La}_3\text{Zr}_{1.5}\text{Ta}_{0.1}\text{Nb}_{0.4}\text{O}_{12}$ for lithium metal battery. *Journal of Power Sources*, *564*, 232849.
- Sun, C., Liu, J., Gong, Y., Wilkinson, D. P., and Zhang, J. (2017). Recent advances in all-solid-state rechargeable lithium batteries. *Nano Energy*, *33*, 363–386.
- Sun, L. L., Li, Y. F., Li, G., Wang, L. G., & Tong, Y. Y. (2019). Perovskite-type compounds in anion-substituted $\text{LiSr}_{1-0.5x}\text{TiTaO}_{6-x}\text{F}_x$ electrolyte for improving lithium-ion conduction. *Ceramics International*, *45*(2), 2381–2384.
- Takamura, T., Endo, K., Fu, L., Wu, Y., Lee, K. J., & Matsumoto, T. (2007). Identification of nano-sized holes by TEM in the graphene layer of graphite and the high rate discharge capability of Li-ion battery anodes. *Electrochimica Acta*, *53*(3), 1055–1061.
- Tan, J., & Tiwari, A. (2012). Fabrication and characterization of $\text{Li}_7\text{La}_3\text{Zr}_2\text{O}_{12}$ thin films for lithium ion battery. *ECS Solid State Letters*, *1*(6), Q57.
- Tarascon, J. M., & Armand, M. (2001). Issues and challenges facing rechargeable lithium batteries. *nature*, *414*(6861), 359–367.
- Teranishi, T., Kouchi, A., Hayashi, H., & Kishimoto, A. (2014). Dependence of the conductivity of polycrystalline $\text{Li}_{0.33}\text{Ba}_x\text{La}_{0.56-2/3x}\text{TiO}_3$ on Ba loading. *Solid State Ionics*, *263*, 33–38.
- Thangadurai, V., & Weppner, W. (2005). $\text{Li}_6\text{A}\text{La}_2\text{Ta}_2\text{O}_{12}$ (A= Sr, Ba): novel garnet-like oxides for fast lithium ion conduction. *Advanced Functional Materials*, *15*(1), 107–112.

- Thangadurai, V., and Weppner, W. (2006). Effect of sintering on the ionic conductivity of garnet-related structure $\text{Li}_5\text{La}_3\text{Nb}_2\text{O}_{12}$ and In- and K-doped $\text{Li}_5\text{La}_3\text{Nb}_2\text{O}_{12}$. *Journal of Solid-State Chemistry*, 179(4), 974–984.
- Thangadurai, V., Kaack, H., & Weppner, W. J. (2003). Novel fast lithium ion conduction in garnet-type $\text{Li}_5\text{La}_3\text{M}_2\text{O}_{12}$ (M= Nb, Ta). *Journal of the American Ceramic Society*, 86(3), 437–440.
- Thangadurai, V., Narayanan, S., & Pinzaru, D. (2014). Garnet-type solid-state fast Li ion conductors for Li batteries: critical review. *Chemical Society Reviews*, 43(13), 4714–4727.
- Thangadurai, V., Narayanan, S., & Pinzaru, D. (2014). Garnet-type solid-state fast Li ion conductors for Li batteries: critical review. *Chemical Society Reviews*, 43(13), 4714–4727.
- Tian, H. K., Xu, B., & Qi, Y. (2018). Computational study of lithium nucleation tendency in $\text{Li}_7\text{La}_3\text{Zr}_2\text{O}_{12}$ (LLZO) and rational design of interlayer materials to prevent lithium dendrites. *Journal of Power Sources*, 392, 79–86.
- Ue, M. (1994). Mobility and ionic association of lithium and quaternary ammonium salts in propylene carbonate and γ -butyrolactone. *Journal of the electrochemical society*, 141(12), 3336.
- Ueda, A., & Ohzuku, T. (1994). Solid-State Redox Reactions of $\text{LiNi}_{1/2}\text{Co}_{1/2}\text{O}_2$ ($R\bar{3}m$) for 4 Volt Secondary Lithium Cells. *Journal of the Electrochemical Society*, 141(8), 2010.
- Ujiie, S., Hayashi, A., and Tatsumisago, M. (2013). Preparation and ionic conductivity of $(100-x)(0.8\text{Li}_2\text{S}\cdot 0.2\text{P}_2\text{S}_5)\cdot x\text{LiI}$ glass-ceramic electrolytes. *Journal of Solid State Electrochemistry*, 17(3), 675–680.
- Ujiie, S., Hayashi, A., and Tatsumisago, M. (2014). Preparation and electrochemical characterization of $(100-x)(0.7\text{Li}_2\text{S}\cdot 0.3\text{P}_2\text{S}_5)\cdot x\text{LiBr}$ glass-ceramic electrolytes. *Materials for Renewable and Sustainable Energy*, 3(1), 1–8.
- V. M. Goldschmidt. (1926). Die Gesetze der Krystallochemie. *Naturwissenschaften*, 14, 477–485.

- Varez, A., Fernandez-Díaz, M. T., & Sanz, J. (2004). Rhombohedral-cubic transition in $\text{Li}_{0.2}\text{Na}_{0.3}\text{La}_{0.5}\text{TiO}_3$ perovskite. *Journal of Solid-State Chemistry*, *177*(12), 4665–4671.
- Vezzù, K., García-González, E., Pagot, G., Urones-Garrote, E., Sotomayor, M. E., Varez, A., & Di Noto, V. (2022). Effect of Relaxations on the Conductivity of $\text{La}_{1/2+1/2x}\text{Li}_{1/2-1/2x}\text{Ti}_{1-x}\text{Al}_x\text{O}_3$ Fast Ion Conductors. *Chemistry of Materials*, *34*(12), 5481–5499.
- Wang, C., Fu, K., Kammampata, S. P., McOwen, D. W., Samson, A. J., Zhang, L., ... & Hu, L. (2020). Garnet-type solid-state electrolytes: materials, interfaces, and batteries. *Chemical reviews*, *120*(10), 4257–4300.
- Wang, X., Zeng, W., Hong, L., Xu, W., Yang, H., Wang, F., ... & Jiang, H. (2018). Stress-driven lithium dendrite growth mechanism and dendrite mitigation by electroplating on soft substrates. *Nature Energy*, *3*(3), 227–235.
- Whittingham, M. S. (2004). Lithium batteries and cathode materials. *Chemical reviews*, *104*(10), 4271–4302.
- Wu, J., Chen, L., Song, T., Zou, Z., Gao, J., Zhang, W., & Shi, S. (2017). A review on structural characteristics, lithium ion diffusion behavior and temperature dependence of conductivity in perovskite-type solid electrolyte $\text{Li}_{3x}\text{La}_{2/3-x}\text{TiO}_3$. *Functional Materials Letters*, *10*(03), 1730002.
- Xie, H., Alonso, J. A., Li, Y., Fernandez-Díaz, M. T., & Goodenough, J. B. (2011). Lithium distribution in aluminum-free cubic $\text{Li}_7\text{La}_3\text{Zr}_2\text{O}_{12}$. *Chemistry of Materials*, *23*(16), 3587–3589.
- Xu, H., Wang, S., Wilson, H., Zhao, F., and Manthiram, A. (2017). Y-Doped NASICON-type $\text{LiZr}_2(\text{PO}_4)_3$ Solid Electrolytes for Lithium-Metal Batteries. *Chemistry of Materials*, *29*(17), 7206–7212.
- Xu, J., Lin, F., Doeff, M. M., & Tong, W. (2017). A review of Ni-based layered oxides for rechargeable Li-ion batteries. *Journal of Materials Chemistry A*, *5*(3), 874–901.

- Xu, L., Feng, T., Huang, J., Hu, Y., Zhang, L., & Luo, L. (2022). Structural Heterogeneity Induced Li Dendrite Growth in $\text{Li}_{0.33}\text{La}_{0.56}\text{TiO}_3$ Solid-State Electrolytes. *ACS Applied Energy Materials*, *5*(3), 3741–3747.
- Xu, R. C., Xia, X. H., Li, S. H., Zhang, S. Z., Wang, X. L., and Tu, J. P. (2017). All-solid-state lithium-sulfur batteries based on a newly designed $\text{Li}_7\text{P}_{2.9}\text{Mn}_{0.1}\text{S}_{10.7}\text{I}_{0.3}$ superionic conductor. *Journal of Materials Chemistry A*, *5*(13), 6310–6317.
- Y. Inaguma, C. Liqun, M. Itoh, T. Nakamura, T. Uchida, H. Ikuta y M. Wakihara, (1993). High ionic conductivity in lithium lanthanum titanate. *Solid State Communications*, *86*, 689–693.
- Yan, J., Yu, J., and Ding, B. (2018). Mixed ionic and electronic conductor for Li metal anode protection. *Adv. Mater.* *30*, 1705105. doi:10.1002/adma.201705105
- Yao, R., Liu, Z. G., Ding, Z. Y., Jin, Y. J., Cao, G., Wang, Y. H., & Ouyang, J. H. (2020). Effect of Sn or Ta doping on the microstructure and total conductivity of perovskite $\text{Li}_{0.24}\text{La}_{0.587}\text{TiO}_3$ solid electrolyte. *Journal of Alloys and Compounds*, *844*, 156023.
- Yao, R., Liu, Z. G., Ding, Z. Y., Jin, Y. J., Cao, G., Wang, Y. H., & Ouyang, J. H. (2020). Effect of Sn or Ta doping on the microstructure and total conductivity of perovskite $\text{Li}_{0.24}\text{La}_{0.587}\text{TiO}_3$ solid electrolyte. *Journal of Alloys and Compounds*, *844*, 156023.
- Yashima, M., Itoh, M., Inaguma, Y., & Morii, Y. (2005). Crystal structure and diffusion path in the fast lithium-ion conductor $\text{La}_{0.62}\text{Li}_{0.16}\text{TiO}_3$. *Journal of the American Chemical Society*, *127*(10), 3491–3495.
- Young, W. S., Kuan, W. F., & Epps III, T. H. (2014). Block copolymer electrolytes for rechargeable lithium batteries. *Journal of Polymer Science Part B: Polymer Physics*, *52*(1), 1–16.
- Yu, K., Gu, R., Wu, L., Sun, H., Ma, R., Jin, L., ... & Wei, X. (2018). Ionic and electronic conductivity of solid electrolyte $\text{Li}_{0.5}\text{La}_{0.5}\text{TiO}_3$ doped with $\text{LiO}_2\text{-SiO}_2\text{-B}_2\text{O}_3$ glass. *Journal of Alloys and Compounds*, *739*, 892–896.

- Yu, K., Jin, L., Li, Y., Liu, G., Wei, X., & Yan, Y. (2019). Structure and conductivity of perovskite $\text{Li}_{0.355}\text{La}_{0.35}\text{Sr}_{0.3}\text{Ti}_{0.995}\text{M}_{0.005}\text{O}_3$ (M= Al, Co and In) ceramics. *Ceramics International*, *45*(18), 23941–23947.
- Zhang, L., Zhang, X., Tian, G., Zhang, Q., Knapp, M., Ehrenberg, H., ... & Du, F. (2020). Lithium lanthanum titanate perovskite as an anode for lithium ion batteries. *Nature communications*, *11*(1), 3490.
- Zhang, S., Zhao, H., Guo, J., Du, Z., Wang, J., & Świerczek, K. (2019). Characterization of Sr-doped lithium lanthanum titanate with improved transport properties. *Solid State Ionics*, *336*, 39–46.
- Zhang, W. J. (2011). Structure and performance of LiFePO_4 cathode materials: A review. *Journal of Power Sources*, *196*(6), 2962–2970.
- Zhang, Y., Chen, K., Shen, Y., Lin, Y., and Nan, C. W. (2017). Synergistic effect of processing and composition x on conductivity of $x\text{Li}_2\text{S}-(100-x)\text{P}_2\text{S}_5$ electrolytes. *Solid State Ionics*, *305*, 1–6.
- Zheng, J. Q., Li, Y. F., Yang, R., Li, G., & Ding, X. K. (2017). Lithium ion conductivity in the solid electrolytes $(\text{Li}_{0.25}\text{La}_{0.25})_{1-x}\text{M}_{0.5x}\text{NbO}_3$ (M= Sr, Ba, Ca, x= 0.125) with perovskite-type structure. *Ceramics International*, *43*(2), 1716–1721.
- Zhu, Y., He, X., and Mo, Y. Origin of Outstanding Stability in the Lithium Solid Electrolyte Materials: Insights from Thermodynamic Analyses Based on First-Principles Calculations. *ACS Appl. Mater. Interfaces* *2015*, *7*, 23685–23693.
- Zinigrad, E., Larush-Asraf, L., Gnanaraj, J. S., Gottlieb, H. E., Sprecher, M., & Aurbach, D. (2005). Calorimetric studies of the thermal stability of electrolyte solutions based on alkyl carbonates and the effect of the contact with lithium. *Journal of power sources*, *146*(1–2), 176–179.

APPENDICES

มหาวิทยาลัยราชภัฏสุราษฎร์ธานี

APPENDICES A

HISTORICAL DEVELOPMENT OF SOLID ELECTROLYTE, RAW DATA OF EIS,
AND CALCULATION OF BOND DISTANCE

มหาวิทยาลัยราชภัฏสุราษฎร์ธานี

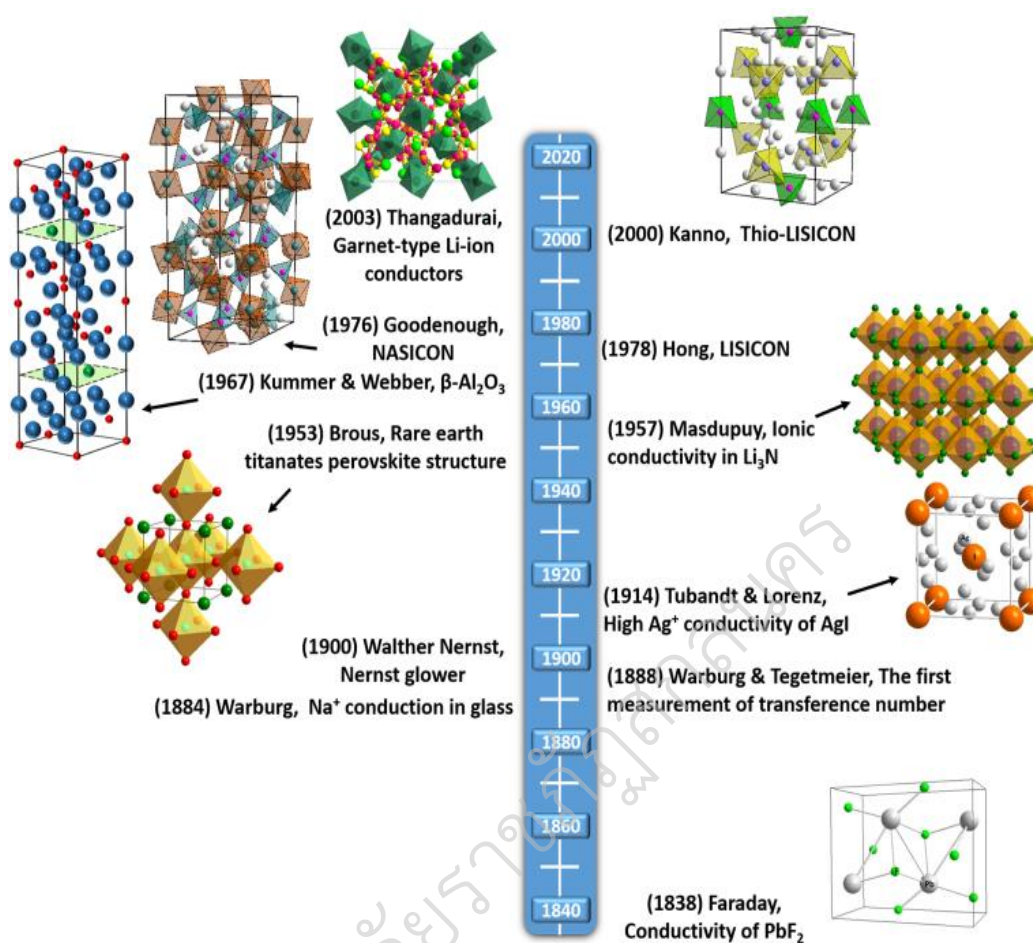


Fig. 1A. A Historical development of solid electrolyte (Wang C. et al., 2020).

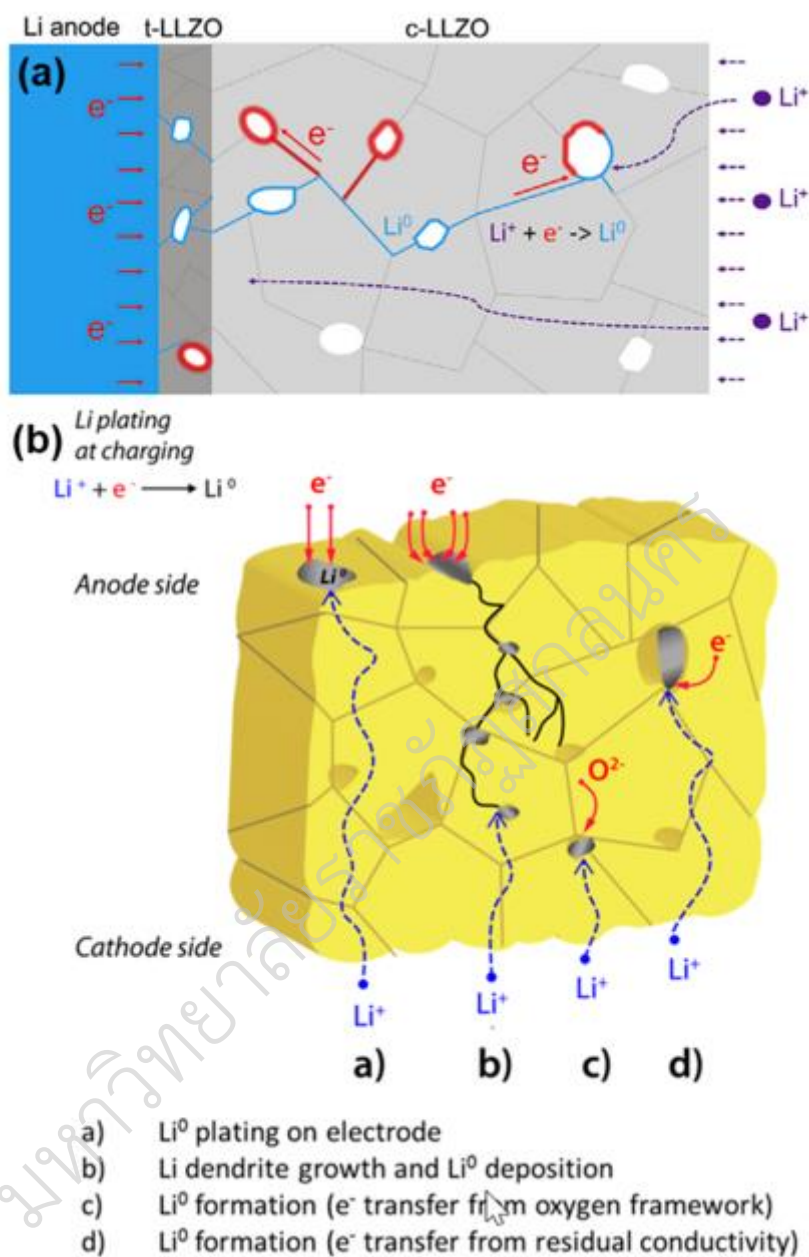


Fig. 2A .A (a) Schematic of metallic Li^0 (blue color) formation on the pore surfaces inside of c-LLZO due to the electron pathway provided by the pore surfaces and possibly grain boundaries. Reproduced with permission from (Tian H. et al., 2018). Copyright 2018 Elsevier. (b) Schematic of the proposed potential Li-ion reduction mechanisms in garnet electrolyte. Reproduced with permission from (Aguesse F. et al., 2017). Copyright 2017 American Chemical Society.

Table 13 Raw data of EIS for LLTO sample.

Frequency	Z' (Ω)	Z'' (Ω)		Frequency	Z' (Ω)	Z'' (Ω)
3.00×10^7	0.016937	-0.817		59857.87	177.54	-76.822
2.38×10^7	8.8957	-3.4788		47546.8	181.86	-92.028
1.89×10^7	17.048	-18.845		37767.76	186.86	-110.64
1.50×10^7	27.89	-32.491		30000	192.76	-133.18
1.19×10^7	37.9	-42.819		23829.85	199.62	-160.8
9486833	49.131	-50.992		18928.72	207.59	-194.5
7535659	61.412	-56.96		15035.62	216.99	-235.89
5985787	74.337	-60.723		11943.21	228.02	-286.87
4754680	87.754	-62.208		9486.833	241.42	-349.34
3776776	100.65	-61.528		7535.659	257.38	-426.83
3000000	112.68	-58.939		5985.787	277.73	-522.3
2382985	123.28	-54.924		4754.68	303.8	-639.93
1892872	132.09	-50.152		3776.776	338.79	-785.16
1503562	139.26	-45.192		3000	385.28	-962.85
1194322	144.79	-40.495		2382.985	448.56	-1180.6
948683.3	148.72	-29.636		1892.872	535.97	-1444.8
753565.9	152.07	-27.833		1503.562	660.04	-1761.4
598578.7	154.65	-26.697		1194.322	829.81	-2134.8
475468	156.81	-26.357		948.6833	1064.6	-2577.6
377677.6	158.64	-26.917		753.5659	1381	-3069.4
300000	160.34	-28.443		598.5787	1807.2	-3610
238298.5	161.95	-31.122		475.468	2352	-4170
189287.2	163.75	-34.814		377.6776	3020.8	-4750
150356.2	165.63	-39.984		300	3771.6	-5300
119432.1	168.11	-46.416		238.2985	4700.7	-5750
94868.33	170.89	-54.422		189.2872	5637.1	-6133.3
75356.59	174	-64.437		150.3562	6568.7	-6449.9

Table 13 (continued)

Frequency	Z' (Ω)	Z'' (Ω)
119.4322	7444.7	-6755.2
94.86833	8230.8	-7106.5
75.35659	8935.9	-7544.1
59.85787	8010.8	-6997.1
47.5468	9904.9	-8978.6
37.76776	10536	-10210
30	10911	-11754
23.82985	11311	-13856
18.92872	11919	-16630
15.03562	12336	-20053
11.94322	12946	-24385
9.48683	13729	-29903
7.53566	14632	-36598
5.98579	15992	-45179
4.75468	17597	-55735
3.77678	19627	-68736
3	22068	-84563
2.38298	25462	-105000
1.89287	28908	-131000
1.50356	34577	-159000
1.19432	39681	-195000
1	49184	-229000

Table 14 Raw data of EIS for $\text{LLSr}_{0.09}\text{TT}_{0.09}\text{O}_3$ sample.

Frequency	Z' (Ω)	Z'' (Ω)		Frequency	Z' (Ω)	Z'' (Ω)
3.00×10^7	-13.676	24.039		59857.87	34.215	-20.106
2.38×10^7	-1.5462	14.511		47546.8	37.53	-20.527
1.89×10^7	2.9964	9.6194		37767.76	40.672	-20.773
1.50×10^7	4.6794	6.5766		30000	43.537	-20.954
1.19×10^7	6.386	3.8132		23829.85	46.086	-21.262
9486833	7.7413	2.1606		18928.72	48.387	-21.85
7535659	8.7035	1.0779		15035.62	50.463	-22.906
5985787	9.3564	0.28327		11943.21	52.372	-24.552
4754680	9.8404	-0.31234		9486.833	54.272	-26.911
3776776	10.182	-0.84159		7535.659	56.168	-30.118
3000000	10.454	-1.3635		5985.787	58.208	-34.366
2382985	10.724	-1.8811		4754.68	60.494	-39.787
1892872	10.982	-2.444		3776.776	63.16	-46.598
1503562	11.271	-3.0646		3000	66.24	-55.022
1194322	11.605	-3.7638		2382.985	69.948	-65.323
948683.3	11.859	-2.571		1892.872	74.437	-77.884
753565.9	12.387	-3.881		1503.562	79.789	-93.086
598578.7	13.022	-5.2468		1194.322	86.495	-111.47
475468	13.793	-6.7013		948.6833	94.547	-133.48
377677.6	14.77	-8.2364		753.5659	104.74	-159.83
300000	15.986	-9.902		598.5787	117.12	-191.27
238298.5	17.49	-11.667		475.468	132.49	-228.62
189287.2	19.375	-13.516		377.6776	151.79	-273.13
150356.2	21.637	-15.35		300	174.83	-324.83
119432.1	24.441	-17.009		238.2985	203.88	-386.48
94868.33	27.559	-18.353		189.2872	239.1	-458.17

75356.59	30.883	-19.394		150.3562	281.96	-541.67
----------	--------	---------	--	----------	--------	---------

Table 14 (continued)

Frequency	Z' (Ω)	Z'' (Ω)
119.4322	333.62	-638.64
94.86833	395.5	-751.16
75.35659	469.74	-880.89
59.85787	542.05	-1025.1
47.5468	660.09	-1202
37.76776	782.05	-1401.9
30	923.24	-1629.2
23.82985	1086	-1891.6
18.92872	1271.9	-2193.6
15.03562	1488.1	-2544.7
11.94322	1731.1	-2950.9
9.48683	2004.2	-3421.5
7.53566	2316.3	-3976.7
5.98579	2664.4	-4628
4.75468	3050.7	-5397.1
3.77678	3486.8	-6307.5
3	3982.4	-7412.2
2.38298	4541	-8721.1
1.89287	5165.9	-10328
1.50356	5895.5	-12204
1.19432	6732.9	-14494
1	7490.2	-16618

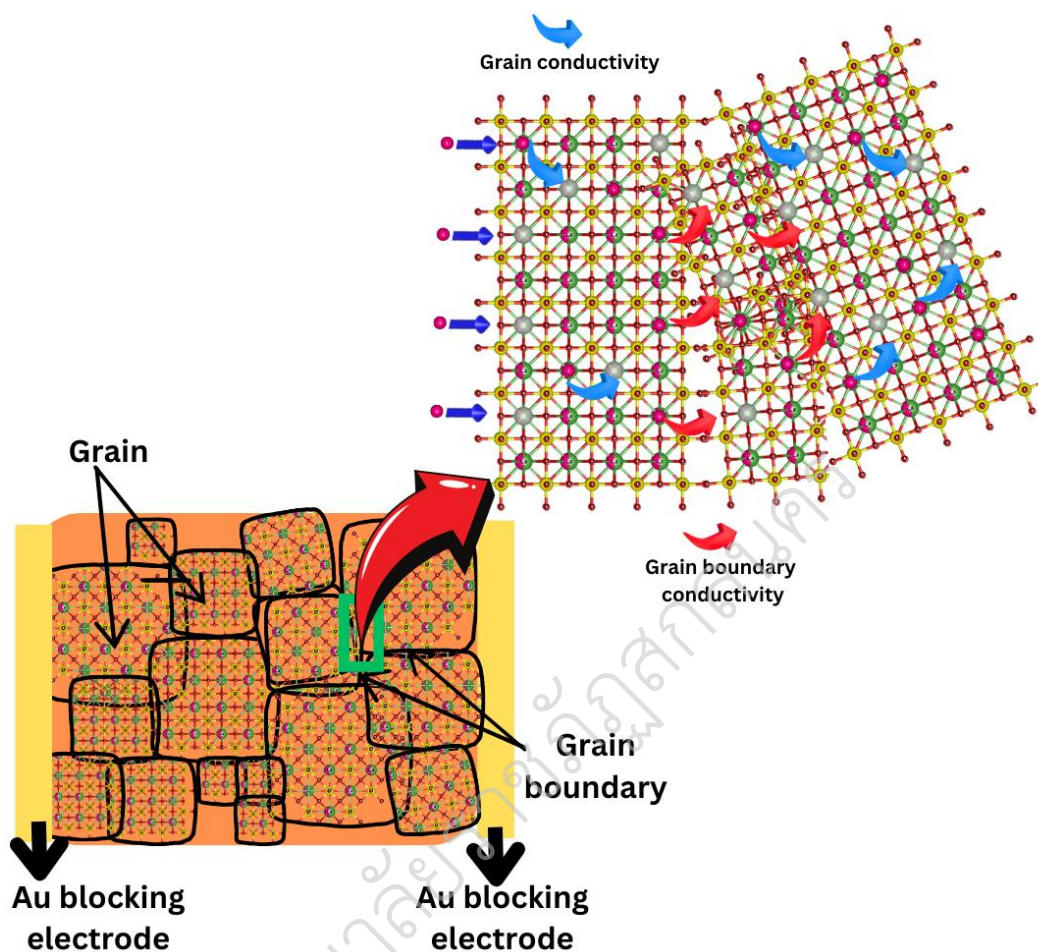


Fig. 3A. Schematic of grain and grain boundary conductivity mechanism

Calculation bond distance of $\text{Li}_{0.5-x}\text{La}_{0.5-x}\text{Sr}_x\text{Ti}_{1-x}\text{Ta}_x\text{O}_3$ ($0 \leq x \leq 0.12$)

The space group structure s of LLTO with different compositions under the heating condition s , it is found that LLTO exhibits a simple cubic structure at the high temperature (>1673 K). Fig. 4A shows the unit cell of high temperature phase LLTO with a conventional perovskite ABO_3 structure. Eight TiO_6 octahedrons sharing corner in pairs form an AO_{12} cuboctahedron, so-called A-cage, in the center of which Li^+ , La^{3+} and vacancies are situated. The O_4 window between two adjacent A-cages is made up of four neighboring TiO_6 octahedrons (see Fig. 4A) (Varez, A., et al., 2004; Harada, Y., et al., 1999; Catti, M., et al., 2007)

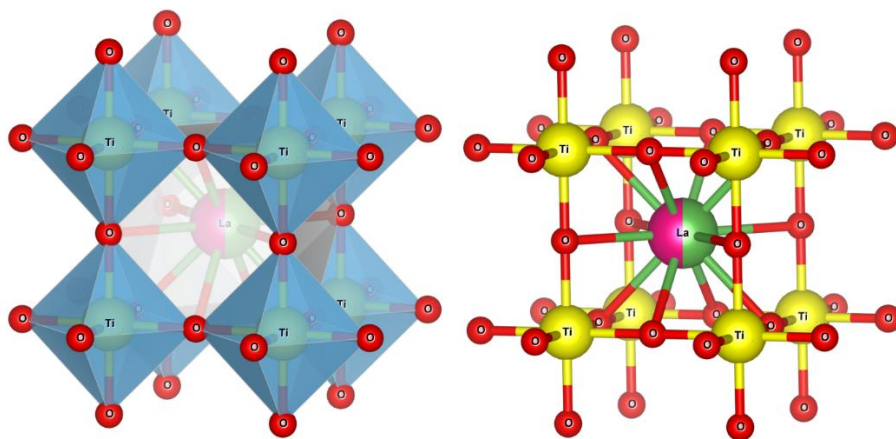


Fig. 4A. Crystal structure of $\text{Li}_{0.5}\text{La}_{0.5}\text{TiO}_3$ via VESTA program.

The materials with cubic structure, cations can be distributed over two interstitial sites, namely, octahedral – A and tetrahedral – B. In this method observed and calculated intensity ratios for the selected pairs of reflections were compared by using following relation;

$$\frac{I_{hkl}^{Obs.}}{I_{h'k'l'}^{Obs.}} = \frac{I_{hkl}^{Cal.}}{I_{h'k'l'}^{Cal.}} \quad 1A$$

Where $I_{hkl}^{Obs.}$ and $I_{hkl}^{Cal.}$ are the observed and calculated intensities of the Bragg's reflections. When the intensities of Bragg's reflections are almost independent to the oxygen parameter, vary in the opposite direction with cation distribution and do not change considerably. A minimum value of agreement factor (R) as defined by equation (2A), describes the matches well the stimulated structure with actual and the corresponding cation distribution was considered [47]:

$$R = \left| \frac{I_{hkl}^{Obs.}}{I_{h'k'l'}^{Obs.}} - \frac{I_{hkl}^{Cal.}}{I_{h'k'l'}^{Cal.}} \right| \quad 2A$$

The relative integrated in intensity (I_{hkl}) of a Bragg's line of XRD pattern was obtained through the relation (Buerger, M. J. (1960);

$$I_{hkl} = |F_{hkl}|^2 P \cdot L_p \quad 3A$$

where P is multiplicity factor, F is structure factor, L_p is Lorentz polarization factor and is given by:

$$L_p = \frac{1 + \cos^2 2\theta}{\sin^2 \cos 2\theta} \quad 4A$$

The atomic scattering factors and multiplicity factors can be found in literature (Warren, B. E. (1990). La^{3+} , Sr^{2+} elements preferred the A-site with fractional amount towards B-site, whereas most of the Ti^{4+} and Ta^{5+} elements prefer B-site. The radius of A-site and B-site increases with the substitution of Sr^{2+} to La-site and Ta^{5+} to Ti-site which has comparatively with a larger ionic radius.

The theoretical lattice parameter ' a_{th} ' and oxygen positional parameter ' u ' were computed through the relations

$$a_{th} = \frac{8}{3}\sqrt{3} \left[(r_A + R_0) + \sqrt{3}(r_B + R_0) \right] \quad 5A$$

$$u = \left[(r_A + R_0) \frac{1}{\sqrt{3}a} + \frac{1}{4} \right] \quad 6A$$

where, r_A , r_B and R_0 are the radii of A-, B-sites and oxygen (1.32 Å) respectively. The variation of ' a_{th} ' and ' u ' with the increasing percentage of Sr^{2+} and Ta^{5+} . In case of BCC cubic structure, the u value was calculated by WPPF mode of XRD (Rigaku, Japan) or FullProf program base on Rietveld refinement method.

The various allied parameters: bond lengths (d_{AX} and d_{BX}), shared tetrahedral edge (d_{AXE}), and shared and unshared octahedral edges (d_{BXE} and d_{BXEU}) were obtained through the relations.

$$d_{AX} = a\sqrt{3} \left(u - \frac{1}{4} \right) \quad 7A$$

$$d_{BX} = a \left[3u^2 - \left(\frac{11}{4} \right) u + \frac{43}{64} \right]^{1/2} \quad 8A$$

$$d_{AXE} = a\sqrt{2} \left(2u - \frac{1}{2} \right) \quad 9A$$

$$d_{BXE} = a\sqrt{2}(1-2u) \quad 10A$$

$$d_{BXEU} = a\left(4u^2 - 3u + \frac{11}{16}\right)^{1/2} \quad 11A$$

The XRD pattern of $\text{Li}_{0.5}\text{La}_{0.5}\text{TiO}_3$ sample was fitted by refinement method in Fig. 5A. Furthermore, the calculation of lattice parameters, peak position, atomic positions and bond distance were shown in Table 14, 15, 16 and 17 respectively.

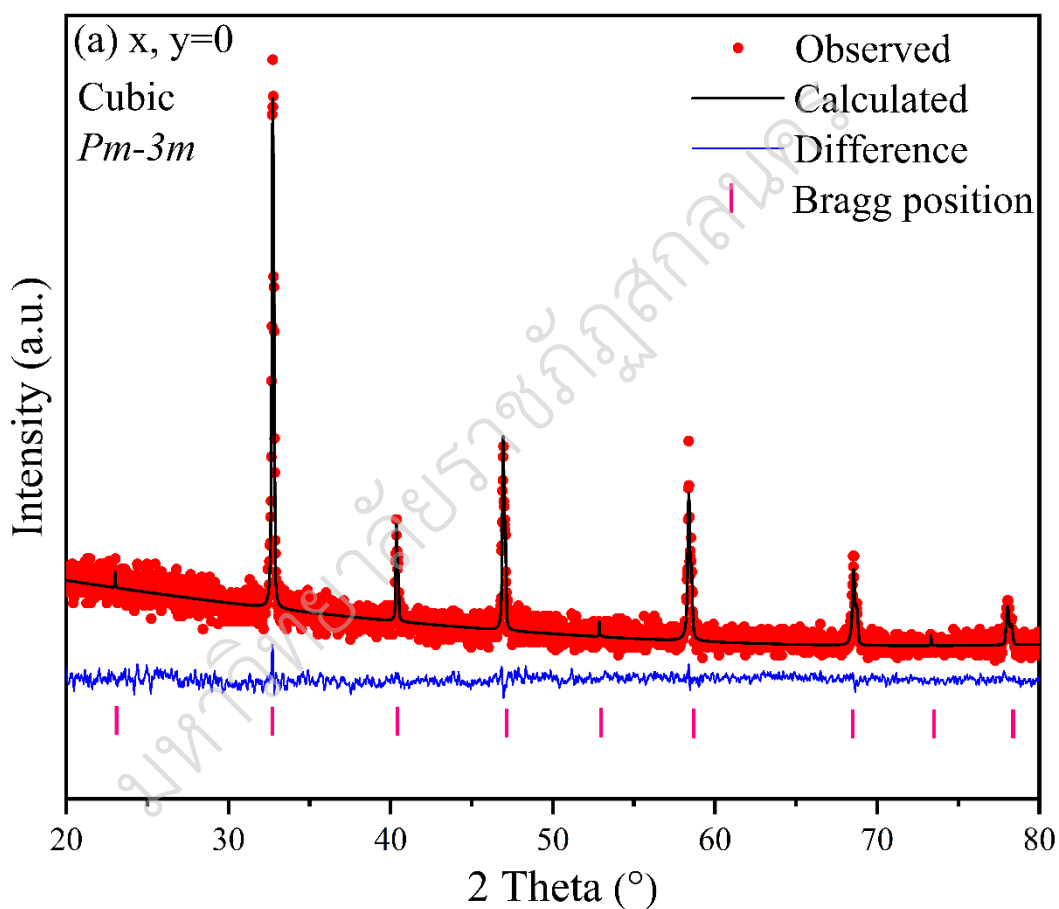


Fig. 5A. The XRD pattern of $\text{Li}_{0.5}\text{La}_{0.5}\text{TiO}_3$ via Rietveld refinement.

Tab 14 The data of $\text{Li}_{0.5}\text{La}_{0.5}\text{TiO}_3$ sample of lattice parameter.

Sample	a (Å)	b (Å)	c (Å)	α (°)	β (°)	γ (°)
$\text{Li}_{0.5}\text{La}_{0.5}\text{TiO}_3$	3.87394(19)	3.87394(19)	3.87394(19)	90.00	90.00	90.00

Tab 15 The data of $\text{Li}_{0.5}\text{La}_{0.5}\text{TiO}_3$ sample of peak position.

No.	2θ (°)	d (°)	hkl	Intensity ratio
1	22.93839	3.86896	100	0.65
2	32.66412	2.73577	110	100
3	40.29070	2.23375	111	17.20
4	46.86672	1.93448	200	45.07
5	52.79834	1.73025	210	0.58
6	58.29495	1.57950	211	35..38
7	68.44491	1.36788	220	23.54
8	73.24259	1.28965	300	0.09
9	73.24259	1.28965	221	0.38
10	77.92192	1.22347	310	14.30

Tab 16 The data of $\text{Li}_{0.5}\text{La}_{0.5}\text{TiO}_3$ sample of atomic position.

Atom	x	y	z	Occ	B	No.
La1(La)	0.0000	0.0000	0.0000	0.5000	0.5000	1
Ti1(Ti)	0.5000	0.5000	0.5000	1.0000	0.5000	1
Li1(Li)	0.0000	0.0000	0.0000	0.5000	0.5000	1
O1(O)	0.5000	0.5000	0.0000	1.0000	0.5000	3

Tab 17 The bond distance between the atom of $\text{Li}_{0.5}\text{La}_{0.5}\text{TiO}_3$ sample.

Atom	Bond distance (Å)
La1-Ti1	3.35493
La1-Ti1 (-1+x, y, z)	3.35493
La1-Ti1 (x, -1+ y, z)	3.35493
La1-Ti1 (x, y, -1+ z)	3.35493
La1-O1	2.73929
La1-O1 (-1+x, y, z)	2.73929
La1-O1 (x, -1+ y, z)	2.73929
La1-O1 (x, y, z)	2.73929
La1-O1 (z, -1+x, y)	2.73929
La1-O1 (z, x, -1+y)	2.73929
La1-O1 (y, z, x)	2.73929
La1-O1 (-1+y, z, x)	2.73929
La1-O1 (y, z, -1+x)	2.73929
Ti1-O1	1.93697
Ti1-O1 (x, y, 1+z)	1.93697
Ti1-O1 (1+z, x, y)	1.93697
Ti1-O1 (z, x, y)	1.93697
Ti1-O1 (y, 1+z, x)	1.93697
Ti1-O1 (y, z, x)	1.93697

Titanium reduction mechanism with Li metal anode

The main problem with perovskite-based electrolytes is that Ti^{4+} is chemically unstable in the presence of Li-metal. LLTO reacts rapidly with Li accompanying with its color shift from white to black (Yan et al., 2018). Galvez-Aran et al. (Galvez-Aranda and Seminario, 2020) further confirmed that Ti reduction occurs at the LLTO/Li-metal anode interface. The reaction rate increases as the applied external electric field increases, indicating that LLTO is electrochemically unstable with Li. As evidenced by X-ray photoelectron spectroscopy (XPS) studies, Ti^{4+} in LLTO reduces into lower valence Ti species (e.g., Ti^{3+} , Ti^{2+} , and Ti^0) (Wenzel et al., 2015; Liu et al., 2017). Furthermore, Ti reduction is associated with the production of oxygen vacancies, making the interface electrically conductive and unsuitable as an electrolyte for lithium metal batteries. In detail, the lithiation induces the reduction of adjacent Ti from +4 to +3 state, corresponding to the electron occupation from $3d^04s^0$ to $3d^14s^0$, whereas the oxidation state of La remains unchanged. In an octahedral crystal field, the d electron of transition metal prefers to occupy the d_{xy} orbit and maintains a high spin state. On the other hand, the spin-up Ti^{3+} states, sitting on the left side of the Fermi Level (Fig. 6A (f)), can enter the conduction band upon excitation with a small amount of energy and act as free electrons. This can be attributed to the weak binding electron ability of Ti^{3+} . Thus, the lithiated LLTO demonstrates an increase in electronic conductivity, and accelerated lithium dendrite in LLTO then leads to short circuits (Zhang, L. et al., 2020).

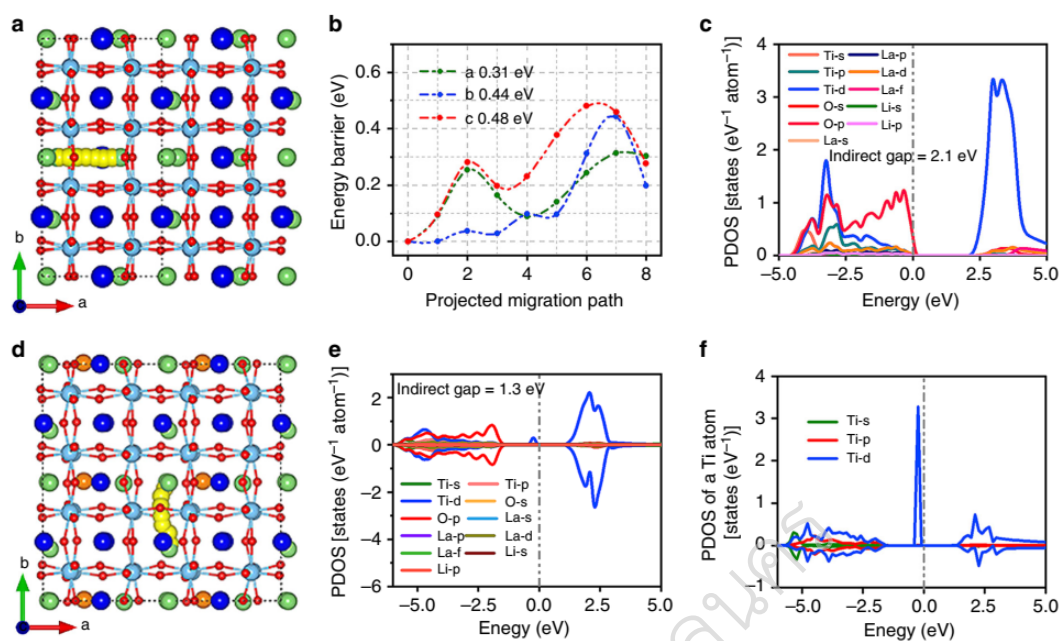


Fig. 6A. Geometric/electronic structures of LLTO and lithiated LLTO. (a) Crystal structure and the Li⁺ diffusion path with the lowest barrier; (b) Diffusion energy barrier at three-dimensional directions; (c) Projected density of states (DOS) of pristine LLTO; (d) Crystal structure with the Li⁺ diffusion path of lithiated LLTO; (e) PDOS of lithiated LLTO; (f) PDOS of magnetized Ti atom adjacent to the inserted Li atom in lithium LLTO. The green, blue, cyan, and red spheres in the crystal structure represent lithium, lanthanum, titanium, and oxygen atoms, respectively

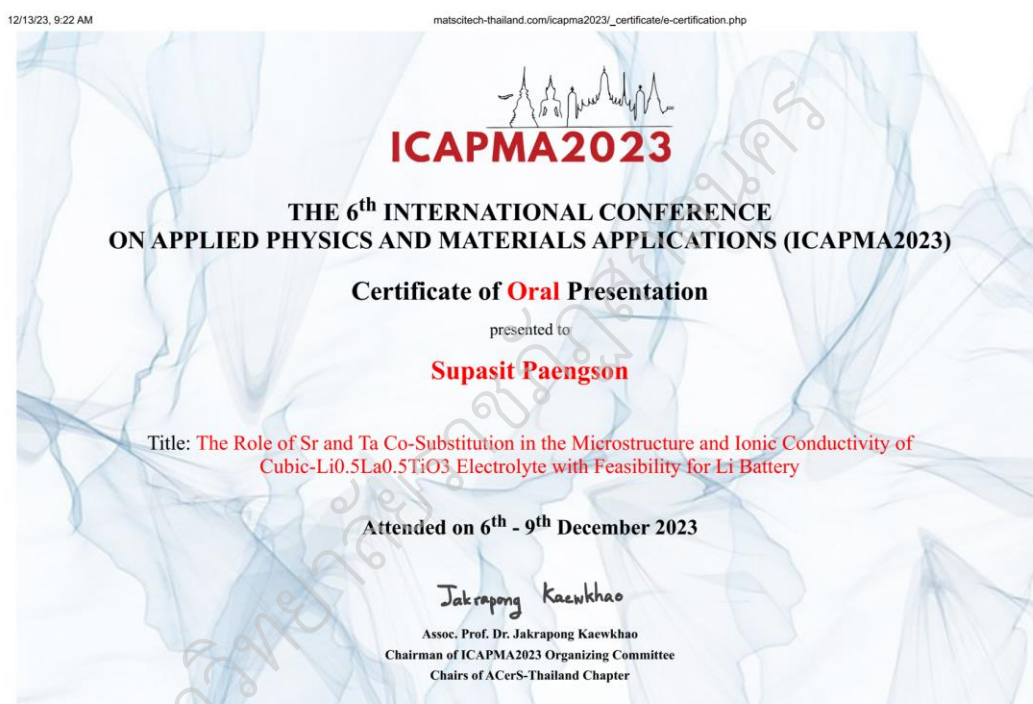
APPENDICE B

INTERNATIONAL CONFERENCES

มหาวิทยาลัยราชภัฏสุราษฎร์ธานี

1. **Supasit Paengson**, Panida Pilasuta, Daisuke Mori, Tosawat Seetawan.

“The Role of Sr and Ta Co-Substitution in the Microstructure and Ionic Conductivity of Cubic- $\text{Li}_{0.5}\text{La}_{0.5}\text{TiO}_3$ Electrolyte with Feasibility for Li Battery”. THE 6th INTERNATIONAL CONFERENCE ON APPLIED PHYSICS AND MATERIALS APPLICATIONS (ICAPMA2023), 6–9 December 2023, Oral Presentation Award.



6 - 9 DECEMBER 2023
PATTAYA
THAILAND



ICAPMA2023

The 6th International Conference on Applied
Physics and Materials Applications



Congratulations

This **Oral Presentation Award** certificate is presented to

Supasit Paengson, Panida Pilasuta, Daisuke Mori, Tosawat Seetawan

for the title: The Role of Sr and Ta Co-Substitution in the Microstructure and Ionic
Conductivity of Cubic- $\text{Li}_{0.5}\text{La}_{0.5}\text{TiO}_3$ Electrolyte with Feasibility for Li Battery

in recognition of your high level of performance in ICAPMA2023

(December 6th – December 9th, 2023)

Jakrapong Kaengkhae

(Assoc. Prof. Dr. Jakrapong Kaengkhae)
Chairman of ICAPMA2023
Chairman of ACerS-Thailand Chapter



APPENDICE C

PUBLICATIONS

มหาวิทยาลัยราชภัฏสุราษฎร์ธานี

First Author

1. **Supasit Paengson**, Panida Pilasuta, Daisuke Mori, Tosawat Seetawan (2024). Effect of Sr and Ta co-substitution on microstructure and ionic conductivity of cubic- $\text{Li}_{0.5}\text{La}_{0.5}\text{TiO}_3$ electrolyte for applications in Li batteries. *Journal of Alloys and Compounds*, 979, 173512. (Quartile 1, Tier 1, Impact Factor 6.2)
2. **Supasit Paengson**, Kanamori Yuzou, Mikami Mao, Nobuyashiki Imanishi, Daisuke Mori, and Tosawat Seetawana. Enhancing lithium-ion conduction of composite polymer electrolytes by garnet-LLZO-Ga filler for quasi-solid lithium metal batteries. (On process)

มหาวิทยาลัยราชภัฏสุราษฎร์ธานี



Contents lists available at ScienceDirect

Journal of Alloys and Compounds

journal homepage: www.elsevier.com/locate/jalcom

Effect of Sr and Ta co-substitution on microstructure and ionic conductivity of cubic-Li_{0.5}La_{0.5}TiO₃ electrolyte for applications in Li batteries

Supasit Paengson^{a,b}, Panida Pilasuta^a, Daisuke Mori^c, Tosawat Seetawan^{a,*}^a Program of Physics, Faculty of Science and Technology, Sakon Nakhon Rajabhat University, 680 Nittayo Road, Muang District, Sakon Nakhon 47000, Thailand^b Battery Research Laboratory, Center of Excellence on Alternative Energy, Research and Development Institute, Sakon Nakhon Rajabhat University, 680 Nittayo Road, Muang District, Sakon Nakhon 47000, Thailand^c Department of Chemistry for Materials, Graduate School of Engineering, Mie University, Tsu, Mie 514-8507, Japan

ARTICLE INFO

Keywords:
Cubic-perovskite
Semi solid electrolyte
Lithium battery
Co-substitutions
Bottleneck

ABSTRACT

All-solid-state lithium batteries (ASSBs) have gained significant attention in recent years because of their potential to offer higher energy density and enhanced safety compared to conventional liquid-electrolyte-based lithium-ion batteries (LIBs). Lithium lanthanum titanate (LLTO) is a promising solid electrolyte for next-generation lithium batteries owing to its high ionic conductivity of approximately 10^{-3} S·cm⁻¹ at room temperature (RT). The Sr and Ta co-doped Li_{0.5-x}La_{0.5-x}Sr_xTi_{1-x}Ta_xO₃ perovskites were synthesized by solid-state reaction. In this study, Sr²⁺ and Ta⁵⁺ with larger ionic radii, were used for co-substitution in the La³⁺ and Ti⁴⁺ sites, respectively, to increase the bottleneck size of the A-site and expand the average bond length of the B-site on the perovskite structure (ABO₃), thereby increasing the Li⁺ ion mobility. The LLSr_xTTa_xO₃ (0 ≤ x ≤ 0.12) pellets have high relative densities, and high grain conductivities, where the total conductivity of LLSr_{0.09}TTa_{0.09}O₃ reached 4.12×10^{-3} S·cm⁻¹. Compared with the pure specimen, the total conductivities of the doped specimens are approximately more than 2.7 times at RT. The assembled semi-solid LFP/10 wt% LLSr_{0.09}TTa_{0.09}O₃/Li full battery has a 0.1 C specific discharge capacity of 156 mAh·g⁻¹ and a 1 C capacity retention rate of 86% after 290 cycles at RT.

1. Introduction

Presently, lithium-ion batteries find widespread application in various sectors, including electric vehicles, solar energy storage systems, and portable electronic devices [1]. However, the conventional liquid electrolyte raises substantial concerns stemming from the formation of lithium dendrites. These dendritic structures can give rise to short-circuits within batteries, thereby instigating thermal runaway and a cascade of safety-related issues, encompassing fires and explosions. Moreover, liquid electrolytes present inherent incompatibilities with high-capacity, high-voltage cathodes, and lithium metal anodes, complicating the fulfillment of stringent requirements for high-energy storage solutions [2–7].

All-solid-state lithium batteries (ASSBs) represent a significant and intricate research frontier, where the enhancement of ionic conductivity, stability, energy density, and safety stands as a paramount challenge. Recent studies have documented that the ionic conductivity of solid-state electrolyte (SSE) materials hovers around $\sim 10^{-3}$ S·cm⁻¹ at

room temperature (RT), a value notably lower than that of conventional commercial liquid electrolytes, which typically exhibit around $\sim 10^{-2}$ S·cm⁻¹. Nevertheless, SSE materials present distinct advantages, including elevated energy density, expanded electrochemical windows, and superior safety attributes, such as heightened thermal resilience and the absence of flammable gas emissions [8–10]. Nevertheless, the primary challenge in the advancement of SSE materials lies in addressing their low ionic conductivity. Additionally, the presence of significant interfacial resistance is a critical concern that must be mitigated during the fabrication process when incorporating active cathode materials and Li-metal anodes. This resistance is not limited to the surface but may also manifest within the SSE material, a phenomenon exacerbated by low-temperature sintering or excessive doping levels. Such interfacial resistance directly impacts the chemical stability of the battery cell [11–13]. Furthermore, the complexity of fabricating battery cells, particularly for large-scale commercial production, has a direct bearing on the overall cost of battery cell manufacturing.

Several studies have been conducted on different types of solid

* Corresponding author.

E-mail address: t.seetawan@snru.ac.th (T. Seetawan).<https://doi.org/10.1016/j.jallcom.2024.173512>

Received 28 August 2023; Received in revised form 5 January 2024; Accepted 9 January 2024

Available online 11 January 2024

0925-8388/© 2024 Elsevier B.V. All rights reserved.

electrolytes, including NASICON [14–16], sulfide [17–20], garnet [21–25], and perovskite [26–30]. Among the different types of solid-state electrolytes, perovskite $\text{Li}_{0.5}\text{La}_{0.5-x}\text{Ti}_x\text{O}_3$ (LLTO) has attracted considerable attention due to its high grain conductivity of approximately $10^{-3} \text{ S cm}^{-1}$ at room temperature (RT), and it has a potential for improving the grain boundary conductivity [31,32]. In recent years, the ABO_3 -perovskite structure of LLTO has been extensively used in substitution or doping techniques to increase the bottleneck size for Li^+ ion migration across the lattice crystals, thereby improving the total ionic conductivity. For example, the substitution of La^{3+} sites (A-sites) with larger ionic radii, such as Ba and Sr, increases the ionic conductivity. In comparison, substituting smaller ionic radii such as Ca, Pr, and Sm decreases the ionic conductivity by decreasing the lattice constant and bottleneck size [33–36]. Furthermore, the Ti^{4+} site (B-site) is affected by doping with larger ionic radii, such as Nb, Sn, Ta, and Al, resulting in increased conductivity, particularly grain boundary conductivity, by increasing sinterability [37–39]. Yu et al. used a co-substitution strategy with cubic perovskite $\text{Li}_{0.355}\text{La}_{0.35}\text{Sr}_{0.3}\text{Ti}_{0.995}\text{M}_{0.005}\text{O}_3$ ($\text{M} = \text{Al}, \text{Co}, \text{and In}$) ceramics; however, they reported a decrease in ionic conductivity [40]. In contrast, Li et al. reported that the Sr and Ta co-substitution strategy in the tetragonal perovskite of $\text{Li}_{0.33}\text{La}_{0.557}\text{TiO}_3$ increased the ionic conductivity and a change in crystal structure to cubic [33]. All previous studies have aided in our understanding of the conductivity of perovskite-lithium lanthanum titanate. In addition, LLTO perovskites have several different crystal structures and compositions, which can be achieved using different synthesis methods, sintering temperatures, or substitution elements. Additionally, the cubic perovskite structure has exhibited high ionic conductivity owing to the bottleneck or O_4 window during the bonding of Ti–O in the Li^+ ion pathway, which is large in the cubic structure [33,41]. The data reported in this study seem to confirm the assumption that co-doping with larger ionic radii in La^{3+} at the A-site and Ti^{4+} at the B-site can increase both the grain and grain boundary conductivities. Furthermore, controlling the doping content in cubic- $\text{Li}_{0.5}\text{La}_{0.5}\text{TiO}_3$ can help maintain its cubic structure, which supports fast Li^+ ion migration.

In this study, the cubic- $\text{Li}_{0.5}\text{La}_{0.5}\text{TiO}_3$ structure was selected for the co-substitution of the La site with Sr and Ti site with Ta, both of which have larger ionic radii at different concentrations, to enhance the bottleneck size for Li^+ migration channels and maintain the cubic structure, leading to an increase in ionic conductivity. Additionally, Sr and Ta co-substitution improved the pellet sample density during sintering. The Sr and Ta co-substitution was significantly effective in enhancing the total conductivity of cubic- $\text{Li}_{0.5}\text{La}_{0.5}\text{TiO}_3$, making it a potential candidate for use as a composite polymer electrolyte in perovskite-type Li metal batteries.

2. Experimental details

The of $\text{Li}_{0.5-x}\text{La}_{0.5-x}\text{Sr}_x\text{Ti}_{1-x}\text{Ta}_x\text{O}_3$ ($0 \leq x \leq 0.12$) pellets were synthesized using the solid-state reaction method. High-purity raw materials, including Li_2CO_3 (>99.9%, Ar), La_2O_3 (99%, Ar), SrO_2 (99%, Ar), TiO_2 (99%, Ar), and Ta_2O_5 (99.9%, Ar), served as the starting materials. The raw powders were weighed in the appropriate stoichiometric proportions and then mixed using a planetary ball mill with agate balls and a vial in ethanol for 24 h at 350 rpm. Subsequently, they were dried at 80°C for 24 h, with an additional 20 mol.% excess of Li_2CO_3 to compensate for lithium volatilization. Furthermore, the La_2O_3 raw material powders were pre-calcined at 800°C for 10 h in an air atmosphere to eliminate moisture vapor.

The mixed powder was then subjected to calcination at 1000°C for 12 h in the air atmosphere. Following this, the calcined powder was uniaxially pressed at 200 MPa to form pellets with a diameter of 20 mm. To prevent lithium loss during the sintering process, the green pellets were coated with a layer of mother powder. The sintering process took place at 1300°C for 10 h in an air atmosphere, with a heating rate of 5°C per minute.

The microstructures of all sintered powders were examined using X-ray diffraction (XRD), which utilized Cu K α radiation from 10° to 80° (2θ) with a step interval of 0.02° (Rigaku SmartLab SE, Japan) at room temperature. Scanning electron microscopy (SEM) was employed with a Field Emission Scanning Electron Microscope (FESEM) (JEOL JSM-7610 F Plus). This was used to study the microstructure, and energy dispersive X-ray (EDX) analysis was conducted to investigate the distribution of La, Sr, Ti, and Ta elements in all the samples. Furthermore, the lithium content was analyzed by inductively coupled plasma optical emission spectroscopy (ICP-OES) (PerkinElmer Optima 8000) confirmed the content of sample. The chemical state and composition of the $\text{LiSr}_{0.09}\text{Ta}_{0.09}\text{O}_3$ sample were measured by x-ray photoelectron spectroscopy (XPS) (AXIS Ultra DLD) with Al K α radiation.

The ionic conductivity of all samples was determined using an impedance analyser (Solartron SI 1260) through electrochemical impedance spectroscopy (EIS) across a frequency range from 1 Hz to 18 MHz. These measurements were conducted over a temperature range of 298 K to 373 K, with an AC amplitude of 10 mV. For EIS measurements, both sides of the sintered samples were initially polished using silicon carbide abrasive paper. Subsequently, they were coated with gold (Au) via sputtering to ensure good conductive contact for blocking electrodes. To distinguish the influence of electronic conductivities resulting from Sr and Ta doping, electronic conductivity was measured via direct current (DC) polarization with a constant voltage of 4 V applied to the testing pellets for 1000 s.

The semi-solid full cell $\text{LiFePO}_4/\text{Li}$ cell was fabricated using a composite polymer electrolyte (CPE) and a Li metal anode, offering the possibility of using a Li metal anode without the short-circuit effect resulting from the decomposition of Ti^{4+} to Ti^{3+} compared to the solid $\text{LiSr}_{0.09}\text{Ta}_{0.09}\text{O}_3$ pellet. Before preparing the precursor solution, Poly (vinylidene fluoride-co-hexafluoropropylene) (PVDF-HFP), Lithium bis (trifluoromethanesulfonyl) imide, (LiTFSI) and sintered powder $\text{LiSr}_{0.09}\text{Ta}_{0.09}\text{O}_3$ were vacuum dried at 80°C for 24 h. Initially, PVDF-HFP and LiTFSI (with a weight ratio of 3:2) were dissolved in Dimethylformamide (DMF) within a glove box, and the mixture was stirred at 60°C for 12 h to create a salt solution. Subsequently, sintered powder $\text{LiSr}_{0.09}\text{Ta}_{0.09}\text{O}_3$ was added to the salt solution in weight ratios of 0 (CPE–0), 5 (CPE–5), 10 (CPE–10), 15 (CPE–15), and 20 wt% (CPE–20) relative to the combined weight of LiTFSI and PVDF-HFP. The resulting solution, constituting the CPE, was stirred at 60°C for 12 h, yielding a ready-to-use solution. The CPE solution was poured into a Teflon tray to prepare the CPE film. Subsequently, the film was treated with N_2 gas for 12 h and dried under vacuum for an additional 60 min for 12 h, thus rendering the CPE film ready for assembly full cells. The EIS of the CPE membrane was sandwiched between two stainless steel (SS) blocking electrodes to determine the ionic conductivity, and performed on the AC impedance method using a frequency response analyser multichannel with potentiostat/galvanostat (Bio-Logic Science Instrument VSP-300) in the frequency range from 100 mHz to 7 MHz at RT. In addition, the EIS of CPE–0 and CPE–10 in contact with lithium metal was examined by tests of a Li/CPE/Li symmetric cell with applied 5 μL of liquid electrolyte (1 M LiPF $_6$ in EC: DEC v/v%), which was prepared by sandwiching lithium metal foils, and the CPE in a coin cell 2032 type battery shells as the same the frequency range at RT.

All battery components were assembled within an argon-filled glove box, using 2032-type battery shells with LiFePO_4 (LFP) electrodes measuring 12 mm in diameter and loaded with approximately 2 mg of active material. During the assembly process, 5 μL of liquid electrolyte was applied to the surface of the composite polymer electrolyte membrane to minimize interface impedance at the cathode and Li metal anode. The LFP cathode was prepared with a composition of active material, Super-P, and PVDF binder in a weight ratio of 7:2:1, respectively. NMP solvent was added to these mixtures, and the well-mixed slurry was cast onto aluminum foil using the doctor blade technique. The cathode film was dried at 80°C for 6 h and dried under vacuum at 80°C for 12 h to remove residual solvent. The mass loading of active

materials on each aluminum current collector for the coin cell was approximately 2 mg.

3. Results and discussion

The perovskite $\text{Li}_{0.5}\text{La}_{2/3-x}\text{TiO}_3$ (LLTO)-types ($0.04 < x < 0.16$) with ABO_3 structure shown in Fig. 1 has Li, La (La-rich and La-poor layers), and vacancies occupying the A-sites, and Ti-O occupying B sites that are octahedrally coordinated by oxygen [26,42]. The stack layer of LLTO consists of La-rich and La-poor layers, in which Li^+ -ion migration mainly occurs on the La-poor layers. The mechanism of Li^+ -ion migration was explained by the movement through O_4 windows on a high concentration of vacancies, in which Li^+ -ion conduction between the neighboring vacant A-site was connected with O_4 windows or a bottleneck. The O_4 windows or bottleneck of cubic-LLTO ($Pm\bar{3}m$) structure are larger than those of other structures such as the tetragonal ($P4/mmm$) and orthorhombic ($Pmma$) structures owing to their larger lattice parameters. [32, 34,42,43]. Therefore, Li^+ -ion conduction of cubic-LLTO structure often exhibits high ionic conductivity. The structure of LLTO affects Li^+ -ion conduction; in addition, the conduction depends on factors such as lithium and vacancy concentrations, number of grains, ionic radii of other A and B atoms, temperature, and pressure. Ionic conduction could be improved by enhancing ionic conductivity through three approaches: (I) the La-site was substituted by Sr^{2+} with larger ionic radius to enlarge O_4 windows or bottleneck. (II) The Ti-site was substituted by Ta^{5+} with a larger ionic radius to expand the Ti-O bonding. (III) After co-substitution, the samples maintained a cubic structure with a large area of O_4 windows or bottleneck.

Fig. 2(a) shows the XRD patterns of $\text{Li}_{0.5}\text{La}_{0.5-x}\text{Sr}_x\text{Ti}_{1-x}\text{Ta}_x\text{O}_3$ ($0 \leq x \leq 0.12$) powders, which were obtained following the sintering of the ground pellets. The main phases of all samples present a cubic perovskite structure (ICDD #01-089-4928) with the space group $Pm\bar{3}m$, and a small amount of Li_2TiO_3 phase of samples $x = 0, 0.01$ and 0.03 , whereas at samples of $x = 0.06, 0.09$ and 0.12 the $\text{Li}_2\text{Ti}_3\text{O}_7$ phases are observed [44,45]. The undoped lithium sample with a high concentration of 0.5 is closely related to the Sr or Ge doped cubic-structured $\text{Li}_{0.35}\text{La}_{0.5}\text{TiO}_3$ [41,47]. However, $\text{Li}_{0.5}\text{La}_{0.5}\text{TiO}_3$ and $\text{Li}_{0.35}\text{La}_{0.55}\text{TiO}_3$ differ in that the undoped $\text{Li}_{0.5}\text{La}_{0.5}\text{TiO}_3$ sample adopts a cubic structure [46,48,49], whereas $\text{Li}_{0.35}\text{La}_{0.5}\text{TiO}_3$ exhibits a tetragonal structure [33].

The co-doping of Sr and Ta was confirmed by XRD, which indicated that Sr^{2+} and Ta^{5+} were substituted in the LLTO structure. To reveal the effects of the dopants, the strongest peak in the XRD pattern was magnified for ease of comparison, as shown in Fig. 2(b). With an increasing amount of A-site La^{3+} ($r = 1.36 \text{ \AA}$) substituted by

Sr^{2+} ($r = 1.44 \text{ \AA}$) and B-site Ti^{4+} ($r = 0.605 \text{ \AA}$) substituted by Ta^{5+} ($r = 0.640 \text{ \AA}$) with a larger ionic radius. The XRD peaks shifted to the low-angle region, indicating a positive relationship between the Sr^{2+} and Ta^{5+} doping concentrations and lattice expansion (Table 1). In addition, the XRD changes were thoroughly examined using the calculated bond distances (Fig. S-1) corresponding to the La-Ti, La-O, and Ti-O bond distances, which increased with increasing Sr^{2+} and Ta^{5+} contents, resulting in increasing cell volume. Therefore, Sr and Ta are successfully substituted for La and Ti [33,38].

All samples exhibited good densification of approximately 94–97% during the sintering process, which is essential for grain connection for easy Li^+ -ion migration [50]. In addition, the increase in the density of the doped samples with the substitution of the heavy element Ta^{5+} was slightly higher than that of Ti^{4+} , and the good sintering by Ta^{5+} aided in connecting neighboring grains [51,52]. However, the effect of Sr^{2+} on the grain size or density was not significant [33,41].

The cross-sectional microstructures of the $\text{Li}_{0.5}\text{La}_{0.5-x}\text{Sr}_x\text{Ti}_{1-x}\text{Ta}_x\text{O}_3$ ($0 \leq x \leq 0.12$) bulk samples are shown in Fig. 3 (a–f). The grain sizes of all the samples are rectangular, which is characteristic of the unit cell of the cubic perovskite structure [53]. All samples exhibited similar microstructures, such as connect area, and small rectangular particles are connected with neighboring grains. The grains have good densities with only a few visible pores. In addition, the grains have smooth surfaces and are in close contact with each other, indicating that the samples have good densities and mechanical properties. The doped samples with x contents of 0.01–0.09 exhibit larger melting areas, predominantly due to the substitution of Ti^{4+} with Ta^{5+} resulting in improved sintering ability. This process results in a low number of visible pores in the samples. However, the separation of grains in the doped sample with x content of 0.12 can be observed because of the increased Ta^{5+} content, thereby influencing the large liquid phase during the sintering process. Subsequently, during cooling, the domain boundary mismatch and low diffusion capacity of Ta^{5+} lead to an increase in the number of grains [38]. We observed a decrease in the mean grain size with increasing x content.

Fig. 4 shows a histogram plotted using the ImageJ software retrieved from a SEM image obtained for measuring the grain size. The grain size of the undoped $\text{Li}_{0.5}\text{La}_{0.5}\text{TiO}_3$ sample is approximately $6.97 \mu\text{m}$, and doped samples with $x = 0.01, 0.03, 0.06, 0.09$ have grain sizes of approximately 6.85, 6.73, 6.30, and $5.38 \mu\text{m}$. The grain sizes slightly decreased with increasing doping contents and blended with the large melting area. Furthermore, the average grain size of the doped sample $x = 0.12$ decreased to approximately $4.21 \mu\text{m}$ corresponding to the increasing Ta^{5+} contents to induce the number of grains.

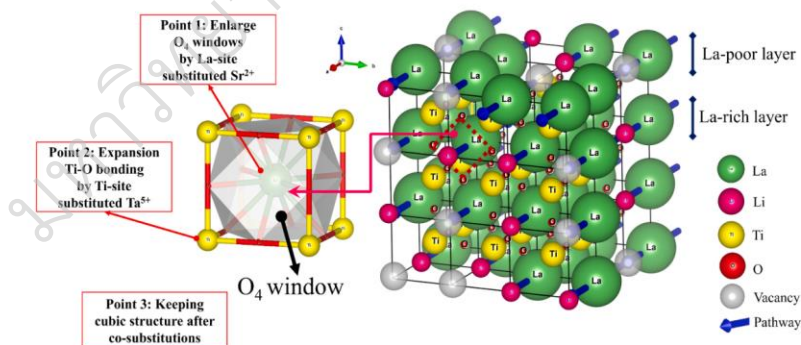


Fig. 1. Crystal structure of Perovskite $\text{Li}_{0.5}\text{La}_{2/3-x}\text{TiO}_3$ (LLTO)-type with ($0.04 < x < 0.16$).

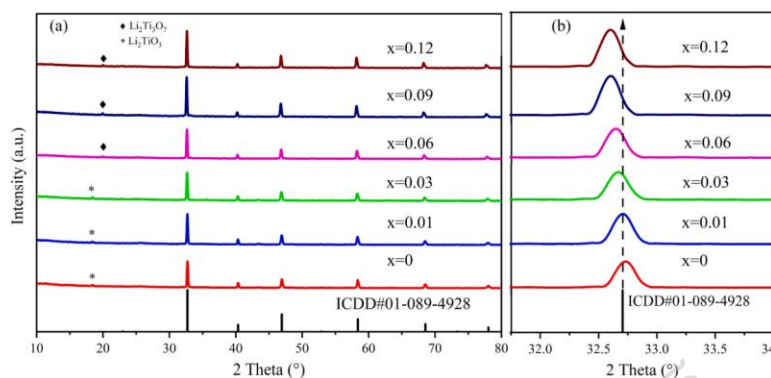


Fig. 2. XRD pattern of (a) $\text{Li}_{0.5-x}\text{La}_{0.5-x}\text{Sr}_x\text{Ti}_{1-x}\text{Ta}_x\text{O}_3$ ($0 \leq x \leq 0.12$) sintered powders, and (b) the 2Theta of $31.5\text{--}34^\circ$.

Table 1

The data of all samples of lattice parameter, cell volume, density, and relative density for $\text{Li}_{0.5-x}\text{La}_{0.5-x}\text{Sr}_x\text{Ti}_{1-x}\text{Ta}_x\text{O}_3$ ($0 \leq x \leq 0.12$).

Sample	Contents	Lattice parameter (Å)	Cell Volume (Å ³)	Density (g/cm ³)	Relative density (%)
$\text{Li}_{0.5}\text{La}_{0.5}\text{TiO}_3$	$x = 0$	3.8739(4)	58.1378(1)	4.55	94.10
$\text{LLSr}_{0.01}\text{TTa}_{0.01}\text{O}_3$	$x = 0.01$	3.8756(2)	58.2134(8)	4.57	94.55
$\text{LLSr}_{0.03}\text{TTa}_{0.03}\text{O}_3$	$x = 0.03$	3.8760(2)	58.2315(0)	4.60	95.34
$\text{LLSr}_{0.06}\text{TTa}_{0.06}\text{O}_3$	$x = 0.06$	3.8791(3)	58.3717(8)	4.61	95.48
$\text{LLSr}_{0.09}\text{TTa}_{0.09}\text{O}_3$	$x = 0.09$	3.8824(5)	58.5217(9)	4.69	97.68
$\text{LLSr}_{0.12}\text{TTa}_{0.12}\text{O}_3$	$x = 0.12$	3.8856(7)	58.6675(2)	4.72	97.62

To discern the doping composition and distribution of Sr and Ta in the $\text{LLSr}_{0.09}\text{TTa}_{0.09}\text{O}_3$ pellet, the cross-sectioned non-polished areas of the sample were observed by EDX mapping. Fig. 5 shows a pellet with a

homogeneous elemental distribution of O, La, Sr, Ti, and Ta, throughout the sample. This confirms that Sr and Ta were successfully co-doped into the cubic-LLTO structure. The EDX analysis in Fig. S-2 demonstrates that the Sr and Ta substitution contents in all the samples align with the expected stoichiometric ratios. Furthermore, the Li concentration in the undoped $\text{Li}_{0.5}\text{La}_{0.5}\text{TiO}_3$, as measured by ICP-OES, is approximately 1.871%wt., aligning with the calculated Li content of 2.055%wt.

The XPS was performed to acquire further information on the composition and chemical state of Ta and Sr co-doped $\text{LLSr}_{0.09}\text{TTa}_{0.09}\text{O}_3$ ($x = 0.09$). The main peaks of La, Sr, Ti, and Ta shown in Fig. 6 confirm the substitution at the La and Ti sites. The component centers of La 3d are separated into spin orbits of La $3d_{5/2}$ at 834.1 and 838.3 eV, and La $3d_{3/2}$ at 851.2 and 855.3 eV. The La 3d orbital was measured for the $\text{LLSr}_{0.09}\text{TTa}_{0.09}\text{O}_3$ sample, and the confirmation of La^{3+} in this sample is in accordance with the previous study shown in Fig. 6(a) [33]. The Sr 3d spectrum had a Sr $3d_{5/2}$ peak at 133.1 eV, and Sr $3d_{3/2}$ peak at 134.7 eV,

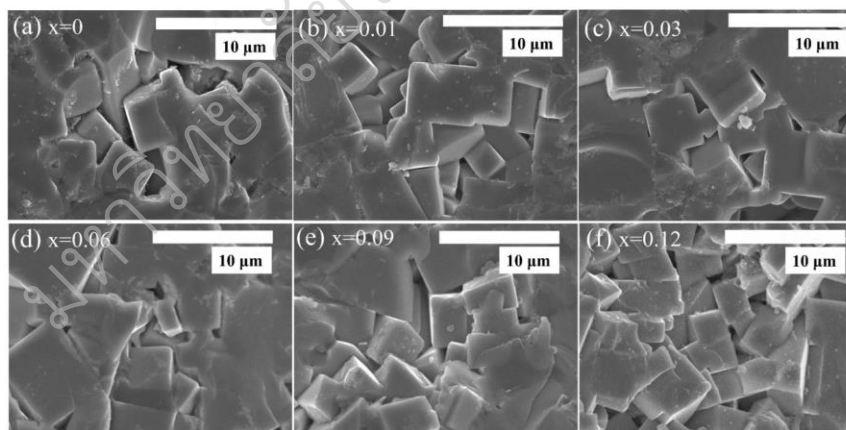


Fig. 3. The SEM of bulk samples (a) undoped $x = 0$, (b) $x = 0.01$, (c) $x = 0.03$, (d) $x = 0.06$, (e) $x = 0.09$, and (f) $x = 0.12$.

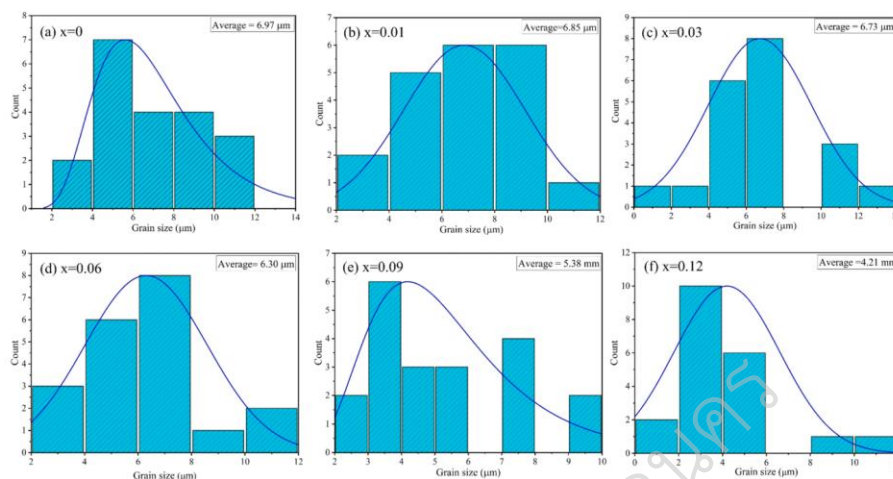


Fig. 4. The histograms of grain size of bulk samples (a) undoped $x = 0$, (b) $x = 0.01$, (c) $x = 0.03$, (d) $x = 0.06$, (e) $x = 0.09$, and (f) $x = 0.12$.

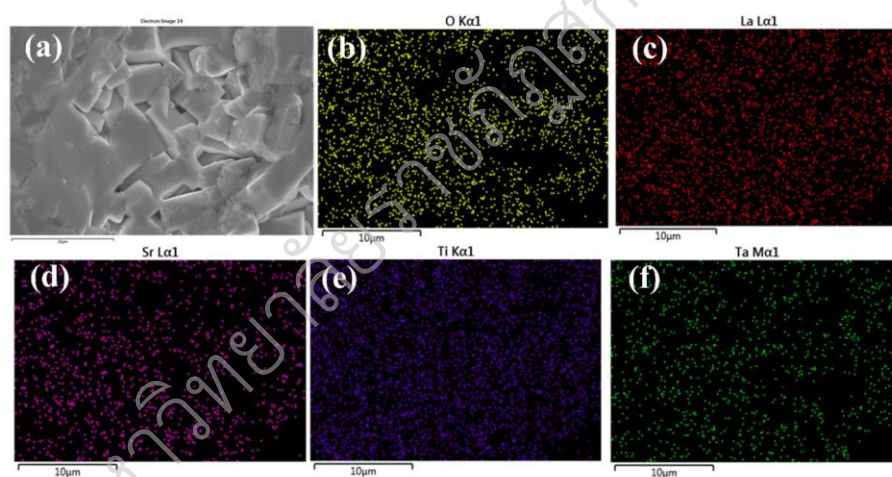


Fig. 5. The elemental mapping of the images of $\text{LLSr}_{0.09}\text{TTa}_{0.09}\text{O}_3$ (a) SEM surface, (b) Oxygen, (c) Lanthanum, (d) Strontium, (e) Titanium, and (f) Tantalum.

which correspond to the $3d_{5/2}$ and $3d_{3/2}$ peaks of the Sr^{2+} -containing oxides, respectively, demonstrating that La^{3+} was partially substituted by Sr^{2+} in the LLTO pellet (Fig. 6(b)) [51]. The Ti 2p XPS spectrum consists of two peaks centered at Ti $2p_{3/2}$ at 458.1 eV, and Ti $2p_{1/2}$ at 463.8 eV, which correspond to Ti^{4+} ; no other centered peaks corresponding to Ti^{3+} are observed in the low-energy side in Fig. 6(c). Analyzing the Ti 2p spectra, we observed that the main peaks originate from Ti^{4+} . The $\text{Ti}^{3+}/\text{Ti}^{4+}$ area ratios decreased with increasing Ta^{5+}

doping contents from 0.14 to 0.03 in the undoped and doped ($x = 0.09$) samples, as shown in Fig. S-3. The reduction in the peak area of Ti^{3+} and Ti^{2+} in the spectra of doped samples is a crucial factor in the substitution of Ta^{5+} or changes in the Ti-site content. Furthermore, the decomposition of Ti^{4+} to Ti^{3+} significantly accelerates dendrite formation and the induction of short circuits in battery cells with a Li metal anode. Therefore, reducing the amount of Ti^{3+} can lead to a decrease in short circuits, as evidenced by previous studies [52–55]. In addition, the Ta

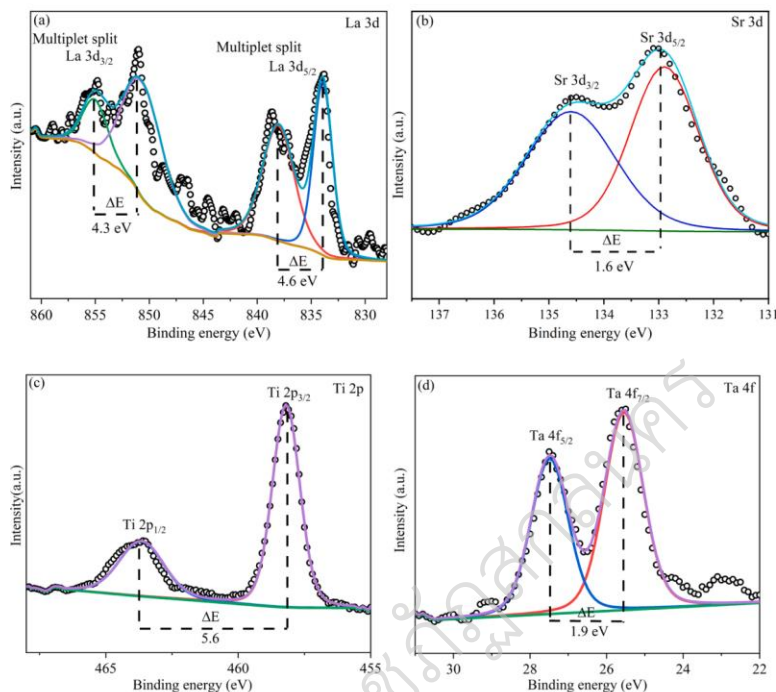


Fig. 6. The XPS analysis of (a) La 3d, (b) Sr 3d, (c) Ti 2p, and (d) Ta 4f of cubic-perovskite $\text{LLSr}_{0.09}\text{TTa}_{0.09}\text{O}_3$ sample.

4f peak could be deconvoluted into two peaks centered at $4f_{7/2}$ at 25.4 eV, and $4f_{5/2}$ at 27.3 eV, which could be attributed to Ta^{5+} in (Fig. 6(d)).

EIS was performed at RT (298 K) to calculate the ionic conductivity and activation energy of Li^+ migration in the solid electrolyte. The EIS plots of all samples are composed of two semicircles at high frequencies (1 Hz–18 MHz) and an approximately straight line at low frequencies. The total resistance of all samples was attributed to the grain and grain boundary resistances and then fitted with the equivalent circuit model shown in Fig. 7. In addition, the equivalent circuit depends on the cell structure; wherein, R_g and CPE_g are the resistance and constant phase element of Li^+ migration in the grain, respectively. R_{gb} and CPE_{gb} represent the resistance and constant phase element for Li^+ migration across the grain boundary, respectively; and CPE_{el} is affected by the polarization between the Au blocking electrodes. The total ionic conductivity was calculated using Eq. (1):

$$\sigma_{\text{total}} = \frac{L}{R_{\text{total}} \times A} \quad (1)$$

where σ_{total} , R_{total} , A , and L represent the total conductivity, total resistance (grain + grain boundary resistance), cross-sectional surface area, and thickness of the pellet, respectively.

Fig. 7(a) shows the grain impedance of $\text{Li}_{0.5-x}\text{La}_{0.5-x}\text{Sr}_x\text{Ti}_{1-x}\text{Ta}_x\text{O}_3$ samples with varying amounts of x ($0 \leq x \leq 0.12$) at 298 K. The substitution of $x = 0.01$ and 0.03 dopant contents can enhance the grain

conductivity of the samples by increasing the conductivity due to bottleneck expansion and increasing the unit cell volume as the lattice parameter increases. However, this phenomenon originates because of the restricted space of the A-site vacancies that impact ionic conductors. In this case, the optimal bottleneck size required for Li^+ -ion diffusion was determined. Notably, excess doping, a factor that influences ionic conductivity, leads to a significant reduction in the conductivity [41].

Nevertheless, as shown in Fig. 7(b), the grain boundary conductivity resistance decreases with increasing x content. The grain boundary resistance begins decreasing for $x = 0.01$ and reaches the smallest value at $x = 0.09$, corresponding to the highest total ionic conductivity and an expanding lattice constant with a bottleneck in the unit cell. Additionally, the partial substitution of Ti–O bonds with Ta^{5+} with a larger ionic radius increases the interatomic Ti–O bond distance, corroborating the bottleneck expansion and TiO_6 filling [41,53]. However, the reduction in samples with $x = 0.12$ was influenced by over-doping and a low diffusion coefficient of Ta^{5+} , which resulted in structure-induced grain separation and an increasing number of grains. This phenomenon, as shown in the SEM image in Fig. 3(f), interrupts the Li^+ migration.

The calculations of R_g , R_{gb} , R_{total} , σ_g , σ_{gb} , and σ_{total} for all samples are listed in Table 2. The LLTO structure material system has a boundary impedance that is much larger than the bulk impedance, and the total conductivity is dominated by the grain boundary conductivity. The highest σ_{total} is $4.12 \times 10^{-5} \text{ S}\cdot\text{cm}^{-1}$ at 298 K in $\text{LLSr}_{0.09}\text{TTa}_{0.09}\text{O}_3$ which is approximately 2.7 times higher than that of the undoped sample $1.49 \times 10^{-5} \text{ S}\cdot\text{cm}^{-1}$.

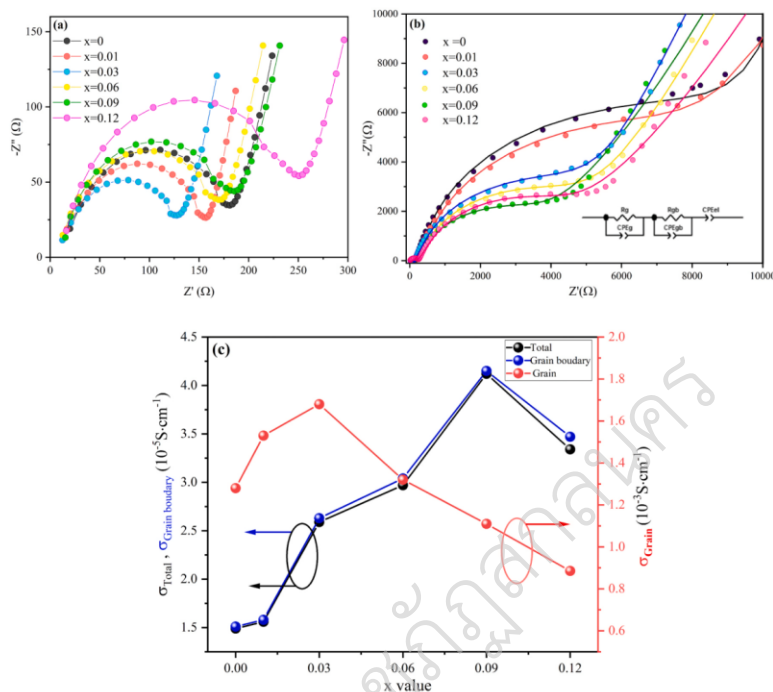


Fig. 7. EIS plots of $\text{Li}_{0.5-x}\text{La}_{0.5-x}\text{Sr}_x\text{CrTi}_{1-x}\text{Ta}_0.5\text{O}_3$ ($0 \leq x \leq 0.12$) at 298 K (a) grain impedance, (b) grain boundary impedance with equivalent circuit model, and (c) conductivities of all specimens.

Table 2

The parameters of bulk resistance (R_b), grain-boundary resistance (R_{gb}) and total resistance (R_{total}) as well as corresponding ionic conductivity grain (σ_g), grain boundary (σ_{gb}), and total (σ_{total}), obtain from the EIS curve fittings and calculations.

Samples	R_b (Ω)	R_{gb} (Ω)	R_{total} (Ω)	σ_g (S cm^{-1})	σ_{gb} (S cm^{-1})	σ_{total} (S cm^{-1})
$\text{Li}_{0.5}\text{La}_{0.5}\text{TiO}_3$	176.44	14996	15172.44	1.28×10^{-3}	1.51×10^{-5}	1.49×10^{-5}
$\text{LLSr}_{0.01}\text{TTa}_{0.01}\text{O}_3$	152.09	14765	14917.09	1.53×10^{-3}	1.58×10^{-5}	1.56×10^{-5}
$\text{LLSr}_{0.03}\text{TTa}_{0.03}\text{O}_3$	129.65	8314.7	8447.05	1.69×10^{-3}	2.63×10^{-5}	2.59×10^{-5}
$\text{LLSr}_{0.06}\text{TTa}_{0.06}\text{O}_3$	173.54	7534.8	7708.34	1.3×10^{-3}	3.04×10^{-5}	2.97×10^{-5}
$\text{LLSr}_{0.09}\text{TTa}_{0.09}\text{O}_3$	207.70	5597	5624.7	1.11×10^{-3}	4.15×10^{-5}	4.12×10^{-5}
$\text{LLSr}_{0.12}\text{TTa}_{0.12}\text{O}_3$	259.41	6608.6	6868.01	8.85×10^{-4}	3.47×10^{-5}	3.34×10^{-5}

Arrhenius plots based on the total, grain, and grain boundaries at different temperatures are shown in Fig. 8(a–c). The conductivities exhibit an excellent linear relationship fit as a function of temperature and are also affected by the migration of Li^+ in the grains and across the grain boundaries, which can be determined by the change in conductivity with temperature, following the Arrhenius equation for ion conductivity, as given in Eq. (2),

$$\sigma_{total} = \sigma_0 \exp\left(\frac{-E_a}{k_B T}\right), \quad (2)$$

where σ_0 , k_B , E_a and T are the pre-exponential factor, Boltzmann constant, activation energy, and absolute temperature, respectively.

As shown in Fig. 8(d), the total activation energy of

$\text{LLSr}_{0.09}\text{TTa}_{0.09}\text{O}_3$ is approximately 0.47 eV. The lowest grain boundary activation energy was approximately 0.38 eV for the $\text{LLSr}_{0.03}\text{TTa}_{0.03}\text{O}_3$ sample, which corresponds to its grain conductivity. Therefore, Sr^{2+} and Ta^{5+} substitution helps expand the bottleneck, allowing Li^+ ions to move more easily, while the strength of partial Ta–O bonds increases and that of Li–O bonds decreases, improving Li-ion mobility and enhancing the ionic conductivity [40,57].

The electronic conductivities σ_e of the undoped sample with $x = 0$ and the doped sample with $x = 0.09$ were calculated using Eq. (3).

$$\sigma_e = \frac{I \cdot l}{U \cdot A}, \quad (3)$$

where U , I , l , and A are the constant DC voltage (4 V), stable current,

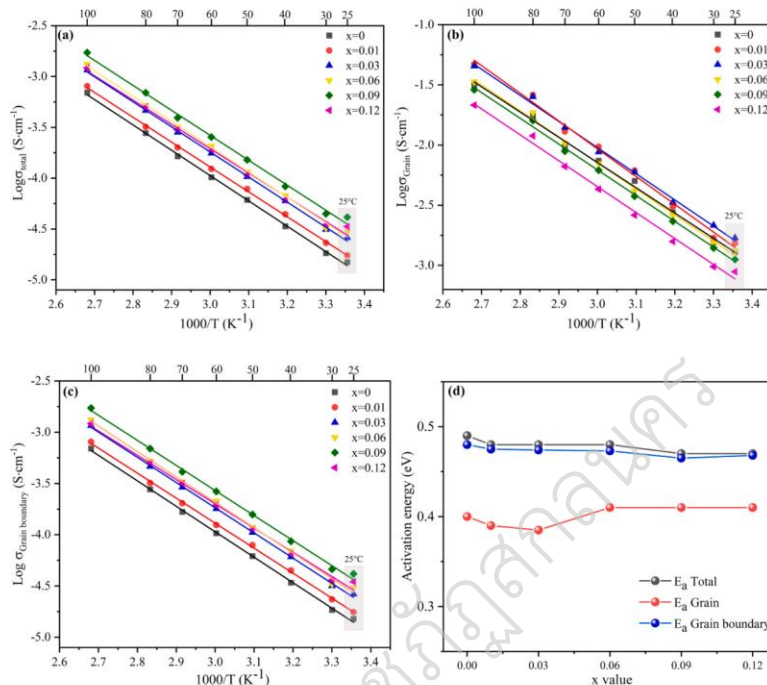


Fig. 8. Arrhenius plot of $\text{LLSr}_{0.99}\text{La}_{0.5-x}\text{Sr,Ti}_{1-x}\text{Ta}_{0.99}\text{O}_3$ ($0 \leq x \leq 0.12$) at a temperature rang 298 to 373 K. (a) total conductivity, (b) grain conductivity, (c) grain boundary conductivity, and (d) the activation energy with doping contents.

thickness of the sample, and surface area of the sample, respectively. Ideally, an excellent ionic conductor should have high ionic conductivity and low electronic conductivity. As shown in Fig. 9, the potentiostatic polarization measurement is applied to survey the leakage current of $\text{Li}_{0.5}\text{La}_{0.5}\text{TiO}_3$ and $\text{LLSr}_{0.99}\text{TTa}_{0.99}\text{O}_3$ ceramics, then the direct current decreases and remains stable at approximately 0.327 and 0.066 μA , respectively. Moreover, the Au electrode is a blocking electrode, and the

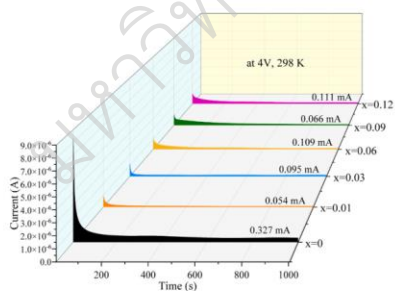


Fig. 9. Potentiostatic polarization patterns of all samples under 4 V at 298 K.

stable current is mainly contributed by electrons [33,40,54–57]. The σ_e value of $\text{LLSr}_{0.99}\text{TTa}_{0.99}\text{O}_3$ (approximately $1.66 \times 10^{-9} \text{ S cm}^{-1}$) is lower than that of the undoped sample (approximately $8.19 \times 10^{-9} \text{ S cm}^{-1}$). Their ionic conductivities of approximately $4.12 \times 10^{-5} \text{ S cm}^{-1}$ demonstrate that $\text{LLSr}_{0.99}\text{TTa}_{0.99}\text{O}_3$ electrolytes are optimal lithium-ion electrolyte materials.

In addition, the practical application of the $\text{LLSr}_{0.99}\text{TTa}_{0.99}\text{O}_3$ electrolyte membrane was evaluated in solid-state Li-ion cells by employing a Li metal anode and a LiFePO_4 cathode operating at 60 °C. However, during the assembly (Fig. S-4), the decomposition of titanium from Ti^{4+} to Ti^{3+} caused by the Li-metal anode leads to an inability to assemble the cells, resulting in short circuits [12]. Consequently, the addition of sintered 10 wt% $\text{LLSr}_{0.99}\text{TTa}_{0.99}\text{O}_3$ powder mixed with PVDF-HFP/LiTFSI (3:2) as the CPE for semi-solid $\text{LiFePO}_4/\text{CPE}/\text{Li}$ full cell assembly, is a viable solution.

The EIS curve exhibits the highest ionic conductivity of $1.35 \times 10^{-3} \text{ S cm}^{-1}$ (Fig. S-5) when using CPE containing CPE-10 at 30 °C, aligning with the ionic conductivity of Li-symmetric cells $2.42 \times 10^{-3} \text{ S cm}^{-1}$ (Fig. S-6). The ionic conductivity of CPE-10 in Li-symmetric cells was calculated from the resistance of CPE (R_{CPE}) using Eq. 1, excluding the charge transfer resistance1 (R_{CT1}) and charge transfer resistance2 (R_{CT2}). Therefore, the CPE-10 was selected to fabricate the full cell $\text{LiFePO}_4/\text{Li}$. Fig. 10 (a) and (b) show the rate capability and voltage profile of the semi-solid $\text{LiFePO}_4/\text{Li}$ full cell, demonstrating a significantly stable voltage plateau of 2.5–4.0 V with capacities of 156.4,

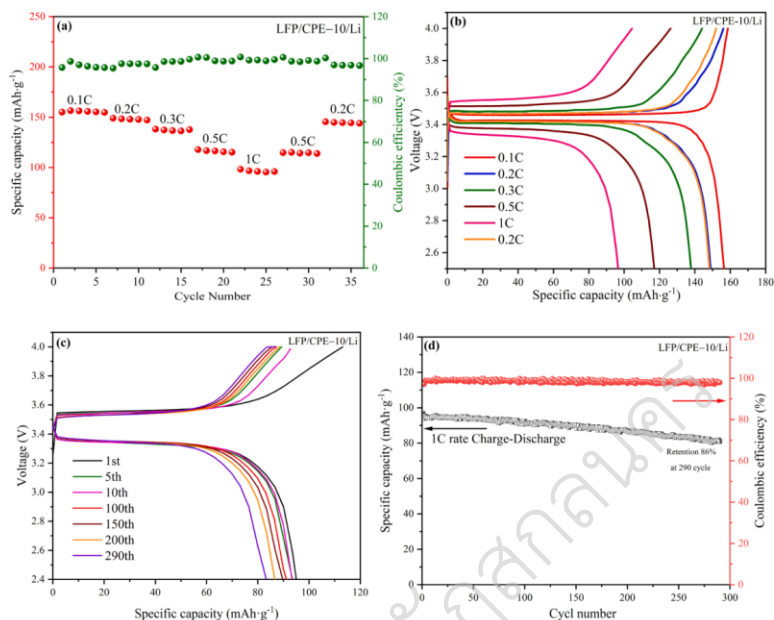


Fig. 10. Electrochemical performance of LiFePO₄/Li full cell (a) rate capability with 0.1 C to 1 C, (b) charge-discharge profile in different C rate, (c) 1 C rate charge-discharge profile stability of 290 cycles, and (d) cycling performance a 1 C rate and coulombic efficiency.

148.7, 137.6, 117.1, and 96.7 mAh·g⁻¹ at 0.1, 0.2, 0.3, 0.5, and 1 C rates, respectively. While returning to 0.2 C, the reversible capacity recovers to 145.5 mAh·g⁻¹, achieving a Coulombic efficiency of 99% during the testing. Fig. 10 (c) and (d) illustrate the long-term cycling performance, voltage profile, and capacity retention of the CPE-10 cells at 1 C rate, corresponding to voltage profile and specific capacity of 80.9 mAh·g⁻¹ with Coulombic efficiency of 98% and capacity retention of approximately 86% at 290 cycles. These findings demonstrate the feasibility of this design for practical applications in semi-solid-state Li batteries with LLSr_{0.09}TTa_{0.09}O₃ perovskite materials.

4. Conclusions

Li_{0.5}La_{0.5}TiO₃ cubic perovskites co-substituted with Sr and Ta with similar doping contents ($x = 0 - 0.12$) were successfully synthesized using a solid-state reaction. All samples exhibited a cubic structure with the space group $Fm\bar{3}m$ and an increasing lattice parameter in the substituted samples. This suggests enhancement of the A site as a bottleneck for Li⁺ migration. Furthermore, the average bond length of the B site was enhanced by the partial substitution with Sr²⁺ and Ta⁵⁺ which increased the highest grain conductivity at $x = 0.03$. However, the grain boundary conductivity, which mainly contributes to the total conductivity, increased with increasing Sr²⁺ and Ta⁵⁺ contents, reaching a maximum at $x = 0.09$. The LLSr_{0.09}TTa_{0.09}O₃ sample achieved the highest total ionic conductivity at approximately 4.12×10^{-5} S·cm⁻¹ at 298 K, with the lowest activation energy at 0.47 eV. Moreover, LLSr_{0.09}TTa_{0.09}O₃ exhibited good separation properties with extremely low electronic conductivity of 1.66×10^{-9} S·cm⁻¹. A practical solution was adopted using perovskite LLSr_{0.09}TTa_{0.09}O₃ with full LiFePO₄/Li

cells, in which 10 wt% polymer electrolyte was mixed to prevent the detrimental effects of Ti⁴⁺ decomposition to Ti³⁺, which could lead to short-circuiting of the battery cells. The assembled LFP/CPE-10/Li full battery exhibited a specific discharge capacity of 156 mAh·g⁻¹ at 0.1 C rate and 1 C charge-discharge capacity retention rate of 86% after 290 cycles at RT.

CRedit authorship contribution statement

Paengson Supasit: Writing – original draft, Methodology, Investigation, Formal analysis, Data curation, Conceptualization. **Pilasuta Panida:** Methodology, Investigation, Formal analysis. **Mori Daisuke:** Writing – review & editing, Resources, Methodology, Funding acquisition, Conceptualization. **Seetawan Tosawat:** Writing – review & editing, Supervision, Resources, Project administration, Funding acquisition, Conceptualization.

Declaration of Competing Interest

The authors declare that they have no known competing financial interests or personal relationships that could have appeared to influence the work reported in this paper.

Data Availability

No data was used for the research described in the article.

Acknowledgments

This research project is supported by the National Research Council of Thailand (NRCT) grant number NRCT5-RGJ63015-149 through the Royal Golden Jubilee 22 scholarship (RGJ22) Ph.D. Program, and Fundamental fund project of Sakon Nakhon Rajabhat University grant number 3/2566. The authors thank the staff of the Imanishi group at Mie University for characterizations and discussions.

Appendix A. Supporting information

Supplementary data associated with this article can be found in the online version at doi:10.1016/j.jallcom.2024.173512.

References

- Y. Ma, J. Wan, Y. Yang, Y. Ye, X. Xiao, D.T. Boyle, Y. Cui, Scalable, ultrathin, and high-temperature-resistant solid polymer electrolytes for energy-dense lithium metal batteries, *Adv. Energy Mater.* 12 (15) (2022) 2103720.
- H. Sun, S. Kang, L. Cui, Prospects of LLZO type solid electrolyte: from material design to battery application, *Chem. Eng. J.* (2022) 140375.
- L. Du, B. Zhang, X. Wang, C. Dong, L. Mai, L. Xu, 3D frameworks in composite polymer electrolytes: synthesis, mechanisms, and applications, *Chem. Eng. J.* (2022) 138787.
- L. Zhang, L. Xu, Y. Nian, W. Wang, Y. Han, L. Luo, Atomic defect mediated Li-ion diffusion in a lithium lanthanum titanate solid-state electrolyte, *ACS nano* 16 (4) (2022) 6898–6905.
- Y. Zhang, Z. Zheng, X. Liu, M. Chi, Y. Wang, Fundamental relationship of microstructure and ionic conductivity of amorphous LLTO as solid electrolyte material, *J. Electrochem. Soc.* 166 (4) (2019) A515.
- Feng, Y., Wang, M., Gao, L., He, Z., Chen, K., Li, Z., & Lin, Y. (2022). Novel Fast Ionic Conductor Ceramic Composite Separator for High-performance Safe Li-ion Power Batteries. *Journal of Materiomics*.
- S.G. Booth, A.J. Nedoma, N.N. Anthonisamy, P.J. Baker, R. Boston, H. Bronstein, S. A. Cussen, Perspectives for next generation lithium-ion battery cathode materials, *Appl. Mater.* 9 (10) (2021) 109201.
- H. Zhang, H. Zhao, M.A. Khan, W. Zou, J. Xu, L. Zhang, J. Zhang, Recent progress in advanced electrode materials, separators and electrolytes for lithium batteries, *J. Mater. Chem. A* 6 (42) (2018) 20564–20620.
- Z. Jiang, H. Xie, S. Wang, X. Song, X. Yao, H. Wang, Perovskite membranes with vertically aligned microchannels for all-solid-state lithium batteries, *Adv. Energy Mater.* 8 (27) (2018) 1801433.
- Z. Qin, X. Meng, Y. Xie, D. Qian, H. Deng, D. Mao, Y. Huang, Fast Li-ion transport pathways via 3D continuous networks in homogeneous garnet-type electrolyte for solid-state lithium batteries, *Energy Storage Mater.* 43 (2021) 190–201.
- Z. Wan, K. Shi, Y. Huang, L. Yang, Q. Yun, L. Chen, Y.B. He, Three-dimensional alloy interface between Li₆4La₃Zr₁4Ta₀6O12 and Li metal to achieve excellent cycling stability of all-solid-state battery, *J. Power Sources* 505 (2021) 230962.
- L. Xu, T. Peng, J. Huang, Y. Hu, L. Zhang, L. Lao, Structural heterogeneity induced Li dendrite growth in Li_{0.33}La_{0.56}TiO₃ solid-state electrolytes, *ACS Appl. Energy Mater.* 5 (3) (2022) 3741–3747.
- Lu, X., Li, X., Duan, M., Hai, J., & Liu, S. (2022). Preparation of hybrid perovskite-type Li_{0.33}La_{0.56}TiO₃ by adding ionic liquids. *Journal of Rare Earths*.
- A. Daidouh, C. Pico, M.L. Veiga, Structure features and ionic conductivity of the AM₄(PO₄)₃ orthophosphates (A = Na, K, Rb; M = Ni, Mn), *Solid State Ion.* 124 (1–2) (1999) 109–117.
- J. Li, Y. Chen, Z. Tian, Y. Wang, L. Guo, Mechanisms and principles of Na₃V₂(PO₄)₃ modification by carbon materials, *Curr. Opin. Electrochem.* (2022) 101200.
- A. Rossbach, F. Tietz, S. Grieshammer, Structural and transport properties of lithium-conducting NASICON materials, *J. Power Sources* 391 (2018) 1–9.
- Ö.U. Kudu, T. Famprikis, B. Elogut, M.D. Braid, T. Le Mercier, M.S. Islam, C. Masquelier, A review of structural properties and synthesis methods of solid electrolyte materials in the LiZS–P2S5 binary system, *J. Power Sources* 407 (2018) 31–43.
- S. Zhao, W. Jiang, X. Zhu, M. Ling, C. Liang, Understanding the synthesis of inorganic solid-state electrolytes for Li ion batteries: Features and progress, *Sustain. Mater. Technol.* (2022) e00491.
- J. Li, Y. Li, J. Cheng, Q. Sun, L. Dai, N. Ci, L. Ci, In situ modified sulfide solid electrolyte enabling stable lithium metal batteries, *J. Power Sources* 518 (2022) 230739.
- Y. Li, J. Cheng, J. Li, Z. Zeng, Y. Guo, H. Zhang, L. Ci, Indium doped sulfide solid electrolyte with tamed lithium dendrite and improved ionic conductivity for all-solid-state battery applications, *J. Power Sources* 542 (2022) 231794.
- R. Murugan, V. Thangadurai, W. Weppner, Fast lithium ion conduction in garnet-type Li_{1-x}La_{2x/3}Zr_{x/3}O₁₂, *Angew. Chem. Int. Ed.* 46 (41) (2007) 7778–7781.
- A.J. Samson, K. Hofstetter, S. Bag, V. Thangadurai, A bird's-eye view of Li-stuffed garnet-type Li_{1-x}La_{2x/3}Zr_{x/3}O₁₂ ceramic electrolytes for advanced all-solid-state Li batteries, *Energy Environ. Sci.* 12 (10) (2019) 2957–2975.
- Y. Kim, I. Waluyo, A. Hunt, B. Yildiz, Avoiding CO₂ improves thermal stability at the interface of Li_{1-x}La_{2x/3}Zr_{x/3}O₁₂ electrolyte with layered oxide cathodes, *Adv. Energy Mater.* 12 (13) (2022) 2102741.
- V. Gajraj, A. Kumar, S. Indris, H. Ehrenberg, N. Kumar, C.R. Mariappan, Influence of Al on structure and ion transport in garnet-type Li_{1-x}La_{2x/3}Al_{x/3}Zr_{x/3}O₁₂ solid electrolytes for Li-ion batteries, *Ceram. Int.* (2022).
- Y. Tian, Y. Zhou, W. Wang, Y. Zhou, Effects of Ca–Ba Co-doping on the morphology and conductivity of Li_{1-x}La_{2x/3}Zr_{x/3}O₁₂ electrolyte synthesized by sol-gel method, *Ceram. Int.* 48 (1) (2022) 963–970.
- Y. Inaguma, C. Lique, M. Itoh, T. Nakamura, T. Uchida, H. Ikuta, M. Wakihara, High ionic conductivity in lithium lanthanum titanate, *Solid State Commun.* 86 (10) (1993) 689–693.
- J. Wu, L. Chen, T. Song, Z. Zou, J. Gao, W. Zhang, S. Shi, A review on structural characteristics, lithium ion diffusion behavior and temperature dependence of conductivity in perovskite-type solid electrolyte Li₃La_{2/3-x}TiO₃, *Funct. Mater. Lett.* 10 (03) (2017) 1730002.
- Y. Kong, Y. Li, J. Li, C. Hu, X. Wang, J. Lu, Li ion conduction of perovskite Li_{0.375}Sr_{0.625}Ti_{0.25}Ta_{0.75}O₃ and related compounds, *Ceram. Int.* 44 (4) (2018) 3947–3950.
- Lu, X., Duan, M., Xiang, J., Liang, Y., & Liu, S. (2022). Enhancement of ionic conductivity and fracture toughness by infiltrating porous Li_{0.33}La_{0.56}TiO₃ pellets. *Journal of Rare Earths*.
- Feng, Y., Wang, M., Gao, L., He, Z., Chen, K., Li, Z., & Lin, Y. (2022). Novel Fast Ionic Conductor Ceramic Composite Separator for High-performance Safe Li-ion Power Batteries. *Journal of Materiomics*.
- X. He, S. Li, G. Cao, J. Hu, J. Zhang, R. Qiao, G. Shao, In situ atomic-scale engineering of the chemistry and structure of the grain boundaries region of Li₃La_{2/3-x}TiO₃, *Scr. Mater.* 185 (2020) 134–139.
- M.E. Ling, Y. Jiang, Y. Huang, Y. Zhou, X. Zhu, Enhancement of ionic conductivity in Li_{0.5}La_{0.5}TiO₃ with Ag nanoparticles, *J. Mater. Sci.* 55 (9) (2020) 3750–3759.
- R. Li, K. Liao, W. Zhou, X. Li, D. Meng, B. Cai, Z. Shao, Realizing fourfold enhancement in conductivity of perovskite Li_{0.33}La_{0.557}TiO₃ electrolyte membrane via a Sr and Ta co-doping strategy, *J. Membr. Sci.* 582 (194–202) (2019).
- T. Teranishi, A. Kouchi, H. Hayashi, A. Kobimoto, Dependence of the conductivity of polycrystalline Li_{0.33}Ba_{1-x}La_{0.55-2x/3}TiO₃ on Ba loading, *Solid State Ion.* 263 (2014) 33–38.
- J.Q. Zheng, Y.F. Li, R. Yang, G. Li, X.N. Ding, Lithium ion conductivity in the solid electrolytes (Li_{0.25}La_{0.25})_{1-x}M_{0.25}NbO₃ (M = Sr, Ba, Ca, x = 0.125) with perovskite-type structure, *Ceram. Int.* 43 (2) (2017) 1716–1721.
- M. Itoh, Y. Inaguma, W.H. Jung, L. Chen, T. Nakamura, High lithium ion conductivity in Bi³⁺ perovskite-type compounds Ln_{1/2}Li_{1/2}TiO₃ (Ln = La, Pr, Nd, Sm), *Solid State Ion.* 70 (1994) 203–207.
- Y. Jiang, Y. Huang, Z. Hu, Y. Zhou, J. Zhu, X. Zhu, Effects of B-site ion (Nb⁵⁺) substitution on the microstructure and ionic conductivity of Li_{0.5}La_{0.5}TiO₃ solid electrolytes, *Ferroelectrics* 554 (1) (2020) 89–96.
- R. Yao, Z.G. Liu, Z.Y. Ding, Y.J. Jin, G. Cao, Y.H. Wang, J.H. Ouyang, Effect of Sn or Ta doping on the microstructure and total conductivity of perovskite Li_{0.24}La_{0.557}TiO₃ solid electrolyte, *J. Alloy. Compd.* 844 (2020) 156023.
- Vezzu, K., García-González, E., Pagot, G., Urones-Garrate, E., Sotomayor, M.E., Varela, A., & Di Noto, V. (2022). Effect of Relaxations on the Conductivity of La_{1/2x}/Li_{1/2-x}Ti_{1-x}Al_xO₃ Fast Ion Conductors. *Chemistry of Materials*.
- K. Yu, L. Jin, Y. Li, G. Liu, X. Wei, Y. Yan, Structure and conductivity of perovskite Li_{0.33}La_{0.35}Sr_{0.3}Ti_{0.995}M_{0.005}O₃ (M = Al, Co and In) ceramics, *Ceram. Int.* 45 (18) (2019) 23941–23947.
- S. Zhang, H. Zhao, J. Guo, Z. Du, J. Wang, K. Świerczek, Characterization of Sr-doped lithium lanthanum titanate with improved transport properties, *Solid State Ion.* 336 (2019) 39–46.
- A. Morata-Orrantia, S. García-Martín, M.A. Alario-Franco, Optimization of lithium conductivity in La/Li titanates, *Chem. Mater.* 15 (21) (2003) 3991–3995.
- M. Catti, First-principles modeling of lithium ordering in the LLTO (Li_{1-x}La_{2x/3-x}/TiO₃) superionic conductor, *Chem. Mater.* 19 (16) (2007) 3963–3972.
- A. Chouiekh, A. Tahiri, N.E.H. Boufilla, A. Nfissi, L. Bih, A. Faik, M. Najji, Experimental and DFT analysis of structural, optical, and electrical properties of Li₃La_{2/3-x}TiO₃ (3x = 0.1, 0.3 and 0.5) solid electrolyte, *Ceram. Int.* 49 (15) (2023) 25920–25934.
- A. Jonderian, M. Ting, E. McCalla, Metastability in Li–La–Ti–O perovskite materials and its impact on ionic conductivity, *Chem. Mater.* 33 (12) (2021) 4792–4804.
- M.E. Ling, X. Zhu, Y. Jiang, J. Zhu, Comparative study of solid-state reaction and sol-gel process for synthesis of Zr-doped Li_{0.5}La_{0.5}TiO₃ solid electrolytes, *Ionics* 22 (2016) 2151–2156.
- Z. Hu, J. Sheng, J. Chen, G. Sheng, Y. Li, X.Z. Fu, C.P. Wong, Enhanced Li ion conductivity in Ge-doped Li_{0.33}La_{0.56}TiO₃ perovskite solid electrolytes for all-solid-state Li-ion batteries, *N. J. Chem.* 42 (11) (2018) 9074–9079.
- Y. Deng, S.J. Shang, A. Mei, Y.H. Lin, L.Y. Liu, C.W. Nan, The preparation and conductivity properties of Li_{1-x}La_xTiO₃/inactive second phase composites, *J. Alloy. Compd.* 472 (1–2) (2009) 456–460.
- V. Avila, B. Yoon, R.R.I. Neto, R.S. Silva, S. Ghose, R. Raj, L.M. Jesus, Reactive flash sintering of the complex oxide Li_{0.5}La_{0.5}TiO₃ starting from an amorphous precursor powder, *Scr. Mater.* 176 (2020) 78–82.
- J.H.L. Silva, Y.G.S. Alves, A. Almeida, J.A. Moreira, R. Vilarinho, J.C.A. Santos, R. S. Silva, Study of the ionic conductivity of Li_{0.5}La_{0.5}TiO₃ laser-sintered ceramics, *J. Eur. Ceram. Soc.* 40 (15) (2020) 5619–5625.
- B. Huang, B. Xu, Y. Li, W. Zhou, Y. You, S. Zhong, J.B. Goodenough, Li-ion conduction and stability of perovskite Li_{3/8}Sr_{7/16}Hf_{1/4}Ta_{3/8}O₃, *ACS Appl. Mater. Interfaces* 8 (23) (2016) 14552–14557.
- W.J. Kwon, H. Kim, K.N. Jung, W. Cho, S.H. Kim, J.W. Lee, M.S. Park, Enhanced Li⁺ conduction in perovskite Li_{1-x}La_{2x/3-x}TiO₃ solid-electrolytes via microstructural engineering, *J. Mater. Chem. A* 5 (13) (2017) 6257–6262.

Co–Author

1. Panida Pilasuta, **Supasit Paengson**, Kunchit Singsoog and Tosawat Seetawan.
(2022) “Role of Al Substitution in the Enhancement of High–Temperature Thermoelectric Properties of ZnO Compound.” *Integrated Ferroelectrics*, 222(1), 28–37. **(Quartile 4, Impact Factor 0.7)**
2. Panida Pilasuta, **Supasit Paengson**, Kunchit Singsoog and Tosawat Seetawan.
(2021, September). “P–Ca₃Co₄O₉/n–Zn_{0.98}Al_{0.02}O module for high temperature thermoelectric generator.” In *Journal of Physics: Conference Series* (Vol. 2013, No. 1, p. 012022). IOP Publishing. **(Quartile 4, Impact Factor 0.48)**
3. Suprayoga, E., Putri, W. B., Singsoog, K., **Paengson, S.**, Hanna, M. Y., Nugraha, A. R., ... & Hasdeo, E. H. (2021). Investigation of electron and phonon transport in Bi–doped CaMnO₃ for thermoelectric applications. *Materials Research Bulletin*, 141, 111359. **(Quartile1, Impact Factor 5.4)**
4. Inthachai, S., **Paengson, S.**, Jamradloedluk, J., Seetawan, T. (2021). “Fabrication and simulation of TE modules for a feasibility study on harvesting solar heat energy from roof tiles.” *Journal of Renewable Materials*, 9(10), 1685–1697 **(Quartile 3, Impact Factor 2.1)**
5. Mingmuang, D., Talangkun, **S., Paengson, S.**, & Seetawan, T. (2019, April). “Thermoelectric cell produced from AA1100 aluminium alloy coating on metakaolin by friction surfacing process.” In *Materials Science Forum* (Vol. 947, pp. 130–134). Trans Tech Publications Ltd. **(Quartile 3, Impact Factor 0.5)**

APPENDICE D

RESEARCH VISITING AT MIE UNIVERSITY JAPAN

มหาวิทยาลัยราชภัฏสุราษฎร์ธานี

